NUMERICAL SIMULATIONS OF SOUND GENERATION FROM JET FLOWS THROUGH ORIFICES AND LOBED MIXERS

Kaveh Habibi

Doctor of Philosophy

McGill University

Montreal, Quebec

2019-04-15

Presented in Partial Fulfilment of the Requirements for the

Degree of Doctor of Philosophy

To my father, Ali

ABSTRACT

The design of modern aircraft turbofan engines with low noise emissions requires a thorough understanding of noise generation and absorption phenomena in turbulent mixing jets as well as passive noise reduction devices, *e.g.* lobed mixers or acoustic liners. At the design stage, such understanding should be provided by reliable and accurate prediction tools to avoid prohibitively expensive experiments. Common acoustic prediction tools are either based on semi-empirical models limited to specific applications, or high-order computational fluid dynamics (CFD) codes, involving prohibitive costs for complex problems. The present study investigates the application and validation of a relatively novel approach in Computational Aeroacoustics (CAA) in which the unsteady near-field flow that contains important noise sources is simulated using a three-dimensional Lattice Boltzmann Method (LBM). The far-field sound pressure is predicted using the Ffwocs Williams-Hawkings (FW-H) surface integral method. The effects of turbulence modelling, Reynolds number, Mach number and non-isothermal boundary conditions were tested for canonical jet noise problems. A commercial code, *PowerFLOW*, based on the Lattice Boltzmann kernel was utilized for the simulations. In the first part of this study, turbulent jet simulations were performed for various configurations including a circular pipe, the SMC000 single-stream nozzle, and internal mixing nozzles with various types of forced mixers. Mean flow and turbulence statistics were obtained as well as sound pressure levels in the far-field. Predictions were compared with experimental data at similar operating conditions for verification. In most cases in which direct comparison were made with experimental data, 1/3 octave band spectral levels were found in good agreement with measured values up to Strouhal number (*St*) of ~3.0-4.0, also the overall sound pressure levels from simulation were mostly within ~1.0 dB range of measured sound levels. In all case studies, the actual nozzle including various mixer configurations was included in the computational domain in order to achieve realistic flow conditions. In some cases, inflow conditions needed to be imposed using forcing functions in order to mimic experimental conditions and induce enough perturbation for jet transition to turbulence. Both regular and high-order D3Q19 LBM schemes were tested in this study. The former method was restricted to a relatively low Mach numbers up to 0.5, where the latter can technically simulate the flow-field within the higher subsonic range through high-order terms in the discretized momentum equations. In another parallel study, the problem of sound absorption by turbulent jets was studied using a similar Lattice Boltzmann technique. The sound and turbulent flow inside a standing wave tube terminated by a circular orifice in presence of a mean flow was simulated. The computational domain comprised a standard virtual impedance tube apparatus in which sound waves were produced by periodic pressure imposed at one end. A turbulent jet was formed at the discharge of a circular orifice plate by the steady flow inside the tube. The acoustic impedance and sound absorption coefficient of the orifice plate were calculated from a wave decomposition of the sound field upstream of the orifice. Simulations were carried out for different excitation frequencies, amplitudes and orifice Mach numbers. Results and trends were in quantitative agreement with available analytical solution and experimental data. Altogether, the work documented here supports the accuracy and validity of the LBM for detailed flow simulations of complex turbulent jets. This method offers some advantages over Navier-Stokes based simulations for internal and external flows.

RÉSUMÉ

La conception de réacteurs d'avions modernes suppose une compréhension approfondie des phénomènes de génération et d'absorption du bruit dans les jets à mélange turbulent ainsi que dans les dispositifs de réduction sonore passifs, tels que les tuyères lobées ou les ailes acoustiques. Dans le but de diminuer les coûts, des outils de prédiction fiables et précis sont indispensables. Ces outils de prédiction usuels sont basés soit sur des modèles semi-empiriques limités dans leur nombre d'applications possibles ou sur des codes de dynamique numérique des fluides d'ordre plus élevé. L'utilisation de ces derniers devant faire face à des défis pour résoudre des problèmes complexes dans des délais raisonnables. La présente étude concerne l'application ainsi que la validation d'une nouvelle approche aéroacoustique numérique dans laquelle la région d'écoulement instable en champ proche est simulée à l'aide d'une méthode de Boltzmann sur Réseau tri-dimensionnelle. La pression acoustique du champ lointain est prédite grâce à la méthode d'intégrale de surface de Ffowcs Williams-Hawkings (FW-H). Les effets de la modélisation de la turbulence, du nombre de Reynolds, du nombre de Mach, et des conditions limites non-isothermes furent testés pour plusieurs problèmes de bruits de jet. Un code commercial, *PowerFLOW*, basé sur la méthode de Boltzmann sur Réseau, fut utilisé dans le cadre des simulations. Dans la première étape de cette étude, des simulations turbulentes de jets furent effectuées pour différentes configurations incluant une pipe circulaire, la tuyère « SMC000 » à flux unique, et divers autres types de tuyères à mélange interne. Les statistiques du débit moyen et de la turbulence furent obtenus, ainsi que la pression acoustique dans le champ lointain. Dans le but de vérifier les résultats, ceux-ci furent par la suite comparés avec des données expérimentales obtenues à des conditions d'opérations similaires. Une concordance raisonnable fut notée. Les différentes configurations de tuyères d'éjection furent incluses dans le domaine de calcul afin d'obtenir des conditions d'écoulement réalistes. Dans certains cas, les conditions d'écoulement durent être imposées à l'afflux, à l'aide de fonctions de forçage. Le but étant d'imiter les conditions expérimentales et d'induire assez de perturbation pour favoriser la transition vers la turbulence. Deux versions du schéma de Boltzmann sur réseau, la version normale et la version D3Q19 d'ordre plus élevé, furent testées dans le cadre de cette étude. La première version est restreinte à un nombre faible de Mach de 0.5. La deuxième permet des simulations d'écoulement à un nombre de Mach subsonique plus élevé, et ce à travers l'inclusion de termes d'ordre élevé dans les équations discrétisées de quantité de mouvement. Dans une seconde partie, la question de l'absorption du son par les jets turbulents fut étudiée grâce à l'aide d'une méthode similaire de Boltzmann sur Réseau. Le bruit et l'écoulement turbulent à l'intérieur d'un tube d'ondes stationnaires, clôturé par un orifice circulaire et en présence d'un débit moyen, furent simulés. Le domaine de calcul comprend un dispositive de tube d'impédance virtuelle dans lequel les ondes sonores sont produites par le biais d'une pression périodiquement appliquée à l'une de ses extrémités. Au sein du tube, le débit moyen a permis la formation d'un jet turbulent à la sortie d'un diaphragme. Par la suite, l'impédance acoustique et le coefficient d'absorption du son du diaphragme furent calculés grâce à une décomposition du champ sonore en amont du diaphragme. Les simulations furent effectuées à différentes fréquences d'excitation, amplitudes et nombre de Mach au niveau du diaphragme. L'analyse des résultats et des tendances a permis de mettre en valeur leur concordance avec les données expérimentales et solutions analytiques. Dans l'ensemble, le présent travail confirme l'exactitude et la validité de la méthode de Boltzmann sur Réseau pour effectuer des simulations détaillées d'écoulements de jets turbulents complexes. Cette méthode offrant par ailleurs des avantages par rapport aux simulations basées sur les équations de Navier-Stokes, que ce soit pour les écoulements internes ou externes.

ACKNOWLEDGEMENTS

I would like to thank my supervisor, Professor Luc Mongeau, for giving me the opportunity to enter the world of aeroacoustics and working on an interesting research project on the application of Lattice Boltzmann Method for simulation of jet noise. I have greatly enjoyed my time working in his research group. I should also thank to Dr. Mihai Mihaescu, Dr. Stephane Moreau, Dr. Jeffery Brgthorson, Dr. Jovan Nedic and Dr. Laurent Mydlarski for their presence in my thesis committee and for their valuable comments and suggestions. Sincere thanks also go to Dr. Siva Nadarajah, ,Dr. Phoi-tack (Charlie) Lew, Dr. Damiano Casalino at Exa Corporation and Dr. Alireza Najafi-Yazdi who provided answers to many questions and shared their experience in jet noise simulation. Special thanks to Hao Gong (M.Sc.) who provided assistance for preparing CAD models and handling some of the simulations for the project and Dr. Yasser Rafat who provided experimental data to validate LBM simulation of acoustic flows; colleagues and friends Shahin Amiri, Mostafa Najafi-Yazdi, Daniel Armstrong, Neda Latifi and Rayane Ait Oubahou who provided a fun and stimulating environment during my stay in Mongeau's research group. My lovely wife and my family members also deserve special acknowledgments for their endless love and support.

This work was partially sponsored by Pratt and Whitney Canada (PWC) and Green Aviation Research and Development Network (GARDN). The rest of the work related to the application of high Mach subsonic Lattice-Boltzmann scheme was supported by Exa Corporation through the supply of academic licenses.

This research was enabled in part by support provided by Calcul Québec (www.calculquebec.ca) and Compute Canada (www.computecanada.ca). Computations were performed on "Colosse" and Mammouth Parallel II clusters under the auspices of Calcul Québec formed by the merger of the Réseau québécois de calcul de haute performance (RQCHP) and the "Consortium Laval UQAM McGill et Est-du-Québec (CLUMEQ)".

Table of contents

Table of tables

Table of figures

Nomenclature

Roman Symbols

A	Area
A_m	Area of the mixing plane
c_0	Reference speed of sound
c_i	Particle speed along i^{th} lattice direction
C_p	Specific heat capacity at constant pressure
C_v	Specific heat capacity at constant volume
C_s	Physical speed of sound
c_s	Lattice speed of sound
D	Diameter
D_m	Diameter of the mixing plane
D_o	Orifice Diameter
E	Macroscopic energy of the fluid particle
e	Internal energy of the fluid particle
F_D	Low-pass filter at downstream region
f	Frequency
f^*	Characteristic frequency
f_m	Cut-off frequency
f_i	Distribution function
f^{eq}	Equilibrium distribution function
g	Gravity
H_{mp}	Height of mixing plane
H_m	Height of mixer lobe
I	Three-dimensional identity tensor

I_a	Acoustic intensity
K	Permeability in porous formulation
L	Nozzle nominal mixing length
L_a	Anechoic length of the impedance tube
L_{sc}	Scalloping depth
l_r	Turbulent characteristic length scale
m	Mass
M	Mach number
M_c	Convective Mach number
M_o	Orifice Mach number
p	Pressure
p_0	Reference pressure
R	Ideal gas constant
Re_D	Jet Reynolds number ($Re_D = U_j D_j / \upsilon_j$)
S	Symmetric parts of the velocity gradient tensor
r	Radial distance
T	Temperature
T_m	Temperature of the mixing plane
T_{ref}	Reference Temperature
t	Time
t_a	Acquisition time
t_s	Settling time
t_t	Transient (Simulation) time
U	Streamwise velocity
$\hat{u}$	Mesoscale particle velocity vector

$\vec{u}$	Macroscopic particle velocity vector
w_i	Weight parameter for lattice model
x,y,z	Cartesian coordinates
S_{ij}	Strain rate tensor
St	Strouhal number
St_o	Orifice Strouhal number
$\hat{x}$	Cartesian coordinate of fluid particle
k	Turbulent kinetic energy
ν	Fluid viscosity

Greek Symbols

α	Thermal expansion coefficient
β^*	Secondary to primary area ratio
Δt	Time resolution
Δr	Space resolution
ε	Turbulent dissipation
Φ	Viscous dissipation terms
γ	Specific heat ratio
κ	Turbulent kinetic energy
λ	Thermal conductivity (diffusivity)
λ^*	Secondary to primary velocity ratio
ρ	Fluid density
ρ_0	Reference density
Γ	Complex wave number
δ^*	Secondary to primary velocity ratio

μ	Dynamic viscosity
μ'	Bulk viscosity
ξ	Normalized frequency
$\underline{\underline{\sigma}}$	Stress tensor
Π	Normalized acoustic pressure
τ	Relaxation or retarded time
$\underline{\underline{\tau}}$	Shear stress tensor
τ_r	Turbulence characteristic time scale
υ	Kinematic viscosity
η	Passability in porous formulation
θ	Observer's angle
Ψ	Acoustic dissipation terms
Ω	Anti-symmetric parts of the velocity gradient tensor
ω	Angular velocity (phase speed)

Other symbols

$(\cdot)_a$	Ambient condition
$(\cdot)_\infty$	Freestream condition
$(\cdot)_{char}$	Characteristics value
$(\cdot)_{eff}$	Effective quantity
$(\cdot)_J$	Jet quantity
$(\cdot)_{PC}$	Potential core parameter
$(\cdot)_o$	Orifice parameter

$(\cdot)_{ref}$	Reference parameter
$(\cdot)_{rms}$	Root mean square
$(\cdot)^{PC}$	Post-collision state property
$\overline{(\cdot)}$	Arithmetic averaged value
$(\cdot)'$	Perturbation from mean value; acoustic variable
$\frac{\partial}{\partial x}, \frac{\partial}{\partial y}, \frac{\partial}{\partial z}$	Partial spatial derivative operators in Cartesian coordinates
$\frac{\partial}{\partial t}$	Partial time derivative operator

Abbreviations

BGK	Bhatnagar-Gross-Krook
BPR	Bypass ratio
CAA	Computational Aeroacoustics
CFD	Computational Fluid Dynamics
dB	Decibel
DNS	Direct Numerical Simulation
FW-H	Ffowcs-Williams & Hawkings
LBM	Lattice Boltzmann Method
LES	Large Eddy Simulation
LHS	Left Hand Side
LAA	Lighthill's Acoustic Analogy
NPR	Nozzle Pressure Ratio
NS	Navier-Stokes
NTR	Nozzle Temperature Ratio
ISL	Inner Shear Layer in dual stream flows

OASPL	Overall Sound Pressure Level
OSL	Outer Shear Layer in dual stream flows
RANS	Reynolds Averaged Navier-Stokes
RHS	Right-Hand Side
RMS	Root Mean Square
SGS	Sub-grid-Scale
SL	Shear Layer
SPL	Sound Pressure Level
SPL	Sound pressure level
STL	Stereolithography, *aka* Standard Tessellation Language
TKE	Turbulence kinetic energy
TR	Temperature Ratio

Part A- Jet noise generation and radiation

Chapter 1

Introduction

1-1 Motivation

Jet noise is the dominant noise source in moderate bypass ratio turbofan engines during takeoff, and yet remains one of the most challenging problems in aeroacoustics due to its intrinsic complexity. The complex behaviours of turbulent jets and related acoustic sources are still not well understood. Turbulence itself is one of the few unsolved problems in engineering underlies noise generation and absorption mechanisms of jet flows. Thus, there is a need for more accurate prediction models, and further understanding of noise generation and absorption mechanisms of turbulent jets. This will help to implement accurate noise models in the design process of aircraft engines. Increasingly stringent noise regulations on the other hand, create a need for the development of more effective noise suppression techniques.

The design factors of complex nozzles for modern aircraft engines include net thrust and noise emissions. Aeroengines might also come equipped with jet noise suppression devices such as chevrons, lobed mixers, exhaust tabs, diverters, and microjet injection to decrease sound power levels. Noise suppression devices must be designed to ensure minimum loss in thrust coefficient and optimal fuel efficiency. Such noise reduction devices can systematically alter the flow pattern in the exhaust region, creating a very complex mixing field.

Experimental studies on full scale or even reduced scale engine nozzles are expensive as they require very large high-performance wind tunnels or blowdown facilities, with large anechoic chambers, high precision anemometers, microphone arrays and advanced data acquisition devices (Mengle *et al.*, 2002). In addition to the instrumentation costs and the manpower, experimental studies provide only a limited amount of information at certain locations along the jet plume or internal streams. A detailed parametric study to independently investigate all important variables at different operating conditions would be prohibitively expensive using experimental methods. A comprehensive study of jet noise generation and absorption mechanisms can be done through numerical simulations in which all flow parameters including velocity components, pressure, temperature and turbulence can be extracted at any moment and location within the computational domain.

As high-performance computing (HPC) costs decrease over time, it is becoming more feasible for aeronautics industries to utilize computational tools in their design process. Computational tools with high accuracy, high efficiency, stability, and relatively low cost are still needed to elucidate the flow and noise characteristics of jet noise problems that includes complex nozzle geometries such as internal mixing nozzles with forced mixers. The time-consuming process of grid generation and the significant computational demands of high-order numerical methods such as Direct Numerical Simulations (DNS) or the conventional Large Eddy Simulation (LES) based on Navier-Stokes formulation make them quite challenging to be used as standard tools for acoustic design in industrial applications. As an alternative, LES techniques based on the Lattice Boltzmann Method (LBM) have been investigated in our study to tackle the problem of high performance noise simulation in presence of complex nozzle geometries.

In the present study, complex nozzle geometries with focus on both single-stream nozzles (Habibi *et al.*, 2011b) and dual-stream internal mixing nozzles with lobed mixers were studied numerically using the LBM at both moderate and high Mach subsonic flow conditions (Habibi *et al.*, 2013b; Habibi *et al.*, 2014). The effects of heat transfer on noise were also studied using appropriate thermal models. In a parallel study, a baseline approach for numerical study of sound absorption by turbulent jet flows through orifices was developed that can be used to simulate sound attenuation inside the air passages or as a platform to design acoustic liners (Mann *et al.*, 2013; Habibi and Mongeau, 2015).

1-2 Subsonic jet noise: literature review

1-2-1 Single-stream jet

After more than six decades since the advent of jet noise theories by Lighthill (1952), which related the sound pressure field with quadrupole sources within turbulent mixing flows, considerable number of experimental, analytical and numerical studies have been performed to investigate the generation and propagation mechanisms of noise sources from turbulent shear flows. The quadrupole noise sources appeared as double spatial derivation in Lighthil's theory and the directivity pattern for a lateral quadrupole looks like a clover-leaf pattern; The description of monopoles, dipole and quadrupole sources will be discussed later in section 2-2 of this document. Lighthill's theory also known as acoustic analogy implies that the problem of turbulence-generated sound waves is equivalent to the radiation of a distribution of quadrupole sources with strength T_{ij} in Eqn. (1.1) into an ideal stationary fluid (Howe, 2003). Lighthill's initiative was to recast the conservation of mass and momentum equations, which is treated as an inhomogeneous wave equation where all nonlinear terms are shifted to the right-hand side (RHS) of the equation as source terms, *i.e.* sources of sound. The problem of calculating the turbulence-generated sound is then reduced to solving the radiation of a distribution of sources into an ideal fluid at rest (Howe, 2003). A short form of Lighthill's equation (Lighthill, 1952) can be written as

$$\left(\frac{1}{c_0^2}\frac{\partial^2}{\partial t^2}+\nabla^2\right)p^{'}=\frac{\partial^2 T_{ij}}{\partial x_i \partial x_j}, \tag{1.1}$$

in which T_{ij} is known as Lighthill's stress tensor, given by

$$T_{ij}=\rho u_i u_j+\left(p-p_0-c_0{}^2\left(\rho-\rho_0\right)\right)\delta_{ij}+\sigma_{ij}, \tag{1.2}$$

where u_i and u_j are the flow velocity components, and ρ_0, p_0 and c_0 are the reference density, pressure, and speed of sound related to the ambient condition. The shear stress tensor is σ_{ij} that also includes the dissipation terms. The first term in Eqn. (1.2), is the Reynolds stress term which is normally the most significant source of sound in turbulent flows. The second term represents entropy variations and nonlinear amplitude modulation of sound waves in the source region. The third term is related to the attenuation of sound waves due to viscous effects and is normally neglected due to small order of magnitude compared to other two terms. Due to the presence of the double divergence operator, $\partial^2 / \partial x_i \partial x_j$, in the Lighthill's source term, T_{ij} , the acoustic sources in free-field shear flows are commonly referred to as "quadrupole" sources. The Lighthill's equation is the exact derivation from the nonlinear N.S. equations that allows for near-field turbulent sources to appear in the right hand side (RHS) of the inhomogeneous wave equation. In Lighthill's formulation, all effects aside from propagation in a homogenous stationary medium, such as refraction, self-modulation of sound due to non-linearity and attenuation due to thermal action are lumped into the RHS (Lyrintzis, 2003). It is also understood that most of T_{ij} does not radiate into the far field. However, what the RHS of Eqn. (1.1) does provide is an exact connection between the near field turbulence and the far-field noise and thus serves only as a nominal acoustic source; however, determination of T_{ij} is not straightforward and would be computationally expensive. To compute the far-field sound, Lighthill assumed that the source generating mechanism is compact and in an unbounded flow coupled with the free-space Green's function and Fraunhofer's approximation (Lew *et al.*, 2005) Further details regarding different sources are available in section 2-2 of this document. Using acoustic analogy, Lighthill (1954) showed that the acoustic intensity, I_a, of the sound radiated from a relatively low Mach number jet with exit diameter of D_J and velocity of U_J, is given by

$$I_a = K \frac{\rho_J^2 D_J^2 U_J^8}{\rho_0 c_0^5 R^2}, \tag{1.3}$$

where ρ_J is the jet density, K is a constant of the order of 10^{-5}, and R is the radius at which the sound pressure levels are calculated or measured. Eqn. (1.3) is also referred as U^8 power law which is used to estimate sound intensity for various Jet velocities and distances from a reference point at which the sound intensity is known. Lighthill (1952) also discussed the effect of convection of acoustic sources. Further studies were also performed by Ffowcs Williams (1963). They showed that the Doppler shift due to the convection of quadrupole sources results in much stronger radiation toward aft angles, such that the acoustic intensity is equal to

$$I_a = K\frac{\rho_J^2 D_J^2 U_J^8}{\rho_0 c_0^5\left[\left(1-M_c\cos\theta\right)^2+\left(\dfrac{l_r}{\tau_r c_0}\right)^2\right]^{5/2} R^2}, \tag{1.4}$$

where $M_c = U_c/c_0$ is the convective Mach number, l_r and τ_r are the turbulence characteristic length and time scales, respectively. The term $(1-M_c\cos\theta)$ captures the effects of the Doppler shift (Toman, 1984), whereas the term $l_r/\tau_r c_0$ takes into account the spatial distribution of turbulent eddies. The latter term is of significance in directions normal to the Mach waves, where $M_c\cos\theta$ is equal to unity. In Eqn. (1.3), there is a strong correlation between sound intensity and jet velocity, *i.e.* the eighth power, thus, reducing the jet speed would be normally the most efficient noise reduction mechanism. For instance, a high bypass ratio turbofan engine in which the mean exit velocity is much less than a low-pass ratio engine would be normally quieter. Despite the high-order velocity dependence, the acoustic intensity of jet is very small magnitude compared to the total power density of the jet flow. A 130 dB jet engine during takeoff only produces ~10 kW of net acoustic power or ~ 10 W/m^2 of acoustic intensity whereas the total power generated by the jet engine is ~100 MW, factor of 10^4 (Noise, 1992); this makes jet flows very inefficient method of making noise.

One of the drawbacks of primary format of Lighthill's Acoustic Analogy (LAA) was that the convection and refraction of the sound waves are integrated into the source term that can lead to inaccurate predictions for jet noise especially at higher Mach numbers; consequently, several variants of the basic theory were proposed (Phillips, 1960; Goldstein and Howes, 1973; Lilley, 1974; Goldstein, 2003) to take propagation effects into account by including the corresponding terms in the wave operator. Among these studies, Phillips (1960) has proposed a convected wave equation in which convective term have been moved to the left-hand side of LAA in Eqn. (1.1). Such recast led to the appearance of a second-order material time derivative in the wave operator. The spatial derivatives of the speed of sound have also been included in the wave operator to account for the acoustic refraction. Lilley (1974) has proposed adjustments to Philips's equation and argued that the velocity fluctuation term representing aerodynamic sources should be included in the wave operator. The result was a third-order wave equation as

$$\frac{D}{Dt}\left[\frac{D^2\Pi}{Dt}-\frac{\partial}{\partial x_i}\left(c^2\frac{\partial\Pi}{\partial x_i}\right)\right]+2\frac{\partial u_j}{\partial x_i}\frac{\partial}{\partial x_j}\left(c^2\frac{\partial\Pi}{\partial x_i}\right)=-\frac{\partial u_j}{\partial x_i}\frac{\partial u_k}{\partial x_j}\frac{\partial u_i}{\partial x_k}+\Psi, \tag{1.5}$$

where Ψ is acoustic dissipation terms and Π is the normalized acoustic pressure given by

$$\Pi=\frac{1}{\gamma}\ln\frac{p}{p_0}, \tag{1.6}$$

in which γ is the specific heat ratio.

The formulation proposed by Lilley was well received by several authors, also the asymptotic solution of Lilley's equation was used in several prediction tools such as the one used in General Electric's MGB approach (Najafi-Yazdi, 2011); also more validation studies and extensions were performed on Lilley's generalized theory (Tester and Morfey, 1976; Khavaran *et al.*, 1994; Goldstein, 2003); For instance, Goldstein (2003) proposed a generalized LLA formulations that includes set of linearized Euler equations with source terms representing perturbations of shear-stress and energy flux tensors. Apart from Lighthill's primary formulation, almost all variations of acoustic analogies involve high-order, nonlinear differential operators with no analytical solution. This implies that a quantitative prediction of the far-field acoustics requires a numerical solution of partial differential equations, which can be computationally expensive.

The variations of jet noise properties with jet exit velocity and reception angle, θ, has led to different jet noise theories. Lush (1971) for instance, compared measured data for subsonic jets with the predictions from Lighthill's theory to explain the convective amplification resulting from the theory. An extensive comparison between general theories can be found in the review by Goldstein (1984) and the discussion in Bogey and Bailly (2005).

Several broadband jet noise prediction models for subsonic jets were inherited from studies on coherent structures of supersonic jets. The trends shown in the experimental studies at different directions suggest that high speed jet noise spectra are made of two basic components (Tam *et al.*, 1996; Viswanathan, 2002). Following an exhaustive review of supersonic jet noise data, Tam *et al.* (1996) showed far-field sound pressure spectral densities (PSD) can be predicted using two similarity spectra. The shape of the spectrum dominating the shallow aft angles was related to Mach wave radiation by large scale coherent structures of supersonic jet. Hence, this spectrum is commonly referred to as the Large Scale Similarity (LSS) spectrum (Morris, 2009). The second spectrum was used to fit the sound pressure spectra radiated toward sidelines. Tam *et al.* (1996) argued that the sound radiated toward sidelines is generated by small-scale structures. Hence, the second spectrum is commonly designated as the Fine Scale Similarity (FSS) spectrum. At intermediate angles, a combination of the two spectra is needed to match the experimental data.

For subsonic single-stream jets, the mixing noise mechanisms have been extensively reviewed by Tam (2008b). According to his work, which came from the results of analyzing large collected experimental data, the sound field in the downstream sector of the turbulent jet is coherent radially along any polar arc (Fig. 1-1). This is consistent with the idea that sound pressure spectra at relatively small emission angles are mostly formed by the coherent large turbulence structures of the jet flow. The sound field in the sideline directions, mostly towards the nozzle is more random in nature, with large frequency bandwidth and little spatial correlation. This is consistent with the idea that such waves towards the sidelines are generated by fine-scale turbulence.

The dependence of jet noise on the Reynolds number was also found helpful to characterize the sound sources (Boersma, 2004). For instance, Crighton (1981) found that the radiated sound behaviour of a turbulent jet changes by Reynolds numbers ($\mathrm{Re}_D = U_J D_J / \nu$) smaller than $\cong 100{,}000$, where U_J is the mean inlet jet velocity, D_J is the jet diameter, and ν is the kinematic viscosity. As the Reynolds number decreases, the downstream noise component from the large-scale turbulent structures are not significantly modified, whereas the sideline noise tends to decrease. Thus, for low-Reynolds jets, the prediction of the overall sound pressure levels dominated by larger scales can still be comparable with experimental data (Lew *et al.*, 2010b; Habibi *et al.*, 2011b).

To investigate jet noise generation mechanisms, another approach is to search for direct correlations between the near field and the sound radiation. Pairing and break down of vortical structures in the turbulent shear layer can be linked to characteristics of acoustic waves (Hileman and Samimy, 2001; Bogey *et al.*, 2003). It was also shown by Bogey and Bailly (2005) that quasi-periodic entrainment of vortical structures into the jet at the end of the potential core can be correlated to the sound radiated downstream in low-frequency bands.

1-2-2 Dual-stream subsonic jet noise

Despite greater industrial application of dual-stream jets compared to single-stream flows, less research efforts have been conducted on the analysis of the noise generation mechanisms within coaxial nozzle jets. On the other hand, single-stream nozzles such as SMC types are extensively used in experimental studies (Tanna, 1977; Fleury *et al.*, 2008; Bridges and Wernet, 2010), also for validation of numerical schemes including the present work. Development of robust and high-fidelity jet noise prediction models applicable to dual stream flows is of great interest to turbofan engine manufacturers.

The mixing phenomenon between fan and core flows in turbofan engines normally occurs via two different mechanisms based on the engine model. Firstly, *internal mixing nozzles,* in which both flows are mixed inside the main nozzle by passing through a mixer and a centre body (Fig. 1-2 (a)), then a premixed jet with partially developed inner shear layer exits the main nozzle. Second model is commonly referred to as *external mixing nozzles* in which the mixing process takes place outside of the main nozzle (Fig. 1-2(b)). For the external mixing configurations, chevrons, are currently one of the most popular noise-suppression devices (Fig. 1-2(b)). The axial vorticity generated by the chevrons tends to enhance mixing in the shear layers of the jet, which leads to a decrease or increase in noise over certain frequency bands. Chevrons usually reduce the low-frequency noise at aft angles, whereas increase the high-frequency noise at broadside angles with respect to the jet plume. The ultimate goal in chevron design is to decrease the low-frequency noise as much as possible while preventing a significant increase high-frequency noise. Chevrons strengthen the streamwise vortices that increase mixing within the plume to accelerate jet potential core decay. Enhanced mixing typically increases the smaller scales of flow field, and thus increases high-frequency noise components. The breakdown of the larger scale turbulence into smaller scales reduces the low-frequency noise at its peak directivity angle close to the jet axis and subsequently reduces the overall sound pressure level. Callender *et al.* (2005); Callender *et al.* (2008) conducted extensive experiments to study the near-field and characteristics of chevrons nozzles in dual-stream jets. They found that the presence of chevrons moved the peak noise directivity angle away from the streamwise axis and reduced its acoustic levels in the far field. Additionally, increasing chevron penetration depth caused in reshaping the noise spectra, *i.e.*, increasing the high-frequency noise and reducing the low-frequency noise as expected. Bridges and Brown (2004) used a single flow nozzle with chevrons to study the impact of the chevron penetration on the noise. They found that chevrons reduce noise equally well in heated and unheated jets. Some of the parameters that can be varied for this problem are the chevron count, chevron penetration, and chevron length. Chevron count controls the spacing between the axial vortices generated by the chevrons, chevron penetration controls the strength of the axial vorticity, and chevron length controls the distribution of vorticity within the axial vortices (Bridges and Brown, 2004).

The focus of present study will be on internal mixing nozzles with forced lobed mixers for the moderate and high Mach flow conditions. From a turbulent flow physics standpoint, unlike single-stream jets, the dual-stream jets are affected by the strong interaction between two turbulent shear layers; therefore, dual-stream jets exhibit a different distribution of the turbulent kinetic energy (TKE) in the plume compared to a single-stream jet. In addition to the different mixing patterns, the primary stream of coaxial jets is usually heated, which might affect the noise sources due to density gradient and entropic dipole sources. The presence of dipole sources in mixing shear layer of turbulent jets has been a debatable topic described by Viswanathan (2004). In a dual-stream jet, in fact, the interaction and entrainment process between cold and hot turbulent eddies lead to different thermal mixing phenomena compared to a single-stream jet where the ambient cold air is passively mixed by the heated eddies inside the shear layer. Hence, the spectral properties of the entropy fluctuations of single and coaxial jet flows are different (Casalino *et al.*, 2014a).

Based on the measurements by Tinney and Jordan (2008) in the near pressure fields of a coaxial short-cowl nozzle, with and without serration on the secondary nozzle lip, two distinct signatures in acoustic field were identified: a low-frequency component that primarily radiates toward aft angles, characterized by large axial coherent structure and a high-frequency component that radiates mostly toward sideline directions with less coherent behaviour. Moreover, it was found that increasing the temperature and velocity of the core jet led to stronger acoustic components with negligible effects on hydrodynamic components. Thus, the authors concluded that the near-field of coaxial jets is mainly governed by turbulent eddies in the secondary shear layer, whereas the acoustic pressure is mainly generated by the mixing layers between the core and bypass flows. The measurements by Tinney and Jordan (2008) along with other small-scale coaxial noise measurements by (Guitton *et al.* 2007), were used to validate several CFD codes for aerodynamic prediction of coaxial jets based on large-eddy simulations (Fayard *et al.*, 2008; Bogey *et al.*, 2009; Koh *et al.*, 2013), as well as detached-eddy simulations (Eschricht *et al.*, 2008). Earlier LES studies of coplanar jets were performed by Andersson *et al.* (2005b), Vuillemin *et al.* (2005), Viswanathan *et al.* (2006), Mihaescu *et al.* (2006), and Tristanto *et al.* (2006). More recently, Casalino and Lele (2014) used LBM to simulate coaxial jets using the same geometry as that described in (Tinney and Jordan, 2008). The primary and secondary nozzle diameters were D_p=135.9 mm and D_s = 273.4 mm, respectively, and the corresponding lips had a thickness of 0.92 mm and 1.20 mm and PowerFLOW 5.0 solver was used for this simulation.

Other approach to model dual stream jet noise is using the power spectral or scale laws that were found to be a reliable approach for several benchmark designs (Khavaran and Bridges, 2010). Scaling approach is based on the assumption that the sound pressure spectra of mixing flows are the superposition of appropriate single-stream coaxial jets. First the near-field is divided into several mixing regions and noise generation in each region is modeled using spectral power laws developed for single stream jets as a function of jet properties such as temperature, Mach number and observer angle. Fisher *et al.* (1993) pioneered a scaling method for jet noise prediction in dual stream setup from a fluid mechanics perspective. In the light of turbulence and velocity measurements, they separated a coaxial jet into several noise-producing sections. Such noise-generating regions have several similarities with more study suggested by Stone *et al.* (2003), but they differed in their modeling details. Later, Fisher *et al.* (1998) extended the noise model to heated jets with a dipole-equivalent correction factor that represented the entropy effect in the transition jet. These studies were limited in their scope and applicability of the velocity, area, and temperature ratio between the two streams. Also, they did not examine important geometrical details such as a recessed secondary flow typically in modern turbofan engine designs. However, many aspects of Fisher’s model for unheated subsonic flow was consistent with experimental observations, especially those performed by Ko and Kwan (1976).

A well-known four-source similarity model developed by Khavaran and Bridges (2010) indicates that jet noise in dual stream nozzles can be considered as a combination of four single stream jets representing primary-secondary, secondary-quiescent, transition, and fully mixed zones. A schematic of such combination is shown in Fig. (1-3). The overall sound pressure levels can be computed by superposing the contribution from each region given by

$$10^{SPL/10}=10^{(SPL/10)_{primary}}+10^{(SPL/10)_{secondary}}+10^{(SPL/10)_{transition}}+10^{(SPL/10)_{fully-mixed}}, \qquad (1.7)$$

where, SPL denotes the sound pressure level at a 1/3 octave centre frequency, and the summation is performed after each noise component has been treated with an appropriate high- or low-pass filter (Khavaran and Bridges, 2010). Two low-pass filters were defined as

$$\begin{aligned} F_1(\xi) &= \left(1+\xi+\frac{\xi^2}{25}+\frac{\xi^3}{125}+\frac{\xi^4}{250}\right)e^{-\xi} \\ F_2(\xi) &= \left(1+\xi+\frac{\xi^2}{2}+\frac{\xi^3}{6}\right)e^{-\xi} \end{aligned}, \qquad (1.8)$$

in which $\xi = m\, f \,/\, f^*$ and m = 2. The characteristic frequency, f^*, depends on the velocity to diameter ratio in each component, and f is a third-octave band centre frequency. A high-pass filter is obtained when a low-pass filter is subtracted from unity. Frequency filter are designed to highlight spectral contribution from each jet. The fully mixed jet is defined as a single-stream jet with diameter, velocity and temperature at the mixed region. The characteristic frequency f^* in the fully mixed region additionally depends on primary to secondary diameter ratio (Khavaran and Bridges, 2010). The secondary jet is defined through jet parameters in the secondary region and was argued to contribute to high frequency components of sound pressure spectra. The required high-pass filter shall be compatible with that of the fully mixed region to address the case in which the core flow becomes relatively weak. In that case, the fully mixed and the bypass jets are identical, and the two filters must recover a single flow with secondary properties. The application of similarity rules within transition region is relatively more complicated and requires a more delicate process (Khavaran and Bridges, 2010). One approach is to consider primary flow condition with an effective diameter. Khavaran and Bridges (2010) argued that the noise level is attenuated by ~60 percent in this region due to reduced turbulence level when compared to the self-similar regions. Additionally, a low-pass filter is used as an appropriate characteristic frequency. Finally, the primary jet was defined at primary, *i.e.* core jet, conditions subject to flight speed of U_∞. The required high-pass filter is bound by the limiting requirements when secondary velocity is very small. Also, when the secondary jet is relatively weak, the fully mixed jet will be equivalent to the primary jet.

The four-source model suggests that the low frequency noise in unheated jets was emitted from the fully mixed region at wide range of velocity ratios, whereas the high frequency noise was dominated by the secondary stream when the velocity ratio was larger than ~0.80. The fully mixed and transition jets were equally contributing to the emission of low frequency noise in heated jets. A prediction sample by such four-source model is shown in Fig. (1-4) that compares predicted 1/3 octave spectral levels from the model with experimental data in which U_s/U_p, A_s/A_p and T_p/T_s were 0.75, 1.43 and 1.1 respectively. It was related to run number 8301 in (Khavaran and Bridges, 2010) with nozzle pressure ratio (NPR) of 1.51 in the core stream and 1.30 in the bypass stream. The superposed spectrum in Fig. (1-4(a,b)) is compared with measured data at the observer's angle of 90^o and 150^0 with respect to the inlet. A sudden drop at either side of each noise component is related to the low- or high-pass filter that are designed for each component. Due to empirical nature of such filters, predictions made by source modeling are highly sensitive to the nozzle's geometry and the range of operating conditions. The predictions in (Khavaran and Bridges, 2010) were limited to area ratio of ~2.0 and bypass ratio from 0.80 to 3.40, and the temperature ratio between 0.74 and 1.1. In a later study, Khavaran and Dahl (2012) showed that adjustments were necessary on a number of parameters such as diameter, characteristic frequency, and the spectral filter both secondary and the fully mixed region in order to improve the discrepancy seen in mid-to high-frequency range mostly at small aft angles, *e.g.* 150^o in Fig. (1-4).

1-2-3 Internal mixing nozzles with forced mixers

Lobed mixers have been found to yield significantly enhanced mixing with acceptable pressure losses for low and moderate bypass ratio engines (Vlasenko *et al.*, 2010). The main application of lobed mixers is for internal mixing engines. Mixers are utilized to mix the cold bypass and hot core flows internally upstream to the nozzle exit plane (Crouch *et al.*, 1977; Packman *et al.*, 1977). A typical nozzle with lobed mixer is shown in Fig. (1-2(b)). According to the study by Waitz *et al.* (1997) the specific shape of the lobed mixers guides the core and bypass streams along two unparalleled directions near the lobe sidewalls. The radial velocity components of the two streams in the mixer exit plane produce large-scale streamwise vortices that interacts with Kelvin-Helmholtz instability (Eckerle *et al.*, 1992) and enhances dual-stream mixing process. Figure (1-5) shows the formation process of streamwise vortices by lobed mixers. The breakdown of large coherent turbulent structures downstream of the mixer into smaller scale eddies, tends to decrease low-frequency broadband mixing noise; however, this benefit is often traded off with a measurable increase in high-frequency noise. Unlike the regular unscalloped lobed mixers, the side walls of the scalloped mixers are cut off for a more gradual mixing of the two streams inside the nozzle. The purpose of such removal is to reduce the high-frequency noise generated by sudden mixing between the two streams immediately downstream of the mixer exit plane, thereby reducing the high frequency noise produced by the lobed mixers. A better uniformity of the flow velocity profile at the nozzle exit plane, as well as the control of the turbulent kinetic energy tend to reduce overall sound pressure levels. This benefit may need to be traded off against potential pressure losses.

From a performance point of view, a mixer with small pressure loss and high mixing efficiency is desirable. The mixing process itself leads to an increase in entropy. The net performance gain depends on the balance between improved mixing, exit velocity profile and the pressure loss.

The key design parameters of nozzles with forced mixers include lobe number, lobe penetration depth, scalloping depth, perimeter of the trailing edge and mixing length. Experimental studies of lobed mixer performance and noise have been conducted over the past few decades. The theoretical thrust gains for ideal mixing were tested and reported by Frost (1966) and Hartmann (1969). Since then, far-field noise data and detailed measurements of aerodynamic properties have been reported by several authors (Kuchar and Chamberlin, 1980; shumpert, 1980; Larkin and Blatt, 1984). Kozlowski and Kraft (1980) confirmed the enhanced performance of lobed mixers through measurements of variations associated with modifying the lobe geometry. In later studies, forced mixers were shown to reduce the exit jet velocity without significant thrust penalties for turbofan engines (Barber, 1988; Barber *et al.*, 1988a; Barber *et al.*, 1988b). Booher *et al.* (1993) reported that a lobed mixer with high penetration yielded substantial performance improvements for operating conditions typical of subsonic cruise, compared to an unmixed nozzle configuration. Meade (1994) also found that internal forced mixing yielded a significant reduction in jet noise over confluent mixing. Publications by Presz *et al.* (1987; 1988; 1994) also showed that mixing between the core and the bypass flows was significantly enhanced by the lobed mixer, while noise was reduced and the net thrust was increased.

Efforts have been made to understand the physics underlying the enhanced mixing of lobed mixers. Measurements conducted by (Paterson, 1981) have quantified the radial outflow in the core region and the radial inflow in the fan region at the lobe exit plane. The results revealed the existence of large-scale streamwise vortices which were suggested to be responsible for the enhanced mixing. Werle *et al.* (1987) and Eckerle *et al.* (1992) suggested a three-step mechanism.

Streamwise vortices were postulated to form, intensify, and then break down. They suggested that the turbulence added from vortex breakdown improved mixing. reported the separate role of the streamwise vorticity and the increased interfacial area on mixing; they also reported that the mixing enhancements of the lobed mixers increased with the bypass ratio. Following Manning's work, Belovich *et al.* (1996) performed flow visualization and found that the fraction of mixing enhancement due to streamwise vorticity, *i.e.* relative to mixing enhancement from increased interfacial contact area, increased as velocity ratio increased. Elliot *et al.* (1992) also reported two primary contributors to the mixing process in lobed mixers, namely spanwise vortices due to the Kelvin–Helmholtz instability and increased interfacial contact area due to the trailing edge shape. Once the flow has passed the trailing edge of the mixer, vortices are developing. Their strength is a result of the difference in radial momentum between the core flow in the lobes and the fan flow in the valleys.

Based on the visualization of vortical and turbulent structures within lobed mixer flows, McCormick and Ennett (1994) proposed that the interactions between the spanwise Kelvin–Helmholtz vortices and streamwise vortices also contribute to enhanced mixing. More recently, Mengle *et al.* (2002) published comprehensive data on the effects of scalloping, lobe number, lobe penetration and mixer-nozzle configuration on radiated noise for wide range of engine operating conditions. These data were used for verifications of computational tools in numerical simulation studies. A reduction in mid-to-high frequency noise from scalloped lobed mixers was reported following experiments by Mengle *et al.* (2002). However, the underlying noise reduction mechanism due to scalloping is not well understood.

Lobed mixer design has so far proceeded by a trial and error approach. Semi-empirical approaches based on multisource approximations generally yield reliable trends, but occasionally fail to correctly predict the noise emissions. A systematic study of the effects of lobed mixers parameters is not feasible without complementary numerical simulations and optimization studies. Previous computational studies have been confined to the region downstream of the lobe exit because of the challenges in performing internal and external flow simulations simultaneously (Birch *et al.*, 1978; Kreskovsky *et al.*, 1984; Povinelli and Anderson, 1984). The accuracy of radiated sound predictions depends on the quality of three-dimensional velocity fields at the lobe exit, and that of the turbulence levels. To tackle this issue, Barber *et al.* (1986a; b) and Koutmos and McGuirk (1989) have proposed some basic models for the flow through the lobed mixer. Later on, Malecki and Lord (1990) as well as Abolfadl and Sehra (1991) created an analytical modeling of the mixer utilizing the Navier-Stokes equations. Their results provided insights into the design and development of lobed mixers. Lobed mixer flows have also been investigated using Reynolds Averaged Navier-Stokes (RANS) CFD analysis. Salman *et al.* (1999; 2001) used both structured and unstructured grids to study lobed mixers jet flows. Garrison *et al.* (2005) carried out RANS simulations based on a two-equation shear stress transport (SST) turbulence model, and the results were found to capture several features of lobed mixers. From Garrison's work, turbulence kinetic energy (TKE) computed from the RANS model was used in a two-source model for a number of lobed nozzle configurations that were initially proposed and used by Tester *et al.* (2004) and Tester and Fisher (2004) in which the mixers were modelled by superposing a fully mixed jet for the low frequencies and a fully mixed jet for the high frequencies that includes the initial portion of the outer shear layer. Garrison *et al.* (2004; 2005) enhanced the upstream source by adding the turbulence terms that covers the interaction of the streamwise vortices generated by the forced mixer. The idea was almost similar to the four-source modeling that was described in the section 1-2-3 for external mixing nozzles. However, the filters in four-source model by Khavaran and Bridges (2010) were mostly derived from semi-empirical relations, whereas the filter input of the two-source model for lobed mixers are extracted from RANS solution. Despite their limitations, both methodologies are widely used in turbofan industries. A schematic of two-source decomposition of near-field is shown in Fig. (1-6). In the two-source model approach, the low frequency segment of the noise spectrum from downstream region is modeled by filtered fully mixed jet, given as

$$SPL_D(\theta, f) = SPL(V_m, T_m, D_m, \theta, f) + 10\log_{10}\left(F_D(f_m, f)\right) + 40\log_{10}\left(\Gamma_D^*\right), \tag{1.9}$$

where SPL_D refers to the noise from the downstream fully mixed jet source and *SPL* refers to a single-stream jet using the fully mixed jet velocity, V_m, diameter, D_m and temperature, T_m defined by

$$V_m = V_p\left(\frac{1+\lambda^{*2}\beta^*\delta^*}{1+\lambda^*\beta^*\delta^*}\right), \tag{1.10}$$

$$D_m = D_p\left(\frac{\left(1+\lambda^*\beta^*\right)\left(1+\lambda^*\beta^*\delta^*\right)}{1+\lambda^{*2}\beta^*\delta^*}\right)^{1/2}, \tag{1.11}$$

$$\text{and } T_m = T_p \frac{1+\lambda^*\beta^*}{1+\lambda^*\beta^*\delta^*}. \tag{1.12}$$

where V_p and T_p are the ideal primary flow fully expanded velocity and temperature, D_p is the primary flow diameter and λ^*, β^*, and δ^* are the secondary to primary flow ratios of velocity, area, and density, respectively. The ideal fully expanded flow properties are determined using the assumption that the flow in each stream expands from the total pressure to the ambient pressure through an isentropic path. The low-pass filter, F_D, is applied to the spectrum to remove the high frequency components, which corresponds to sources located in the upstream region of the fully mixed single-stream jet. This filter, was formulated by Fisher *et al.* (1998) using source location data of single jets, and defined as

$$F_D = \exp\left(-4\frac{f}{f_m}\right)\left[1+\left(4\frac{f}{f_m}\right)+\frac{1}{2}\left(4\frac{f}{f_m}\right)^2+\frac{1}{6}\left(4\frac{f}{f_m}\right)^3\right], \tag{1.13}$$

where f_m is the cut-off frequency of the filter derived from a semi-empirical relation given as

$$f_m = \frac{V_m}{D_m}\frac{(x/D)_{PC}}{L_U}, \tag{1.14}$$

where $(x/D)_{PC}$ is location of the potential core and L_U is the length of enhanced upstream region that both are derived from semi-empirical models based on the assumption that a Strouhal number of unities is associated with noise sources near the end of the potential core. On physical perspective, Eqn. (1.13) corresponds to the amount of acoustic energy radiated from all sources downstream of the potential core, which is the fully mixed region. The cut-off frequency is related to the location where the term $10log_{10}(F_D)$ is equal to -3 dB. As a result, the total noise at the cut-off frequency is the sum of equal parts of both upstream and downstream sources. The source reduction term, $40log_{10}(\Gamma_D)$, is a function of the ratio of turbulence intensities that shifts the fully mixed jet noise spectra down. Γ_D is defined as

$$\Gamma_D = \frac{TI_D}{TI_0}, \tag{1.15}$$

where TI_D is peak turbulence intensity in the downstream portion of the actual jet plume and TI_0 is the peak turbulence intensity in the plume of a single stream jet. The high frequency portion of forced mixer noise spectrum is modeled as an enhanced, filtered, fully mixed jet, given as

$$SPL_U(\theta, f) = SPL(V_m, T_m, D_m, \theta, f) + 10\log_{10}(F_U(f_m, f)) + 40\log_{10}(\Gamma_U), \quad (1.16)$$

where SPL_U is the sound pressure level related to the upstream fully mixed jet source and SPL refers to a single jet predicted level using the fully mixed jet parameters. The high-pass spectral filter, F_U, removes the low frequency components of the single-stream jet predicted noise levels, which corresponds to sources that are predominately found in the downstream region of the jet flow. Such filter is given as,

$$F_U = 1 - F_D, \quad (1.17)$$

A sample of two-source model for a jet with a 20-lobe mixer is shown in Fig. (1-7) that compares the superposed spectra from the upper and downstream region with available experimental data for 90^o and 150^o aft angles (Garrison *et al.*, 2006). Like the four-source model for external mixing nozzles, the two-source model also demonstrates better predictions at large aft angles. Discrepancies at shallow angles start to appear at mid-high frequencies. This is also the case in most LES simulation, where accuracy of high-frequency spectra are limited to the grid resolution.

The two-source method was later used by Tester and Fisher (2006) and Meslioui *et al.* (Meslioui, 2007; 2007) for several different mixer models , *e.g.* different lobe numbers and few scalloped models, that demonstrated acceptable noise trends comparable to experimental data. It was also argued that further refinements on the model and filters are necessary for special lobed mixer designs and/or operating conditions (Meslioui, 2007).

Garrison *et al.* (2006) also introduced the multi-source model as an extension to two-source model. Formulation of the multi-source model was similar to the two-source model, but the upstream portion of the jet plume was divided into a small number of additional segments. In multi-source model, the upstream spectra can be generalized as

$$SPL_i(\theta, f) = SPL(V_i, T_i, D, \theta, f) + 10\log_{10}(F_i(f_i, f)) + 40\log_{10}(\Gamma_i), \quad (1.18)$$

where T_i and V_i, are the characteristic jet properties in a given section from CFD code, also Γ_i is the enhancement term that is calculated from the peak turbulence intensities in a given section; and F_i values are the filter functions for each segment. Garrison *et al.* (2006) followed the same process in (Fisher *et al.*, 1998) to formulate the filter functions for each upstream segment by integrating a model source distribution function and calculate the fraction of the total energy radiated between two axial locations in the plume. Such general filters can be expressed as

$$F_i = \frac{\int_{x_1}^{x_2} S(x)dx}{\int_0^{\infty} S(x)dx}, \tag{1.19}$$

where S(X) is a source distribution function and for multi-source analysis (Garrison *et al.*, 2006), the source function was selected as

$$S(x) = x^3 \exp\left(\frac{-4x}{x_{PC}} \frac{D_m}{V_m} f \right), \tag{1.20}$$

which is the function of frequency and location of the source with respect of the end of potential core. Garrison *et al.* (2006) tried four segments in for the upstream terms and compared the results for number of lobed mixers with the two-source model. A sample of their comparison is shown in Fig (1-8) in which results from two models were compared with experimental data at a shallow observer's angle of 150^o. It was found that the high-frequency region was slightly improved with four-segment model compared to the two-source model.

Despite relatively low computational costs of the RANS method, a successful prediction of the sound field using source modeling methods would highly depend on the accuracy of the turbulence model and TKE data computed by the RANS solver. In case the difference between two nozzle and/or mixer test models are minor, *e.g.* slightly modified inner contour of the nozzle, or small change in scalloping depth or length of the centre body which is a common exercise for shape optimization process, RANS solution might fail to predict correct turbulence characteristics and hence, far-field spectra using the two-source model. Based on numerous investigations world-wide, it seems to be generally accepted that the accurate prediction of a wide range of aerodynamic and industrial turbulent flows with large-scale separation is beyond the capabilities of the classical RANS approach (Travin *et al.*, 2004) . On the other hand, time-resolved numerical schemes such as Navier-Stokes based LES or Lattice Boltzmann method can better resolve transient effects of even small design changes in both inner and outer shear layers of dual-stream configuration and provide more accurate near-field data for the acoustic model.

Some recent studies were focusing on unsteady RANS, *aka*. URANS in which fluctuations, or unsteady behaviour are captured in the mean quantities, which seems to be an intermediate between RANS and LES. In case of internal mixing nozzles, Brinkerhoff *et al.* (2013) simulated hydrodynamic characteristics of 12-lobed mixer such as mixing effectiveness; the Medium- and large-scale unsteady motions were resolved by the fine spatial and temporal resolution of the URANS scheme, and small-scale turbulence was captured using shear-stress transport (SST) turbulence model (Menter, 1994). Hydrodynamic results were found to be in reasonable agreement with results from hot wire anemometry experiments (Brinkerhoff *et al.*, 2013). It is argued that URANS could mimic the fundamental strength of LES, *i.e.* the resolution of the dominant inviscid eddies. In simple words, switching RANS scheme to time-accurate mode in a Navier-Stokes solver results in a URANS scheme. However, URANS does not look to have a rational theoretical justification. The extended averaging method implemented in the RANS formulation assumes steady solutions with a low-frequency externally imposed perturbation, that would cause a spectral discrepancy between the unsteadiness frequency and internal frequencies of turbulence which the latter scale with the shear rate (Tennekes *et al.*, 1972). such gap is more prevalent in deeply separated turbulent flows as well as solid-fluid interaction cases (Travin *et al.*, 2004); This could potentially impair correct capture of acoustic sources in the near-field of turbulent flows; Even by neglecting such weakness of URANS and recognizing that it may give better accuracy than RANS in some cases, it seems that this scheme, in contrast to LES, can resolve only some of the large dominant eddies which the size and resolution cannot be tuned using spatial filters in LES.

1-2-4 Effects of thermal mixing on jet noise

The temperature of the exhaust gasses strongly influences acoustic noise emissions through at least two basic mechanisms; (a) Density fluctuations and (b) the convection of density inhomogeneities within heated jets that produce monopole or dipole sound, respectively (Hoch *et al.*, 1973). Gradients in the speed of sound due to temperature difference also causes scattering and refraction of sound waves within the near-field of the jet (Viswanathan, 2004). A good understanding of the fundamental physics of sound production by turbulent heated jets is needed to guide design and accurately quantify noise emission levels from first principles and known boundary conditions.

Experimental studies of noise from heated jets have been performed using flow visualization, aerodynamic and aeroacoustic measurements. There are number of experimental studies in the literature focusing on the effect of temperature on the sound radiation of turbulent jets. Hoch *et al.* (1973) launched a joint test program at the National Gas Turbine Establishment in England and SNECMA in France aiming to clarify the effect of density on jet noise at various jet exit velocities. It was found that the overall sound pressure levels increased with density at low jet velocities ($M_J \cong 0.7$) while the levels decreased at very high velocities in subsonic flow regimes. The $M_J = 0.7$, is the inflection point at which the reduction of quadrupole sources surpasses the increase in dipolar sources due to entropy fluctuation. Similar phenomena were observed in experiments by Fisher *et al.* (1973) by changing the temperature and hence the density. An important observation in several experiments confirmed that the potential core length is shortened by increasing the temperature, T_j (Witze, 1974; Lau, 1981; Lepicovsky, 1999; Kearney-Fischer *et al.*, 2009). It was also pointed out by Lau (1981) that the value of the turbulence intensity at the tip of the potential core (~ $6D_J$) does not change much but the peak value on the other hand increases and shifts farther downstream by increasing the jet temperature. It is argued that this phenomenon is mostly related to instability waves at low Strouhal numbers that are evolved more gradually closer to the nozzle exit than waves at higher Strouhal numbers and attain their peak amplitudes close to the end of the potential core. The location of maximum intensity is also affected by density gradient and energy transfer from mean flow to instability waves (Viswanathan, 2004).

The length of the potential core was reported to be following the decay rate of the centreline velocity (Lepicovsky, 1999). He also reported that the shortening of the potential core is caused by a more rapid decay of the centreline velocity. These tendencies correspond to those observed for variable-density turbulent jets and can therefore be attributed to the reduction of density, local buoyancy, convection and thermal entrainment in heated jets (Pitts, 1991) (Russ and Strykowski, 1993; Amielh *et al.*, 1996).

The effects of Reynolds number, *Re*, of scale-model nozzles are rarely appreciated or investigated thoroughly. Normally the effect of Reynolds number is estimated through testing nozzles of different diameters at the same jet operating conditions. When the jet is heated at a fixed nozzle pressure ratio (NPR) or outlet Mach number, the Reynolds number decreases with increasing temperature. At the higher temperature ratio, the measured nozzle discharge coefficient values for the smaller nozzle decrease further, while the values for the larger nozzle is seen to decrease at low NPR. Thus, the aerodynamic characteristics are seen to be subject to the effects of

Reynolds number (Viswanathan, 2004). Temperature is found to have varying effects depending on the Reynolds number. For lower Reynolds number, O (10^4) or less, and with respect to the isothermal jets, the shear layers appear to spread more rapidly with stronger large-scale structures and weaker fine-scale turbulence for the hot jets at decreasing Reynolds numbers (Bogey and Marsden, 2013). For higher Reynolds number, O (10^5) and beyond, the shear layer displays smaller structures near the nozzle exit elongated in the streamwise direction, as typically observed in turbulent boundary layers. This was also consistent with findings by Viswanathan (2004) in which he had found a threshold Reynolds number (~ 0.4×10^4) below which turbulent structures as well as sound power spectra were varying with temperature and seemed more universal for higher Reynolds numbers. Dampening of instability waves and viscous dissipation in general, are also the byproduct of lowering the Reynolds number. Increasing the dissipation rate can also be related to the entrainment process that controls the length of the potential core. It is argued that the lowering the Reynolds number could slightly increase the length of potential core by slowing down the entrainment process; if the *Re* is kept constant by simultaneous increasing the temperature and velocity, the length of potential core will decrease (Russ and Strykowski, 1993; Bogey and Marsden, 2013).

Detailed experimental data on sound generated from subsonic and supersonic heated jets have been reported (Tanna *et al.*, 1976; Tanna, 1977). Tanna's experiments confirmed the findings of Hoch *et al.* (1973) for various Mach numbers. Zaman (1986) performed experimental studies to investigate the mean flow and acoustics of a M_J =0.5 subsonic heated air jet. For the case of high-speed jets, Seiner *et al.* (1992) conducted a detailed study of the effects of temperature on the radiated sound of an expanded M_J = 2.0 jet which clarified the relation between the Kelvin Helmholtz instability and the Mach wave emissions of high speed jets. Zaman (1998) also measured the diffusion rate of turbulent jets for various Mach numbers and temperature ratio. More detailed studies of noise sources in hot jets have been conducted by Bridges and Wernet (2003) and also by Viswanathan (2004). In the latter study, uncertainties in previous data from Tanna (1977) were questioned. It was found that sound pressure measured for hot subsonic jets, $M_J \leq 0.6$ and $Re_D <$ 400,000, may in some cases be contaminated by extraneous background or test rig facility noise. These findings also challenged previous theoretical studies in the field, (Morfey, 1973; Tester and Morfey, 1976; Morfey *et al.*, 1978) in which they revealed that heating the jet flows reduces the strength of the quadrupole sources existing in unheated jets by decreasing the density, while creating excess dipolar sources. Previous experimental data was re-examined by Tester and Morfey (2009) and Morris and Harper-Bourne (2010). They concluded that the different sound spectral levels close to the peak Strouhal (*St*) number is still pure jet mixing phenomena caused by generation of dipole sources for heated jets and is not affected by the rig noise. Further experiments performed by Bridges and Brown (2010), Zaman (2012) and Karon and Ahuja (2013), proved that the differences between measurements obtained at different facilities was mostly from changes in nozzle's geometry and exit conditions and not from the noise contamination as suggested by Viswanathan (2004). This also indicates the importance of including the nozzle within computational domain in simulations for better prediction of the jet noise; as similar exit condition deems necessary to recover important features such as peak levels on the spectra. The effects of the temperature difference between jet flow and the surrounding fluid on radiated sound and flow structure was investigated numerically by Lew *et al.* (2005; 2007) for $M_J = 0.9$ and temperature ratio of 1.7 and 2.7 that were consistent with near-field data in Zaman (1998) and Tanna's far-field data for $M_J = 0.9$. For supersonic flows, the effect of temperature ration on jet noise was studied numerically by Semlitsch *et al.* (2013). A complete review of temperature effects on jet noise can be found in Bogey and Marsden (2013). For supersonic jets, there are number of more recent numerical studies focusing on the effects of temperature on far-field sound and screeching tones (Gojon *et al.*, 2017; Chen *et al.*, 2018). The temperature ratios in those studies were ranging from 1.0 to 3.0 (from 293 K to 879 K for the total temperature). were considered for a over-expanded supersonic jet. It was found that the shock structures of the jet were considerably affected by the temperature. Also the number of shock cells decreased when the jet temperature was increased due to change in the decay rate and density gradient. The Overall Sound Pressure Level (OASPL) revealed an intensified screech feedback mechanism when the temperature was increased and strong flapping motions of the jet along the minor axis were observed (Chen *et al.*, 2018).

1-3 Computational aeroacoustics for jet noise studies

In order to provide robust and accurate prediction of sound emissions from aircraft airframes and engines, a relatively new discipline, Computational Aeroacoustics (CAA), has emerged. CAA, is dealing with accurate predictions of small amplitude flow-induced acoustic fluctuations and their propagation as sound waves into the far-field. In most cases, CAA can be categorized into three basic approaches:

The Direct Approach, in which the complete, fully compressible flow is solved in macroscopic (*i.e.* conventional Navier stokes equation) or mesoscopic scale (e.g. Lattice Boltzmann scheme). The computational domain contains both the acoustic sources and the far-field receptors. Sound generation and propagation as well as the absorption phenomena are part of the solution. In case of the aircraft noise simulation, the computational domain could be very large. If a high order and low dissipation numerical scheme is used, the direct approach could be very expensive and the application would be limited to the fundamental studies and academic configurations.

The *Indirect Approach* includes two steps. First, the transient flow field is solved using either Large Eddy Simulation (LES) or Direct Numerical Simulation (DNS) in the near-field to cover all important acoustic sources in the computational domain. Second, the transient flow characteristics are fed into an acoustic analogy method such as the Lighthill analogy, the Ffowcs Williams - Hawkings method, or the Kirchhoff-Integral to obtain the far-field noise. More information about those methods are available in section 2-2 of this document. The acoustic analogy provides the exact solution for the sound propagation to the far-field at a significantly lower computational cost than the direct approach. Acoustic wave scattering through shear layers and convection of sources might not be well captured in this method.

In *Semi-empirical Approach*, a steady (RANS) or unsteady Reynolds Averaged Navier-Stokes computation is performed to obtain some information about turbulence length and time scales. This information is then transformed into sound-source spectra by using empirical relations. Although, this approach is inexpensive, the reliability of the results is heavily dependent on the validity and accuracy of the empirical relations for the case to be considered.

In any aeroacoustic problem, proper simulation of the unsteady flow characteristics in the near-field and if applicable, the application of sub-grid scale models are of great importance. With the recent advancement in computing power, the application of Direct Numerical Simulation (DNS) and Large Eddy Simulation (LES) for jet noise prediction are becoming more feasible. Most numerical schemes for jet noise simulations are based on the Navier-Stokes equations that are solved via temporal and spatial discretization of the governing equations on a computational grid. Unlike some simplified laminar flow regimes, one cannot find closed form analytical solution for turbulent flows. To solve a flow field in transition and turbulent region, the Navier-Stokes (NS) equations must be solved numerically to get instantaneous flow field. Direct Numerical Simulation is a method that solves the NS equations without the use of any sub-grid scale model. For such scheme, a simulation setup should capture the full range of scales in a turbulent flow and capture the broadband kinetic energy. The computational domain must be large enough to accommodate the largest scales and the grid resolution must be sufficiently fine to capture the energy content of the smallest scales. Large Eddy Simulation methods on the other hand, solves the unsteady conservation of mass, momentum, and energy partial differential equations directly at the large scales of motion, while modeling the effect of the smallest eddies on the smaller scale flow motions.

The width of the spectrum of turbulent scales increases with the Reynolds number (*Re*). The ratio of the Kolmogorov length scale to the integral scale, which are the length scales for the largest and smallest scales, respectively, is proportional to $Re^{-3/4}$. Thus, since the resolution requirements are roughly the same in each coordinate direction, the computational requirements for a DNS scale approximately with $Re^{9/4}$. For this reason, DNS simulations are typically limited to low-Reynolds number flows (Freund, 1999; Pope, 2000). Direct numerical simulations are often performed using fully-spectral, or pseudo-spectral methods (Peng *et al.*, 2010). These methods are used because of their superior accuracy and computational efficiency. Spectral methods transform the Navier-Stokes equations into the frequency domain in order to represent the flow field as a finite set of basic functions. The governing equations are then solved in the spectral space. Since the derivatives in the Navier-Stokes equations do not need to be approximated in these methods, they are essentially free of truncation errors, and thus are very accurate. Another advantage of spectral methods is that the solution of the Poisson equation for pressure (for incompressible flows), which is usually a very computationally expensive operation, is reduced to a simple division in the spectral space. This makes spectral codes computationally very efficient. Spectral methods work very well for problems with simple geometry, especially those with periodic boundaries. However, the implementation of these methods is considerably more difficult for problems with complex geometries because choosing appropriate basis functions that satisfy the boundary conditions is not easy. For this reason, finite difference and finite volume methods are often used for problems with complex geometries.

Most turbulent jet flows in industrial problems are at Reynolds numbers greater than 100,000; and the cost of DNS would be prohibitive in those Reynolds numbers; hence LES method with relatively coarser resolution and fraction of computational cost would be preferable. Most LES studies were combined with a variant of acoustic analogy to predict far-field sound (Bogey and Bailly, 2003; Uzun *et al.*, 2004); similar studies were also performed on supersonic jet flows (Semlitsch, 2014). These studies have helped to establish standard benchmarks in terms of numerical schemes, boundary conditions and inlet flow specifications. The application of LES to study sound radiation from simple round jets has been investigated by several researchers for both low Reynolds (Mankbadi *et al.*, 1994; Lyrintzis and Mankbadi, 1996) and high Reynolds number flows (Choi *et al.*, 1999; Zhao, 2000; Constantinescu and Lele, 2001; Bogey and Bailly, 2003; Uzun *et al.*, 2004; Bodony and Lele, 2005; Najafi-Yazdi, 2011); however, none of which had included nozzle's geometry in their studies. A comprehensive review of LES studies can be found in Bodony and Lele (2008). Due to the high velocity and temperature gradient at the solid-fluid interface, the inclusion of a solid body into the computational domain could be very costly. According to a study by Bogey and Baily (2010; 2011), the boundary layer momentum thickness at jet discharge location plays an important role in development of the jet shear layer; and, hence, the acoustic field. Unrealistic laminar flow and vortex pairing might cause a spurious elongation of the potential core and a reduction of centreline turbulence kinetic energy. The inclusion of the nozzle in the computation provides more realistic inflow conditions and could be computationally affordable if implemented in low-order numerical schemes such as *Finite Volume* (*FVM*) or the *Lattice Boltzmann* (*LBM*) schemes. For high-order codes on the other hand, including nozzles with complex geometries would be laborious to reproduce using body-fitted meshing technique, which is even more vital issue for industries that need to test and commission several prototypes every year. A few Recent LES studies have included nozzle in their computations utilizing specific meshing techniques (*e.g.* overset grids) and complex data structures (Paliath and Morris, 2004; Andersson *et al.*, 2005a; Shur *et al.*, 2005a; b; Uzun and Hussaini, 2006; 2007); however, such complex meshing was designed for a specific geometry that makes it hard to perform numerical experiments on different models in relatively short period of time for industrial applications. Although several LES studies have so far reported rather good agreement with experimental data for simple canonical nozzle geometries, further work is needed to develop computational methods with high accuracy and stability that are relatively inexpensive and fast for nozzles with arbitrary shape accompanied by noise suppression module and large temperature ratios.

Numerical methods based on the kinetic theory offer a potential to complement Navier-Stokes based methods in computational aeroacoustics (CAA) (Lew *et al.*, 2010a). Among several kinetic-based methods, the Lattice Boltzmann Method (LBM) has been proposed as an alternative to the well-established Navier-Stokes based numerical schemes due to its unique advantages in simulations of complex flows with acoustic interactions. The LBM has various unique features that make it a remarkable candidate for simulating complex turbulent flows (Chen and Doolen, 1998).

The convection operator in the LBM is linear. This is in contrast to the second-order nonlinearity in the Navier-Stokes equations that is very time consuming to solve numerically. The LBM recovers the same nonlinear behaviour as the NS equations through a relaxation process that models the particle interactions.

The LBM discretizes the Boltzmann equation in velocity space and only retains a minimal set of particle velocities that are needed to recover the proper macroscopic behaviour. This makes the LBM considerably more computationally efficient than other particle-based methods. It can be shown that the LBM is isotropic to second-order, and thus the orientation of the computational grid only has a small effect on the solution. This is ideal for computations of turbulent flows due to the three-dimensional nature of turbulent structures. If the orientation of the computational grid influences the solution, the orientation of these structures will be affected. The pressure in the LBM is computed from the ideal gas law, and so it does not require the solution of a Poisson equation to determine the pressure. This is often the most expensive operation in a finite difference method.

The LBM is also very simple to implement. It is completely explicit and thus does not require any matrix inversion. Each time step can be split into a collision and streaming step. The particle distributions are first relaxed towards their equilibrium values in the collision step, then the post-collision distributions are advected to their neighboring lattice sites in the streaming step. This simple implementation reduces the development time required for LBM codes and makes them simple to modify for complex geometries.

Because of the minimum stencil length among other the implementation of the LBM is very amenable to parallelization on modern high-performance computers. The collision step is intrinsically parallel by definition, and the streaming step requires very little transfer of data between processors. For this reason, the LBM has very good parallel performance. This is important for DNS since the computational cost necessitates the use of parallel computers.

The simplicity of the underlying explicit characteristics of the scheme allows a very straightforward implementation and coding. Basically, the core of the scheme is a simple shift operation, involving only the adjacent grid points, and the absolute local collision operation. Having such property, the method has the ability to be implemented on parallel computers with minimal floating point operation in second (FLOPS); this even works well for a fine-scaled parallelism. It is common that equidistant square lattices (Voxels) used for LBM schemes which allow for an efficient grid generation (Wenisch *et al.*, 2007). The complex solid body will immerse into the pool of voxels using the simple particle collision rules on the surface. The computational cost is effectively reduced to a minimum (Kollmannsberger *et al.*, 2009).

There are, however, a number of limitations to the LBM (Chen and Doolen, 1998). Despite the regular 19-stage LBM is restricted to solving weakly compressible problems ($Ma < 0.5$), it is in fact a transient compressible method. This means that the density does vary with pressure and temperature. Hence the method is suitable to capture acoustic pressures provided that timesteps are small enough to be compatible with the time scale of the sound propagation. The high-order LBM has also been introduced to cover the wide range of Mach numbers.

Conventional LBM scheme does not have enough degrees of freedom to allow for temperature variations. Adding an extra degree of freedom for temperature is challenging and often makes the code unstable and may violate conservation laws at macroscopic scale. To alleviate this problem and extend LBM for cases including heat transfer, the LBM is coupled with other Navier-Stokes based schemes by which the energy equation is solved separately. The energy equation is then coupled with the Lattice Boltzmann equations using appropriate body forces (Zhou *et al.*, 2004).

The LBM equations have been derived on the uniform cubic lattice platform. If the grid setup is made on either non-uniform or stretched format, an interpolation must be done and there would be a mismatch between predefined lattice velocity directions. It is still possible to manage non-uniform lattice by performing interpolation at the interface of neighboring lattices, however this would add the computational costs and reduce the actual order of accuracy.

1-4 Research objectives and contributions

In this work, the lattice Boltzmann method (LBM) is used as an alternative to traditional macroscopic LES or DNS methods based on Navier-Stokes formulations for jet noise studies. The focus of this study was to simulate jet noise problems that include complex nozzle geometers in the computational domain. This work was the first attempt in the literature to tackle heated jet noise problem and internal-mixing dual-stream jets using LBM. Also this research was the first attempt in the literature for time-resolved simulation of lobed mixers in which we studied several features of turbulent characteristics in the near-field, inside and outside of the nozzle that could justify the unique directivity and spectral behaviour of radiated sound in the far-field. A comprehensive parametric study was performed for different mixer models. As a side study, We also developed a framework to study sound absorption by jets for internal flow applications which is a basis of several studies by other authors on development of impedance boundary conditions and simulation of sound absorption by liners.

The PowerFLOW®[1] solver with D3Q19 Lattice Boltzmann kernel was used for all simulations in this study which is licensed by Exa Corporation.

The first aim of this work was to show LBM-LES technique, combined with thermal models and surface integral acoustic model can be used to predict the sound radiated from cold and heated jets. An under-resolved DNS approach, *aka* Pseudo DNS, was used for aeroacoustics study of a circular nozzle at low-Reynolds, and low-Mach flow conditions ($M_J \sim 0.2$). In this part, EXA PowerFLOW 4.2c was used and the turbulence model was turned off. It was the first time that heat transfer model was coupled to LBM for shear-flow simulations.

The second objective was to assess turbulence modeling in combination to LBM. Such method is also known as Very Large Eddy simulation (LBM-VLES). Turbulence modeling was used to upgrade the previous case to more complex SMC000 nozzle at high-Reynolds flow condition. PowerFLOW 4.3d was used in this part of our studies. As a side study, LBM-VLES method was

[1] PowerFLOW is a registered trademark of Exa Corporation (*Dassault Systèmes®- SIMULIA)*.

also combined with the porous model in PowerFLOW 4.3d to study the effect of porous extensions and flow resistance on the shear layer as well as the acoustic signatures. The SMC000 nozzle's geometry was provided by Exa corporation.

Third objective of the present research was to use regular LBM-VLES technique in PowerFLOW 4.3d to upgrade the setup from single-stream nozzles into dual-stream internal mixing nozzles with forced mixer at moderate Mach numbers ($M_J \sim 0.5$). The setup was used to perform parametric study on lobed mixers such as the effect of lobe numbers, thermal mixing, penetration depth, bypass ratio and scalloping.

The fourth objective was to use high-order D3Q19 LBM, for jet noise simulation at high-Mach subsonic condition, *i.e.* SP07 and SP46 benchmark problems. Similar approach was also used to simulate an internal mixing nozzle with lobe mixers using realistic Boundary conditions and make comparison with available experimental results. PowerFLOW 5.0 with high-Mach flow solver was used in this section. A similar SP07 and SP46 test case with some modifications were used as a benchmark case in similar collaborative studies by Exa and the author (Lew *et al.*, 2010b; Casalino *et al.*, 2014b).

The last part of this study is dedicated to simulation of sound absorption by jet flows using the LBM. In this section, a novel one-microphone technique was developed in a virtual impedance tube. Sound absorption characteristics of the jet flow was calculated numerically using LBM at different Mach numbers. Results were compared with available experimental data. PowerFLOW 4.3d was used in this study. Simulation of oscillatory flow over flat plate was also performed a side study to show LBM capability in simulation of acoustic flows in presence of solid boundaries.

For far-field noise calculations, PowerACOUSTICS version 2.0 was used in which the FW-H surface integral solver has been implemented.

1-5 Organization of the thesis

The thesis document is divided into two parts. The problem of sound radiation from subsonic single-stream and internal-mixing nozzles with forced mixers were studied in Part A, and the sound absorption by turbulent jets was the subject of Part B. Chapter 1 covers introductory topics and literature survey regarding jet noise problem, complex nozzles and computational aeroacoustics.

Chapter 2 presents the governing equations of the Lattice Boltzmann scheme including turbulence modeling and non-isothermal LBM models that are used in the PowerFLOW solver. Far-field sound prediction using FW-H surface integral technique is also presented in chapter 2. This model was implemented in PowerACOUSTICS 2.0 solver which is used throughout the present study. The LBM results for pseudo-DNS model for the circular jet were presented in Chapter 3. Chapter 3 also covers the high-Reynolds jet flow simulation using NASA SMC000 nozzle at $Re_D \cong$ 590,000 and $M_J = 0.5$ flow condition. Chapter 4 is dedicated to the simulation of internal mixing nozzles with forced mixers at moderate Mach numbers, *i.e.* $M_J = 0.5$. The impact of various mixer models and inflow conditions were evaluated on aerodynamic and aeroacoustic performance of such complex nozzles. Validation of High-Mach subsonic LBM scheme for jet noise problems, *i.e.* single-stream and dual-stream cases are presented in chapter 5. Chapter 6 presents a novel method to simulate sound absorption by turbulent jets. Concluding remarks and suggestions for future work are presented in Chapter 7.

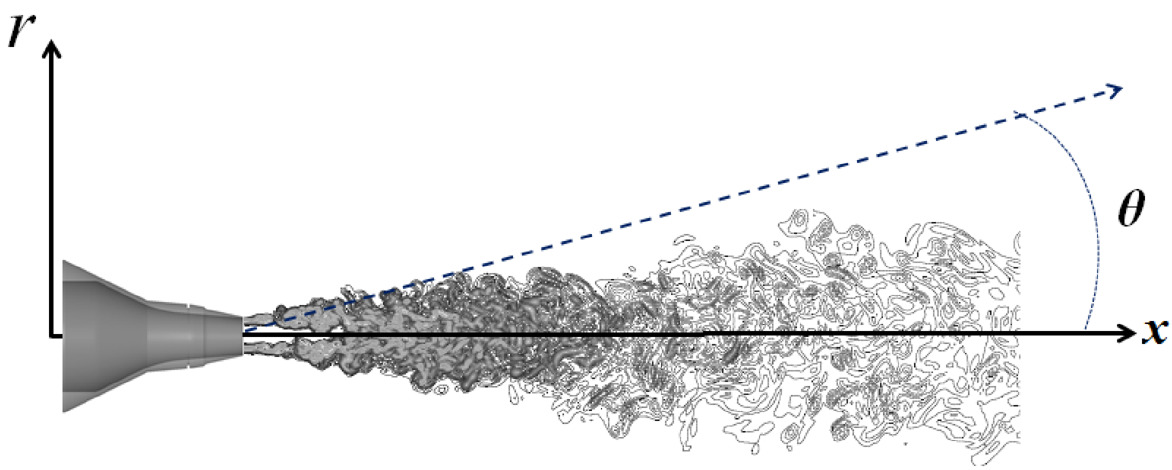

Fig. 1-1 Directivity angle(θ) of sound waves as considered for a jet flow simulation.

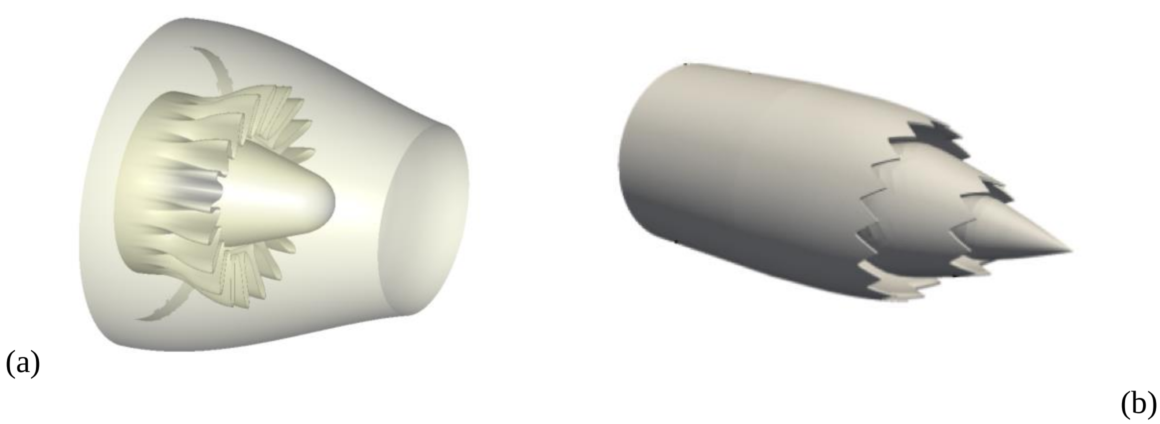

Fig. 1-2 (a) Internal mixing nozzles with forced lobed mixer (current study), (b) External mixing chevron nozzles, retrieved from: https://www.gauss-centre.de/results/computational-and-scientific-engineering/article/reducing-jet-noise-with-chevron-nozzles/, Copyright: AIA, RWTH Aachen University

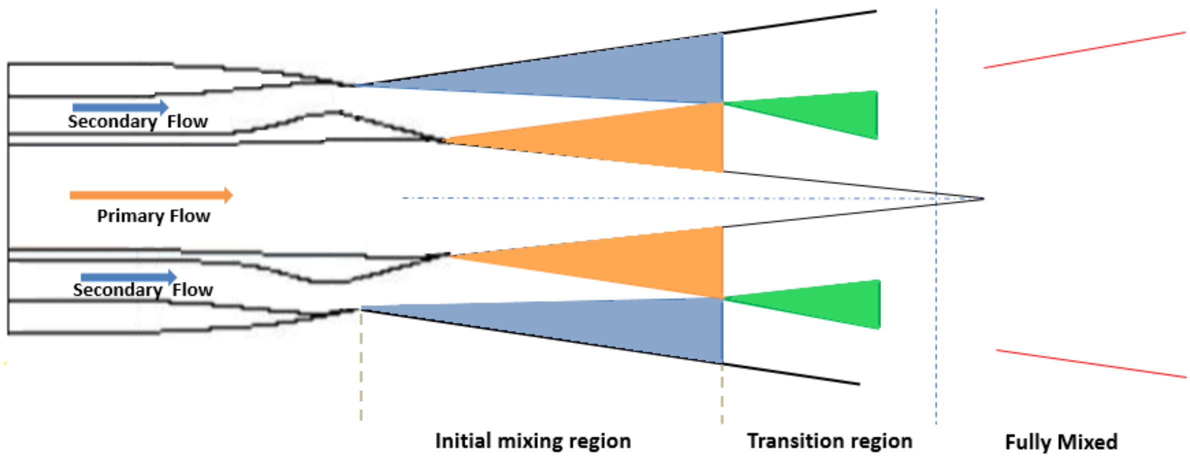

Fig. 1-3 Schematic of an external dual stream jet showing mixing zones core/bypass, bypass/quiescent, the transition, and the fully mixed regions

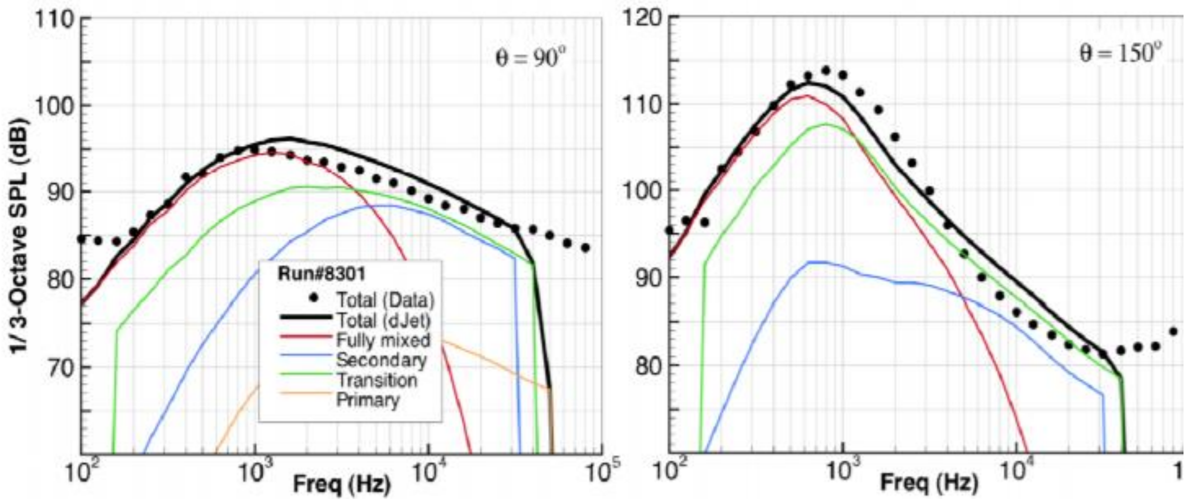

Fig. 1-4 Prediction and data in a dual stream jet at 90° and 150° inlet angles (Khavaran and Bridges, 2010)

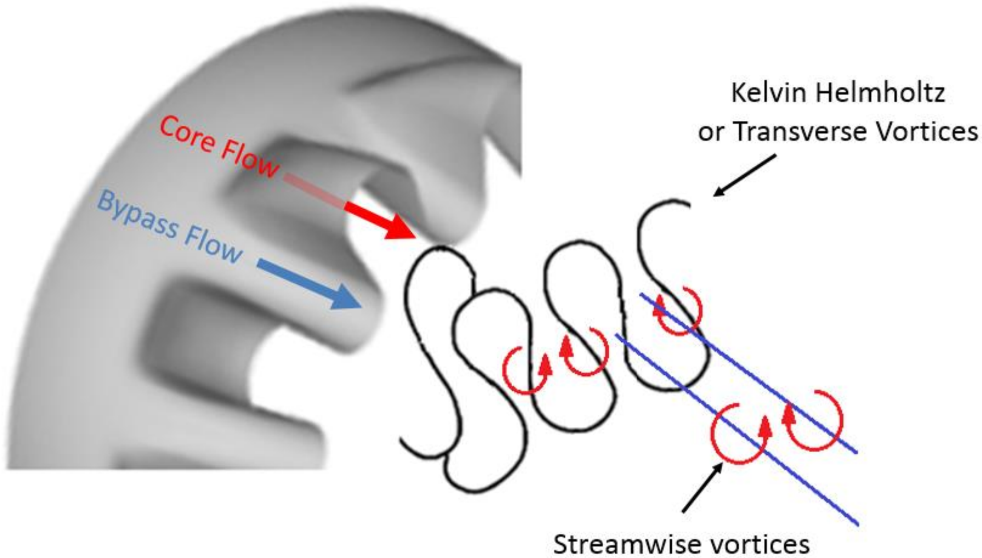

Fig. 1-5 Creation and development of Streamwise vortices through dual-stream lobed geometry

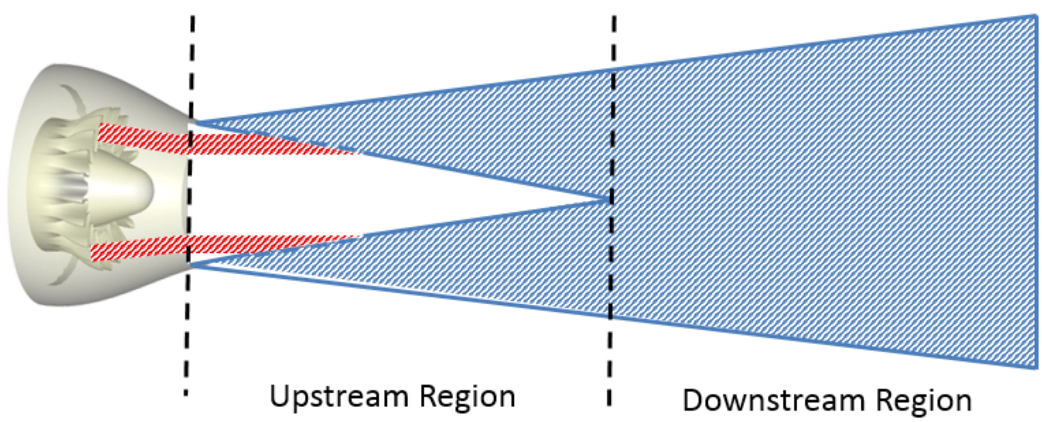

Fig. 1-6 Two-source model source segments in the plume of a jet with a 20-lobed internal forced mixer

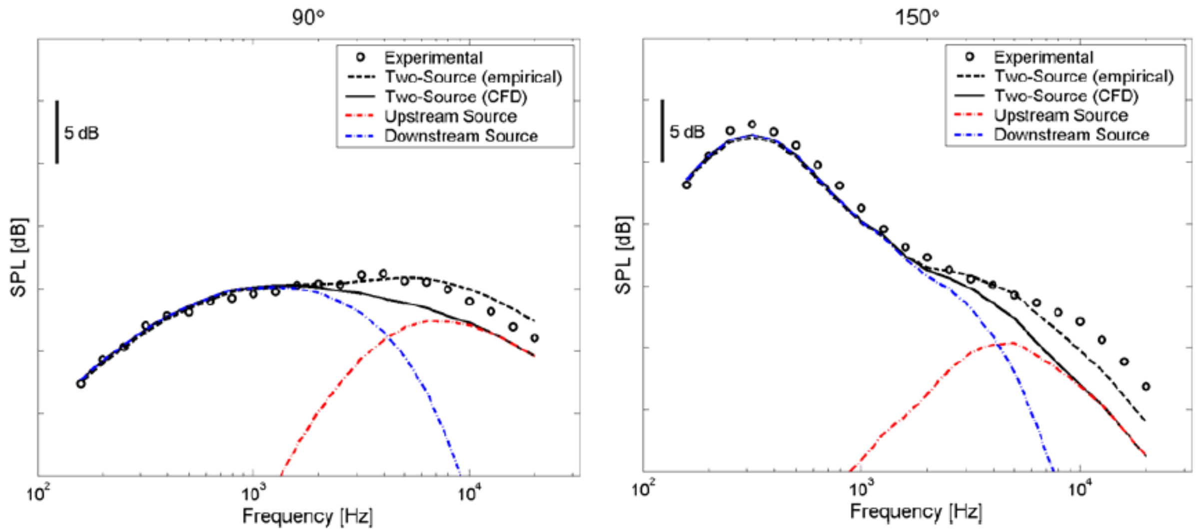

(a) **(b)**

Fig. 1-7 Two-source model prediction of normalized sound pressure levels of a jet with a 20-lobed internal forced mixer at observer's angles of (a) 90º and (b) 150º , plots were extracted from (Garrison *et al.*, 2006)

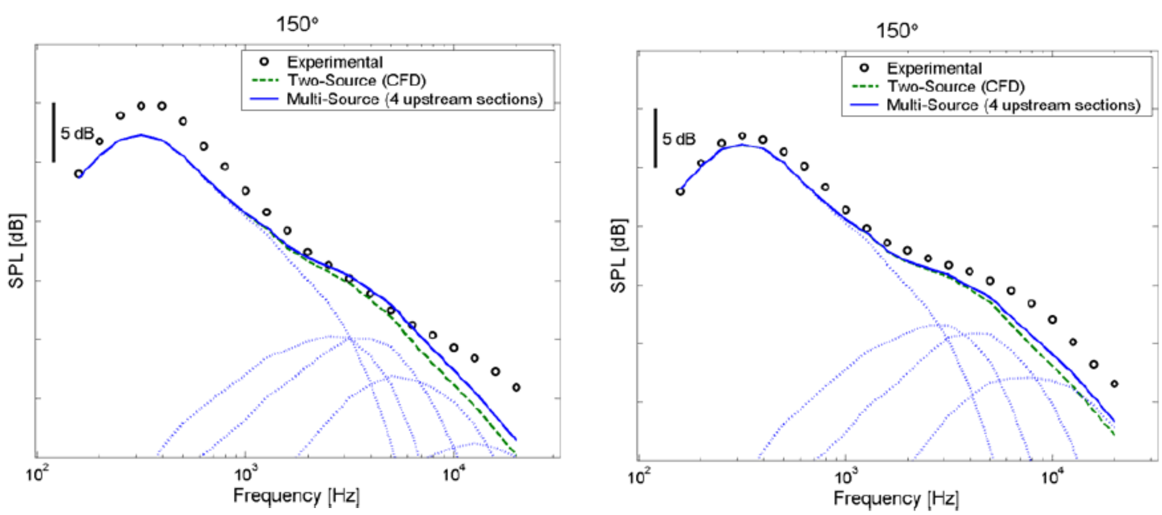

(a) **(b)**

Fig. 1-8 comparison of predicted SPL using two-source and multi-source (four sections) models for a jet with (a) 12-lobed and (b) 20-lobed internal forced mixer at observer's angles of 150º plots were extracted (Garrison *et al.*, 2006)

Chapter 2

Theoretical background

2-1 Lattice Boltzmann scheme

Numerical simulations of fluid dynamics based on solutions of the macroscopic Navier-Stokes equations involve the explicit calculation of macroscopic fluid properties by imposing conservation laws. An alternative approach, the Lattice Boltzmann Method (LBM), is based on kinetic theory. In this method a particle distribution function is considered in a discrete lattice domain. Transient macroscopic fluid properties are obtained by imposing streaming and collision laws governed by the lattice-Boltzmann equation (LBE), through the Chapman-Enskog expansion (Chapman and Cowling, 1970), the LBE recovers the compressible Navier-Stokes equation at the hydrodynamic limit (Chen *et al.*, 1992a; Chen *et al.*, 1997; Chen and Doolen, 1998). The conserved variables such as density, momentum and internal energy are obtained by performing a local integration of the particle distribution function.

2-1-1 The history of LBM

The LBM was derived from the well-known theory of Lattice Gas Cellular Automata (LGCA) in which the fluid flow is studied and modeled by tracking the dynamic evolution of particles on a discrete lattice platform (Wolf-Gladrow, 2000). In a lattice-gas system, each lattice node is connected to its neighbors by discrete number of lattice velocities; there can be either 0 or 1 particles at a lattice node moving with a specific lattice velocity. After each timestep, each particle will move to the neighboring node in its direction which is known as propagation or streaming step. In case more than one particle arrives at the same node from different directions, they change their velocities according to specific collision rules. The Lattice Boltzmann Method in form of a discrete equation, has appeared within the scientific community in the early nineties. The LBM scheme was initially introduced as an improvement to molecular-based methods by introducing particle distribution function that in a continuum fluid domain. When compared to other computational methods based on the classical Navier-Stokes equations , LBM was found to have advantages in terms of simplicity and accuracy in predicting the macroscopic behaviour of the fluid flow (Chen and Doolen, 1998) . The former LGCA method used the same collision and streaming concepts as the modern LBM schemes but lacked a unifying theoretical framework.

The collision operator in the LGCA was based on uncorrelated sets of collision rules, instead of a relaxation process as in the LBM. The LGCA method was able to recover the macroscopic characteristics of the compressible fluid, but was highly impaired by noise and instabilities that made it difficult to extend to three dimensions (Wolf-Gladrow, 2000). McNamara and Zanetti (1988) applied a single particle distribution, f_i, as an ensemble average of neighboring particles instead of Boolean occupation numbers for each particle, n_i, to reduce the numerical noise, but retained the same collision rules as the LGCA. Since the collision rules from LGCA models were still in force, the viscosity could not be changed. To alleviate this issue, Higuera and Jimenez (1989) proposed a linear collision mechanism that contained a few tunable coefficients that could be adjusted to change the viscosity. The role of the linearized collision operator was to relax the pre-collision particle density distributions at a specific location towards their local equilibrium distribution. The key parameter in this model is the relaxation time, that is directly related to the fluid thermophysical transport properties such as viscosity and thermal conductivity. The Bhatnagar-Gross-Krook (BGK) (Bhatnagar *et al.*, 1954) assumption of one single relaxation time helped to further increase the numerical efficiency of the particle collision calculations. The application of the BGK approximation was proposed by Chen *et al.* (1991). A similar formulation was also reported independently by Qian (1990). Later, a specific form of the equilibrium distribution function, suggested by Koelman (1991), allowed the LBM to be applied to any regular lattice configuration. Importantly, the new distributions eliminated unphysical effects that were observed in the old models, such as the dependence of pressure on the velocity or the violation of Galilean invariance[1] (Succi *et al.*, 2004).; such corrections were crucial in order to recover basic characteristics of continuum mechanics at the macroscopic scale. Advances in collision and relaxation models allowed the extension of the LBM scheme to three dimensions, which was very

[1] Galilean invariance states that the laws of motion are the same in all inertial frames. In the LBM, since a finite set of discrete speeds can only support a finite number of these excitations, breaking of Galilean invariance cannot be avoided, but it is possible to get closer to ideal invariance by tuning the equilibrium function with proper velocity terms.

difficult in traditional LGCA schemes (Chen *et al.*, 1992b). Eventually, the LBM scheme became known as an independent numerical scheme with unique characteristics distinct from LGCA. The combination of the LBM and the BGK assumption is referred as the LBGK method. It was shown that the LBM can be derived from the Boltzmann equation by discretization in both phase (*i.e.* velocity) and space which was also shown to be independent variables (He and Luo, 1997) . This derivation is presented in Appendix A of this document.

The intrinsic unsteady characteristics of the LBM as well as the capability of altering the viscosity, makes it suitable for simulating turbulent flows which is crucial for aeroacoustics problems . Benzi and Succi (1990) performed the first simulations of turbulent flows using the LBM. They simulated isotropic turbulence in two dimensions and compared turbulent kinetic energy spectra, the time evolution of entropy and total energy with DNS results from a high-order spectral method. The periodic boundary conditions were applied along all three outflow directions. To match the initial conditions in both methods, these conditions had to be transformed from spectral to physical space and used to set the initial particle distributions for the LBM. The initial conditions for the spectral method were determined using a random Gaussian distribution for the total energy spectrum. The energy spectra at downstream locations, *i.e.* in the decay region, were compared using both methods. Despite minor discrepancies at high wavenumbers, the inertial range in the energy cascade from the LBM was found to be in reasonable agreement with the DNS results. It was also shown that the computational cost of the LBM was nearly equal to that of the spectral method. While the LBM requires a smaller time step to maintain stability, *i.e.* slower evolution, it has a shorter stencil and required less computation per time step than the spectral methods. These two benefits were found to offset each other. A similar study was performed by Luo *et al.* (2002) in which the LBM results were compared with DNS from a pseudo-spectral code. They also observed the discrepancy at higher wave numbers, attributed to be due to the fact that the LBM is only second order accurate both in time and space and expected to be more dissipative than spectral schemes. Similar investigate performed on three-dimensional field by (Chikatamarla *et al.*, 2010) in which an extensive comparisons of various global and local statistical quantities obtained with an incompressible-flow spectral element solver.

Several benchmark turbulent flow problems such as flow over cylinders and airfoils (Shock *et al.*, 2002; Li *et al.*, 2004; Shur *et al.*, 2005a) , or flow above a cavity (Crouse *et al.*, 2006b) have been shown to be accurately modeled using LBM.

The lattice Boltzmann method is particularly suited for aeroacoustic simulations. Most aeroacoustic studies were performed by the PowerFLOW solver based on the LBM kernel. For example Crouse *et al.* (2006b) have studied series of canonical acoustic sound propagation problems and problems involving strong interactions between flow and sound using PowerFLOW. The applicability of LBM to simulate jet flows and radiated sound has been demonstrated by Lew *et al.* (2010a). In a similar study, Habibi (2011b) and Lew (2013) illustrated the applicability of the LBM-LES method for the simulation of heated jets and jet noise suppression using an array of impinging microjets. For airframe noise applications, several complex cases such as landing gear or full scale fuselage (Casalino *et al.*, 2014c; Casalino *et al.*, 2014d; Khorrami *et al.*, 2014) as well as wind turbine noise (Perot *et al.*, 2012) have been simulated. Also LBM was tested for simulation of three-dimensional jet plumes in volcanic flows by (Brogi *et al.*, 2015). These studies have also yielded results that were comparable with analytical solution or experimental data.

2-1-2 Conservation laws at the macroscopic form

The LBM consists of predicting the fluid particle distribution at the mesoscopic scale; conversion of the transport variables in LBM to their macroscopic counterparts should converge to flow characteristics obtained from conservative equations. In this section, first the macroscopic conservative laws are briefly summarized; later it is shown that conservative laws can be derived from the Boltzmann equation.

In continuum mechanics, for an invariant system that undergoes Galilean transformations, it can be shown that mass, momentum and energy are conserved. The governing partial differential equations in fluid mechanics are derived from these conservation laws. The description throughout this section is based on the formulation by Hirsch (2007).

For a closed system, in absence of a source term, the continuity equation in a differential form is

$$\frac{\partial \rho}{\partial t} + \nabla \cdot \left(\rho \vec{u} \right) = 0, \qquad (2.1)$$

where ρ is the macroscopic fluid density and $\vec{u}$ is the velocity vector.

The Navier Stokes equations govern the fluid flow at macroscopic scales. It expresses the balance between inertial force, pressure force, tension forces and body forces. The closed form of compressible Navier Stokes equation is

$$\rho\frac{\partial\vec{u}}{\partial t}+\rho\left(\vec{u}.\nabla\right)\vec{u}=-\nabla p+\mu\left[\Delta\vec{u}+\frac{1}{3}\nabla\left(\nabla.\vec{u}\right)\right]+\mu'\nabla\left(\nabla.\vec{u}\right)+\rho\vec{b}\,, \tag{2.2}$$

where the dynamic shear viscosity, μ, and the dynamic bulk or volume viscosity, μ', contribute to the magnitude of the viscous forces. The latter is in most practical applications negligible. The body forces ($\vec{b}$) such as gravity are negligible in aeroacoustic problems with air as a working fluid. Finally the energy equation can be derived from the first law of thermodynamics and the Fourier's law for the conduction of heat within the fluid volume. The differential form of the energy equation is given as

$$\frac{\partial\left(\rho E\right)}{\partial t}+\nabla.\left(\rho E\vec{u}\right)=\nabla.\left(\lambda.\nabla T\right)+\left[\rho\vec{b}.\vec{u}+q_h\right]+\nabla.\left(\underline{\underline{\sigma}}.\vec{u}\right), \tag{2.3}$$

where λ is thermal conductivity of working fluid, q_h is the net volumetric heat flux generated within the control volume. The scalar quantity, ρE, is the energy per unit volume. The total energy, E consists of the internal energy, e and, the kinetic energy with respect to an inertial coordinate system given by

$$E=e+\frac{\vec{u}.\vec{u}}{2}\,, \tag{2.4}$$

The stress tensor, $\underline{\underline{\sigma}}$, in Eqn. (2.3) is related to the forces acting on the control surface which can be decomposed into the normal and shear components as

$$\underline{\underline{\sigma}}=-pI+\underline{\underline{\tau}}\,, \tag{2.5}$$

where $\underline{\underline{\tau}}$ is the shear stress tensor, p is the static pressure and I is the identity tensor.

2-1-3 Lattice Boltzmann equation

The continuum Boltzmann equation is used to derive the discretized lattice Boltzmann equation (LBE). The complete derivation is discussed in Appendix A of this document. It is shown in that the resulting macroscopic behaviour of the system follows the Navier-Stokes equation when the Knudsen number is small(Chen and Doolen, 1998). The lattice Boltzmann equation (LBE) in the generic form, can be presented as

$$f_i(\hat{x}+c_i\Delta x, t+\Delta t) - f_i(\hat{x},t) = \Omega_i\left(\hat{x},t\right), \tag{2.6}$$

in which f_i is the particle density distribution function showing the probability of a particle being present at location x at time t with discrete velocity c_i. Here c_i (i = 0, 1, 2, …, k) is a set of vectors with constant values that spans the particle velocity space, Δt and $c_i\Delta t$ show the evolution in time and space respectively. Both terms in the left hand sides (LHS) are referred to streaming phase. In the above derivation, since both x and ($x + c_i\Delta x$) are lattice centroid locations, this directly implies a unity CFL (Courant-Friedrichs-Lewy) number, $\left|c_i\Delta x\right|/\Delta t = 1$, which is also the stability limit of current single-relaxation LBM. On the right hand side (RHS) of Eqn. (2.7), $\Omega_i\left(x,t\right)$ is the known collision term that governs the particle velocity distributions during the particle-particle interactions. Different models have been proposed for the collision term depending on which conservation laws, such as mass, momentum, etc., is selected to be followed. The Bhatnagar-Gross-Krook (BGK) approximation (Bhatnagar *et al.*, 1954; Qian *et al.*, 1992) which describes the effects of collision as a process to alter particle distribution towards its local equilibrium as

$$\Omega_i\left(x,t\right) = -\frac{f_i(\hat{x},t) - f_i^{eq}(\hat{x},t)}{\tau}, \tag{2.7}$$

where τ is a single relaxation time parameter that represents the average time for the current particle distributions to relax to their local equilibrium after several collisions, and $f_i^{eq}(\hat{x},t)$ is the local equilibrium distribution function which depends on local flow properties. The basic flow variables, such as velocity and fluid density are obtained through summations of moments at each discrete velocity direction from

$$\rho = \sum_i f_i(\hat{x}, t), \tag{2.8}$$

and

$$\rho \hat{u}(x,t) = \sum_i c_i f_i(\hat{x}, t). \tag{2.9}$$

The three-dimensional D3Q19 model (Chen *et al.* (1991); Qian *et al.* (1992)), shown in Fig. (2-1), was used in the present study in which the particle density distribution functions are cell-centreed. The particles interact with their neighborhood (either fluid particle or solid boundary) to model the fluid dynamics. The local equilibrium distribution function in D3Q19 has a form as

$$\begin{aligned} f_i^{eq}(\hat{x},t) = \rho(\hat{x},t) w_i [1 + \frac{c_i.\hat{u}(\hat{x},t)}{T_0} + \frac{\left(c_i.\hat{u}(\hat{x},t)\right)^2}{2T_0^{\,2}} - \frac{\hat{u}(\hat{x},t)^2}{2T_0} + \\ \frac{\left(c_i.\hat{u}(\hat{x},t)\right)^3}{6T_0^{\,3}} - \frac{c_i.\hat{u}(\hat{x},t)}{2T_0^{\,2}} \hat{u}(\hat{x},t)^2], \end{aligned} \tag{2.10}$$

such that the recovered macroscopic hydrodynamics satisfy the conservation laws. In Eqn. (2.10), the temperature in lattice scale, $T_0 = 1/3$ for the D3Q19 model. From Fig. (2-1), the weighting parameters, w_i, are given by

$$w_i = \begin{cases} 1/18 & for\ i = 0,...,5. \ \ (coordinate\ directions) \\ 1/36 & for\ i = 6,...,17. \ (bi-diognal\ directions)\ . \\ 1/3 & for\ i = 18. \qquad (particle\ at\ rest) \end{cases} \tag{2.11}$$

Such definition for the equilibrium function should meet the conservation of mass and momentum, which implies that equalities

$$\sum_i f_i(\hat{x},t) = \sum_i f_i^{eq}(\hat{x},t)\,, \tag{2.12}$$

and

$$\sum_i c_i f_i(\hat{x},t) = \sum_i c_i f_i^{eq}(\hat{x},t)\,, \tag{2.13}$$

are satisfied. If the timestep, Δt is set to unity, equation (2.7) can be solved in two steps which is also illustrated in Fig. (2-2). First in a “collision Step” that calculates the new (*i.e.* post collision) distribution is calculated by

$$f_i^{PC}(\hat{x},t) = f_i(\hat{x},t) - \frac{f_i(\hat{x},t) - f_i^{eq}(\hat{x},t)}{\tau}, \tag{2.14}$$

here, f_i^{PC} is the post-collide particle distribution function. Secondly, a streaming (advection) step directly exchanges particle distributions between two neighbors along the discrete velocity direction by

$$f_i(\hat{x}+c_i, t+\Delta t) = f_i^{PC}(\hat{x},t). \tag{2.15}$$

It is obvious that, in the collision stage, the equilibrium distribution is calculated using only local flow properties, *i.e.* ρ and $\hat{u}$, on the same node as defined in equation (2.8), (2.9) and (2.11). In the streaming step, only two neighboring lattice sites are communicating to exchange flow information. Such local behaviour of this collision-streaming operations, along with the linearity of the LB in equation 2.7, make the scheme very easy to implement in a computer code, and can achieve excellent scalability for parallel processing (Pohl *et al.*, 2003; Clausen *et al.*, 2010).

In weakly compressible limit (Mach number ≅ 0.5), one can obtain the Navier-Stokes equations from LBE through a Chapman-Enskog expansion (Chen *et al.*, 1992a). Equating the full compressible Navier stokes with extend LBE will result in linear correlation between pressure, density and temperature similar to equation of state for ideal gasses as

$$P = \rho T_0, \tag{2.16}$$

which also implies a constant speed of sound $c_s = 1/\sqrt{3}$ in lattice scales. It was shown that the relaxation time that appears in the LBE is related to the kinematic viscosity of the fluid, ν in lattice scale through the expression (Frisch *et al.*, 1987; Chen *et al.*, 1991)

$$\nu = \left(\tau - \frac{\Delta t}{2}\right)T_0. \tag{2.17}$$

With such definition, LBE expansion includes high-order terms, causes numerical errors to become a part of the viscosity. In the ill-conditioned case in which τ is nearly 0.5, the fluid viscosity would be small, the local Reynolds number would be high and the particle distributions might become negative, $f_i(\hat{x},t) \leq 0$, in some lattice sites followed by numerical instabilities throughout the computational domain. In order to avoid the negative distributions and improve numerical stability, a protection procedure has been applied in the LBM solver, *i.e.* PowerFLOW, which ensures positive distributions in all timesteps (Li *et al.*, 2004). In this method a new local relaxation time τ' in each cell is defined by

$$\tau = \max\left[\left(\nu / T_0 + \Delta t/2 \right), \Delta t \left(1 - \frac{f_i^{eq}\left(\hat{x}, t\right)}{f_i\left(\hat{x}, t\right)} \right) \right], \tag{2.18}$$

where i = 1, 2, …,18.

A positive distribution is guaranteed after each collision as long as it is positive before the collision. The addition of a local viscosity lower bound, which depends on the local distribution, makes it possible to keep distributions positive and avoid numerical instabilities.

2-1-4 Lattice unit conversion

In most lattice Boltzmann simulations Δx which is the basic unit for lattice spacing, is directly converted in the physical space. If the domain of length L has N lattice units along its length, the space unit is simply defined as $\Delta x = L/N$. This is also the case for mass. The mass unit is similar in both lattice and physical spaces. The time unit in the LBM simulations is the elementary lattice time-step. To convert the time in physical space, the speed of sound is used as the scale factor (Succi, 2001) given as

$$\Delta t = \frac{c_s}{C_s} \Delta x \,, \tag{2.19}$$

where, c_s is the constant lattice speed of sound ($=1/\sqrt{3}$) and C_s is physical speed of sound which varies with the temperature for ideal gasses, *i.e.* 343.2 m/s at air temperature of 20^{o}C. For small-scale flows or purely aerodynamic problems with no acoustic calculations, it is common to raise the lattice speed of sound otherwise, operating with the true speed of sound can lead to unacceptably short timesteps for given grid resolution which is not required to obtain averaged flow field.

2-1-5 Boundary conditions

(a) Inflow and outflow boundary conditions

For most wind tunnel or jet flow simulations, it is common that velocity and turbulence kinetic energy are imposed at the inflow boundaries, whereas the static pressure is set to constant at the outflow boundary. Other flow properties are extrapolated from the simulation domain. In most cases in LBM, the inflow or outflow boundary conditions are implemented based on extrapolations of flow characteristics by assuming local equilibrium $f_i \equiv f_i^{eq}$ on the boundary (Zou and He, 1997; Fares, 2006) based on the desired velocity and density values, the normal collision process is allowed take place . More complex conditions such as impedance boundary conditions (Sun *et al.*, 2013) or non-reflecting unsteady boundary conditions (Thompson, 1990; Najafi-Yazdi and Mongeau, 2012a) could be also implemented. To damp acoustic waves at outflow boundaries, it is important to use non-reflecting schemes. The boundary conditions are implemented in an under-relaxation manner to avoid large local gradients, especially during the initialization process. This is an important measure to avoid numerical instabilities. Therefore, the prescribed inlet/outlet values are not completely fixed but may change slightly according to the local flow behaviour.

(b) Wall boundary condition

For simple geometries with parallel or perpendicular sides, the standard bounce back boundary condition for no slip or the specular reflection for free slip condition are used (Chen and Doolen, 1998) . The bounce-back reflection boundary condition is used to simulate a “friction wall” condition. In the bounce-back process, the velocity of a particle is completely reversed after the wall-particle interaction (Fig. 2-3). This process is realized in terms of particle distribution as

$$a)\ f_i^{'} = f_i \quad , \quad b)\ c_i^{'} = -c_i \, . \tag{2.20}$$

The specular reflection boundary condition on the other hand, is usually employed to model free-slip boundary conditions; the particle distribution should be modified in a way that particles incidence and reflection angles are equal (Fig. 2-4). During the specular reflection process, the reflected particle distribution is equal to that of the incident distribution. The velocity magnitude should be conserved after the collision. Although the normal velocity component changes sign, the tangential component is restored so that a frictionless wall property is achieved. The reflected velocity, $C_i^{'}$, is related to the incident velocity, C_i, using

$$f_i^{'} = f_i \,, and \;\; c_i = c_i^{'} - 2\hat{n}\left(c_i^{'} . \,\hat{n}\right), \;\; if \;\; c_i^{'} . \,\hat{n} \geq 0, \tag{2.21}$$

in which $\hat{n}$ is the surface normal vector. The above formulations for the bounce-back and specular reflections do not produce very accurate results on non-lattice aligned curved surfaces. Higher order interpolation modifications have been proposed in the literature, but do not yield in satisfactory smooth behaviour close to the boundary (Filippova and Hänel, 1998). The boundary condition which is implemented in PowerFLOW and applied in our study is based on a volumetric formulation near the wall (Chen, 1998). In this method, the surface is facetized within each volume element (Voxel) intersecting the wall geometry using planar surface elements called Surfels. A particle bounce-back (no-slip) or specular reflection (free slip) is then applied on each of them and further weighted averaging and linear interpolation ensure the conservation of mass and momentum in the reflection process. For wall surface with area, A, and surface normal vector, $\hat{n}$, within total particle impact period of Δt and along the incident velocity direction, c_i, only the particles from the spatial volume $\cancel{V}_i$ can reach the wall boundary; this control volume is defined

$$\cancel{V}_i = \left|c_i . \hat{n}\right| A\Delta t, \;\; if \;\; c_i . \hat{n} \leq 0. \tag{2.22}$$

The total density of incoming particles, ξ_i, can be obtained as

$$\xi_i = f_i \cancel{V}_i = f_i \left|c_i . \hat{n}\right| A\Delta t, \;\; if \;\; c_i . \hat{n} \leq 0. \tag{2.23}$$

In case of the bounce-back reflection, the reflected particles will have the same volume as the incident particles given by

$$\xi_i^{'} = f_i^{'} \cancel{V}_i^{'} = f_i^{'} \left|c_i^{'} . \hat{n}\right| A\Delta t, \;\; if \;\; c_i^{'} . \hat{n} \geq 0. \tag{2.24}$$

This definition must ensure zero net mass introductions in the control volume. By substituting Eqns. (2.20) and (2.21) into Eqns. (2.23) and (2.24) one can obtain as

$$\sum_i \xi_i^{'} - \sum_i \xi_i = 0; \tag{2.25}$$

hence, the local mass is conserved through volumetric bounce-back reflection. It can also be shown that this is the case for the specular reflection condition. Since the bounce-back reflection reverts both the tangential and normal velocity components of particles, the corresponding particle momentum change is directly related to the net normal or tangential forces, F, defined as

$$|F| = (1/A\Delta t)\left(\sum_i c_i^{'}\xi_i^{'} - \sum_i c_i\xi_i\right), \tag{2.26}$$

which is imposed on the fluid particles. It can be shown that the normal and tension forces on the surface in lattice scale can be written in terms of the surface pressure , *p*, and the wall shear stress, τ_w, in the hydrodynamic macroscopic scale as (Chen, 1998)

$$F = p\hat{n} + \tau_w\hat{t}\,. \tag{2.27}$$

The volumetric formulation for wall boundary conditions (Chen, 1998) is shown to have small vanishing numerical errors along an arbitrarily oriented surface and across variable resolution regions (VR) close to the surface. This is essential to obtain a correct wall turbulent momentum flux and eases the implementation of enhanced wall models for turbulent flows. Arbitrary complex boundaries are easy to define within the computational domain without need for body-fitted mesh generation.

2-1-6 Grid generation in LBM

In LBM, a structured grid system with Cartesian cubic lattice cells is generally used for discretization of the spatial fluid domain; the solid boundaries are represented by a surface grid, *i.e.* known as surfels, and is directly connected to the adjacent fluid mesh to generate the fluid-solid interface. In the PowerFLOW solver, the surface grid of the original CAD model is used to define surfels. The resulting planar surface elements are written in common stereolithography (STL) format for direct user import during simulation setup. An STL file describes a raw unstructured triangulated surface by the unit normal and vertices of the triangles using a three-dimensional Cartesian coordinate system. There is no scale information on the STL files. They are later assigned by the PowerFLOW discretizer module. Figure (2-5) shows an example of complex nozzle's geometry merged into Cartesian fluid cells. In the PowerFLOW solver, the detection of the boundary surface is automated during the discretization process. Such a Cartesian grid approach is unique regardless of the complexity of the geometry. It significantly minimizes the overall cost associated with the generation of body-fitted meshes with very complex geometries (Aftosmis, 1997). Also, such approach alleviates the need for the mesh translation from computational space to physical space using conformal mapping methods. Figure (2-5(a)) shows a lobed mixer geometry, presented using a facetized CAD model.

The computational domain is divided into structured lattice arrays with variable resolution or variable refinement (VR) regions. The fluid elements (voxels) are distributed inside the VRs. Figure (2-5(b)) indicates the distribution of voxels near surface of the annular solid boundary. Figure (2-6) shows standard fluid and surface elements that are used in LBM near the solid boundary. The VR transitions allow for grid refinement and stretching, as seen in the discretized domain of the finite difference (FDM) or finite volume (FVM) schemes. Unlike finite difference or finite volume schemes in which the stretching factor could be selected arbitrarily, the grid refinement in LBM is always by a factor of 2. The integer stretching factor ensures consistency of particle velocity directions from finer to coarser VR regions. This process is illustrated in Fig. (2-7). The cells at every VR level are uniform in size in all directions. The transport of the velocity distributions f_i across the VRs is conducted following the procedure described in (Filippova and Hänel, 1998). The transition must also ensure conservation of mass and momentum via a volumetric formulation (Chen, 1998). The physical timestep, Δt, used on each VR is accordingly proportional to the local grid size, Δx, for the lattice Boltzmann solution. The finest lattice cells are updated at every timestep. The second level cells having the twice the length of the finest grids are updated every two timesteps (Fig. 2-7). This trend continues to the coarsest levels. This timestep update strategy has a direct impact on the sampling frequency of fluidic probes to record near-field flow characteristics or acoustic data. Sampling on finer cells allows for a higher sampling rate due to dependence of timestep to grid resolution in the LBM. This also affects the resolved frequency based on the Nyquist criterion.

2-1-7 Turbulence modelling

In engineering applications, specifically in aeroacoustics, almost all flows of interests are turbulent and consist of a broad spectrum of turbulent structures and vortices, over which the turbulence kinetic energy is distributed. As briefly discussed in section 1-3, the resolution of all small scales, *i.e.* (DNS simulation), is not computationally affordable for realistic Reynolds (*Re*) numbers. To resolve this issue, two methodologies were followed in the present study.

(a) Psuedo-DNS LBM scheme

For low-Reynolds numbers and a simple nozzle's geometry, a pseudo-DNS LBM scheme was used in which only very large turbulent scales are resolved with no sub-grid model. The Reynolds number is lowered to a level that resolved turbulent scales covers crucial acoustic sources in the near-field to obtain mean flow characteristics as well as sound pressure spectra in the far-field that are comparable with experimental data. In this approach, the smallest voxel size on the acoustic sampling surface limits the cut-off frequency of the simulation. The LBM is a 2nd order scheme and the under-resolved turbulent energy will be dissipated numerically in regions with coarse grids close to the outermost boundaries. This process is of great importance to maintain simulation stability. It is important to consider very large computational domain around the source to dissipate under-resolved energy sources as well as outgoing acoustic waves. The latter is also important to avoid unwanted reverberation of sound waves inside the computational domain.

(b) LBM-VLES scheme

For relatively high Reynolds number flows and more complex geometries, sub-grid-scale models were used to resolve small turbulent structures near solid boundaries. In LBM simulations, this methodology is also commonly referred to as Very Large Eddy Simulation (LBM-VLES). The LBE-VLES based description of turbulent fluctuations carries flow history and upstream information, and contains high order terms to account for the non-linearity of the Reynolds stress (Chen *et al.*, 2003; Shan *et al.*, 2006). This is in contrast with the Navier-Stokes based schemes, which use the linear eddy-viscosity based Reynolds stress closure models. The latter approach produces excessive dissipation and is unsuitable for unsteady simulations for aeroacoustics studies (Chen *et al.* (2003, 2004)). In the VLES method, large scales are directly simulated. In order to account for sub-grid scale turbulent fluctuations, the LBE is extended by replacing its molecular relaxation time scale, τ , in Eqns. (2.7) and (2.17) with an effective turbulent relaxation time scale, τ_{eff} . The time scale is derived from a systematic renormalization group (RNG) procedure (Yakhot and Orszag, 1986) defined by

$$\tau_{eff} = \tau + C_{\mu} \frac{k^2 / \varepsilon}{\left(1+\tilde{\eta}^2\right)^{1/2}} \quad , \tag{2.28}$$

where C_μ is constant and $\tilde{\eta}$ is a combination of a local strain parameter ($k\left|S_{ij}\right|/\varepsilon$), and a local vorticity parameter ($k\left|\Omega_{ij}\right|/\varepsilon$). In Eqn. (2.28), k represents the turbulence kinetic energy and ε, is the turbulent dissipation.

A modified two-equation "k-ε" model based on the original RNG formulation describes the sub-grid scale turbulence contributions (Yakhot and Orszag, 1986; Chen *et al.*, 2003). The turbulence model energy production and dissipation equations can be written as

$$\rho\frac{Dk}{Dt}=\frac{\partial}{\partial x_j}\left[\left(\frac{\rho v_0}{\sigma_{k_0}}+\frac{\rho v_T}{\sigma_{k_T}}\right)\frac{\partial k}{\partial x_j}\right]+\tau_{ij}S_{ij}-\rho\varepsilon, \tag{2.29}$$

And

$$\rho\frac{D\varepsilon}{Dt}=\frac{\partial}{\partial x_j}\left[\left(\frac{\rho v_0}{\sigma_{\varepsilon_0}}+\frac{\rho v_T}{\sigma_{\varepsilon_T}}\right)\frac{\partial \varepsilon}{\partial x_j}\right]+C_{\varepsilon 1}\tau_{ij}\frac{\varepsilon}{k}S_{ij}-\left[C_{\varepsilon 2}+C_\mu\frac{\tilde{\eta}^3\left(1-\tilde{\eta}/\eta_0\right)}{1+\beta\tilde{\eta}^3}\right]\rho\frac{\varepsilon^2}{k}, \tag{2.30}$$

where the parameter, $\upsilon_T = C_\mu\, k^2/\varepsilon$, is the eddy-viscosity in the RNG formulation and and β are constants, either derived from the RNG procedure or tuned for internal and external flow configurations. The constant values are listed in table 2.1. In Eqn. (2.28), (2.29) and (2.30), τ_{ij} is the stress tensor, S_{ij} is the strain rate tensor defined as:

$$\tau_{ij}=2\mu_t S_{ij}-\frac{2}{3}\rho k\delta_{ij}, \tag{2.31}$$

$$S_{ij}=\frac{1}{2}\left(\frac{\partial u_i}{\partial x_j}+\frac{\partial u_j}{\partial x_i}\right), \tag{2.32}$$

$$\Omega_{ij}=\frac{1}{2}\left(\frac{\partial u_i}{\partial x_j}-\frac{\partial u_j}{\partial x_i}\right), \tag{2.33}$$

And

$$\mu_t=\rho C_\mu\frac{k^2}{\varepsilon}. \tag{2.34}$$

Equations (2.29) and (2.30) were solved using a modified Lax-Wendroff explicit second order finite difference scheme (Teixeira, 1998; Pervaiz and Teixeira, 1999). The volumetric boundary formulation described in section 2-1-5 is necessary for LBM-VLES to achieve an accurate particle bounce-back algorithm on complex geometries and simulate the no-slip wall boundary conditions

(Chen *et al.*, 2003). This algorithm is well customized for complex geometries such as lobed mixers. Turbulent wall boundary conditions were applied using a generalized LBM slip algorithm and a modified wall-shear stress model, that significantly reduces the near wall grid resolution required for capturing turbulent structures near the solid boundaries.

2-1-8 Wall models for LBM-VLES scheme

For jet flows that includes nozzle internal flows within the computational domain, in cases where the Mach number and Reynolds numbers are relatively high, the velocity and thermal gradients in Boundary layers are much greater in normal to the wall directions than in the streamwise direction. In the LES methods, it is customary to use a grid that is stretched with a high aspect ratio near the wall to resolve all necessary scales inside the turbulent boundary layer. This helps to avoid the need for large numbers of grid points inside the boundary region. In the current LBM approach, such stretched grids are not practically implemented. As discussed earlier in section 2-1-5, the grid refinement must be performed by factors of 2.

In the present study, an extended logarithmic law of the wall was used that accounts for pressure gradient and helps to accurately predict the flow separation and transition to turbulence for unsteady jet flow simulations (Teixeira, 1998; Pervaiz and Teixeira, 1999). This method has been implemented in PowerFLOW solver and has been successfully validated and tested in several aerodynamic studies (Alexander *et al.*, 2001; Shock *et al.*, 2002; Fares, 2006). Unlike direct simulations, the use of a turbulence model implies a non-zero velocity at the solid boundary (Fig. 2-8). In this model, if the first grid point is located within the scaled boundary layer coordinate, $y^+ \leq 5$ (*i.e.* viscous sub-layer), the turbulent characteristics are independent of the geometry. The standard law of the wall

$$u^+ = y^+ , \qquad for \qquad y^+ \leq 5 , \tag{2.35}$$

is used where the normalized y coordinate is $y^+ = y\left(u_\tau / \nu_0\right)$, the scaled tangential velocity component, $u^+ = u/u_\tau$, and the friction velocity is $u_\tau = \sqrt{\tau_w/\rho}$. If $5 \leq y^+ \leq 30$, the law of the wall region obeys the logarithmic rule,

$$u^{+}=\frac{1}{\kappa}Ln\left(y^{+}\right)+B,\quad \kappa=0.4,\quad B=5.0. \tag{2.36}$$

For $y^{+}\geq 30,$ Eqn. (2.35) is extended to account for the pressure gradient, ∇P to implicitly calculate the friction velocity u_{τ} and turbulent quantities at the first cell centre near the wall (Teixeira, 1998). The formulation is an extension of the standard wall model expressed as

$$u^{+}=f\left(y^{+},k_{w},\zeta(\nabla p)\right),\quad k_{w}=u_{\tau}^{2}\big/\sqrt{C_{\mu}}, \tag{2.37}$$

where k_w is surface roughness. The function $\zeta(\nabla p)$ includes the influence of adverse and favorable pressure gradients. The combination of the LBE-VLES approach and the wall model yields an efficient and accurate prediction of turbulent engineering flows at high Reynolds numbers (Pervaiz and Teixeira, 1999) has been used in several aeroacoustic studies at high Reynolds numbers (Casalino *et al.*, 2014b; Casalino *et al.*, 2014d; Khorrami *et al.*, 2014; Fares *et al.*, 2016).

2-1-9 Thermal models for LBM

A hybrid thermal LBM was used to study the effect of temperature on acoustic characteristic of jet flows. Thermal lattice-Boltzmann methods (TLBM) fall into one of three categories: (1) the thermal energy distribution (He *et al.*, 1998); (2) the multi-speed approach (McNamara *et al.*, 1997), and (3) the hybrid or passive scalar method (Shan, 1997; Zhang and Chen, 2002; Zhou *et al.*, 2004; Gopalakrishnan *et al.*, 2013).

In the first approach, a third degree of freedom, which is the internal energy, is defined in lattice scale followed by a thermal energy distribution which is shown to recover the energy equation in the macroscopic limit (He *et al.*, 1998). The local fluid temperature is obtained in terms of the distribution function, and the conservation of energy is applied accordingly. Such approach was not used in PowerFLOW solver due to its known limitations (Zhang and Chen, 2002; Zhou *et al.*, 2004), which include numerical instabilities, the restrictive assumption of a Prandtl number close to unity, and the violation of the global *H* theorem[1] in some cases. The maximum temperature limit

[1] *The H theorem is the basis of non-equilibrium statistical mechanics that provides a conceptual link between the reversible laws in microscale with macroscopic phenomena. It is also a fundamental concept in computational physics, where compliance with an H theorem is often perceived as a byword for numerical stability. The H function*

is the main drawback of this method as it restricts its application for practical heated jet noise problems.

The multispeed approach consists of a straightforward extension of the isothermal LBE. In this method, the conservative form of energy equation is recovered by introducing additional speeds and by including high-order velocity terms in the equilibrium distribution function (*e.g.* D3Q34 or D3Q54 methods). Despite theoretical feasibility, the multispeed approach suffers from significant numerical instability. Also, as for the energy distribution method, the temperature range that can be handled is rather limited and usually the computation is more expensive.

In the passive scalar approach, which is implemented in PowerFLOW and used for the present jet noise study, the temperature field is passively advected by the fluid flow and can be simulated as an additional component of the fluid system. This means that one only needs to solve an auxiliary transport equation in order to solve for the temperature field in the single-phase isothermal LBE framework. In this passive approach, unlike the multispeed approach, the thermal diffusivity is defined independently and does not correlate with the viscosity. This results in a flexibility of Prandtl number in the simulations. Most importantly, the passive scalar approach has the same stability as the regular LBM scheme as does not require the implementation of an energy distribution in the lattice scale.

In the PowerFLOW solver, and for relatively low Mach numbers, the energy equation is solved separately using a finite difference approach on the same Cartesian grid used for the LBE. The momentum equation is coupled with the energy equation using appropriate body forces. The complete procedure is outlined by Zhang and Chen (2002). By neglecting the additional heat source and kinetic energy, Eqn. (2.3) can be written as

$$\rho(\frac{\partial}{\partial t}+\vec{u}.\nabla)e=-p\nabla.\vec{u}+\nabla.\lambda\nabla T+\Phi, \tag{2.38}$$

and used as a supplemental heat equation in the LBM solver. In Eqn. (2.38), *e,* is the local internal energy, assumed equal to c_vT, λ is the fluid thermal conductivity, and Φ represents viscous dissipation terms equal to the last term on the RHS of Eqn. (2.3). It can be shown that the

is defined as $\int f \ln f dv$. A simultaneous conservation of mass, momentum and energy minimizes the *H* function. (Succi *et al.*, 2002).

dissipation term, can be neglected (Bergman *et al.*, 2011) for weakly compressible flows at moderate speeds in subsonic region (*Ma* <<1). The heat conductivity, λ can also be defined via the constant Prandtl number, $Pr = \mu c_P / \lambda$. It is known experimentally (Bergman *et al.*, 2011) that *Pr* number for air is constant over a wide range of temperatures (≅0.71) , *i.e.* the heat conductivity scale similarly with temperature as the molecular dynamic viscosity. Such characteristics enables the extension to turbulent flow via the Boussinesq approximation (Wilcox, 1998). The effective viscosity, μ_{eff} ,and hence an effective heat conductivity, λ_{eff} ,as a sum of molecular and a turbulent components are used in Boussinesq's hypothesis and implemented in the turbulence model discussed in section (2.8). The relaxation time used in Eqn (2.17) is modified using the effective values as

$$\mu_{eff} = \mu + \mu_T \,, \tag{2.39}$$

$$\lambda_{eff} = \lambda + \lambda_T = \frac{\mu c_p}{Pr} + \frac{\mu_T c_p}{Pr_T} \,. \tag{2.40}$$

The dimensionless turbulent Prandtl number, Pr_T ,is assumed to be constant , *i.e.* $pr_T = 0.9$ for air, (Pope, 2000) for many engineering applications. A dynamically determined pr_T on the other hand which varies with distance from the wall (Yakhot *et al.*, 1987) offers and improved performance for heat transfer predictions which could be a valid assumption for thermal boundary layers as well as the free shear flows. The PDE for the temperature evolution can be summarized as

$$\rho c_p \frac{DT}{Dt} = -p\nabla.\vec{u} + \nabla.\left(\left(\frac{\mu c_p}{pr} + \frac{\mu_t c_p}{pr_T} \right) \nabla.T \right) . \tag{2.37}$$

This equation is solved using a Lax-Wendroff second-order finite difference scheme as for the discretization of the used *k-ε* RNG turbulence model described in section (2.8). This process enhances the efficiency of the hybrid LBM code as both the turbulence and heat transfer auxiliary equations are solved using the same scheme on the same grid used for LBE. Both LBM and Lax-Wendroff FD schemes are second-order which makes the hybrid scheme consistent in terms of numerical error.

For a moderate temperature range, *i.e.* $\Delta T < 100^{o}\,C$, the density variations are relatively small; hence, the temperature would have minimal impact on the overall flow characteristics. This also implies that the momentum equation, *i.e.* LBE, is not coupled with the energy equation, and the temperature will behave as a passive scalar. Base on the Boussinesq approximation (Bergman *et al.*, 2011) all flow properties are assumed to be temperature independent for moderate temperature ranges and the correct flow is recovered with an addition for a virtual volumetric force describing the buoyancy due to the temperature driven density variation (Zhou *et al.*, 2004). For practical jet simulations, the temperature dynamic range may exceed $600^{o}\,C$ and the density variations would have significant effects on the flow and the acoustic fields. The PowerFLOW solver provides the active interaction between the energy and momentum equations using modified body forces that extends the range of temperatures dynamic range. This implementation has been initially proposed by Zhou *et al.* (2004) and later modified by Gopalakrishnan *et al.* (2016). Base on Zhou *et al.*'s approach, under the Boussinesq approximation, the buoyancy force can be calculated in a straightforward manner based on the temperature field variation, using

$$F_b\left(x,t\right)=\rho\left(x,t\right).g.\alpha.\left(T\left(x,t\right)-T_{ref}\right), \tag{2.38}$$

where g represents gravity, T_{ref}, is the reference temperature which is constant. For heated flow simulations, T_{ref}, equals to the ambient temperature, and α, is the thermal expansion coefficient defined as

$$\alpha=-\frac{1}{\rho}\left(\frac{\partial\rho}{\partial T}\right)_P. \tag{2.39}$$

The momentum term associated with the buoyancy force was proposed by Martys and Chen (1996) by ignoring higher order contributions of the local Knudsen number. The appropriate buoyancy force that needs to be introduced into the LBE can be expressed as

$$\Delta f_i\left(x,t\right)=\frac{w_i}{\rho T_0}c_i.F_b\left(x,t\right), \tag{2.40}$$

where the constant weights w_i and T_0 are directly determined by the particular LBE model for the corresponding non-buoyant case, the lattice temperature, T_0 = 1/3, and the coefficients, w_i, are determined using Eqn. (2.11). the term $\Delta f_i\left(x,t\right)$, is directly introduced to the RHS of LB equation and updated by spatial distribution of temperature, *i.e.* solution of Eqn. (2.37), at every timestep.

In more recent approach proposed by Gopalakrishnan *et al.* (2016) which is also applicable for High-Mach subsonic version of D3Q19 LBM, the body force is correlated to the equation of state given by

$$g_i\left(x,t\right)=\rho w_i\left(1-\frac{P\left(\rho,T\left(x,t\right)\right)}{\rho T_0}\right), \tag{2.41}$$

where ρ is the macroscopic fluid density and $T\left(x,t\right)$ is given by Eqn. (2.37) at every time step. In this approach, a thermodynamic step is added to the particle collision step; however, this new step is substantially independent of and separate from the collision step. The modified LB advection process can be formulated as

$$f_i\left(\hat{x}+c_i\Delta t,t+\Delta t\right)=f_i\left(\hat{x},t\right)+\Omega_i\left(x,t\right)+\left[g_i\left(\hat{x}+c_i\Delta t,t+\Delta t\right)-g_i\left(\hat{x},t\right)\right], \tag{2.42}$$

where $\Omega_i\left(x,t\right)$ is the collision operator as defined in Eqn. (2.7). For purpose of computational stability in a parallel domain, temperature coupling to momentum equation is performed using a nine-step process as described by Gopalakrishnan *et al.* (2016).

It can be shown that both the pressure derivative and the dissipation term, in Eqn. (2.37), can be neglected for slightly compressible flows at moderate speeds M_J <<1 (Zhou *et al.*, 2004). The heat conductivity, κ, can be also defined via the constant Prandtl number $Pr = \mu c_p / \kappa$. It is known from experiments that $Pr \cong 0.71$ for air is constant over a wide range of temperatures, *i.e.* the heat conductivity scales similarly with temperature as the molecular dynamic viscosity (Baehr and Stephan, 2004). Such coupled thermal scheme was implemented in PowerFLOW 4.2 which was used for all low-Mach test cases (up to 0.5) in the present study.

2-1-10 Thermal wall model for LBM

Standard similarity laws (Schlichting *et al.*, 2000; Kays *et al.*, 2012) are used to develop a thermal wall function for predicting temperature in turbulent boundary layers. Similar to momentum wall function in Eqns. (2.35) and (2.36) , the thermal wall function can be described as (Zhang and Chen, 2002; Zhou *et al.*, 2004)

$$T^+ = A\ln y^+ + F(Pr), \tag{2.43}$$

where A represents a constant and $F(Pr)$ a function for the local Pr number. A further modification to account for the viscous regime $y^+ < 30$ is also included as for the fluid viscous sub layer $u^+ = y^+$. The normalized temperature can be described by the wall temperature, T_w, the wall heat flux,

q_w, and the near wall temperatures, T, evaluated at the centre of the closest voxel in the vicinity of the wall, described by

$$T^+ = \frac{\left(T_w - T\right)\rho c_p u_\tau}{q_w}. \tag{2.44}$$

Equations (2.43) and (2.44) relate the near wall temperatures, T, to the wall temperatures, T_w ,and the wall heat fluxes, q_w . In case of heated jet flow simulations where the nozzle body is included in the computational domain, it is important that the wall temperature or the heat flux is set correctly. Therefore, the wall model can be used either to determine the wall heat flux if the wall temperatures are given as a surface boundary condition or vice versa.

2-1-11 Extension of LBM to simulate flow in porous media

In the LBM, by altering the local particle distributions during the collision step on can simulate the effect of external forces exerted to the body of fluid particles. A similar technique was discussed earlier in section (2-10) to bundle the energy and momentum equation using body forces and also to account for the buoyancy effects due to gravity. The PowerFLOW solver used in the present study implements a porous medium model by applying flow resistivity as an external force; thus, Porous medium regions can be processed with very little additional computational expense compared to ordinary fluid. The external force would be a nonlinear function of local flow velocity derived from the extended Darcy model for porous media (Freed, 1998). This model can be used to predict pressure losses that affect the time-averaged flow field solution and, at the same time, the instantaneous acoustic perturbations. The nonlinear relation between the pressure gradient and local velocity is

$$\frac{\partial p}{\partial x_i} = -\rho\left(R_i + I_i\left|\hat{u}\right|\right)u_i, \tag{2.45}$$

where i indicates the principal axis index, x_i, is the spatial variable along axis i, ρ is local fluid density, density, Ri is viscous coefficient of resistance towards direction i, u_i , is velocity along axis i. The parameter I_i , is the inertial coefficient of resistance and $\left|\hat{u}\right|$, is the velocity magnitude.

2-1-12 Extension of D3Q19 LBE to cover high Mach subsonic flow regimes

In the present study, in order to simulate jet flows with higher Mach numbers with wider industrial application, the extended high-order LBM method was used for some test cases. For flow solutions in the high subsonic Mach number range, *i.e.* flows with local velocity Mach number greater than 0.5, a standard D3Q19 LBM is applied with modified collision operator. The BGK collision operator in Eqn. (2.7) was replaced by a regularized collision operator which can significantly increase both numerical stability and accuracy when local flow Mach number is high (Chen *et al.*, 2013). For D3Q19, if we change the collision operator as

$$f_i^{'}\left(\hat{x},t\right)=f_i^{eq}\left(\hat{x},t\right)+C_i\left(\hat{x},t\right), \tag{2.46}$$

then he regularized collision function can be derived as

$$C_i\left(\hat{x},t\right)=\left(1-\frac{1}{\tau}\right)\frac{w_i}{2T_0}\left[\left(1+\frac{c_i.\hat{u}\left(\hat{x},t\right)}{T_0}\right)\left(\frac{c_ic_i}{T_0}-1\right)-\frac{c_i\hat{u}\left(\hat{x},t\right)+\hat{u}\left(\hat{x},t\right)c_i}{T_0}\right]:\Pi^{neq}\left(\hat{x},t\right), \tag{2.47}$$

where $\Pi^{neq}\left(\hat{x},t\right)$ is the non-equilibrium part of the LBE given by

$$\Pi^{neq}\left(\hat{x},t\right)=\sum_i c_i^{'}c_i^{'}\left[f_i\left(\hat{x},t\right)-f_i^{eq}\left(\hat{x},t\right)\right], \tag{2.48}$$

and $c_i^{'}$ is defined as

$$c_i^{'}=c_i-\hat{u}\left(\hat{x},t\right). \tag{2.49}$$

In order to resolve the high-Mach compressibility effects, the equation of state was modified by an interaction force in the governing LB equations which can effectively reduce the speed of sound in lattice scale (Gopalakrishnan *et al.*, 2013), such that high Mach number flows can be achieved in simulations by a low order LB scheme (Nie *et al.*, 2009b; Gopalakrishnan *et al.*, 2013). Then in order to take into account the flow heating due to compression work and viscous dissipation, a modified hybrid approach was applied for the thermodynamics of energy field, by solving the entropy equation through a Lax-Wendroff finite difference scheme on the Cartesian LB mesh. These LBM extensions enable accurate calculation of high Mach subsonic CFD/CAA problems for realistic turbofan engine configurations (Casalino *et al.*, 2014b; Habibi *et al.*, 2014; Lew *et al.*, 2014), with an efficient Cartesian grid system.

In this method, the interaction force, F_g, is introduced in the LBE , *i.e.* Eqns. (2.6), (2.7) … (2.10)) as

$$F_g = -\nabla \Psi = G(|c_i|)\sum_i \Psi(\hat{x} + c_i)c_i , \tag{2.50}$$

where ψ is defined as

$$\Psi = -\frac{g}{2}\rho T , \tag{2.51}$$

where the function *G* specifies the accuracy of the derivative and constant *g* determines the strength of the force. Because of this interaction force, the equation of state changes to

$$p = \rho T + \Psi = \rho RT , \tag{2.52}$$

where the gas constant *R* is derived from *g*:

$$R = \left(1 - \frac{g}{2}\right). \tag{2.53}$$

If a correct energy equation is included, the speed of sound becomes

$$c_s = \sqrt{\gamma RT} . \tag{2.54}$$

As mentioned earlier, the entropic representation of the energy equation was found to be the most practical and stable approach in order to couple energy transport with Lattice Boltzmann momentum equations for high-Mach flow simulations. The modified entropic energy equation can be formulated as

$$\frac{\partial S}{\partial t} + \vec{u}.\nabla S = -\frac{1}{\rho T}\nabla \vec{q} + \frac{\Phi}{\rho T} , \tag{2.55}$$

Where the entropy, *S*, is defined by the density, *ρ*, and temperature, *T* as

$$S = c_v \ln\left(\frac{T}{\rho^{\gamma-1}}\right). \tag{2.56}$$

The heat flux vector, $\vec{q}$, is calculated via Fourier's law as

$$\vec{q} = -\lambda \nabla T . \tag{2.57}$$

Here, c_p and c_v are specific heat at constant pressure and volume respectively and λ is the heat diffusivity. Viscous dissipation terms, Φ, can often be neglected for subsonic shear flows. The entropic thermal solver was implemented in PowerFLOW 5.0 was used in chapter 5 of the present study for simulation of jet flows at high Mach subsonic conditions.

2-1-13 Parallelization of LBM for jet noise problems

Lattice Boltzmann methods are perfect choice for massive parallelization. The BGK algorithm does not have any global operators such as mix derivatives of shear stresses as seen in many NS codes that has to solve Poisson equation to obtain pressure field; LBM does not even involve solving diagonal matrix systems or matrix multiplication. All interactions are strictly local. In the collision stage (step 1), the updated equilibrium distribution functions of one node are evaluated using only the distribution functions of the same node. In the propagation (streaming) stage (step 2), each node will exchange the distribution functions with 18 out of 26 nodes in neighboring voxels (Körner *et al.*, 2006). The spatial domain can be decomposed into equally sized subdomains which are assigned to different processors. The message passing interface (MPI) is used in PowerFLOW solver to perform domain decomposition. MPI can be run on either shared or distributed memory architectures and each process has its own local variables; however, parallelization performance is limited by the communication network between the nodes (Cappello and Etiemble, 2000). During streaming stage of LBM, many discrete velocity components, c_i , are zero; this leads to significant reduction in number of required floating point operations (Flops), Also, pre-computing of common expressions at different timesteps due to compact stencil and lack of global operation, will result in less than 200 Flops per cell update for the D3Q19 BGK scheme on single nose platform(Wittmann *et al.*, 2013).

When it comes to the computational performance of LBM compared to well-stablished finite difference/ volume /element methods, the work presented by (Bernsdorf *et al.*, 1999; Succi, 2001; Bhandari, 2002) or the recent comparison in (Geller *et al.*, 2006) demonstrate that LBM is very competitive; however, the LBM has high memory requirements and in many cases, the memory access time could be significant compared to arithmetic operations. The computational efficiency of LBM stands out for problems involving complex geometries complex physics, and aerodynamic problems at moderate Mach numbers. In order to evaluate scalability of PowerFLOW in jet noise problems, simple jet flow case (M_J = 0.2) with coarse grid was used. The execution time until transient convergence was chosen as a criterion to test the effectiveness of process distribution. First, we executed the program with 128 cores which yields an execution time ≅76 hours. Next, the code was executed over increased number of processors. The speedup obtained by this process is shown in Fig (2-9). As expected the speedup trend was approximately linear.

2-2 Far-field sound studies

2-2-1 Introduction

In the previous section we discussed the CFD method based on the lattice Boltzmann scheme to model flow properties in the near-field. As discussed in section 1-2, the indirect approach will be used for far-field calculations; the idea is to use near-field flow characteristics to predict far-field sound pressure levels spectral distribution as well as directivity of sound waves. Two practical methodologies for indirect approach are known as Lighthill's acoustic analogy (LLA) (Lighthill, 1952; Lyrintzis, 2003) and surface integral methods (Lyrintzis, 2003).

Lighthill's acoustic analogy allows computing of sound field radiated by a bounded region of turbulent flow by solving an analogous problem of forced oscillation, *i.e.* wave equation, provided that the near-field flow characteristics are known.

The modified wave equation used in LLA can be derived using continuity and momentum equations in macroscopic scale, *i.e.* Eqns. (2.1) and (2.2), by neglecting all external forces and assuming that flow outside of the turbulent flow sources is at rest with uniform pressure and density p_0 and ρ_0 respectively (Lighthill, 1952; Pierce, 1981). The acoustic quantities p' and ρ' are defined as

$$(a)\ p = p_0 + p' \ \text{ and } \ (b)\ \rho = \rho_0 + \rho'. \tag{2.58}$$

If the compression and expansion of the fluid is considered to be isentropic, there is a linear relationship between the acoustic pressure and acoustic density that is

$$p - p_0 = c_0^{\,2}\left(\rho - \rho_0\right) \quad \Leftrightarrow \quad p' = \rho' c_0^{\,2}, \tag{2.59}$$

where c_0 depends on the fluid thermophysical properties and is the velocity at which acoustic waves propagate through the medium (Pierce, 1981; Anderson, 1990). For ideal gasses, c_0 is defined by

$$c_0{}^2 = \left.\frac{\partial p}{\partial \rho}\right|_{S=const} = \gamma RT\,. \tag{2.60}$$

The speed of sound is in fact a function of the adiabatic gas constant γ, the specific gas constant R and the thermodynamic temperature T. Considering Stokes' hypothesis (White and Corfield, 2006), the bulk viscosity could be presented as

$$\mu' = -\frac{2}{3}\mu\,. \tag{2.61}$$

Then the time derivative of the Eqn. (2.1) and the divergence of the Eqn. (2.2) are taken and both equations are combined in order to remove momentum density $\rho\vec{u}$. Using tensor notation and subtracting the term $c_0{}^2\partial^2\rho/\partial x_i{}^2$ from both sides as well as inserting undisturbed pressure and density terms, p_0, and, ρ_0 ,the modified wave equation can be written as

$$\frac{\partial^2\rho'}{\partial t^2} - c_0{}^2\frac{\partial^2\rho'}{\partial x_i{}^2} = \frac{\partial^2 T_{ij}}{\partial x_i \partial x_j}\,, \tag{2.62}$$

and

$$T_{ij} = \rho u_i u_j + \left(p - p_0 - c_0{}^2\left(\rho - \rho_0\right)\right)\delta_{ij} + \mu\left[-\frac{\partial u_i}{\partial x_j} - \frac{\partial u_j}{\partial x_i} + \frac{2}{3}\left(\frac{\partial u_k}{\partial x_x}\right)\delta_{ij}\right], \tag{2.63}$$

where δ_{ij} , is Kronecker delta function and Eqn. (2.49) is the RHS of Eqn. (2.48), which is called the Lighthill tensor. The term $\rho u_i u_j$, exhibits the convection of momentum component, ρu_i , by velocity component, u_j . Also, $p - p_0 - c_0{}^2\left(\rho - \rho_0\right)$, is derived from a state where all fluctuations are isentropic; and the last term in RHS of T_{ij} is the transport of momentum due to viscous stress. In most cases the direct convection of momentum appears as fluctuation Reynolds stresses, is much larger than the transport of momentum due to viscous stresses; hence the viscous term could be neglected. If the acoustic domain could maintain isentropic condition, $p - p_0 - c_0{}^2\left(\rho - \rho_0\right)$ would be a very small quantity and can be neglected. In this case the Lighthill tensor can be simplified as

$$T_{ij} = \rho u_i u_j = \rho\begin{pmatrix} u_1{}^2 & u_1 u_2 & u_1 u_3 \\ u_2 u_1 & u_2{}^2 & u_2 u_3 \\ u_3 u_2 & u_3 u_2 & u_3{}^2 \end{pmatrix}. \tag{2.64}$$

The far-field sound pressure is then given in terms of a volume integral over the domain containing the sound source. The major drawback of acoustic analogy is that the sound sources are not necessarily compact in some complex flows such as high-speed shear flows. There might some errors in calculating the sound field, unless the computational domain could be widely extended toward downstream to cover all convective sources; moreover, an accurate prediction of acoustic emission time requires keeping a long record of the converged transient solution of the sound source, which results in storage issues.

Kirchhoff's (Pilon and Lyrintzis, 1996; 1998) and porous FW-H methods (Ffowcs Williams and Hawkings, 1969) are to major surface integral methods that have been widely employed in CAA studies as it was found that the memory requirements are a fraction of that required in LLA. In this approach, unsteady flow information is stored on a control surface surrounding non-linear sound sources such as near-field of a jet flow, and the sound is propagated to the far-field by solving surface integrals on either open ended or closed surface using flow acoustic information.

Kirchhoff's method, is based on the similarities between the aeroacoustics and electrodynamic equations, is a surface-integral representation of linear wave equation. The control surface is assumed to encase all non-linear acoustic sources, which might not be realistic in some complex flows. Additional nonlinear sources, such as quadrupole in waked regions, can be added outside the control surface (Pilon and Lyrintzis, 1998).

Ffowcs Williams-Hawkings (FW-H) method, is originally derived based on the conservation laws on macroscopic scale rather than the linear wave equation in the Kirchhoff's method. The control surface does not have to enclose all the non-linear acoustic sources and thus, this approach can be adopted in many applications. The porous FW-H formulation can be applied on the surfaces in the non-linear region unlike the Kirchhoff's method. The FW-H formulation is equivalent to the Kirchhoff's formulation plus a volume integral of quadrupole sources when the integration surface is located in the linear wave propagation region. Due to the flexibility of this method as well as computational advantages, we have used the FW-H scheme for far-field analysis in present study.

2-2-2 Formulation of basic Ffowcs Williams-Hawkings method

In the FW-H method, the fluid domain is partitioned into separate regions by a mathematical surface which represents the boundaries between a body and the surrounding flow field. This process is shown in Fig. (2-10). Outside the surfaces, the flow is identical to the physical flow, inside the surfaces it can be specified arbitrarily. Additional source terms might be needed on the boundaries to alleviate discontinuities between interior and exterior flows. The surface S is defined by the equation $f(\vec{x},t)=0$. Note that the function $f(\vec{x},t)$ represents both the shape and motion of the surface. FW-H starts with generalized equation of mass and momentum in integral form and derive the differential form by adopting the surface function and the divergence theorem. The modified inhomogeneous mass and momentum equations using tensor notation can be written as

$$\frac{\partial \rho}{\partial t}+\frac{\partial}{\partial x_i}\left(\rho u_i\right)=\rho_0 u_i \delta\left(f\right)\frac{\partial f}{\partial x_i}, \tag{2.65}$$

and

$$\frac{\partial\left(\rho u_i\right)}{\partial t}+\frac{\partial}{\partial x_j}\left(\rho u_i u_j+\sigma_{ij}\right)=\sigma_{ij}\delta\left(f\right)\frac{\partial f}{\partial x_j}. \tag{2.66}$$

If body forces are neglected in equations (2.2), the only difference between equations (2.1) and (2.2) and equations (2.65) and (2.66) are the presence of mass and momentum source terms on the RHS of equations (2.65) and (2.66) respectively. The source terms ensure that the unbounded fluid remains in its defined state. If there is only one region with no solid boundary, above equations reduce to the original form. Following the same process performed in section 2-2-1 to derive LAA, the inhomogeneous wave equation is derived which is commonly referred as Ffowcs Williams – Hawkings (FW-H) equation that is

$$\frac{\partial^2 \rho'}{\partial t^2}-c_0\frac{\partial^2 \rho'}{\partial x_i^{\,2}}=\frac{\partial^2 T_{ij}}{\partial x_i x_j}-\frac{\partial}{\partial x_i}\left(\sigma_{ij}\delta\left(f\right)\frac{\partial f}{\partial x_j}\right)+\frac{\partial}{\partial t}\left(\rho_0 u_i \delta\left(f\right)\frac{\partial f}{\partial x_i}\right). \tag{2.67}$$

The first term on the RHS of Eqn. (2.67) is identical to Lighthill's equation (2.62). It is a double space derivative related to the so-called *quadrupole sources* that could have four-lobed or two-lobed directivity depending on whether the space derivative is taken in different or uniform directions. It represents the sound radiation due to variations of Reynolds stress tensor. The second forcing term on the RHS is a space derivative, which results in *dipole field* which normally radiates along two major directions. The magnitude of dipole source is proportional to the stress tensor, σ_{ij}, that includes both viscous stress terms and aerodynamic pressure. $\partial f/\partial x_j$ is vector normal to surface $f(\vec{x},t)=0$ in outward direction; hence, the force vector on dipole terms acts from the surface onto the fluid region. Finally, the last term on RHS of Eqn. (2.53), is the time derivative of mass flow rate which is the outward normal velocity of the surface times the fluid density. Unlike other two terms, space derivative is absent in this term which results in a uniform, *i.e.* omnidirectional, directivity pattern known as *monopole.* The strength of the monopole source is proportional to the acceleration of surface in normal direction. A general solution for the monopole and dipole terms of Eqn. (2.67) was proposed by Farassat (1981). Based on his work, the monopole term that is also referred to as *thickness noise* can be calculated as

$$4\pi . p'\left(\vec{x},t\right)=\frac{\partial}{\partial t}\int_{S}\left[\frac{\rho_0 u_n}{r\left|1-M_r\right|}\right]ds\left(\vec{y}\right). \tag{2.68}$$

where *r,* is the distance of the source to the observer, M_r, is the relative Mach number of source located at $\vec{y}$, which is the component of source velocity moving towards the observer, *i.e.* located at $\vec{x}$, divided by characteristic speed of sound, a_0. The velocity term, u_n, is the normal surface velocity. The dipole term which is also known as the *loading noise* was also obtained by Farassat (1981):

$$4\pi . p'\left(\vec{x},t\right)=-\frac{\partial}{\partial x_i}\int_{S}\left[\frac{\sigma_{ij} n_j}{r\left|1-M_r\right|}\right]ds\left(\vec{y}\right). \tag{2.69}$$

where, $\sigma_{ij} n_j$ is the total stress exerted from the surface on to the fluid elements.

2-2-3 Porous Ffowcs Williams-Hawkings method

In order to account for sources outside of the control surface, a modified integral formulation for the porous surface FW-H equation is needed (Lyrintzis, 2003). The original derivation was based on the fact that the FW-H integration surface corresponds to the impermeable body. A convenient way to formulate this is as an extension to the Farassat's original study (Farassat, 1981). This could be performed by adding new variables U_i and L_i and considering the quadruple sources using any common prediction method (Di Francescantonio, 1997). For a porous surface, the thickness and loading noise terms will lose their physical meaning but the quadrupole source terms are still valid outside the porous control surface. New variables are defined as

$$U_i = \left(1 - \frac{\rho}{\rho_0}\right) v_i + \rho \frac{u_i}{\rho_0}, \tag{2.70}$$

and

$$L_i = \sigma_{ij} n_j + \rho u_i \left(u_n - v_n\right), \tag{2.71}$$

where *u* and *v* denote fluid velocity and surface velocity respectively. Using above variables and by rearranging integral form of Eqn. (2.67), the following equations are obtained which is commonly known as Farassat's Formulation I (Farassat, 1981; Farassat and Succi, 1982) and the general format is

$$p'\left(\vec{x},t\right) = \underbrace{p'_L\left(\vec{x},t\right)}_{Loading\ Noise} + \underbrace{p'_T\left(\vec{x},t\right)}_{Thickness\ Noise} + \underbrace{p'_Q\left(\vec{x},t\right)}_{Quadrupoles\ Noise} , \tag{2.72}$$

$$4\pi . p'_T\left(\vec{x},t\right) = \frac{\partial}{\partial t} \int_S \left[\frac{\rho_0 U_n}{r\left|1 - M_r\right|} \right]_{ret} dS , \tag{2.73}$$

and

$$4\pi . p'_L\left(\vec{x},t\right) = \frac{1}{a_0} \frac{\partial}{\partial t} \int_S \left[\frac{L_r}{r\left|1 - M_r\right|} \right]_{ret} dS + \int_S \left[\frac{L_r}{r^2\left|1 - M_r\right|} \right]_{ret} dS . \tag{2.74}$$

Also $p'_Q\left(\vec{x},t\right)$ can be determined by any method currently available, *e.g.* (Brentner and Farassat, 1997; Brentner and Farassat, 2003). In above equations, $[\ ]_{ret}$ operator indicates evaluation of the integrals at the retarded (emission) time, τ, which is obtained by finding the root of

$$g = \tau - t + \frac{\left|\vec{x} - \vec{y}\right|}{a_0} = 0 . \tag{2.75}$$

For subsonic surface velocities, Eqn. (2.75) has a unique solution; however, Eqns. (2.68) and (2.69) are still valid for supersonically moving surfaces. There will be a singularity at sonic point ,*i.e.* $M_r = 1$, which is one of major drawback of retarded time formulation. Equation (2.75) can be solved numerically using nonlinear methods such as Newton-Raphson scheme (Wheatley and Gerald, 1984). This method has been the basis of many aeroacoustics codes and can be easily parallelized (Lyrintzis, 2003). By moving the time derivatives inside the surface integrals, more computationally robust scheme could be achieved. Farassat's formulation 1A (Farassat and Succi, 1982) as well formulation II (Brentner and Farassat, 1997; Di Francescantonio, 1997), have utilized such capability and used successfully for prediction of rotor blade noise. Formulation 1, on the other hand is more memory friendly as it does not require storing time derivatives and also it has fewer operations per each surface integral calculation (Lyrintzis, 2003); However, in formulation I, in order to find the time derivative, integrals have to be evaluated twice. In the specific case of a stationary control surface, the surface integrals are calculated once and used in the next time step. Other approach to implement porous surface without adding terms for quadrupoles is to select or design the control surface far enough from the sources so that the surface sources are negligible. This was discussed in the work of Di Francescantonio (1997) and Morgans (2005).

2-2-4 Porous FW-H method in presence of a mean flow

In many applications such as wind tunnel noise testing or jet noise measurement at flight condition, *i.e.* turbulent jet discharges in the domain with mean free stream, the existing mean flow in the system could affect the far-field noise predictions due to convection of sources and the Doppler effect.

For arbitrary moving noise sources in a quiescent fluid such as car pass-by or aircraft flyover test cases, formulation IA by Farassat and also formulation II which both were developed in the time-domain are computationally efficient and accurate for numerical studies. However, those methods do not explicitly consider the presence of a mean flow in the sound wave propagation, which is the case in the wind-tunnel. For such system, observers are moving in a uniform flow. To tackle this issue, numerous solutions have been suggested. One way is to transform the problem in a way that the noise sources and the observers are assumed to be moving at a constant speed in a quiescent fluid (Brentner and Farassat, 2003; Farassat, 2007), other approach is to utilize inherent assumptions of the wind-tunnel arrangement and account for the presence of a mean flow by simplify and solving the FW-H equation in the convective form. (Wells and Han, 1995; Lockard, 2000; Najafi-Yazdi *et al.*, 2011).

The present work uses a second approach based on the work of (Najafi-Yazdi *et al.*, 2011). This method is also known as formulation 1C that has unique computational advantages over traditional convective methods. The frame of reference is attached to the control surface; hence, acoustic domains inside and outside of the control surface are identified with respect to the origin of the moving frame of reference. In order to obtain a formulation which is suitable for numerical implementation, all spatial derivatives must be converted into temporal derivative. Also, solution for inhomogeneous wave equation is found by subsonic mean flow assumption and use of three-dimensional free-space Green's function for the convective wave equation. Based on formulation 1C, *thickness noise* component can be obtained as (Najafi-Yazdi *et al.*, 2011)

$$
\begin{aligned}
4\pi . p'_T\left(\vec{x},t\right) = & \frac{\partial}{\partial t}\int_{f=0}\left[\frac{U_j n_j}{R^*\left|1-M_R\right|}\right]_{ret} d\eta \\
& -M_0\frac{\partial}{\partial t}\int_{f=0}\left[\frac{\tilde{R}_1 U_j n_j}{R^*\left|1-M_R\right|}\right]_{ret} d\eta \\
& -U_0\int_{f=0}\left[\frac{\tilde{R}_1^* U_j n_j}{R^{*2}\left|1-M_R\right|}\right]_{ret} d\eta ,
\end{aligned}
\tag{2.76}
$$

where here retarded time is defined as

$$\tau = t - \frac{R}{a_0} . \tag{2.77}$$

The surface integral element, *dS*, is transformed to $d\eta$ using the new coordinate system on the moving reference frame so η is a new function which is

$$\eta = \eta\left(\tau, y\right). \tag{2.78}$$

Unlike the distance, *r*, that used in formulation I and II, quantity *R* is not the physical distance between the observer and the source, but the acoustic distance between the two. In Eqn. (2.76), *R* and R^* are calculated as (Najafi-Yazdi *et al.*, 2011)

$$R = \frac{-M_0\left(x_1 - y_1\right) + R^*}{\beta^2}, \tag{2.79}$$

$$R^* = \sqrt{\left(x_1 - y_1\right)^2 + \beta^2\left[\left(x_2 - y_2\right)^2 + \left(x_3 - y_3\right)^2\right]}, \tag{2.80}$$

$$\beta = \sqrt{1 - M_0^2}, \tag{2.81}$$

where M_0, is free stream Mach number. If x_1 is not aligned with the free stream velocity vector, the reference frame can be rotated accordingly to achieve alignment. Radiation vectors $\tilde{R}_1$ and $\tilde{R}_1^*$ in equation (2.76) are computed as (Najafi-Yazdi *et al.*, 2011)

$$a)\,\tilde{R}_1 = \frac{1}{\beta^2}\left(-M_0 + \tilde{R}_1^*\right), \qquad b)\,\tilde{R}_2 = \frac{x_2 - y_2}{R^*}, \qquad c)\,\tilde{R}_3 = \frac{x_3 - y_3}{R^*} \tag{2.82}$$

$$a)\,\tilde{R}_1^* = \frac{x_1 - y_1}{R^*}, \qquad b)\,\tilde{R}_2^* = \beta^2\,\frac{x_2 - y_2}{R^*}, \qquad c)\,\tilde{R}_3^* = \beta^2\,\frac{x_3 - y_3}{R^*} \tag{2.83}$$

$$\beta = \sqrt{1 - M_0^2}, \tag{2.84}$$

The *loading noise* component can also be computed. Similar to the thickness noise, all terms of the integrands are functions of τ and η.

$$4\pi.p_L'\left(\vec{x},t\right) = \frac{1}{a_0}\frac{\partial}{\partial t}\int_{f=0}\left[\frac{L_{ij}n_j\tilde{R}_i}{R^*\left|1-M_R\right|}\right]_{ret} d\eta + \int_{f=0}\left[\frac{L_{ij}n_j\tilde{R}_i^*}{R^{*2}\left|1-M_R\right|}\right]_{ret} d\eta. \tag{2.85}$$

Formulation 1C has been implemented in PowerACOUSTICS 2.0 solver that was used in all jet simulation of current work. The input to the code is discretized FW-H surface grid as well as the time history of the near-field flow solution that was obtained from LBM solver (*i.e.* PowerFLOW), the surface file is normally stored in STL format. Surface elements may be either triangular, quadrilateral, or polygonal (Najafi-Yazdi *et al.*, 2011). To ensure high order accuracy of far-field calculations, flow properties are specified at the vertices of surface element at each time step of the solution.

2-2-5 Atmospheric impact on sound propagation towards far field

Looking at Eqns (2.76) to (2.85) related to the porous FW-H formulation with mean flow, while the effect of mean flow was captured in the local and reference Mach numbers, the gradient of reference Mach number is neglected. In real atmospheric conditions, wind may have effects on noise propagation, by increase or decrease of the relative speed of sound which at short distances, up to ~50m, it has minor impact on the measured sound pressure level. For longer distances, since wind speeds are higher above the ground than at ground level, the resulting speed of sound gradient tends to bend sound waves over large distances related to the significant change of the characteristic impedance, *i.e.* $\rho_0 c_0$. This, however, does not have a significant impact on the prediction of SPL during takeoff or landing. Semi-empirical corrections can be applied to the sound pressure level at large distances to account for the effect of wind profile (Kim, 2010). The same argument can be provided for the effect of temperature for far-field calculations. As discussed earlier in this chapter, the speed of sound is dependent upon temperature. The Earth receives radiation from the Sun by day and gives out radiation by night (dependent upon the season of the year etc). Constant temperature with altitude produces no effect on sound transmission, but temperature gradients can produce bending in much the same way as wind gradients do by affecting the characteristic impedance. Air temperature above the ground is normally cooler than at the ground, and the denser air above tends to bend sound waves upward. With "temperature inversions," warm air above the surface bends the sound waves down to earth. Inversion effects are negligible at short distances, but they may amount to several dB at very large distances. The FW-H surface integral method assumes constant mean flow and speed of sound which is applicable to ideal wind tunnel testing, or short distances from the ground level (Pierce, 1981; Kim, 2010).

Table 2-1 Constant values used in *k*-*ε* equations

Constant	Value
C_{μ}	0.085
$C_{\varepsilon 1}$	1.420
$C_{\varepsilon 2}$	1.680
σ_{k_0}	0.719
σ_{kT}	0.719
σ_{ε_0}	0.719
$\sigma_{\varepsilon T}$	0.719
β	0.012
η_0	4.380

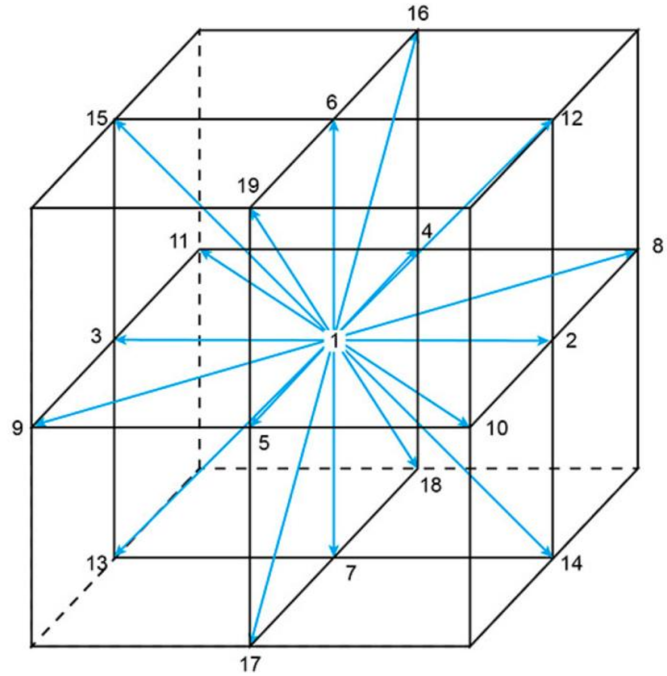

Fig. 2-1 D3Q19 Lattice Boltzmann stencil used in this study

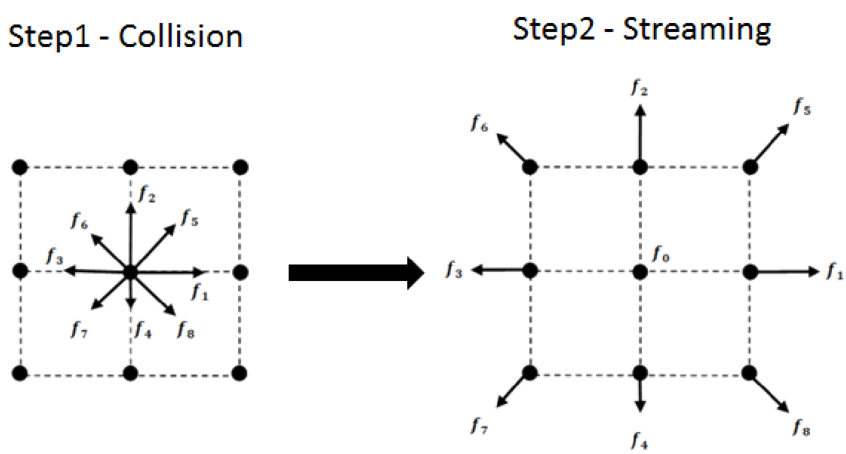

Fig. 2-2 A two-step LBM scheme: left, particle collision; right, particle streaming.

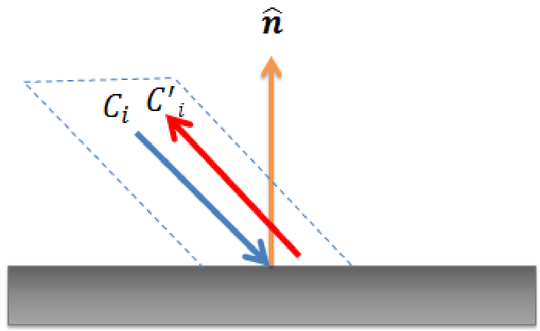

Fig. 2-3 LBM bounce-back reflection boundary condition

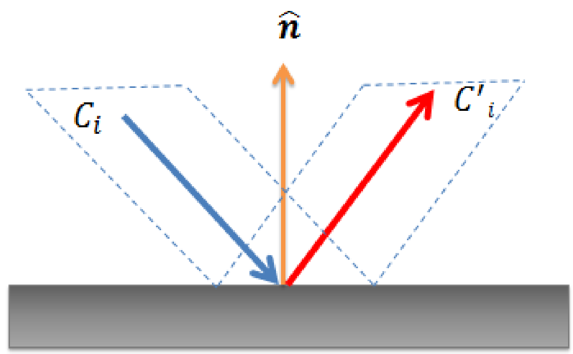

Fig. 2-4 LBM specular reflection boundary condition

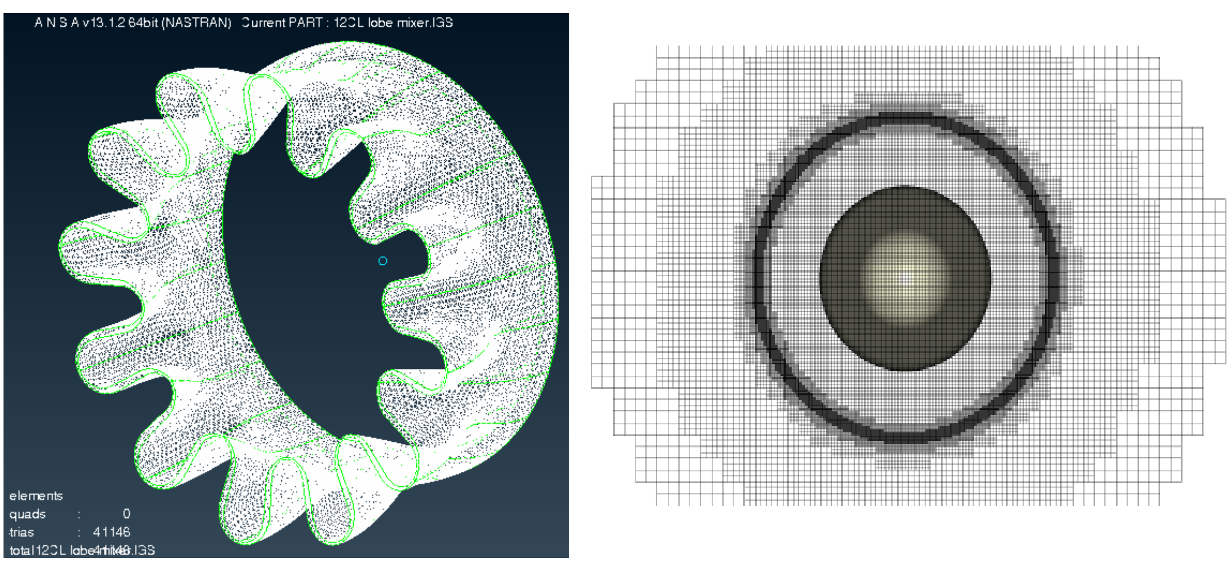

Fig. 2-5 a) Facetized geometry using trigonal planar mesh. b) Voxel-facet intersection.

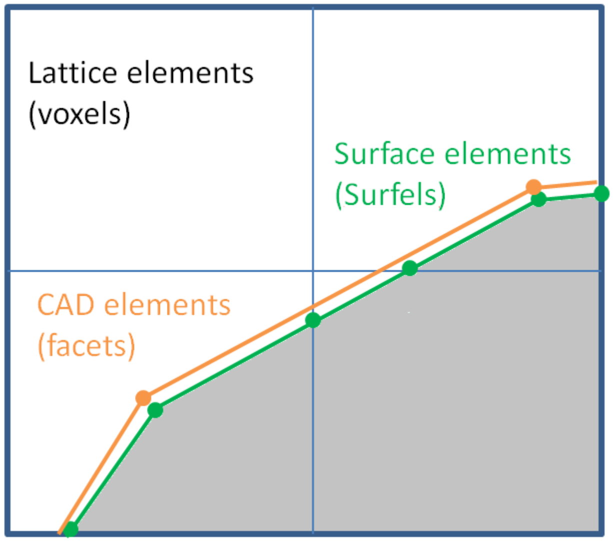

Fig. 2-6 Interaction of CAD elements (facets) with volume meshes (voxels) to create surface elements (*i.e.* surfels)

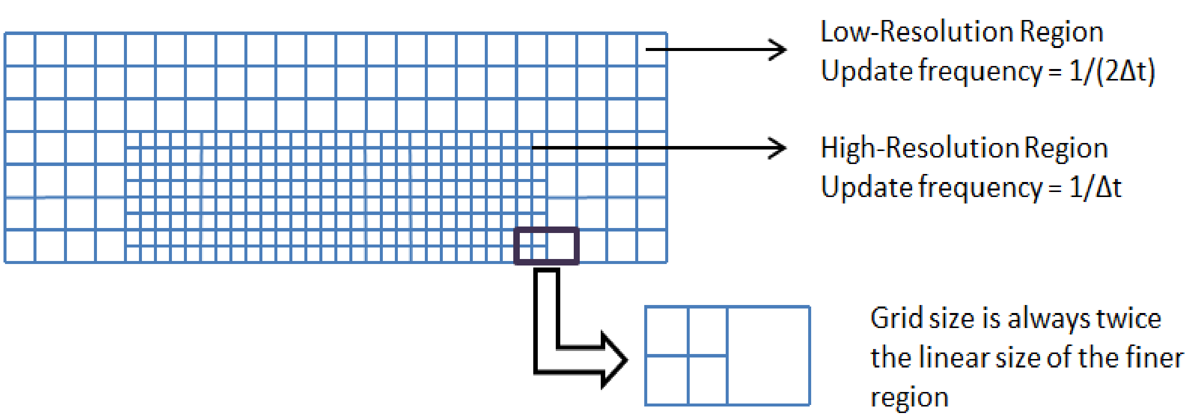

Fig. 2-7 VR-refinement in LBM scheme.

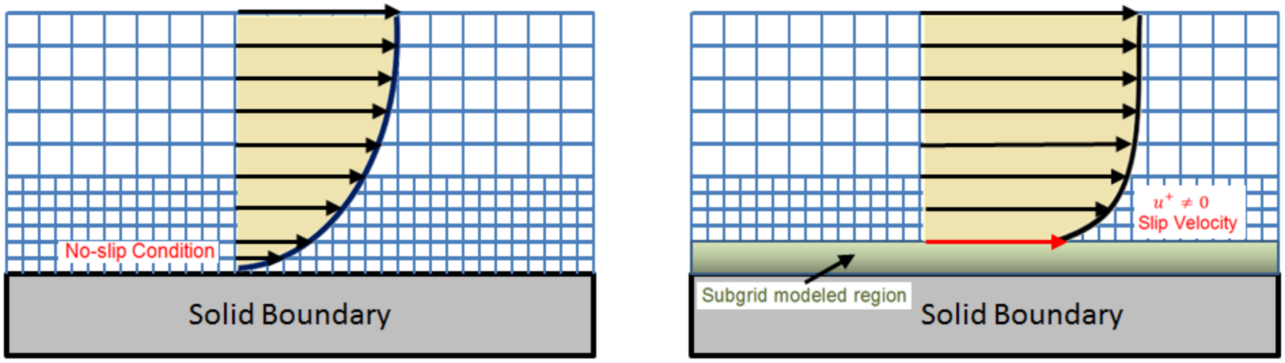

Fig. 2-8 Using turbulence model causes non-zero velocity at the wall boundary.

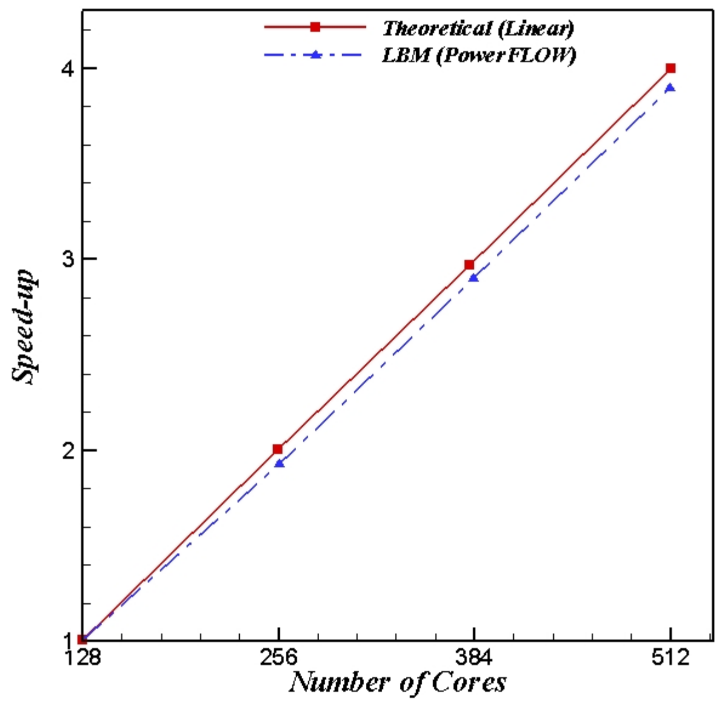

Fig. 2-9 Scalability of PowerFLOW solver by increasing number of nodes on the CLUMEQ cluster

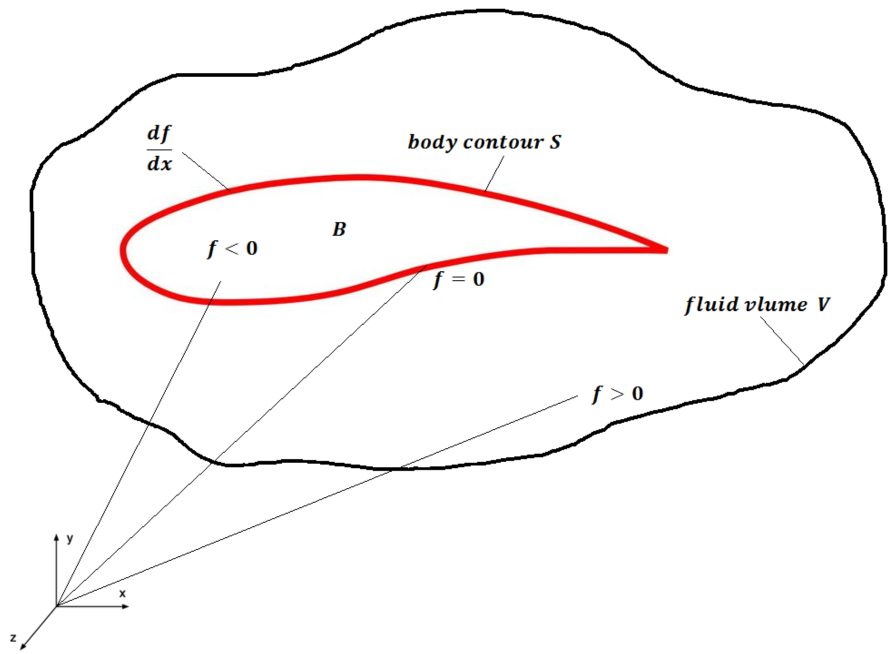

Fig. 2-10 Arbitrary closed FW-H surface inside the computational domain

Chapter 3

Simulation of sound radiated from single-stream jets at low and moderate Mach numbers

3-1 Under-resolved DNS approach for low-Reynolds flow condition

The purpose of this case study was to investigate the near-field and far-field characteristics of axisymmetric jets using the LBM. The LBM was coupled with a hybrid thermal model as discussed in section 2-1-9. PowerFLOW 4.2c solver was used in this section in which the turbulence model was deactivated. This method is like a Large Eddy Simulation (LES) methodology with no sub-grid model which is known as under-resolved or pseudo DNS scheme. As discussed in chapter 2, the LBM is intrinsically transient that could capture some level of turbulence even without turbulence model. Current LBM is second order both in time and space with remarkable dissipation at coarse grid levels; thus, unlike high-order LES methods in which the sub-grid turbulent energy have to be balanced by the stress terms in the turbulence model, the excess energy in LBM simulation can be dissipated numerically while the stability is maintained as the transient flow marches in time and space towards outer boundaries (Yu and Girimaji, 2005; Lew *et al.*, 2010b). The under resolved DNS (uDNS) method is valid for relatively low-Reynolds numbers. This method could potentially predict large-scale features in the near field as well as far-field sound pressure spectra up to moderate frequency range obtained by a surface integral method (Najafi-Yazdi *et al.*, 2011). Despite the adverse effects of low-Reynolds assumption on the peak levels as well as high-frequency bands as argued by Viswanathan (2004), the spectral levels obtained in this section were also shown to compare favourably with available experimental data up to the grid cut-off frequency.

The uDNS method using LBM was previously used by Yu and Girimaji (2005) who applied the same technique to study several low aspect-ratio rectangular turbulent jets which was also tested in more recent studies by Lew *et al.* (2010b) and Habibi *et al.* (2011b) for jet noise simulations.

The test cases performed in this study are listed in Table (3.1). For heated set points, numerical simulations were performed for M_J = 0.2 at three temperature ratios of 1.0, 1.80 and 2.75. The near-field results were compared to experimental data (Bridges and Wernet, 2003; 2010) and LES results that obtained using an in-house high-order Navier-Stokes based code at similar Reynolds number, Mach number and grid resolution. The reason for such comparison was to identify if similar grid resolutions for LBM and high-order LES, *i.e.* more common method for aeroacoustic research, would result in similar turbulent behaviour in the near-field. Far-field results were compared to experimental data by (Tanna, 1977). As discussed in section 2-1-9, in current PowerFLOW solver, the supplemental energy transport equation is coupled with LBM equations and solved numerically using finite difference scheme on the same Cartesian grid.

3-1-1 Computational Setup

A. LBM setup

The selected nozzle's geometry was a circular pipe with a diameter of D_J = 0.0508 *m* (*i.e.* 2 inches) and a length of L=10D_J. The diameter was chosen to be the same as those in the experiments performed by Tanna (1977) and Bridges and Wernet (2003). The thickness of the pipe was 0.05D_J. The inclusion of the nozzle in the computational domain ensures sufficient initial perturbations for turbulent transition, even at low Reynolds numbers. This approach eliminated the need to apply artificial forcing terms that is common in most LES approaches. Also, this is one of the advantages of uDNS over LBM-VLES that forcing would be necessary in some cases to for a proper turbulent transition at nozzle exit plane. By adjusting the viscosity and lowering the Reynolds number, this method is argued to behave similar to LES schemes (Yu and Girimaji, 2005; Lew *et al.*, 2010a; Lew *et al.*, 2013) .

In PowerFLOW solver, the incorporation of solid boundaries into the computational domain follows a straightforward procedure. A solid pipe model was generated in SolidWorks and imported as a STL file format that represents the surface attributes of a three-dimensional body. As shown in Fig (2-6), imported surface mesh, *aka*. Facet is translated to surface elements, *aka*. Surfel, by locating the intersection between fluid elements (voxels) and the facets. The whole process is done using a parallel discretizer implemented in PowerFLOW that automatically determines the fluid/surface intersection without compromising the geometric fidelity. This capability is the result of unique volumetric formulation for boundary conditions (Chen, 1998) which is discussed in section 2-1-5 of this document.

The computational domain was divided into structured lattice arrays with variable resolution (VR). In the numerical setup for this section, eleven levels of variable resolution zones were used. This method allows for grid refinement and stretching, as for the discretized domain used in the finite difference schemes. Figure (3-1) shows the VR distribution in the computational domain that includes streamwise and transverse dimensions. Figure (3-2) shows conical VR regions around the nozzle. Conical VR shape was found to be more efficient for the near field of symmetric jets (Lew *et al.*, 2010b). Figure (3-3) and (3-4) show Cartesian grids in the far field and near the nozzle exit plane. The lattice length from one VR to another always varies by a factor two. This is necessary to keep the velocity directions consistent between lattice interfaces. An equivalent number of 31 Million grid cells (voxels) was used which is a modified based on value update per time step. The smallest voxel size in the shear layer was 3.8×10^{-4} m or 0.38 mm. Based on the grid refinement performed in the present study, the assigned resolution was sufficient to ensure minimal change in the mean flow parameters for consecutive refinement as well as resolving sound waves up to the Strouhal number St $(fU_J/D_J) \cong 3.6$ for the highest acoustic Mach number (C1) and St $(fU_J/D_J) \cong$ [5.8-9.2] for cases C2, C3 and C4 based on their temperature ratio and the acoustic Mach numbers, where f is the frequency of the radiated sound and U_J , is the jet velocity. The domain size of the computational field was $(x, y, z) = (250\ D_J, \pm150\ D_J, \pm150\ D_J)$. These values were chosen to minimize the amplitude of reflected sound waves back into the measurement zones.

The outermost *VR* regions are relatively coarse, causing dissipation of outgoing waves in the sponge zone. At coarser levels, higher viscosity values were set for the coarsest *VR* to enhance dissipation process, moreover, a non-reflective type, *i.e.* anechoic, boundary condition was imposed in the outermost fluid layers of the simulation volume (Sun *et al.*, 2013) . These boundary conditions simulate experimental conditions in an anechoic room or flight conditions at high altitude. It is worth mentioning that the large computational domain is still necessary to dissipate both outgoing waves and internal reflection from VR interface, considering the fact that adding coarse levels in outer regions does not add much to the computational costs (Casalino and Lele, 2014) . Such boundary condition only works in a simulation setup with no turbulence model. In section 3-2, also in chapter 4 and chapter 5, in which turbulence model is active, acoustic buffers with elevated viscosity values can replace the non-reflective BC to dissipate outgoing waves (Casalino *et al.*, 2014b). The macroscopic properties are measured and stored over a conical control surface extending from $x = 2D_J$, from the nozzle exit to $x = 35D_J$. The innermost funnel shaped VR region is the measurement region for near-field flow statistics. Virtual probes were placed along the jet axis centreline and the nozzle lip-line in the streamwise direction for further calculations of turbulent spectral content. The numerical results at probe locations were averaged over two (2) lattice diameter to be consistent with physical mechanism of pressure transducers (*i.e.* microphone).

A velocity profile at the inlet boundary was specified at the $x = -0.5D_J$ prior to the nozzle exit using a tangent-hyperbolic relation (Freund, 2001; Bodony and Lele, 2005) which the general format is

$$u(r) = 0.5U_J\left[1 - tanh\left(\frac{r - r_0}{2\theta}\right)\right], \tag{3.1}$$

where U_J is the inflow jet velocity, and θ is the initial momentum thickness. A value of $\theta = 0.06r_0$ was chosen for the initial momentum thickness, where r_0 is the initial jet radius. The inlet velocity magnitude, U_J, was slightly reduced (5.6%) to yield a maximum Mach number ($M_J = 0.2$) at the exit plane. The adjustment was due to the evolution of turbulent boundary layer inside the tube. Further flow evolution within length of 0.5 D_J, could produce more natural velocity profile at nozzle the exit plane. The constant temperature was imposed in the inlet planes according to the selected set point, and the nozzle walls were considered adiabatic ($\partial T/\partial r = 0$). The kinematic viscosity was adjusted to approximately resolve the effects of small turbulent scales with the available voxel resolution. The jet Reynolds number was roughly $Re_D = (U_J D_J) / \nu_J = 6\times10^3$. A weak free stream flow, $M_{FS} = 0.005$, was set at the inlet surface of outermost VR and also set as the initial condition in computational domain. This helps early transition of the jet near the nozzle exit plane.

The Message Passing Interface (MPI) was used for parallelization and implemented in PowerFLOW 4.2c which was used for this study. The domain decomposition followed a multi-block paradigm in which one block is assigned to every single core. All simulations were evolved on the Mammouth parallel computer located at the Universite de Sherbrooke in Quebec. Each node in this machine has 24 cores and 32 GB of memory. The single-stream jet noise simulations were performed using 10 nodes for a period of 4 days for C1 and 5-7 days for (C2, C3 and C4) with lower Mach number in order to achieve mean flow and acoustic convergence as well as sufficient sampled acoustic data for post processing.

B. LES (Navier–Stokes)

In order to compare LBM results with a Navier-Stokes based method, Large Eddy simulation was performed for selected test cases (C4 Table 1). A computer code was written for Large Eddy Simulations (LES) of non-reacting compressible flows (Najafi-Yazdi, 2011). A sixth-order central difference compact scheme (Lele, 1992) was used to calculate spatial derivations within each block. The fourth-order Runge-Kutta scheme(Najafi-Yazdi and Mongeau, 2012b) was used for time integration. Seven-point overlaps were considered between two adjacent blocks as depicted in Fig. (3-5) to retain high-order accuracy at the interfaces. The arrows illustrate how data is communicated between two blocks at the overlapping nodes. The code employed explicit filtering (Mathew *et al.*, 2003; Bogey and Bailly, 2006) instead of sub-grid modeling, and hence it may be categorized as an implicit LES (ILES) code. The Non-reactive Navier-Stokes Characteristic Boundary Condition (NSCBC) for curvilinear coordinates (Poinsot *et al.*, 1992) was used at the boundaries for effective damping of outgoing acoustic waves.

To study a low-speed heated jet, a circular jet with $M_j = 0.2$ and $Re_D = (U_J D_J) / \nu_J = 6\times10^3$ was considered for the present study. The grid setup of the LES study is shown in Fig. (3-6). The smallest grid size in the shear layer was 3.8×10^{-4} m or 0.38 mm to match the LBM resolution. The main nozzle was not included in the computational domain. For the inlet velocity, Eqn. (3.1) was used similar to the LBM case. The inlet density profile, on the other hand, was imposed as in (Freund, 1999; Najafi-Yazdi, 2011) given by

$$\rho(r) = (\rho_J - \rho_\infty)\frac{u(r)}{U_J} + \rho_\infty, \qquad (3.2)$$

where ρ_J , and ρ_∞ are the jet, and the ambient densities, respectively.

C. Far-field sound calculation setup for LBM

The far-field radiated sound pressure was calculated using a modified porous Ffowcs Williams-Hawkings (FW-H) surface integral acoustic method (Najafi-Yazdi *et al.*, 2011). As discussed in section 2-2-4 that includes corrections for mean flow, moving sources and observers. A funnel-shaped continuous control surface was created and surrounded the flow field at the distance beyond which sound propagation may be considered linear (Fig. 3-7). The FW-H surface that falls inside VR8 which is the third finest VR and had an initial diameter of approximately $6r_o$. It was extended streamwise up to the near end of the physical domain at which point the diameter of the control surface was approximately $30r_0$. Hence, the total streamwise length of the control surface was 52 r_0 (Fig. 3-7). Both upstream and downstream of FW-H surface were excluded from data collection to avoid spurious sound caused by the equality assumption of jet plume convection velocities and speed of sound at surface locus in FW-H calculations. The location and size of FW-H surface may have impacts of on the predicted levels. The surface shall not have any impact with large-scale turbulent eddies in the near-field, but at the same time, it shall be placed as close as possible to the jet plume in order to capture shorter wave lengths and high-frequency phenomena at finer grid-resolution area. In this study the effect of placing the FW-H surface at different VR levels was investigated. If the surface is placed too close to the source, spurious sources may be seen at some locations on the surface that impair far-field spectra. In terms of the length, it was found that the surface should cover at least twice the length of potential core length as suggested by similar studies such as (Uzun *et al.*, 2004) and (Lyrintzis, 2003). Most acoustic sources of turbulent jets are concentrated within twice the potential core length that includes low-frequency components radiated from coherent structures at the upstream of potential core towards shallow aft angles and also high-frequency sources that peak near the end of potential core radiated towards the 90 degrees and larger angles (Viswanathan, 2004; Tam *et al.*, 2008b). More details are available in section 5-2-2.

Acoustic field data were collected on the control surface at every 25 timesteps for over a period of 0.2 seconds. Based on the grid resolution at the control surface, and assuming that the LBM requires 20 cells per wavelength to accurately resolve an acoustic wave, the maximum frequency resolved corresponds to a Strouhal number $3.6 < Sr < 9.2$ based on the temperature ratio and associated jet exit velocity of the test case. The overall sound pressure levels were computed along an arc with a distance of $R = 144r_0$ from the jet nozzle exit as for the Tanna's experimental setup (Tanna, 1977). The observer angle, θ, was measured relative to the centreline jet axis.

3-1-2 Grid resolution study

Resolving turbulent structures inside and outside of the nozzle have different impacts on the prediction of noise. Decreasing the nozzle-exit boundary-layer momentum thickness in initially laminar jets is found to especially affect the flow development (Bogey and Bailly, 2010). It leads in particular to an elongation of the potential core and to a reduction of centreline turbulence intensities. It does not seem however sufficient to get the shear-layer development and the acoustic fields that are experimentally observed, namely for practical jets. Coherent vortex pairings and their strong generated noise are indeed noticed in the initially laminar jets, whatever the exit momentum thickness may be. More realistic flow structures resolved inside the nozzle leads more natural development of shear layer and noise sources. Also, the interior structures do not radiate directly to the far field but may affect the outflow condition at nozzle exit plane including the momentum thickness. In this context, using inexpensive wall conditions, *e.g.* under-resolved, or modelled would make sense compared to the fully-resolved internal flow.

In this study, three grid sizes, Δr, (aka "resolution" in PowerFLOW code) were studied, denoted by "Coarse", "Medium" and "Fine" respectively. The resolution controls simulation timesteps, resolved turbulent scales as well as the maximum Strouhal number captured on the FW-H surface. Table 3-2 shows different grid setups and related simulation parameters, where *FEV* is fine equivalent number of grid points in the fluid domain (voxels) that are updated at each time step and would be less than total number of voxels, *FES* is the fine equivalent number of surface elements. As discussed in chapter 2, timesteps in LBM are directly correlated to minimum grid resolution to keep the CFL number in lattice scale equal to 1.0. Parameters t_t and t_a are transient and acquisition time and will be defined in section 3-1-4.

In our grid study, it was found that the minimum resolution of ~$8.0\times10^{-3}\ D_J$ in the shear layer is required for natural turbulence transition at the nozzle exit plane. It also was found that significant accuracy could be achieved by setting the resolution to "Medium" compared to the "Coarse" setup; however, it was also found that setting grid resolution to "Fine" does not significantly alter mean flow characteristics and despite getting better accuracy on the high frequency sound, not much advantage was gained in prediction of the low-frequency sound due to smaller timesteps and hence, the overall SPL directivity while the simulations time (computational cost) almost doubled; hence, in this work, "Medium" grid setup was used for all single stream jet simulations.

3-1-3 Convergence of flow parameters

In order to capture major noise sources in free shear flows, it is important to sample acoustic data from statistically converged solution of the transient flow in the near field. The FW-H surface must be long enough to enclose major acoustic sources and at least covers up to twice of the jet laminar core length (x_c) and beyond (Lyrintzis, 2003); hence, proper convergence criteria have to be in place to check flow field prior to acoustic sampling on the FW-H surface. One common and effective method is to look at mean flow data. In this study, a virtual probe was placed at x=30D_J along the jet centreline and the convergence criteria were applied on both streamwise mean velocity, $U_c(x,t)$, and the standard deviation, u'_{rms} . It was found that a good acoustic prediction could be achieved when the simulation reached the time when the difference between the absolute values in both variables is less than 2%. From now on, this period is referred as the "Convergence Time (t_c)". By looking at mean flow contours, it can be seen when simulation evolves up to the time step corresponding to t_c, mean flow patterns are becoming almost symmetric in the simulation volume (*e.g.* Fig.3-10 and Fig. 3-16)

In this work, the time step for the LBM simulations was 0.71×10^{-6} seconds for case C1 and C2. The timesteps for the heated cases C3 and C4 were reduced by a factor $(T_J / T_a)^{0.5}$ for CFL matching and stability purposes.

3-1-4 Acoustic sampling

The acquisition time (t_a) is defined on the basis of the minimum frequency to be analysed, the number of spectral averages and the FFT overlap coefficient. It is recommended to use at least 10 spectral averages as well as the overlapping coefficient of 50% in order to achieve an adequate statistical convergence. This is performed by using "smooth optimal" function in

PowerACOUSTICS post-processing tool. Hanning window was also applied to avoid spectral leakage that could introduce sharp transition changes into the measured signal. The sharp transitions are discontinuities and might induce spurious high frequency noise on the far-field spectrum. It is important that acoustic waves are captured up to the minimum frequency of 100 Hz for jet noise problems. It also takes several timesteps for acoustic waves to settle inside the computational domain. Transient time (t_t) is obtained by adding the time required for statistical convergence in the near-field (t_c) to the settling time (t_s) that is computed as a factor of the time required by an acoustic wave to cover a distance equal to 2.5 times the distance between the nozzle and the far-field boundary. This process is shown in Fig. (3-8). The number of checkpoints and frames used for the evaluation of the mean flow field is also set in PowerFLOW solver. The transient and acquisition time is shown for C2, C3 and C4 in Fig. (3-8).

In this study, the simulation was evolved over 0.8×10^6 timesteps for C1 and about 1.2×10^6 timesteps for C2, C3 and C4 to achieve statistical convergence, and recording sufficient amount of acoustic data for FW-H calculations.

3-1-5 Results and discussions

A. near-field flow properties

In this chapter, it is shown that the under-resolved DNS method could predict the overall sound pressure levels for Mach numbers up to ≅0.5 for the isothermal jet and up to ≅0.2 for heated cases. The mean flow and turbulence characteristics of the jet were found to compare favourably with experimental data. The results support the viability of the hybrid approach for heated shear flows at low Mach numbers.

The stability limit of the current 19-stages LBM code that employs under-resolved DNS scheme coupled with heat transfer model restricts the maximum Mach number to 0.2, which is rather small comparing to the practical aerospace applications. Table (3-1) shows different test cases and corresponding experiment denoted by SP. The 'SP' or set point refers to the nomenclature based on the available experimental test matrix (Tanna, 1977). Isothermal jets with $M_J = 0.5$ (C1 in table 3-1) were first considered to verify isothermal LBM simulations through comparisons with available data. Figure (3-9) shows a streamwise velocity isosurface (U_x =20 m/s). This qualitatively represents the diffusion of jet in the quiescent fluid medium interacting with the jet shear layer. Figure (3-9) also shows that the velocity instabilities in the shear layer occur at a distance approximately one jet diameter, as previously observed and illustrated by (Lew *et al.*, 2010a).

The mean flow characteristics were investigated by performing time averaging of flow parameters. The velocity profiles along the jet centreline were obtained using the LBM and the LES methods for case C1 and plotted in Fig. (3-10). These trends are well consistent with data from experiments by Bridges and Wernet (2003).The jet streamwise velocity decay is characterized by the slope of the normalized jet axial velocity, $U_J/U(x)$, with respect to the normalized distance from the nozzle, x/D_J. The calculated slope was 0.146 from LBM results consistent with 0.15 from measured data (Bridges and Wernet, 2003) at the similar operating condition. The empirical correlation by (Zaman, 1998) also suggests 0.16 for the slope value. For heated case (C4), where the results are available for both LBM and LES, the slope value was ≅0.30 using LBM and ≅0.32 using LES. Bodony and Lele (2005) reported a value of ≅0.33 for a case with similar temperature ratio. For the heated cases, the mean streamwise velocity and the turbulence intensity were compared in various test cases. The velocity decay pattern was affected by the jet temperature ratio. The potential core length decreases as the jet core temperature increased. This phenomenon was previously observed experimentally by (Bridges and Wernet, 2003) using particle image velocimetry (PIV). Figure (3-11) shows the mean value of streamwise velocity for C2, C3 and C4 set points. Results indicate that at $M_J = 0.2$, when temperature ratio increases by factor of 1.8 and 2.75, the potential core length decreased by 24% and 41% respectively. The length of the potential core is usually defined based on the location where the jet mean centreline velocity is reduced to 95% of the inflow jet velocity, $U_c(x_c) = 0.95U_j$. Another method known as the Witze correlation (Witze, 1974) may be used to normalize velocity data from subsonic isothermal and heated jets (Bodony and Lele, 2005).

Mean centreline velocity data for various Mach numbers and density ratios are adjusted to a common potential core tip location. Figure (3-12) shows the results of this procedure for the different test cases. Despite different density ratio, all heated test cases collapsed in the vicinity of a value of 0.3 of the Witze parameter (Witze, 1974). Figure (3-12) also shows that the decay rate predicted by LES is consistent with LBM results when $x/x_c < 1.0$, where $x_c = f\,(\rho_j/\rho_\infty, M_J)$ is calculated by the Witze correlation given by

$$x_c = 4.375 D_J \frac{(\rho_J / \rho_\infty)^{0.28}}{1 - 0.16 M_J}, \text{ and } \frac{U}{U_J} = 1 - e^{1.43(1 - x/x_c)}. \quad (3.3)$$

The root mean square of fluctuation x-velocity was investigated both along the nozzle centreline and the lip line. Figure (3-13) shows the shifted u'_{rms} profiles along the jet centreline based on the Witze correlation. Figure (3-14) shows the similar procedure and trend along the nozzle lip line. Qualitative comparisons between the spatial distributions of flow variable statistics were compared with experimental data (Bridges and Wernet, 2003; 2010). A significant difference was observed between the heated and isothermal cases in terms of location of the peak u'_{rms} ; however, the location of peak u'_{rms} did not change much for temperature ratio of 1.80 and 2.75. Scaling of the streamwise location using the Witze correlation caused the axial turbulence velocities for the various cases to collapse on a similar trend. The location of peak u'_{rms} was at a non-dimensional position close to unity. The peak value along the nozzle lip line occurs roughly near zero (*i.e.* on the tip of the potential core) in the Witze scale as shown in Fig. (3-14). The peak position is well predicted by both LBM and LES comparing to experimental data.

The LES method for low Mach number jets seems to over-predict the turbulence intensity values for low Mach number jets. The over prediction of turbulence intensity in the experimental data in comparison with the simulation results might be due to the fact that the Reynolds number in the LBM simulation (≅6000) was much less than that for the experiments (≅500,000). It is argued that a critical value of the Reynolds number has been estimated to be ≅400,000 to avoid the low Reynolds number effects(Viswanathan, 2004). Figure (3-15) shows a close-up view of the instantaneous streamwise velocity, vorticity and temperature contours for the case C4 by LBM compared to LES. In the LES simulation, the nozzle effects were modeled by imposing a predefined initial velocity profile (Eqn. 3.1) together with a forcing function. The lack of solid boundaries in the computational domain together with the low Reynolds number and insufficient grid resolution caused the formation of vortex pairing near the nozzle exit plane in the LES approach (Fig. 3-13). The temperature decay along the centreline of the nozzle is shown in Fig. (3-16) for cases C3 and C4. Due to a greater temperature gradient and convection speeds, it was expected that the decay rate of the higher temperature jet would be larger than that for the lower temperature case. Both graphs are likely to converge asymptotically to the ambient temperature in far downstream regions. Figure (3-17) shows the contour of the mean turbulent kinetic energy for the isothermal case. It was seen that by increasing the temperature, the turbulent kinetic energy become more concentrated near the nozzle. This phenomenon was also observed in experimental studies (Bridges and Wernet, 2003; 2010) at different temperature ratio using particle image velocimetry (PIV) technique. According to Bridges and Wernet (2010), such behaviour can be attributed to density change that increases the rate of turbulent entrainment as a result of the local density-driven mixing near the nozzle exit plane. Similarity behaviour can be archived by adjusting the density and jet Mach number using the Witze correlations (Eqn. (3-3)).

Figures (3-18) demonstrates the axial velocity spectra at location ($x = 20r_0$) at different temperature ratios along the nozzle centreline and lip-line. It is apparent that the jet development is indeed broadband. This is further substantiated by the fact that a portion of the spectra decays according to Kolmogorov's well known -5/3 law (Pope, 2000), indicating that a portion of the spectra falls in the inertial subrange (equilibrated turbulence) prior to dropping at high frequencies. Based on the spatial grid resolution, the maximum Strouhal number ($Sr = f\,D_J/U_J$) for acceptable resolution varies with temperature.

In order to maintain constant jet Mach number as the temperature ratio increase, the jet outlet velocity (or the acoustic Mach number) should also increase accordingly to compensate for the larger speed of sound ($c_j \propto \sqrt{T_j}$); hence, for a constant grid resolution, the maximum resolved Strouhal number decreases in the near-field. Using the Strouhal number to scale the x-axis with jet parameters (*i.e.* jet velocity and characteristic length), energy spectra at different temperature ratios collapse and exhibit similar trends in energy cascade.

Thrust is normally referred as the net static axial component of total force generated by the aircraft engine. This component may be defined as the axial momentum of the exhaust flow in addition to the excess of exit pressure over atmosphere pressure times the projected nozzle area (Saravanamuttoo *et al.*, 2001). In this study the net average thrust was evaluated for both the isothermal and heated jet flows. The calculation of thrust for the case of heated jets is of great importance. In LBM, the inflow boundary condition is imposed inside the nozzle. The evolution of the hydrodynamic boundary layer yields a unique non-uniform velocity profile at the nozzle exit. The net thrust of the jet depends on the velocity profile as well as the density and the jet excess pressure. The net thrust is calculated as

$$F_T = \iint \rho_J \vec{u}_J \left(\vec{u}_J \,.\, \vec{n} \right) dA + A_J \left(P_J - P_a \right), \tag{3.4}$$

and dimensionless thrust coefficient is defined by

$$C_T = \frac{2F_T}{\rho_J {U_J}^2}, \tag{3.5}$$

where F_T is the net thrust and C_T, is thrust coefficient, ρ_J, is jet density, $\vec{u}_J \,.\, \vec{n}$ is the streamwise component of velocity normal to the nozzle cross section, A_J is the nozzle exit surface area, P_J and P_a , are jet and ambient absolute pressure. The Thrust values in terms of thrust coefficient were calculated and summarized in Table (3-3). For a fixed M_J the thrust coefficient does not change significantly. The effects of velocity are reduced because of the lower density when the temperature ratio increases.

B. Far-field radiated sound

For the case C1, Fig. (3-19 (a)) shows the directivity of the overall sound pressure level (OASPL) in the far-field using FW-H analysis. Figures (3-19 (b),(c) and (d)) are related to 1/3 octave band spectra plotted with respect to jet Strouhal number on the linear scale. The comparison between LBM results and those from Tanna's experiment for SP03 (Tanna, 1977) shows almost 1.0 dB over prediction of OASPL, that is consistent with the similar work by *(Lew et al., 2013)*. On the spectral side, at θ = 30^o, the predicted levels were greater than Tanna's results up to $St \cong 1.4$ and under-predicts Tanna's results for larger Strouhal numbers. Similar trend can be seen at θ = 60^o and θ = 90^o; however, the inflection points were at $St \cong 2.0$ and $St \cong 1.6$ respectively. Due to lack of experimental data for M_J=0.2 isothermal jet case (C2), the LBM results were compared with experiments performed by (Tam *et al.*, 2008b) for the same jet diameter at M_J=0.3. Sound power levels in the experimental data were adjusted using available scaling laws for the subsonic jets (Hubbard, 1991; Kandula, 2008) *aka* $M^{8.0}$ Power law for speed corrections (Eqn. (1.3)). As indicated in Fig. (3-20 (a)), predicted OASPL directivity by LBM perfectly followed the trend and levels in Tam *et al.* (2008b) . By looking at the narrowband spectra provided in the Tam *et al.* paper corrected for the outlet Mach number, it can be seen in Fig. (3-20 (b) & (c)) that the narrowband spectra at θ = 30^o and 60^o, under-predict Tam's shifted levels up to $St \cong 0.3$; then follows the same trend for $0.3<St<1.0$ and again begins to under-predict up to the cut-off frequency ($St \cong 3.7$). The ~ 0.7-1.0 dB discrepancy on the higher spectral ends of both shallow and 90^{o} aft angles may be related to the low-Reynolds number and high dissipation rate of under-resolved scheme that fails to capture sufficient small-scale sources. Such deviation is expected to be less significant by increasing the Reynolds number and use of proper turbulence model which is investigated in next section. On the lower spectral range, the deviation can be related to slow convergence of very low-Mach number flow that could be corrected by increasing the simulation time. The overall broadband levels on the other hand, seem to be very well following the experimental trends, that implies that current resolution was sufficient to predict the sound pressure level within 0.7 dB accuracy that is acceptable considering the uncertainty levels in the measurement and Lighthill's law assumptions to adjusts the Mach numbers in the experimental data.

For heated test cases, Fig. (3-21) compares acoustic results between C3 and C4. The levels were compared to Tanna's experimental data SP21 and SP40 with similar temperature ratio and $M_J \cong 0.2$. For the case C3 (SP21), slight correction in SPL's were necessary (using the $M^{8.0}$ power law) to match the Mach numbers between numerical simulation and the experimental data. It can be seen in Fig. (3-21) that by increasing temperature ratio the jet will become noisier at same acoustic Mach number. Both C3 and C4 sound levels qualitatively follow the experimental trends (Tanna, 1977). The discrepancies were mostly occurred in $65^{o} < \theta < 80^{o}$ angles (up to 1.5 dB) at which high frequency sources are dominant (Tam *et al.*, 2008b). LBM results for both C3 and C4 seem to over-predict the experimental data ($\cong$1.0 dB), at $25^{o} < \theta < 40^{o}$ and under-predict measured levels for $\theta > 105^{o}$. Figure (3-21 (b), (c) & (d)) show the 1/3 Octave band pressure levels for heated cases, C3 and C4. In general, LBM simulation succeeded to predict low-frequency sound in heated cases at low-Mach numbers up to $St \cong 1.2$, for almost all small and large angles. Looking at the far-field results, sound pressure levels increased with higher temperature over the entire frequency range up to the grid cut-off frequency, $f \cong 8.4$ kHz ($St \cong 3.0$); such increase is primarily due to higher velocity magnitudes as the jet Mach number remained the same; also in part, related to the thermal effects at low Mach numbers; however, at $\theta = 30^{o}$ and $St > 0.8$, sound levels look identical at high frequency bands based on Tanna's data which was well predicted by LBM around $St \cong$ 2.1; however the trend changes at higher and lower St numbers. The peak sound pressure level in range of $0.30 < St < 0.45$ at different observer angles were also well predicted by the LBM.

Table 3-1 Case studies at low Mach numbers

Case	standard set point	M_J (V_J/a_J)	M_a (V_J/a_0)	T_J/T_a	ρ_J/ρ_0	Re_D
C1	SP03	0.50	0.50	1.00	0.36	6.0×10^3
C2	Tam *et al.**	0.20	0.20	1.00	1.00	6.0×10^3
C3	SP21*	0.20	0.26	1.80	0.56	6.0×10^3
C4	SP40	0.20	0.33	2.75	0.36	6.0×10^3

* Sound pressure levels and spectra were adjusted using M^8 power law to match $M_J = 0.2$.

Table 3-2 Grid refinement scheme (C2, C3 and C4)

Grid Res.	VRs	Δr (mm)	FEV $(\times 10^6)$	FES $(\times 10^6)$	t_t (sec)	t_a (sec)	CPUh$(\times 10^3)$
Coarse	12	0.50	16.4	0.34	0.67	0.2	9
Medium	12	0.38	30.1	0.63	0.67	0.2	21
Fine	12	0.22	55.3	1.16	0.67	0.2	38

Table 3-3 Thrust coefficient magnitude for heated test cases (M_J = 0.2) from LBM simulation.

Case	**Temperature (C)**	**Density (kg/m$^{3)}$**	**Jet Velocity (m/s)**	**Thrust coefficient (C_T)**
C1&C2	20.0	1.20	68.64	2.014
C3	239.9	0.69	90.80	2.014
C4	533.0	0.44	113.83	2.021

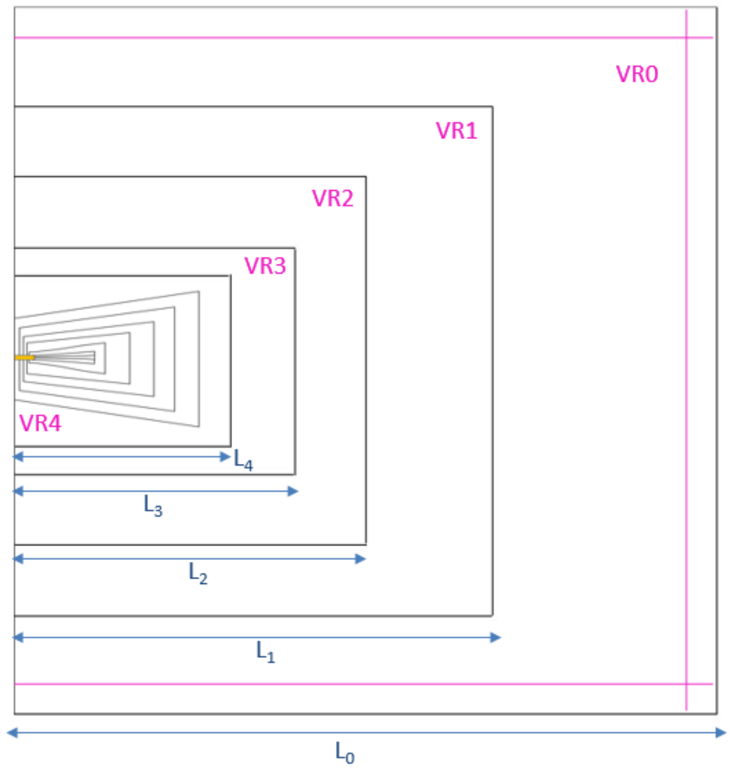

Streamwise dimensions

L_0/D	L_1/D	L_2/D	L_3/D	L_4/D	L_5/D	L_6/D	L_7/D	L_8/D	L_9/D	L_{10}/D
250.0	170.0	125.0	100.0	80.0	69.0	60.0	50.0	41.0	35.0	28.0

Rectangular regions (y/L, z/L)

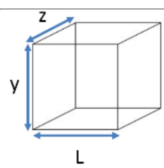

VR0	*VR1*	*VR2*	*VR3*	*VR4*
(0.6,0.6)	(0.6,0.6)	(0.6,0.6)	(0.6,0.6)	(0.6,0.6)

Conical and circular regions (r_1/D, r_2/D)

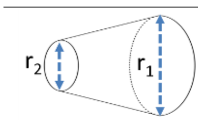

VR5	*VR6*	*VR7*	*VR8*	*VR9*	*VR10*
(22, 13)	(16, 10)	(11,7.0)	(8.0,5.0)	(6.0,3.0)	(2.5,1.0)

Fig. 3-1 VR distribution and sponge buffer in the computational domain

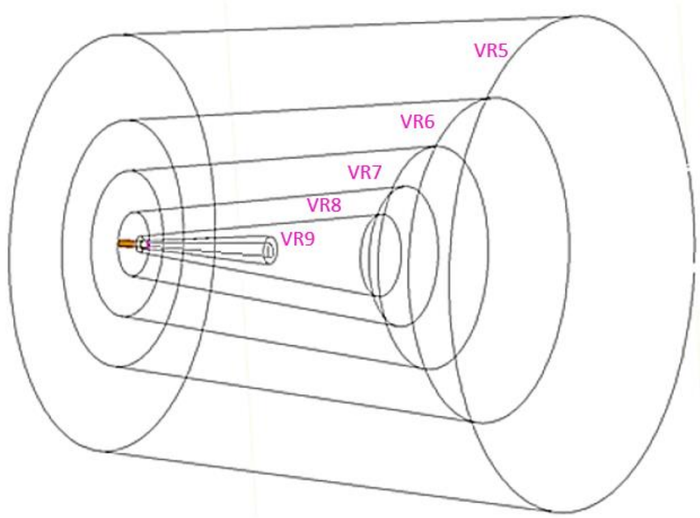

Fig. 3-2 a) Conical and funnel VR regions around the nozzle (VR5, VR6, …, VR9)

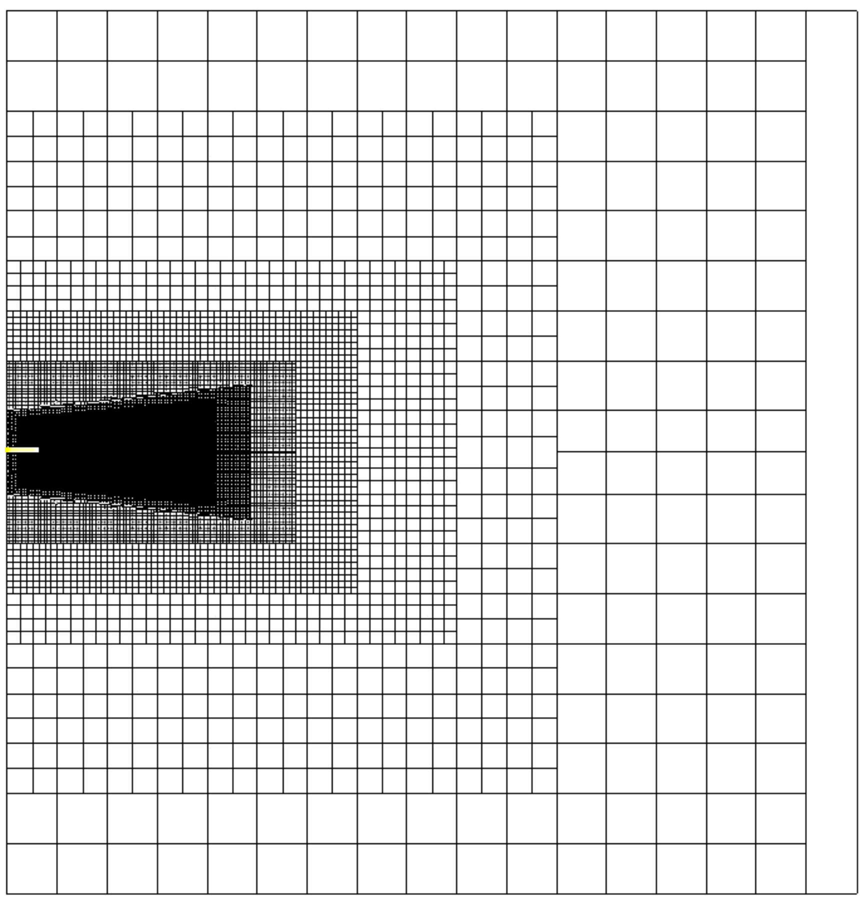

Fig. 3-3 a) Cartesian grid generation around the nozzle

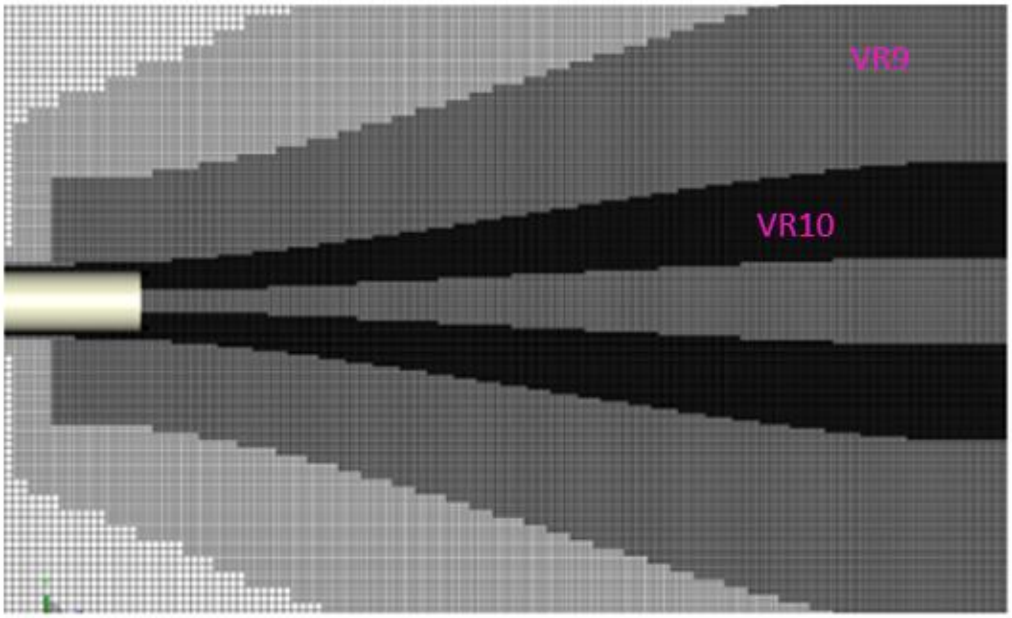

Fig. 3-4   VR and grid distribution in the near field (VR9 and VR10)

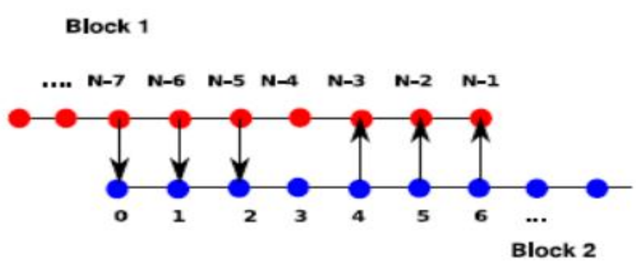

Fig. 3-5   Schematic of a seven-point overlaps at the interface between two adjacent blocks

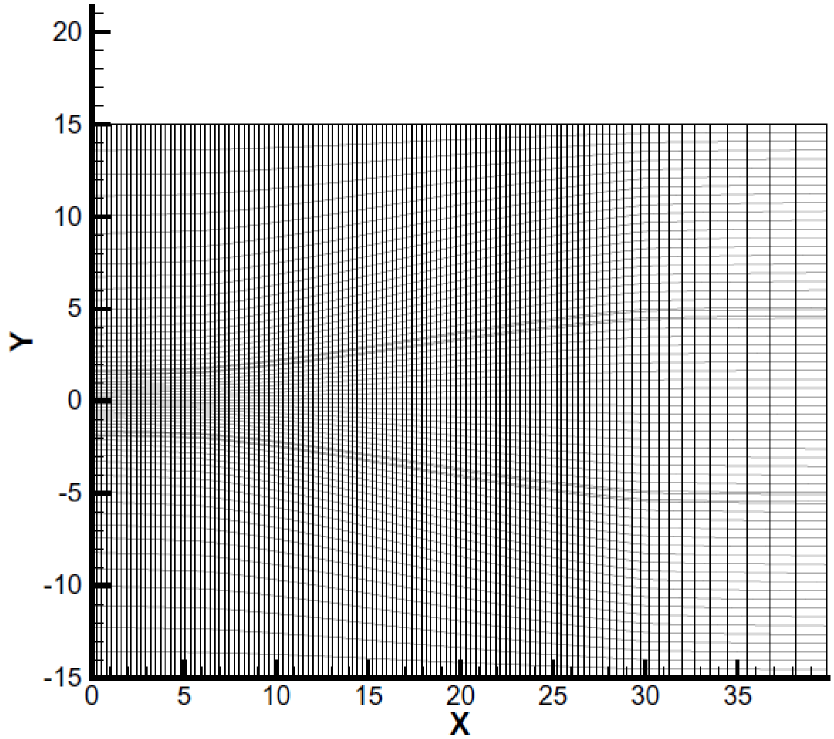

Fig. 3-6 Grid setup for LES simulation in the near-field (Najafi-Yazdi, 2011)

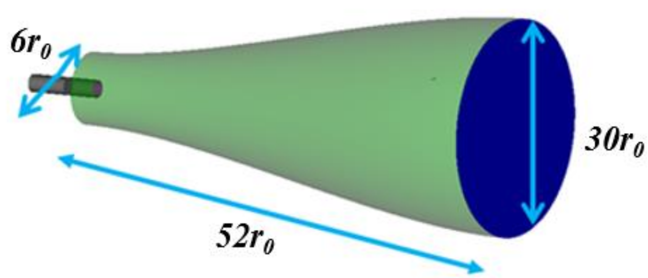

Fig. 3-7 FW-H control surface dimensions

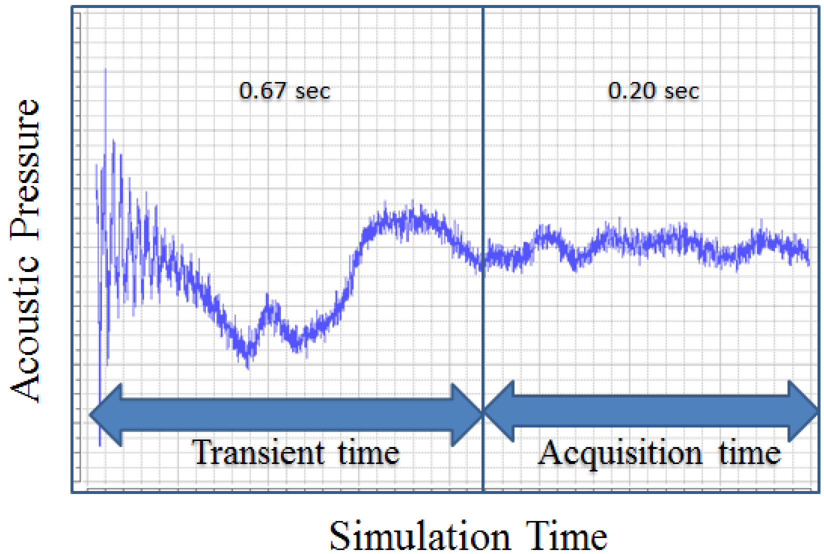

Fig. 3-8 Transient time and acoustic sampling for C2

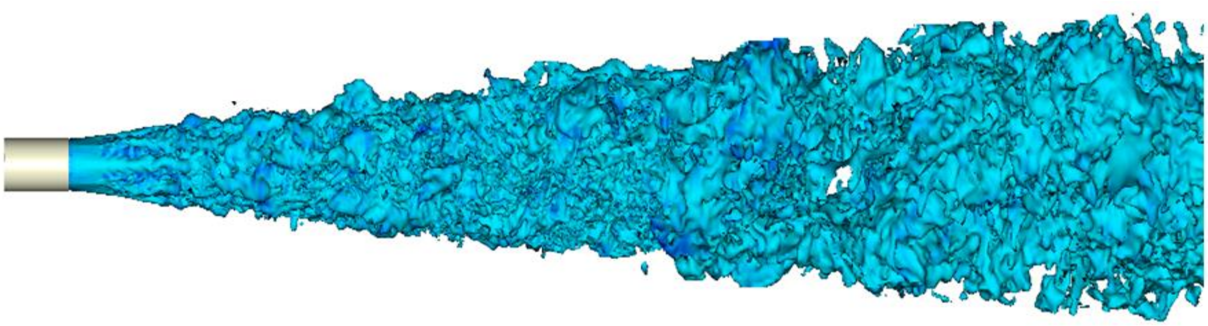

Fig. 3-9 Snapshot of the velocity iso-surface (|*V*|=20 m/s)

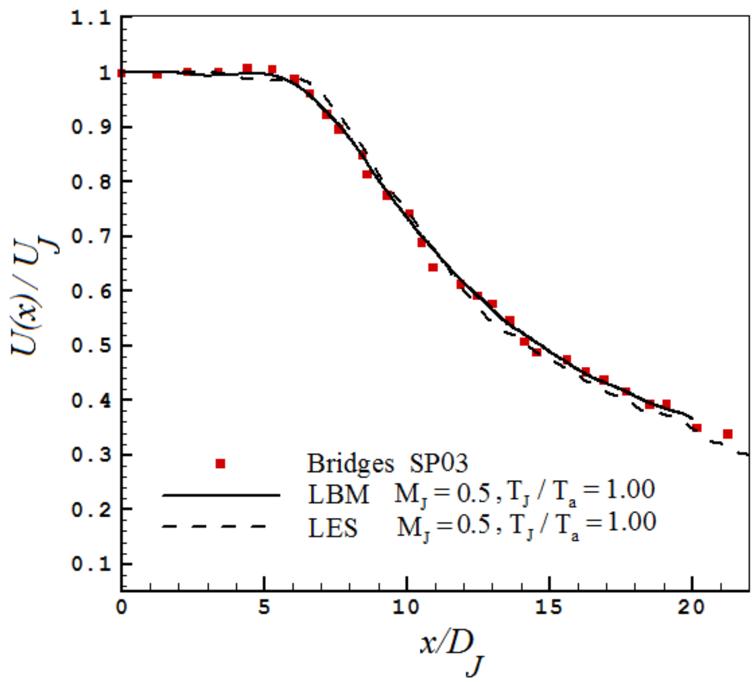

Fig. 3-10 Normalized Mean streamwise velocity profile along jet Centreline, LBM simulation (C1) compared to LES and experimental data.

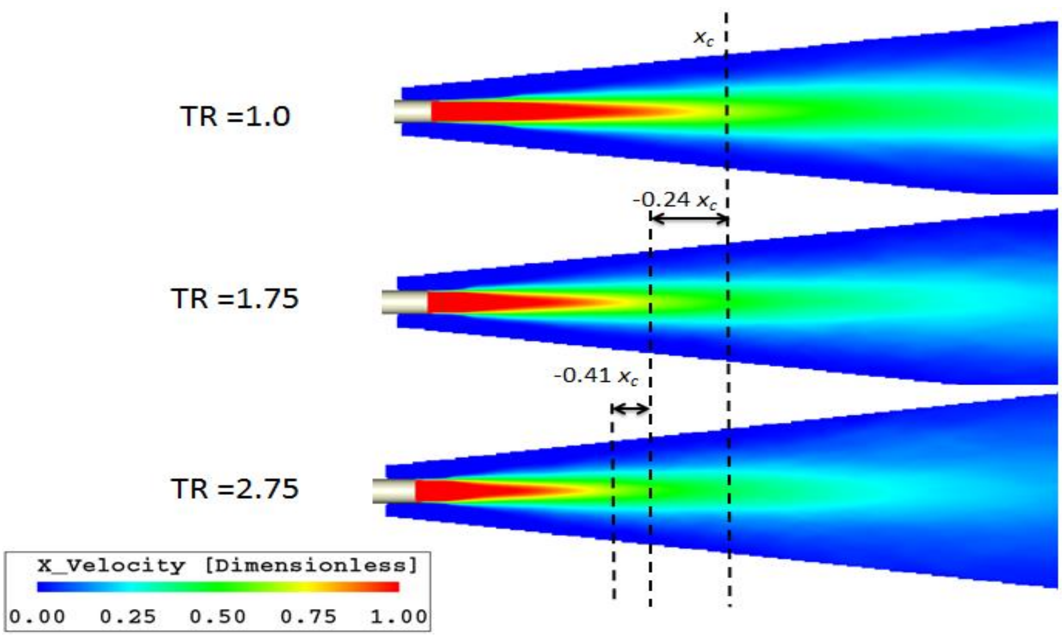

Fig. 3-11 Mean streamwise velocity contours at different temperature ratios.

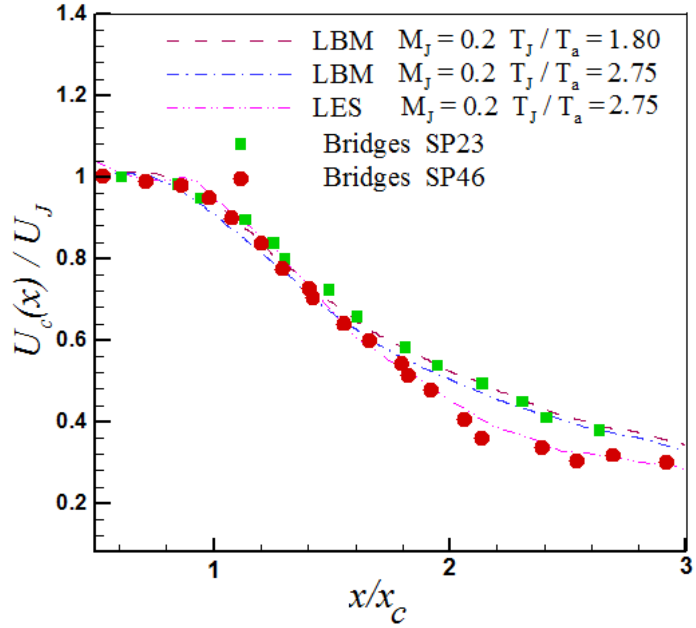

Fig. 3-12 Mean streamwise velocity profile on Witze coordinate system for heated set points.

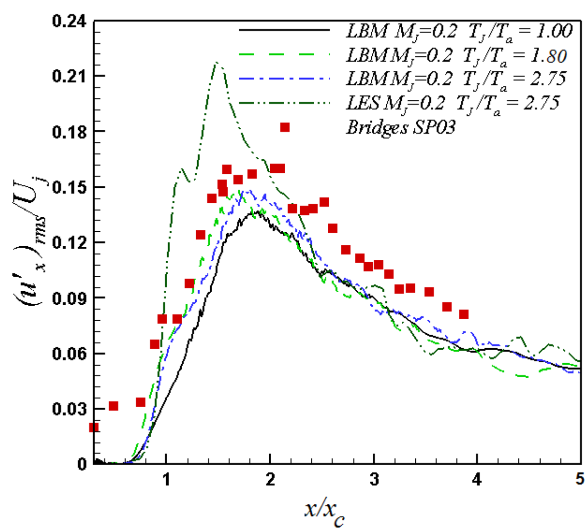

Fig. 3-13 Mean streamwise velocity profile on Witze coordinate system for heated set points.

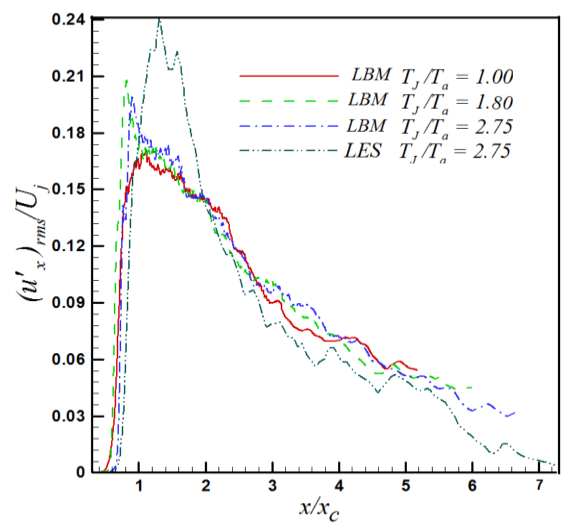

Fig. 3-14 Mean streamwise RMS velocity on Witze coordinate system along the jet lip line.

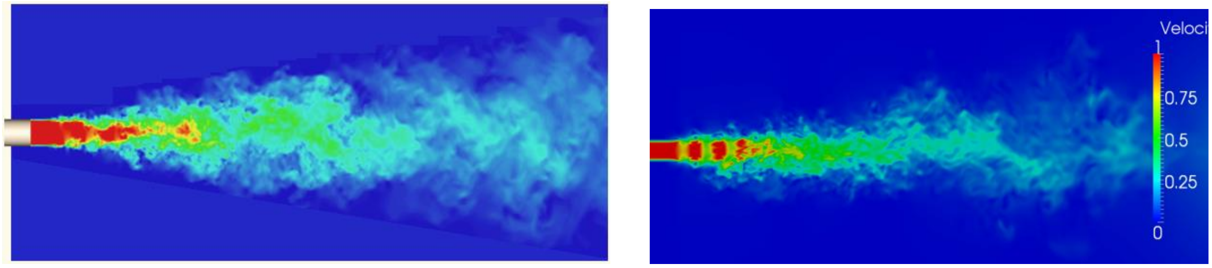

LBM **LES**

(a) Streamwise Velocity magnitude

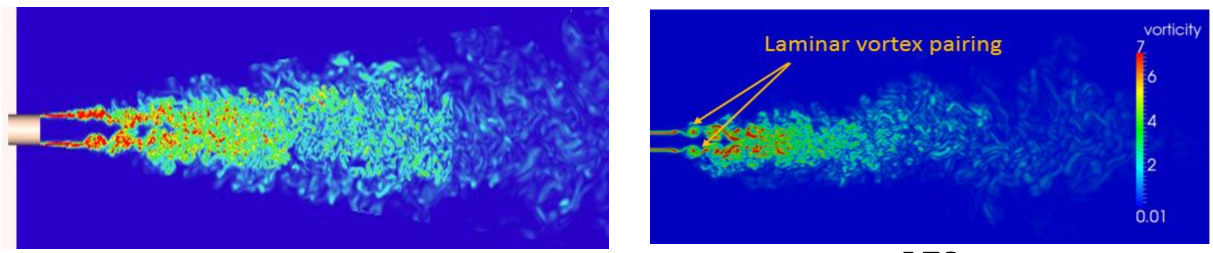

LBM **LES**

(b) Vorticity magnitude

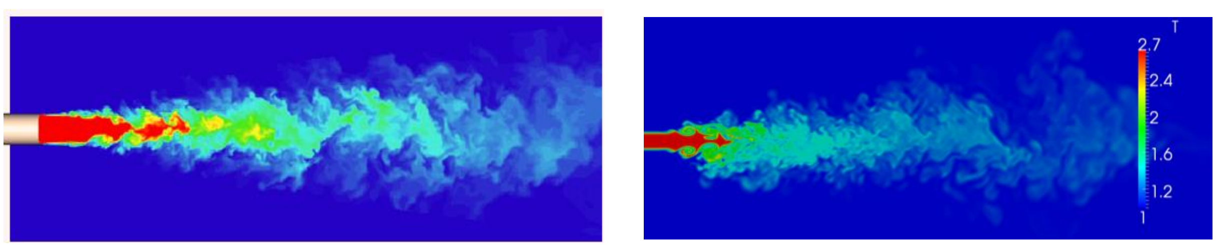

LBM **LES**

(c) Temperature ratio contour

Fig. 3-15 Comparison between LBM and LES results for C4. instantaneous snapshots of (a) streamwise velocity, (b) streamwise vorticity magnitude, and (c) temperature ratio

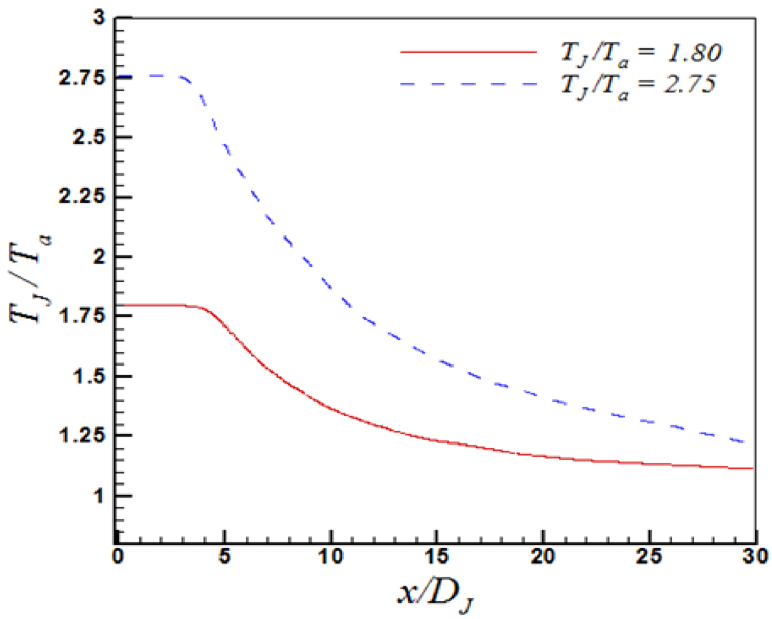

Fig. 3-16 Mean temperature decay profile for two heated set points, C3 and C4

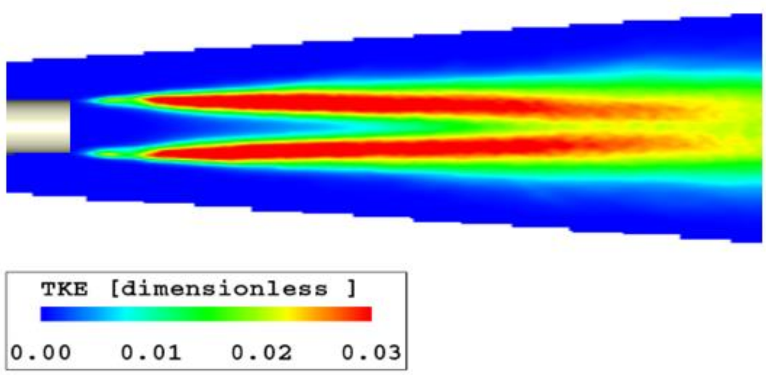

Fig. 3-17 Mean turbulent kinetic energy (TKE) contours.

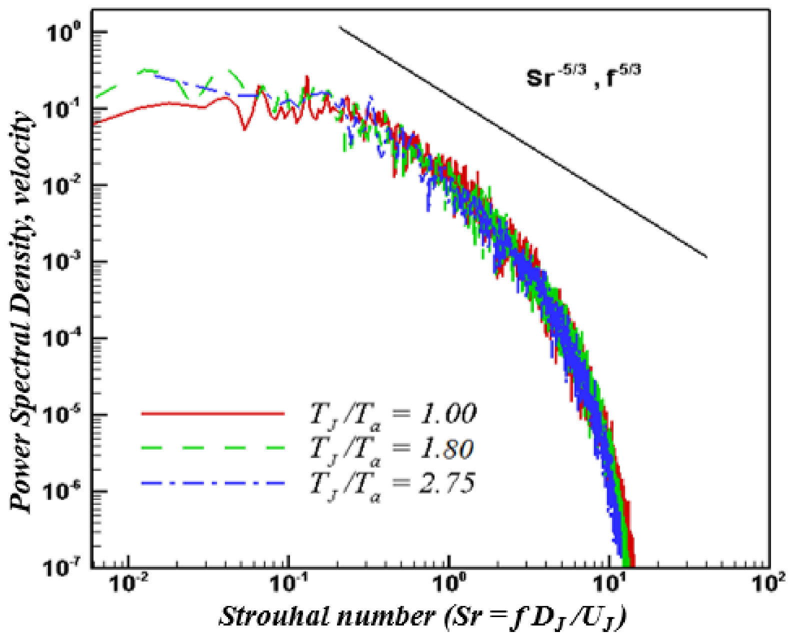

Fig. 3-18 Power spectral density of velocity located at $20r_0$ along jet Central axis.

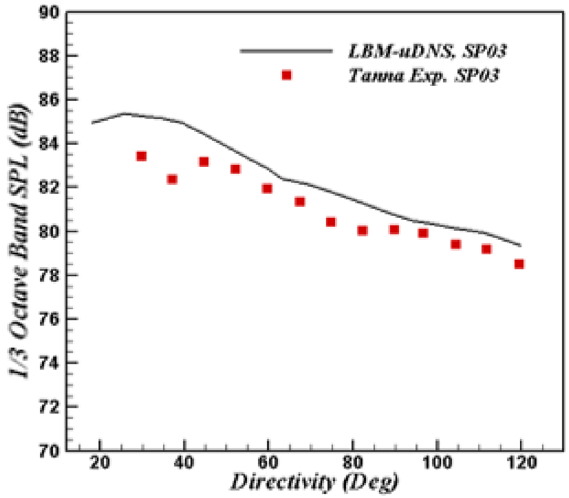

(a) OASPL, *r* = 144 *r₀*

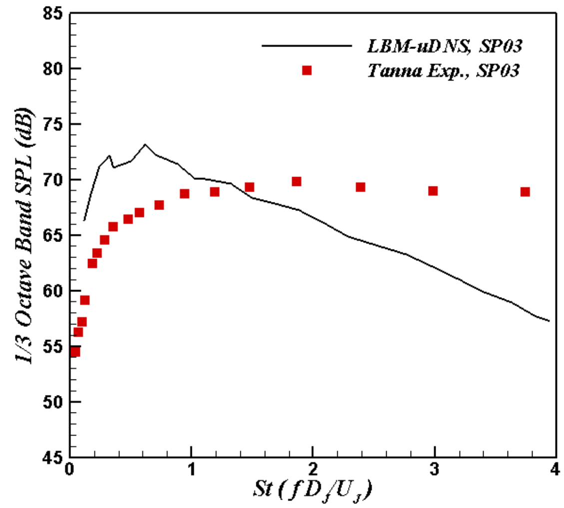

(b) Spectra at θ =30º , *r* = 144 r_0

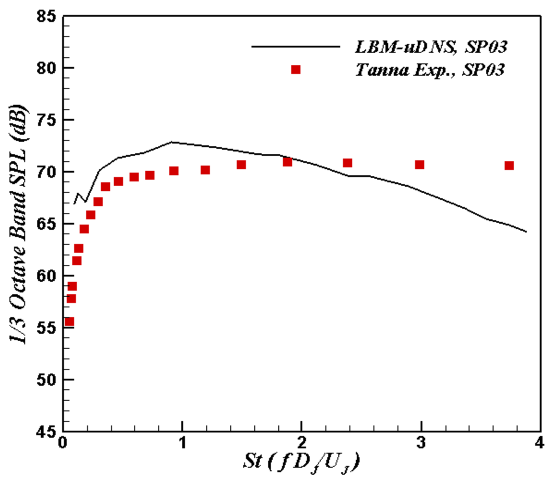

(c) Spectra at θ =60º, r = 144 r_0

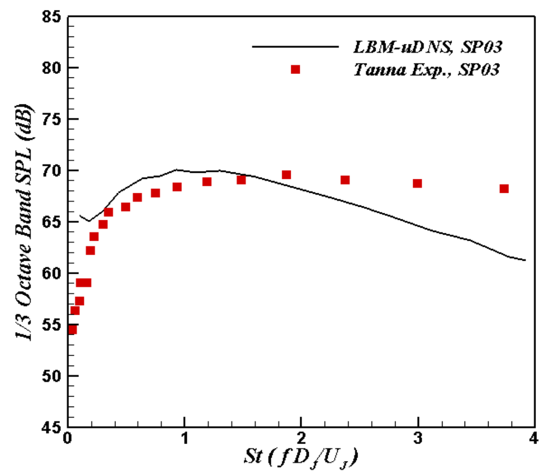

(d) Spectra at θ =90º, r = 144 r_0

Fig. 3-19 SP03-uDNS, (a) Overall sound pressure level directivity. (b) One-third octave spectra for observer angles 30º, (c) 60ºand (d) 90º at *r* =144 r_0.

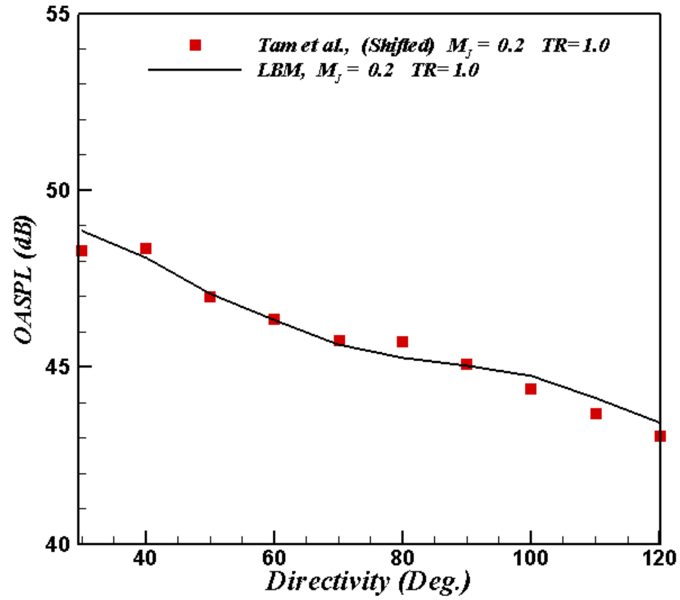

(a) OASPL, r = 144 r_0

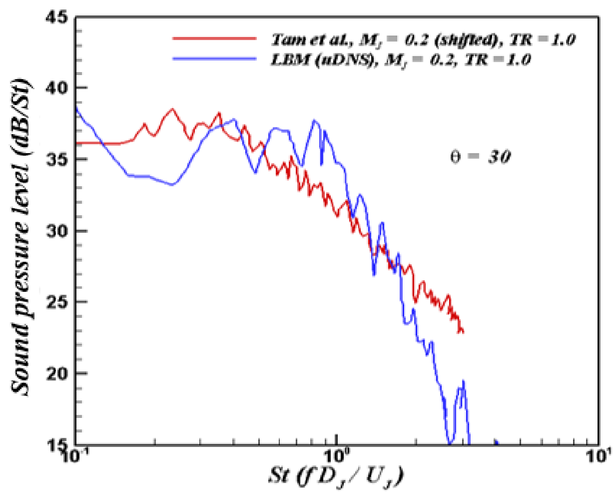

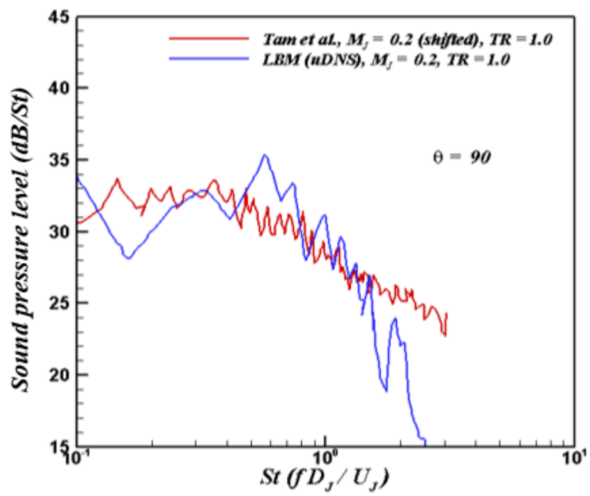

(b) Narrow-band spectra at θ =30º, r = 144 r_0 **(c) Narrow-band spectra at θ =90º, r = 144 r_0**

Fig. 3-20 uDNS, M=0.2 jet, (a) Overall sound pressure level directivity. (b) Narrow-band spectra for observer angles 30º, and (c) 90º at r =144 $r_{0.}$

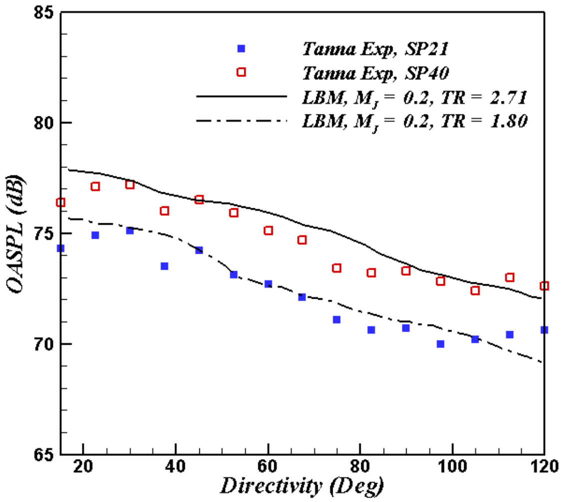

(a) OASPL, r = 144 r_0

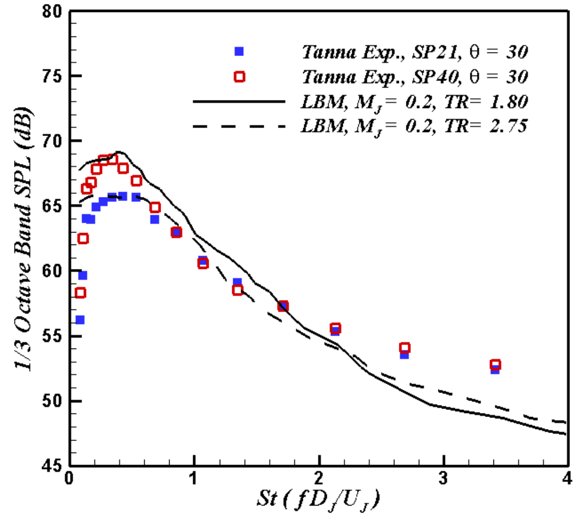

(b) Spectra at θ =30º , r = 144 r_0

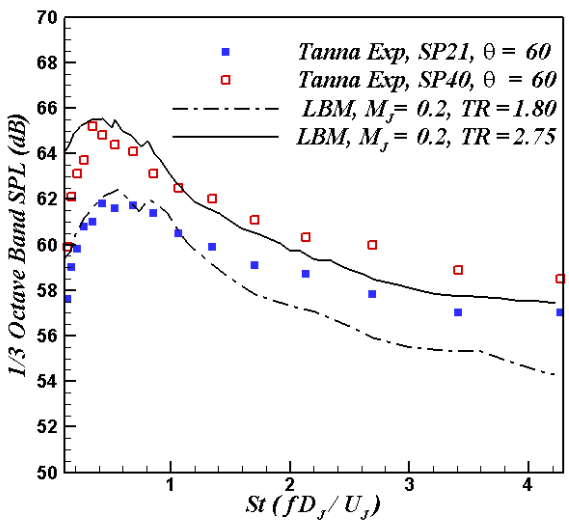

(c) Spectra at θ =60º, r = 144 r_0

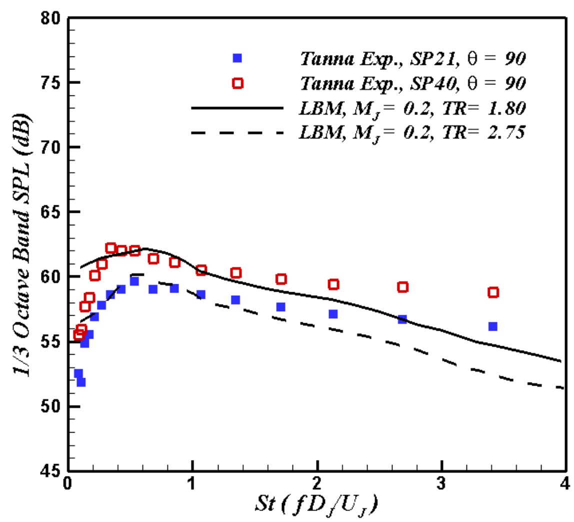

(d) Spectra at θ =90º, r = 144 r_0

Fig. 3-21 SP21 & SP40, uDNS, (a) Overall sound pressure level directivity. (b) One-third octave spectra for observer angles 30º, (b) 60º and (c) 90º at r =144 r_0.

3-2 Very Large Eddy Simulation (VLES) for high Reynolds flow condition and realistic nozzle's geometry

The use of VLES method allows performing jet simulation at higher and more realistic Reynolds numbers. Also using proper turbulent wall models would ease the inclusion of more complex nozzles into the computational domain and achieving velocity profile as for the wind tunnel testing at nozzle exit plane. In section 3-1, for all C1, ..., C4 cases, the Reynolds number was limited to 6,000 and under-resolved DNS scheme was used. In sections 2-1-7, it was shown how two-equation turbulence model based on the RNG variant of κ-ε formulation can be employed and bundled with LBM momentum solver to capture sub-grid scale models in the fluid domain. It was also shown in section 2-1-8 that a proper wall model would be able to mimic realistic turbulent boundary layer and energy transport near solid boundaries that also includes thermal energy transport and temperature profiles close to adiabatic or heated boundaries. Suitable wall models are necessary to capture turbulent characteristics in internal-external flow cases (*i.e.* complex nozzles) to predict flow condition accurately at nozzle exit plane. That would also have major impact on acoustic properties of the jet flows.

In this section, VLES method is employed to simulate realistic nozzle's geometry used in the benchmark experimental studies at high Reynolds numbers. In order to compare data with those reported in the previous section (*i.e.* under-resolved DNS), Tanna SP03 setpoint was selected in which the Mach number was within the valid range of regular D3Q19 LBM scheme for both uDNS and LBM-VLES schemes.

The simulation was performed using PowerFLOW 4.3d solver. Similar setup in this section was later used to validate D3Q19 high-Mach subsonic scheme for jet noise simulation at M_a =0.9 jet (*i.e.* SP46 and SP07) results were also reported in (Casalino *et al.*, 2014b; Lew *et al.*, 2014) . The high Mach subsonic validation of LBM in PowerFLOW 5.0 was a part of a collaborative work between McGill University and Exa Corporation.

3-2-1 Computational setup

The nozzle's geometry considered is a circular SMC000 described in studies by (Bridges and Wernet, 2010) as well as the convergent nozzle used by (Tanna, 1977). The nozzle has a conical slope of 5^o and the exit diameter is $D_J = 0.0508$ m (two inches) which is the same as circular nozzle in the previous section. The nozzle's geometry is shown in Fig. (3-22). The inlet boundary was constant velocity set at the rear end of the nozzle where the velocity magnitude was calculated using continuity equation (*i.e.* $\rho A(x)u(x)$ = constant) inside the nozzle. An active predictor-corrector algorithm was also utilized to adjust inlet velocity based on the achieved Mach number at nozzle exit plane ($M_J = 0.5$ for SP03). Figure (3-23 (a)) illustrates a close view of the grid setup inside and outside of the SMC000 nozzle. The grid setup and size of the simulation volume is completely different compared to the circular nozzle case in the previous section and it was optimized to capture complexity of the convergent nozzle as well as the VLES requirements in which acoustic domain must be clear from any spurious noise generated at the boundaries or different VR interfaces. The entire simulation volume includes a total of 13 VR regions with a domain size set of ($x/D_J, y/D_J, z/D_J$) = (±510 , ±510, ±510), which is significantly larger than uDNS setup in the previous section. Larger volume allows for more effective damping of the outgoing acoustic waves. The FW-H surface was located in VR level 3 (Fig. 3-23 (b)), with dimensions as shown in Fig. (3-23 (d)).

The smallest cell size in the main nozzle shear layer was ≅ 0.38 mm ($\Delta r/D_J = 7.5 \times 10^{-3}$) (table 3-4) similar to the circular nozzle in the previous section which is too coarse for wall bounded turbulent flow studies. The ratio needed to resolve the boundary layer in DNS and regular LES studies would be one order of magnitude less without the implementation of a wall model which would be prohibitively expensive; thus, the wall boundary layer here was approximated by proper wall model as described in section 2-1-8. The finest VR level VR12 (zero would be the coarsest level related to the outermost VR), is offset from the nozzle surface starting one jet diameter upstream until the nozzle exit downstream. The calculated nozzle y^+, related to the closest grid spacing was equal to 85.

The external boundary of the nozzle was extended up to the far-field boundary through conical surface. The nozzle was immersed inside the computational domain with anechoic characteristics.

Three layers of sponge buffers were introduced inside the fluid domain to effectively damp the outgoing acoustic waves (Fig. 3-23 (c)). These buffer layers were staggered with respect to the VR transition boundaries in order to avoid the simultaneous change of the damping constant and mesh resolution, and thus prevent small spurious acoustic reflections. All near-field and FW-H sampling are performed in the most inner sponge buffer. Both the voxel size and viscosity magnitude are larger in outer sponge layers. The viscosity is set by changing ν/T_o parameter on the lattice scale exponentially from 0.005 to 0.5. Two additional boundary conditions were required for the turbulence equations. In this study, turbulence intensity value at inlet was set to 0.01, and the turbulent length scale, $l = C_\mu \kappa^{2/3}/\varepsilon$, was set to $0.038D_J \cong 1.9$ mm, as recommended for internal pipe flows (Pope, 2000). The achieved Reynolds number $Re = (u_J D_J/\nu)$ was ≅592,000. The simulation timestep was 0.28×10^{-6}, and the maximum resolved Strouhal number on the FW-H surface was expected to be $St \cong 3.6$, based on the assumption of 20 voxels per wavelength for current setup and location of FW-H surface at third finest level, VR10. The rest of computational parameters are summarized in table (3-4).

3-2-2 Results and discussions

Figure (3-24) shows the snapshot of the vorticity and pressure contours in grayscale in which the acoustic pressure, $\left|p - p_\infty\right| < 30\,Pa$ and the vorticity contours $\left|\nabla\times\vec{U}\right| < 1.0\times10^4/\sec$. With no forcing function introduced at the inlet, turbulent structures and the transition pattern looks natural and comparable to the under-resolved DNS simulation. With additional dissipation imposed by the turbulence model, it is important to get the natural turbulent shear layer with no laminar vortex pairing in the outlet region. As shown in the section 3-1-5, the presence of laminar vortex pairing would cause an unphysical overshoot on RMS velocity components and the sound pressure spectra due to a sudden release of acoustic energy. It is observed that the jet shear layer breaks-up approximately at one jet diameter downstream of the nozzle exit, very close to the same location observed for uDNS simulations in the previous chapter.

Figure (3-25 (a)) shows the mean velocity contour in the near-field and figure (3-25 (b)) illustrates the root mean square (RMS) of the streamwise velocity (fluctuation component). In VLES simulations, the modelled RMS velocity, $u'_{\mathrm{model}} = \sqrt{2k/3}$ obtained from the solution of turbulence equations was added to the arithmetic RMS, *i.e.* direct statistical analysis, to account for the sub-grid scale energy transport. This helps to obtain more accurate RMS values at regions with a large velocity gradient such as the shear layer at the nozzle exit region. This factor is under the assumption of isotropic turbulence where, k , is the turbulent kinetic energy (TKE). Looking at the RMS contours and comparing Fig. (3-25 (b)) from VLES results with Fig. (3-17) from uDNS, TKE was clearly not fully resolved in uDNS close to the nozzle exit plane as no sub-grid scale model was used.

Figure (3-22) also exhibits a radial symmetric pattern which is an indication that the simulation has achieved statistical convergence. Figures (3-26 (a)) and (3-26 (b)) show the mean streamwise velocity and RMS fluctuation velocity along the jet centreline for SP03 jet using VLES method. The comparison were made with experimental data by (Bridges and Wernet, 2010). The potential core lengths defined when the jet centreline velocity reduces to 95% of the inflow jet velocity, $U_c(x_c) = 0.95U_c(0) = 0.95U_J$. Figures (3-26 (a)) indicates that the potential core length was well predicted by LBM and almost equal to the measured value of 6.8D_j. The decay rate compares well with the experimental data almost up to 21D_j and decays slightly faster towards downstream. Figure (3-26(b)) demonstrates RMS turbulence intensity along the centreline; results obtained by VLES method including the overall trend compare well with experimental data (Bridges and Wernet, 2010). The peak u'_{RMS} value and the streamwise location were also well predicted; However, the computed intensity between the peak location (x/D_J =12) and nozzle exit, slightly under-predicts the measured data which shows some levels of dissipation in the simulation that could be caused by the VLES scheme or the grid setup.

In Fig (3-12 (b)), due to changes in VR levels further downstream of the potential core has led to a relatively unsmoothed behaviour of RMS velocities. Using four-voxel averaging could slightly correct this behaviour in expense of less accuracy, as the RMS velocities shall be based on time-averaged velocities and not the spatial averaged properties; however, due to axisymmetric properties of circular jets, calculation of the RMS values along the nozzle lip can be much smoother, that is achieved by performing circumferential averaging of the RMS values along the nozzle lip at several azimuthal angles.

FW-H calculation was performed at post-processing stage in order to study far-field acoustic characteristics of SP03 jet using VLES scheme. Figure (3-27 (a)) illustrates the directivity of overall sound levels, compared to its uDNS counterpart. It is observed that while uDNS over-predicted sound levels at almost all observer angles by 1-2 dB, VLES results are over-predicting levels up to the shallow angle of 40^o by less than 1.0 dB, then followed the same trend as experimental data up to 85^o, where it starts to decay faster than experimental trend at larger angles. sound emission at large angles is mainly controlled by fine-scale turbulent structures(Tam *et al.*, 1996; Viswanathan, 2002). Based on above observation, although turbulence model was used for VLES case, it looks that the finer scales are either dissipated or not fully resolved by the turbulence model with specified grid resolution. Looking at the spectral levels shown in Fig. (3-27, (b), (c) & (d)), at θ =30^o, low-frequency levels are over-predicted up to *St* =1.3, while at θ =90^o almost all frequencies are under-predicted but mostly seen at high-frequency bands (*St* >1.5). Such behaviour would contribute to the OASPL discrepancy at larger angles. Looking at θ =60^o and moderate angles, the 1/3 octave band levels compares favourably with experimental results. It is recommended to use FW-H sampling with higher resolution (lower VR levels) in order to mitigate dissipation effects. High resolution FW-H surface will be used for high-Mach subsonic jet studies in chapter 5 of this document.

3-3 Chapter highlights and main learning points

From the results obtained in this chapter, it was found that several features of turbulent heated jets can be resolved by the LBM, coupled with an axillary thermal model. The following features were studied in this chapter. (1) Reduction in potential core length and concentration of RMS velocity contours near the nozzle exit that were found consistent with experimental observation at same Mach numbers. (2) Increase in turbulence intensity and slight shifting of the peak intensity towards downstream of jet at higher temperature ratio. Collapse of the velocity Energy spectrum using proper Strouhal definition, *i.e.* normalized by the actual jet velocity that varies based on the jet temperature.(3) Increase of noise levels by increasing the temperature as seen in experimental studies for jet Mach numbers less than 0.7 due to presence of dipolar sources.

Within the stability limits of under-resolved DNS method with thermal model, *i.e.* $M_J < 0.2$, the near-field turbulence characteristics and sound pressure spectra that were obtained from the simulation were compared with experimental results. The OASPL were found to be within 1.0-2.0 dB of the measured data. Most discrepancies were found at shallow aft angles and also the higher frequency bands of sound pressure spectra which is due to higher dissipation and under-resolved turbulent structures in the computational domain.

The use of VLES method allows performing jet simulation at higher and more realistic Reynolds numbers. Also, using proper turbulent wall models would ease the inclusion of more complex nozzles into the computational domain and achieving velocity profile as for the wind tunnel testing at nozzle exit plane. It is observed that while uDNS over-predicted sound levels at almost all observer angles by 1-2 dB, VLES results are over-predicting levels up to the shallow angle of 40^{o} by less than 1.0 dB, then followed the same trend as experimental data up to 85^{o}. Also better accuracy was achieved at shallow aft angles that implies that using the VLES method at higher-Reynolds numbers could better resolve the high-frequency sources in the near field.

Table 3-4 Computational parameters, LBM-VLES scheme for SP03 jet

Setpoint	VRs	Δr (mm)	FEV ($\times10^6$)	FES ($\times10^6$)	t_t (sec)	t_a (sec)	CPUh ($\times10^3$)
SP03	13	0.38	49.43	1.78	0.29	0.19	40

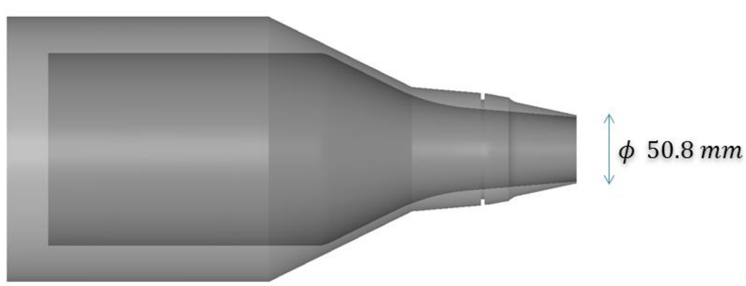

Fig. 3-22 SMC000 Nozzle used for LBM simulation

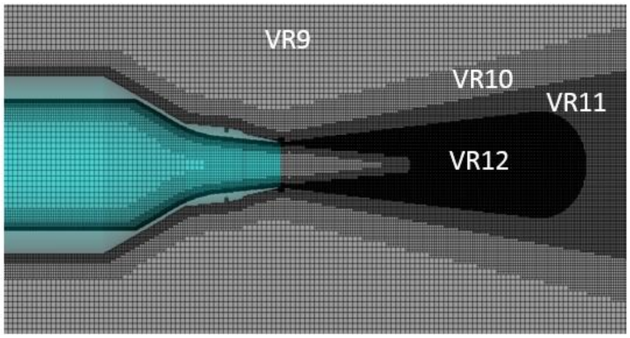

(a) Grid setup in the near-field

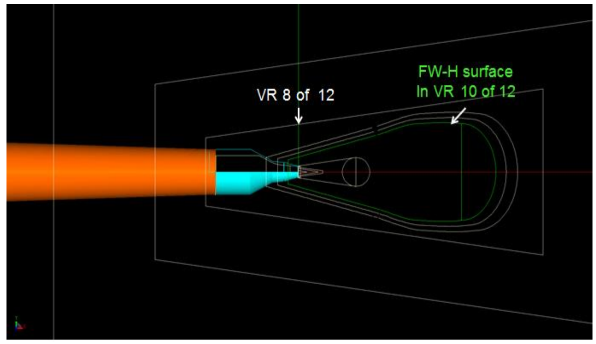

(b) Mesh layout FW-H surface location

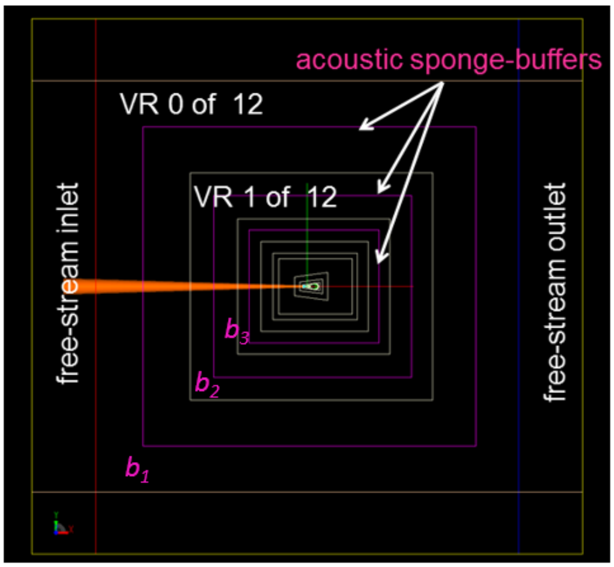

(c) Grid refinement at far-field and location of the sponge layers

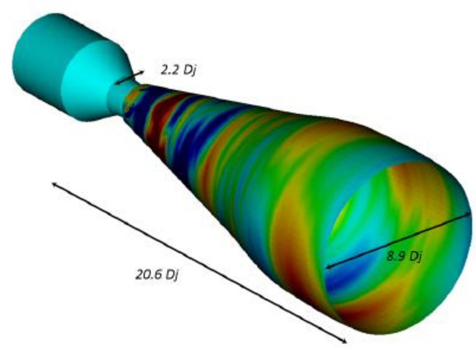

(d) Dimensions of the FW-H surface

Streamwise dimensions

L_0/D	L_1/D	L_2/D	L_3/D	L_4/D	L_5/D	L_6/D	L_7/D	L_8/D	L_9/D	L_{10}/D	L_{11}/D
510.0	230.0	140.0	100.0	83.0	69.0	64.0	46.0	28.0	21.0	12.0	7.0

Buffer zone dimensions

b_1/D	b_2/D	b_3/D
320.0	190.0	125.0

Fig. 3-23 computational setup (a) grid setup in/out side of the nozzle, (b) FW-H surface location at VR#3 (c) far-field VR layout and sponge layers. (d) dimension of the FW-H surface

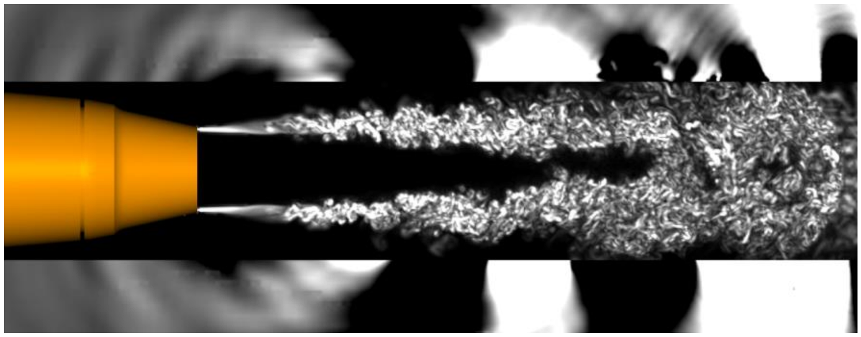

Fig. 3-24 pressure and vorticity contours in the near field

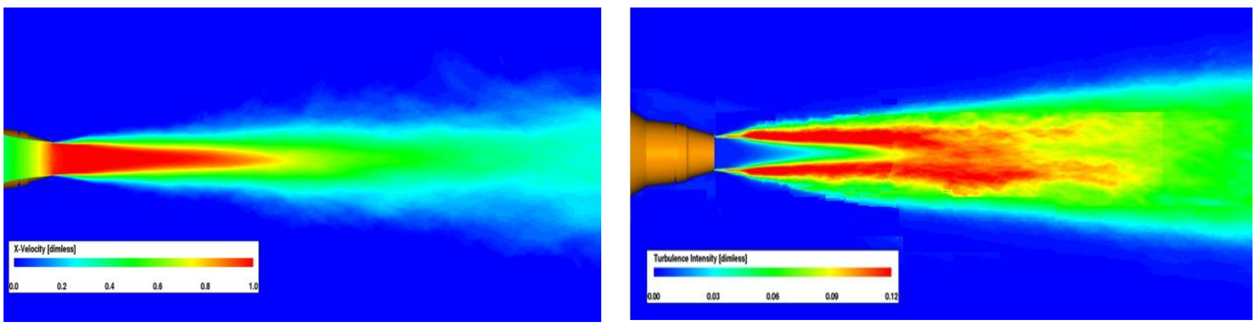

(a) (b)

Fig. 3-25 Mean flow results, SP03 jet using VLES-LBM scheme (a) mean streamwise velocity contours (b) RMS velocity (streamwise turbulent intensity)

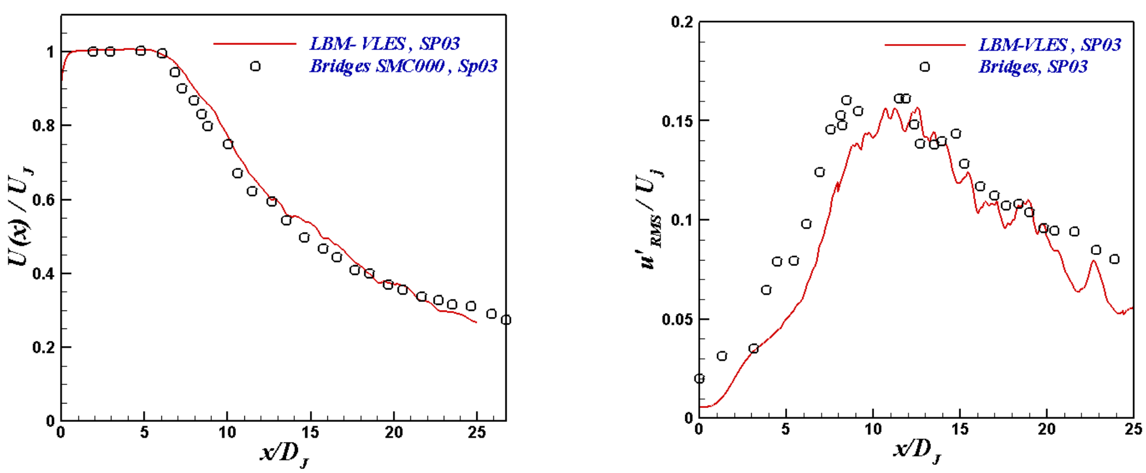

(a) (b)

Fig. 3-26 Mean flow results, SP03 jet using VLES-LBM scheme (a) mean streamwise velocity contours (b) RMS velocity

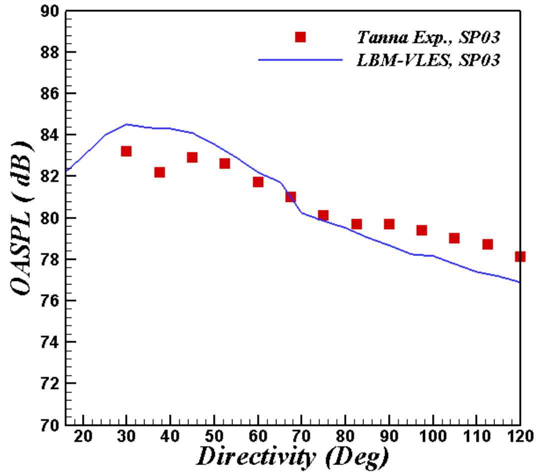

(a) OASPL, r = 144 r_0

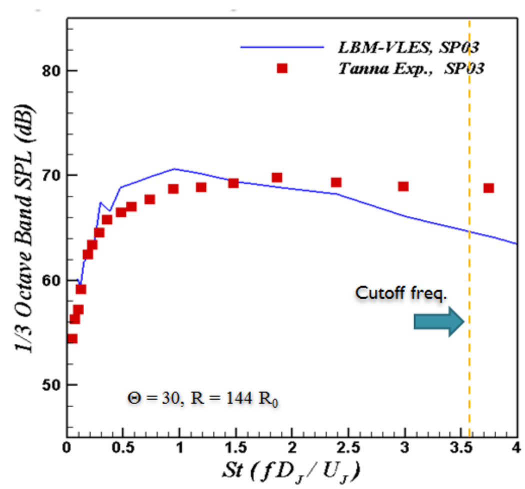

(b) Spectra at θ =30º , r = 144 r_0

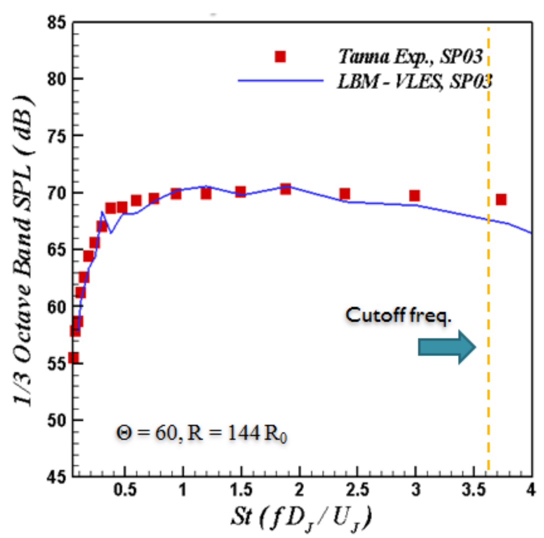

(c) Spectra at θ =60º, r = 144 r_0

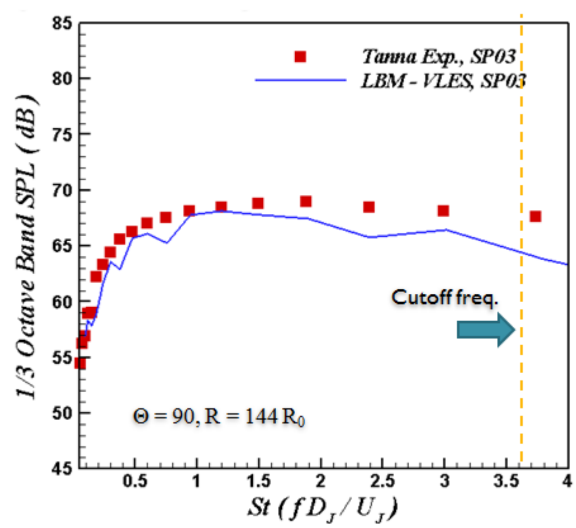

(b) Spectra at θ =90º, r = 144 r_0

Fig. 3-27 SP03-VLES, (a) Overall sound pressure level directivity. (b) One-third octave spectra for observer angles 30º, (c) 60º and (d) 90º at r =144 r_0.

Chapter 4

Internal mixing nozzles with forced mixers: LBM-VLES scheme for moderate Mach numbers

4-1 Introduction

In this part of the study, which was sponsored by Pratt Whitney Canada and Green Aviation Research and Development Network (GARDN), The application of transient CFD model based on the LBM was investigated for design of nozzles with forced mixers. The lobed mixers used in turbofan engine nozzles have a very complex geometry, which may cause challenges to generate a high-quality body-fitted meshing for the conventional Navier-Stokes based LES methods.

In this chapter, for the first time, LBM-VLES method was used to simulate transient compressible flow through internal mixing nozzles with various lobed mixers. *PowerFLOW 4.3d* solver, based on the regular 19-stage LBM platform was used in which the maximum achievable Mach number was about 0.55. The same methodology was examined for a single-stream jet up to M_J = 0.5 in section 3-2. Further studies on high Mach mixing flows were also conducted using high-order LBM scheme using PowerFLOW 5.0 solver which will be discussed in chapter 5. The volumetric bounce-back boundary conditions discussed in section 2-1-5, helps easier handling of complex geometries inside the computational domain (Chen, 1998).

Detailed literature review regarding internal mixing nozzles with forced mixers was provided in section 1-3 of this document. In this part of the study, detailed model of the mixer and the nozzle was created to simultaneously simulate the internal flow through the mixer and the external jet plume. The transient behaviour of the streamwise vortices at the nozzle exit area was visualized and quantified. A confluent mixer was selected as a baseline to investigate the performance of both the low and high penetration lobed mixers. The goal was to better understand the detailed noise reduction mechanisms of lobed mixers, as well as thrust and mixing coefficients. The Reynolds number based on nozzle exit diameter was 1.36×10^{6}, and the peak acoustic Mach number was up to ~*0.5*. The low-Mach operating condition was considered to abide by the constraints of the 19-stage LBM algorithm used in this study. Similar to section 3-2 for single-stream jets, the sub grid scales (SGS) were modeled using the renormalization group (RNG) forms of the standard k-ε equations (VLES scheme) as discussed in sections 2-1-7 and 2-18 as well as section 3-2 for jet flow applications. A coupled thermal model was used along with LBM as discussed in sections 2-1-9 and 2-10. In thermal cases, using VLES in PowerFLOW 4.3d allowed the extension of the maximum Mach numbers to 0.5 contrary to uDNS scheme in which the Mach number was limited to 0.2 due to stability of code with respect to the dynamic range of temperature and velocity gradients. Far-field sound was also computed using the porous Ffwocs William-Hawkings (FW-H) surface integral method which was discussed in section 2-2 and was applied for the single-stream jets in chapter 3.

Effects of the lobe number, penetration depth and heat transfer were investigated in separate sections of this chapter. As a side study of this work, effects of scalloping in mixer models have also been investigated in McGill acoustic group with collaboration of the author. Detailed results are available in the master's thesis by Gong *et al.* (2013) and also in (Gong *et al.*, 2013). In order to cover scalloping effects in this document, only a summary of far-field results has been presented in this chapter.

4-2 Simulation setup

4-2-1 Test cases

In order to study the combined effect of the lobe number and the penetration depth as well as the heat transfer, *i.e.* bypass ratio effects, three sets of one-fourth scale nozzles, mixers and centre-bodies were selected from experimental models at the NASA Glenn Research Centre (Mengle *et al.*, 2002). From the same database, two more mixer geometries were selected to study the effect of scalloping.(Gong, 2013; Gong *et al.*, 2013). Standard names and abbreviations were used as suggested by (Mengle *et al.*, 2002) for different mixer models; The mixers used in the present study include (a) a confluent (CONF) mixer, (b) a 12-lobe low-penetration mixer (12CL), (c) a 20-lobe high-penetration mixer (20UH); (d) a 20-lobe, medially scalloped, high-penetration mixer (20MH); and (e) a 20-lobe deeply scalloped, high-penetration mixer (20DH). These models are shown in Fig. (4-1). The parametric sketch of the nozzle-mixer configuration is shown in Fig. (4-

2) illustrating important geometrical properties of an internal mixing nozzle. Such parameters for simulated models in this work are listed in Table (4-1). The selected contoured nozzle as well as the centre body was the same for all five NASA configurations leading to constant nominal mixing length (L= 279.4 mm). The mixing length to mixing plane diameter ratio was also constant (L/D_{mp} = 1.10). The converging nozzle diameter decreased smoothly from 261.4 mm at core/fan stream inlet to 183.9 mm at the nozzle exit plane (D_J = 183.9 mm). The diameter is ~3.6 times the SMC000 nozzle (D_J = 50.8 mm) in the previous chapter.

Above selection of models was made to cover important features of internal mixing phenomena. Based on acoustic data presented in (Mengle *et al.*, 2002), unscalopped, high-penetration mixer configurations were able to reduce low-frequency sound emissions compared to CONF model; however, such configurations were producing more higher sound pressure levels at high frequency bands. Deeply scalloped mixers on the other hand, did not have significant impact on high frequency noise and hence showed broadband reduction in overall sound pressure levels compared to the CONF models (Mengle *et al.*, 2002).

The 12CL mixer (with no sidewall cutout) was selected to study the combined effects of lobe number and penetration depth when compared to CONF and the 20UH models. The combined effects of the bypass ratio and thermal mixing were investigated by heating the core flow and finally in order to study the effect of sidewall scalloping, 20UH, 20MH, and 20DH mixers were selected to keep the lobe number unchanged and focus on the scalloping diameter and the penetration depth.

4-2-2 Operating conditions

Both cold and heated operating conditions were extracted from NASA reports (Mengle *et al.*, 2002); However, the total pressure ratio, total temperature ratio, and mass flow rates were adjusted to achieve fixed bypass ratios of 3.0 and 5.0 for cold and hot set points respectively. Velocity adjustments were necessary to limit the peak exit Mach numbers below 0.5 (*i.e.* $M_j \leq 0.5$) to stay within the weak compressibility limit of standard D3Q19 LBM model as discussed in section 2-1-3 and 2-1-4. The Peak Mach number in experimental data were 0.85-0.9 based on the operating condition. Despite the Mach number limitation of regular D3Q19 LBM, as discussed later in this chapter, several aerodynamics and acoustic properties of lobed mixers can be recovered and compared with experimental results at higher Mach numbers. Of course, this was the first effort in unsteady simulation of lobed mixers in the literature. More realistic boundary conditions will be applied in chapter 5 using the high-order LBM for direct comparison with the experimental data. The inlet static pressure and velocity for both cold and hot cases were identical; however, due to the change in density, the bypass ratio was greater in the heated case by a factor proportional to the density ratio. For all simulation cases, the ambient pressure and temperature were assumed 101,000 *Pa* and 300*K* respectively. The kinematic viscosity was set to 2.07×10^{-5} m^2/s, which is greater than air viscosity at 300*K* (~ 1.58×10^{-5} m^2/s) in experiment; however, the achieved Reynolds number was 1.36×10^6 that was found sufficiently large to produce important turbulent structure and noise sources in the shear layer and plume region. The minimum viscosity value was limited to the relaxation time and selected grid resolution; hence, the viscosity has to be equal or greater than a minimum value to ensure the selected resolution and relaxation time could maintain the stability of the coupled LBM-VLES model and capture desired macroscopic turbulent scales.

Total pressure values were set at both fan and core stream inlets. For each stream, the mean static pressure and mean velocity were calculated from adjusted total pressure ratio, $NPR_{f,c}$, total temperature ratio, $NTR_{f,c}$, and the mass flow rate, $\dot{m}_{f,c}$. Total pressure can be imposed directly as a boundary condition for the LBM in PowerFLOW solver; however, in this setup, velocity and pressure were imposed separately at each stream. The reason was first to make sure inlet Mach number will be staying within allowable compressibility limit and second, to apply proper velocity profile and forcing function at each stream to achieve better turbulent mixing inside and outside of the nozzle. Calculations were performed directly from definition of static and total flow parameters using isentropic assumption as

$$NPR_{f,c} = p^t_{f,c} \big/ p_{amb} = \left(p^s_{f,c} + \frac{1}{2}\rho_{f,c}\bar{u}^2_{f,c} \right) \Big/ p_{amb} \quad , \tag{4.1}$$

$$T_{c,f} = T_{amb} = 300K \quad , \tag{4.2}$$

$$T^t_{f,c} = T^s_{f,c} + \frac{1}{2}\left(\bar{u}^2_{f,c} \big/ C_p \right) \quad , \tag{4.3}$$

$$\dot{m}_{f,c} = \rho_{f,c} A_{f,c} \overline{u}_{f,c} \quad , \tag{4.4}$$

and

$$p^s_{f,c} = \rho_{f,c} R T_{f,c} \quad , \tag{4.5}$$

Where T is the temperature, p is the pressure, $\dot{m}$ is the mass flow rate, $(\ )_f$ is related to the fan or bypass stream and $(\ )_c$ related to the core stream. $(\ )^s$ and $(\ )^t$ are static and total pressure/temperature values respectively and $\overline{u}$ is the mean streamwise velocity. Thermophysical properties are local density, ρ, specific air constant, R= 287.058 J.kg^{-1} K^{-1}, and specific heat capacity, $C_p \cong$1000 J.kg^{-1} K^{-1}).

In order to estimate Mach number at nozzle exit plane, isentropic flow equations, *i.e.* Eqns (4.8) to (4-10), were recast to show Mach number dependence to total and static flow properties at core and bypass stream as well as the nozzle exit condition, $(\ )_J$, Closure conditions, Eqns (4.6), (4.7) and (4.8) are necessary to find two unique solution from which the subsonic solution would be accepted. Major relations can be summarized by

$$\dot{m}_J = \dot{m}_f + \dot{m}_c , \tag{4.6}$$

$$\dot{m}_J = \rho_J A_J u_J \tag{4.7}$$

$$p^s_J = p_{atm} = 101{,}000 \text{ Pa}, \tag{4.8}$$

$$\frac{p^s_J}{p^t_J} = \left(1 + \frac{\gamma - 1}{2} M_J^2\right)^{\frac{-\gamma}{\gamma - 1}}, \tag{4.9}$$

$$\frac{T_J}{T^t_J} = \left(1 + \frac{\gamma - 1}{2} M_J^2\right)^{-1}, \tag{4.10}$$

and

$$\left(\frac{p^s_J}{p^t_J}\right) = \left(\frac{\rho^s_J}{\rho^t_J}\right)^{\gamma} = \left(\frac{T^s_J}{T^t_J}\right)^{\frac{\gamma}{\gamma - 1}} . \tag{4.11}$$

The simulated Mach number at the exit plane was always less than above estimation due to momentum loss and entropy generation in the mixing region. Isentropic assumption was to ensure that the exit Mach number would not exceed $M_J \cong 0.5$, in the ideal condition in which there is no momentum and energy loss. Table (4-2) shows the non-dimensional nozzle inlet and outlet conditions. The absolute values of the inlet conditions at core and bypass streams are listed in Table (4-3) for both cold and heated operating conditions.

4-2-3 Initial and boundary conditions

The initial condition included the static pressure and three velocity components in the computational domain. The initial pressure was set to the characteristic pressure in LBM which was equal to ambient pressure on the macroscopic scale. A weak free stream velocity, M_{FS} =0.02, was set in the inlet far-field boundary to enhance turbulent transition at outer nozzle shear layer; hence, the initial velocity was set to the free stream velocity. Since the computational scale was far larger than the nozzle length, a non-reflective pressure boundary condition, as for the jet noise simulation in chapter 3, was employed here. Such outlet boundary definition together with layers of sponge zones could effectively damp outgoing acoustic waves.

Based on the mean value for pressure and velocity obtained in 4-2-2, a hyperbolic tangent velocity profile as for the Eqn. (3.1) was imposed at both the core and fan stream inlets (Freund, 2001). Change of coordinate was necessary in Eqn. (3.1) to be applicable for the annular nozzle inlet given by

$$u_{f,c}(r) = \frac{1}{2}\bar{u}_{f,c}\left[1 - \tanh\left[\frac{r - \left(r^i_{f,c} + r^o_{f,c}\right)/2}{2\theta}\right]\right], \tag{4.12}$$

in which $r = \sqrt{x^2 + y^2}$, $r^i_{f,c}$ and $r^o_{f,c}$ are inner and outer radii of the core and fan streams, θ ,is constant selected as 0.06 times the averaged radius for each stream. Uniform pressure distributions were imposed at the nozzle inflow boundaries of each stream based on the static pressure calculated in section 4-2-2. For heated case, a uniform temperature profile was also set to the core and bypass inlets. The inlet planes are shown in Fig. (4-3 (a)).

In order to achieve a more realistic turbulent shear layer at mixing plane and the nozzle outlet, artificial perturbations were forced at both the core and bypass flow inlets. Such forcing function was developed by (Bogey *et al.*, 2011) and designed to mimic wall-bounded turbulent boundary layers. Such perturbations were originally developed to provide nozzle-exit conditions as close as possible to those in the nominally turbulent jets of (Zaman, 2012) and also optimized to reduce spurious sound radiation to the far-field.

In the present study, the boundary layer was perturbed at entry region of the nozzle. Four ring-shape surfaces were isolated from the solid mixer-nozzle geometries to define the forcing velocities on the surface. The forcing surfaces were placed close to the inlet with a length of approximately $0.08D_j$. Figure (4-3 (b)) shows the four surfaces on which the forcing velocities were applied. Those surfaces include the nozzle, mixer (both upper and lower surface), and the centre conical body.

The forcing terms are low-amplitude but random fluctuations in velocity, aim to generate small eddies and perturb the inflow boundary layer. These fluctuations were random both in space and time. The tripping magnitudes altered to achieve statistical a turbulence intensity of 4% at nozzle exit plane; three forcing velocity components were introduced as

$$\begin{Bmatrix} v_r \\ v_\theta \\ v_z \end{Bmatrix} = \begin{Bmatrix} v_r \\ v_\theta \\ v_z \end{Bmatrix} + \alpha u_j \begin{Bmatrix} \varepsilon_r\left(r,\theta,z,t\right) \\ 2\varepsilon_\theta\left(r,\theta,z,t\right) \\ 3\varepsilon_z\left(r,\theta,z,t\right) \end{Bmatrix} \quad , \tag{4.13}$$

where $\varepsilon_r\left(r,\theta,z,t\right)$, $\varepsilon_\theta\left(r,\theta,z,t\right)$ and $\varepsilon_z\left(r,\theta,z,t\right)$ changes randomly in range of (-1,1) every time step at each surface element on the forced surfaces (Fig. 4-3). α =0.00625 was selected here to achieve the desired turbulence intensity level. The "*Rand ( )*" function has been implemented in the PowerFLOW solver.

Two additional boundary conditions were required for the turbulence equations. In this study, turbulence intensity value at inlet was set to 0.01 and the turbulent length scale, $l = C_\mu \kappa^{2/3}/\varepsilon$, was estimated $0.038\times(0.5D_J) \cong 3.2$ mm for dual stream nozzles (Pope, 2000).

4-2-4 Grid setup

The size of computational domain in the near field was $(x,y,z) = (37.0D_J$, $\pm32.8D_J$, $\pm32.8D_J$) in which all data acquisition are performed, the sponge layer with coarse grid and high viscosity was extended to $(x, y, z) = (75.0D_J$, $\pm57.6D_J$, $\pm57.6D_J$). The grid setup is shown in Figs. (4-4) to (4-7). Similar to the single-stream jet simulation, the computational domain was divided into lattice arrays with variable resolution (VR). In the numerical setup, nine (9) levels of VR zones were used. Successive VR regions were concentric and conical starting from the nozzle (VR5) up to VR3 as shown if Fig. (4-4(a)) and Fig. (4-5). Two acoustic buffer zones were considered inside VR0 and VR1 in which Both the voxel size and viscosity magnitude are larger. The viscosity was set by changing ν/T_o parameter on the lattice scale exponentially from the characteristic viscosity up to 0.5 at the coarsest level (VR0). The free stream velocity and outlet pressure boundary conditions were imposed at inlet and outlet sides of VR0 rectangle. The finest regions, *i.e.* VR7 and VR8, were created near solid boundaries, such as the mixer, in the CAD model. The shape and size of each VR zone is shown in Fig. (4-5). For the grid setup, enough space must be considered between successive VR regions in both radial and streamwise directions. Small spacing between VR levels may cause significant change in local acoustic impedance; hence, partial reflection of acoustic waves. In addition to numerical reflection, insufficient VR spacing could lead to the generation of so-called "VR tones" in the far-field spectra that is characterized by high frequency spikes on power spectral density with significant audibility level. One method to check if reflection does exist in the acoustic field is by looking at transient pressure contours or the dilatation rate ($\nabla.\vec{V}$) in locations where VR levels are changed. In this study, numerical experiment was performed to find optimal VR spacing at different levels, and it was found that the distance between VR6 and VR7 (downstream of the nozzle exit) should be at least 12 voxels to avoid acoustic pressure reflection. Final setup was performed using 16 voxels between VR6 and VR7. The lateral views including details of grid setup near the mixer and nozzle tips are shown in Figs. (4-6) and (4-7). Smallest cell size was 3.7×10^{-4} m ($\Delta r/D_J = 1.64 \times 10^{-3}$), that corresponds to $y^+ \cong$ 72. The domain included a total of around 78 million fine equivalent voxels for the CONF and 12CL models. The 20UH, 20MH and 20DH had more voxels, 86 million, due to complexity of the mixer model and more cells inside the closest VR to the mixer. The boundary layer voxels were distributed close to solid boundaries(Fig. 4-4(a)). Although adopted voxel size was not able to fully resolve the boundary layer features, the artificial forcing strategy discussed in section 4-2-3 was helpful to provide enough perturbation leading to natural mixing in the mixing plane and physical jet inflow conditions. As for the single jet simulation in section 3-2, VLES method with wall models was used to be able to simulate high-Reynolds number with relatively coarse grid. A VR region (VR7) with second resolution level was placed right off the finest level to act as a smooth transition from the smallest to coarser grids in the outer region an accurately capture important turbulence scales contributed to sound emission. A high-resolution grid in regions with high shear is essential for accurate prediction of the sound field. The shear layer is characterized by high velocity and turbulence intensity gradients. Flow detachment downstream of the centre-body and at mixer edges combined to streamwise vorticity also affect gradients at inner and outer shear layers, which also contribute to the far-field sound. VR7 and VR6 levels were therefore extended to the downstream of both the mixer and the centre-body to resolve the shear layer, vortex shedding and flow separation. A comparison between initial and later grid setup showed a significant improvement on the resolved flow pattern when the second finest VR level was added. Outside the nozzle, two axisymetric VR regions (VR7 and VR6) were placed downstream of the nozzle tip to cover the development of turbulence in the shear layer. In addition, a larger VR5 was located further downstream of the nozzle exit to yield a smooth transition to the outer and coarser VR regions.

4-2-5 Additional simulation parameters

The same thermal model as for C3 and C4 in section 3-1, was used for set points 4 and 5 of dual-stream nozzles which was described in 2-1-9, and 2-1-10 (Zhang and Chen, 2002; Zhou *et al.*, 2004). The core temperature was set to 1.7 times the ambient temperature to achieve a bypass ratio of ~5.0. The actual temperature ratio in the experiments were about ~2.37 which will be used applied in chapter 5.0 using the high-order LBM. Here the focus was to study the impacts of BPR changes with temperature on the sound pressure spectra. The temperature of the outermost boundaries inside the computational domain was set to the ambient temperature, *i.e.* isothermal boundary condition. The nozzle, mixer and the centre body were assumed to be adiabatic. The smallest timestep was $\cong 6.92\times10^{-7}$ Seconds based on the finest grid resolution. The transient and acquisition time was 0.22 and 0.34 seconds respectively for CONF and 12CL models and 0.26 and

0.34 seconds for scalloped models as indicated in table (4-4). All simulations were evolved on the Mammouth parallel computer located at the Universite de Sherbrooke in Quebec. Each node in this machine has 24 cores and 32 GB of memory. The lobed mixer simulations were evolved on 10 nodes for a period of ~10 days in order to achieve mean flow and acoustic convergence as well as sufficient sampled data for post processing.

4-2-6 Mean thrust calculation and mixing effectiveness

The net average thrust was evaluated for all mixers models to study the effect of mixer geometry on thrust that is directly related to fuel consumption. Thrust values are cast as a coefficient in which the net propulsion force is normalized by dynamic pressure based on the mean outlet jet velocity. The effect of jet excess pressure was considered as well. The net thrust was calculated from Eqns. (3.4) and (3.5) according to the definition of thrust for turbofan engines (Saravanamuttoo *et al.*, 2001) .

For heated test cases, the mixing effectiveness was calculated based on thermal mixing efficiency, η_{th} and the comparison between 100% theoretical mixing compared to the actual mixing. The mixing effectiveness was originally developed by Frost (1966) and can be expressed as

$$\mu_{th} = \frac{Actual\,thrust - \left(fan\ thrust + core\ thrust \right)}{theoretical\,100\%\,mixed\,thrust - \left(fan\ thrust + core\ thrust \right)} \times 100 \quad , \tag{4.14}$$

where theoretical or 100% mixed thrust is obtained by assuming an isentropic mixing. Above expression was later modified by Kuchar and Chamberlin (1980) to correlate thrust values with thermodynamics properties of the fan and core exit stations which was derived as

$$\mu_{th} = \frac{\left(\dfrac{T_{actual\,mixed}}{T_{100\%\,mixed}} \right) \left(\dot{m}_f + \dot{m}_c \right) \left(T_{100\%\,meas} \right)^{1/2} - \left[\dot{m}_f \left(T_f \right)^{1/2} + \dot{m}_c \left(T_c \right)^{1/2} \right]}{\left(\dot{m}_f + \dot{m}_c \right) \left(T_{100\%\,meas} \right)^{1/2} - \left[\dot{m}_f \left(T_f \right)^{1/2} + \dot{m}_c \left(T_c \right)^{1/2} \right]} \times 100 \quad , \tag{4.15}$$

where $T_{actual\,mixed}$, $T_{100\%\,mixed}$ and $T_{100\%\,meas}$ are calculated according to Eqns (4.16) to (4.18) in which the measured vlues is replaced by simulated values obtained by thermal LBM simulation as

$$T_{actual\,mixed} = \left(\int_{exit} \dot{m}_i \left(T_i\right)^{1/2} / \int_{exit} \dot{m}_i \right)^2 \quad , \tag{4.16}$$

$$T_{100\%\,mixed} = \int_{exit} \dot{m}_i T_i \,/ \int_{exit} \dot{m}_i \quad , \tag{4.17}$$

$$T_{100\%\,meas} = \frac{\dot{m}_f c_{p\,f} T_f + \dot{m}_c c_{pc} T_c}{\dot{m}_f c_{p\,f} + \dot{m}_c c_{pc}} \quad , \tag{4.18}$$

where $\dot{m}$ is the mass flow rate, c_p is specific heat at constant pressure and T is the flow temperature. The indices $(\ )_f$ and $(\ )_c$, represent the fan and core properties respectively.

4-2-7 Far-field sound Calculation

As for the jet cases in chapter 3, Far-field sound pressure levels were calculated using a porous Ffowcs Williams-Hawkings (FW-H) surface integral method, formulation 1-C (Najafi-Yazdi *et al.*, 2011). An equivalent methodology, embodied in the PowerACOUSTICS 2.0a package licensed by Exa Corporation, was used in this study. This method includes corrections for mean flow, moving sources and observers. It is useful for cases with mean free stream such as lobed mixer simulations at flight conditions. A conical, open-ended control surface was included in the computational domain and surrounded the flow field such that there was no interaction between the jet shear layer and the FW-H surface Fig (4-8). The FW-H control surface started slightly upstream of the nozzle exit plane (x= -0.02 D_j) and had an initial diameter of $3D_j$. It extended streamwise over a distance of $21D_j$ and had diameter of $11.8D_j$ at the end. The shape of FW-H surface was simpler compared to previous simulation in section 3-2-1 in which a funnel-shaped surface was used, and the length was large enough to enclose the jet laminar core. The entire surface remained in the same VR region, *i.e.* VR4, to avoid different sampling rates and hence the resolved acoustic wave lengths. Both ends of the cone were removed and no data was recorded to avoid spurious noise as discussed in chapter 2. The remaining parts of the surface were used to sample pressure, velocity and density during acquisition time for FW-H calculations. A total of twenty-five (25) virtual microphone coordinates were defined for the FW-H solver at one fixed radial distance (*i.e.* r =80 D_J) from the nozzle exit, covering multiple radiation angles upstream and downstream of the nozzle exit plane (*i.e.* $45^o \leq \theta \leq 160^o$) as shown in Fig. (4-8). Sound pressure levels were calculated over different frequency ranges. The bandwidth of 20 Hz was used for FFT calculations. Spectral analysis was performed via bandpass filtering for select bands between 200 Hz and 4.8 kHz (*St*~4.0) *i.e.* grid cut-off frequency, to study the noise reduction potentials. The grid cut-off was calculated under the assumption that each wavelength is resolved via 20 voxels on the FW-H surface in LBM simulations(Casalino *et al.*, 2014b). Frequencies less than 200 Hz were filtered due to due to relatively small acquisition time compared to acoustic period. Acoustic sampling was initiated after roughly 0.24 sec (~318,000 timesteps), at which the flow statistics in the near field converged to a steady value. Acoustic data were recorded over 0.34 seconds to achieve low-frequency levels with sufficient accuracy (Table 4-4).

4-3 Results and discussions

In this section, flow properties and sound radiation of three unscalloped mixers (*i.e.*, CONF, 12CL, 20UH) were investigated. The combined effects of the lobe number and penetration depth were studies using a confluent mixer (CONF) as a baseline and the 12CL and 20UH lobed configurations. Introducing the lobes will intrinsically change the penetration depth when compared to CONF mixer and cannot be study independently. Also, by heating the core flow, both density and the bypass ratio will change simultaneously; hence, both effects would contribute in aerodynamic and acoustic performance of turbofan engine. This section covers the instantaneous and time averaged plume survey as well as internal flow study. Flow Results include the local velocity distribution, turbulent kinetic energy and RMS velocities at different cross sections and along the jet centreline. Instantaneous flow structures, flow separation, and mixing layers inside the internal mixing nozzles were visualized and quantified. The mean flow characteristics and the flow statistics were obtained inside the nozzle and within the jet plume.

In summary, despite discrepancies in inlet conditions, LBM could predict important aerodynamic and acoustic features of different mixer models consistent with previous experimental studies (Mengle *et al.*, 2002). An increase in thrust coefficient was observed as expected for forced mixers. Directivity of the overall sound pressure levels (OASPL) as well as the directivity of band-filtered sound pressures in the far-field were also presented. On acoustics perspective, the far-field sound analysis showed considerable low-frequency noise reduction (*i.e.* ≅4-5 dB) for the lobed mixers, as well as about 3dB reduction in the overall sound pressure level (OASPL) compared to the baseline confluent nozzle. Major results can be found in published documents (Habibi *et al.*, 2013a; Habibi *et al.*, 2013b; Habibi and Mongeau, 2013).

4-3-1 Near-field flow characteristics

Figure (4-9 (a)) visualizes the snapshot of turbulent jet plume downstream of nozzle exit plane using velocity iso-surface ($u/U_J = 0.47$). It was evident that the onset of the instability waves was fairly close to the nozzle exit plane ($x = 0.23\ D_J$); however, the jet reached at fully turbulent state in almost half jet diameter downstream of the nozzle exit plane which is closer to nozzle lip compared to single-stream jet simulation shown in chapter 3 of this document. Such change in transition location was expected as the grid resolution ratio ($\Delta r/D_J$) for internal mixing simulation was about 60% finer than the single-stream jet case despite the Δr magnitude was greater. The snapshot of streamwise velocity contours are shown in Fig. (4-9 (b)) for 12CL mixer model; the potential core region almost disappeared at $\sim 8D_J$ downstream of the nozzle exit plane which was common experience with three mixer models; Coherent turbulent structures formed within shear layer close to the nozzle outlet region for 12CL and 20UH mixers. Such coherent structures were smaller in 20UH and almost absent in the confluent configurations. Those structures were originated from rotational mixing induced by the lobed geometry and would play an important role in changing aerodynamic sound features.

It can be seen from Fig. (4-10) that significant streamwise vortices are generated by the lobed mixer compared to the confluent model. This was evident by looking at the spanwise vorticity contours in Fig. (4-9 (a)), at mixing zone, *i.e.* x = $0.1D_J$, measured from the crest of mixer. For the CONF model, the mixing occurs within internal mixing layer between the fan and core flow starting at the tip of the mixer, whereas for 12CL and 20UH, significant streamwise vortices were induced in the mixing area. The shapes of streamwise vortices for 12CL and 20UH models were different due to the fact that the penetration depth on 20UH was greater than 12CL and also the lobes had smaller width due to larger number of lobes; hence, the vortical structures were thinner but also taller. Smaller recirculation area was observed at the root of 20UH which is due to different geometry and effect of wall shear stress on diffusion of vortical structures as flow passes through the mixer (McCormick and Ennett, 1994). More interestingly, it was observed that mixer geometry could alter the thickness of internal shear layer downstream of the mixer. As it is visible in the instantaneous vorticity contours in Fig. (4-10(a)), at the same streamwise distance, the mixing layer was thicker and contained smaller scaled eddies for lobed mixers compared to CONF model; similar trend is seen when the lobe number and penetration depth increases (20UH vs. 12CL). Figure (4-10(b)) shows flow separation and mixing zones near 12CL mixer by visualizing streamwise vorticity contours. Flow separation occurred at root of the mixer as well as tip of the centre body. There is an immediate vortex shedding downstream of the centre body due to adverse pressure gradient in the region for all three mixer models. Also, the recirculating flow at this region is characterized by velocity deficit at tip of the centre body. For both 12CL and the 20UH mixers, flow separation occurred near the upper walls of the lobes. For 20UH mixer the vortex shedding process occurred much closer to the mixing plane and almost immediately at the lobe edges ($x = 0.49D_J$). Figure 4-10(b) also shows streamwise vortices began to appear at around one lobe height downstream of the mixing plane for the 12CL mixer. It was found that that the vortex formation points of 20UH were much closer to the nozzle surface, and the vortices which were detaching from the 20UH mixer diverted to the shear layer downstream of the nozzle exit plane. The latter phenomena can be explained by the higher penetration depth of the 20UH mixer compared to 12CL. Figure (4-11) shows the Lambda-2 criterion iso-surface for all three mixer models (iso-surface value = -100). Lambda-2 criterion has been shown to adequately capture vortex structure and to properly visualize the 3D turbulent vortices (Jeong and Hussain, 1995). The Lambda-2 (λ_2) defined by the second eigenvalue of the symmetric tensor $S^2+\Omega^2$, where S and Ω were respectively the symmetric and anti-symmetric parts of the velocity gradient tensor as

$$\nabla\vec{u} = \begin{pmatrix} \partial_x u_x & \partial_y u_x & \partial_z u_x \\ \partial_x u_y & \partial_y u_y & \partial_z u_y \\ \partial_x u_z & \partial_y u_z & \partial_z u_z \end{pmatrix},\ S = \frac{\nabla\vec{u} + \left(\nabla\vec{u}\right)^T}{2},\ \Omega = \frac{\nabla\vec{u} - \left(\nabla\vec{u}\right)^T}{2} \quad . \tag{4.19}$$

Where T in Eqn. (4.19) is the transpose operation. Three Eigen values of $S^2+\Omega^2$ are calculated and ordered in a way that $\lambda_1 \geq \lambda_2 \geq \lambda_3$. It can be shown that a point in the velocity field is part of a vortex core only if at least two of the eigenvalues are negative or simply if $\lambda_2<0$. Comparing Figs. (4-11 (a,b and c)). The 12CL and 20UH mixer featured intensive mixing downstream of mixer, while the confluent mixer did not produce any significant mixing pattern inside the nozzle. Looking at the bypass (fan) stream at the root of the mixers, it can be seen a significant flow recirculation occurs in 12CL model due to wider flow passage and larger valleys in the area, whereas, for the CONF model no lobe is present neither any cavity to generate vortex; for 20UH models, the vortical structures are well damped by the viscous forces, due to greater number of lobes causing flow particles to be blocked and lose their momentum; However, as seen in Fig. 4-11 (c) and discussed earlier in this chapter, for the 20UH model, the vortical structures in the shear layer are smaller. Shifting from large-scale to small-scale turbulent structures in jet shear layer would tend to reduce low-frequency sound that will be discussed later in this chapter.

In order to quantify the jet plume characteristics in each model, the time-averaged flow field was calculated. Figure (4-12 (a)) shows the front view of the averaged flow field at nozzle exit plane ($x = 0$). The confluent mixer had a contour similar to a simple dual stream coaxial jet. The circular ring region of low velocity magnitude indicated the mixing area where interaction between the two streams occurred due to Kelvin-Helmholtz instability. As seen from Fig. (4-12 (a)), there are clear indications of the 12CL and 20UH lobe shapes at the outlet region. The streamwise vortices formed at the crest of mixer and were convected downstream of the nozzle exits plane. This phenomenon was also seen in previous studies (Manning, 1991; Mengle *et al.*, 2002). The greater number of lobes and deeper penetration caused the 20UH mixer to exhibit a relatively more uniform flow profile than that of the 12CL. In comparison to the 12CL mixer, due to the high penetration length, the high velocity region for the 20UH mixer was smaller and closer to edges of the nozzle.

Three-dimensional contours of mean velocity field are shown in Fig. 4-12 (b) for better indication of larger fan stream velocity compared to the core stream in low-Mach simulation. The high-Mach simulation in using realistic boundary conditions in experimental studies (Mengle *et al.*, 2002) is characterized by larger core velocity compared to the bypass stream. The high Mach simulation results will be discussed in chapter 5. Figure (4-13) shows the variations of mean spanwise velocity profiles for all three mixer models at different downstream locations ($x/D_J = 0$, 0.1. 0.5, 1.0, 3.0 and 5.0). Mean transverse velocity contours are also shown for select distances up to $x = 4D_J$. For all cases, the velocity profile looks more complex at the outlet region due to internal mixing and then turn into much smoother shape, as for a simple coaxial jet, further downstream. For all three mixers, a low-velocity region was extended from the tip of the centre body to approximately two (2) jet diameters downstream of the nozzle exit plane. The CONF model did not show any sign of significant mixing. The mid sections of velocity profile continued to increase until one jet diameter downstream; which is also seen in single jet streams and caused by the growth of turbulent mixing layer in the vicinity of nozzle. High-velocity regions were observed at commencement of nozzle outer shear layer. For the confluent mixer, high-velocity gradients were seen at the mixing area where the core and bypass streams interacted within one diameter from the exit plane. High-velocity gradients also occurred in the vicinity of the centreline for all three mixers where the flow deceleration around the centre body caused significant velocity deficit. For the 12CL and 20UH mixer, regions with large velocity gradient were mostly concentrated along the inner layer of the nozzle lip line within one diameter from the exit plane. The low-velocity region around centreline was gradually diminished due to flow entrainment. In 20UH case, the large velocity gradient near the inner surface of the nozzle lip line was diffused immediately downstream of the nozzle exit; the velocity profile varied gently further downstream. This phenomenon can be related to the high penetration depth and enhanced mixing process of the 20UH mixer. The radial gradients in axial velocity will affect turbulence intensity and are strong sources of noise. The jet plume generates sound not only from the radial gradient in velocity at the nozzle outer shear layer, but also from velocity peaks and streamwise vortices. These are excess noise sources, in the sense that they do not occur in a jet with equivalent uniform velocity at the nozzle exit plane.

The mean streamwise velocity contours are compared in Fig. (4-14 (a)). Velocity contours qualitatively show the impact of mixer on flow downstream of nozzle. It can be seen the streamwise vortices has significantly altered the flow pattern in the laminar core region where the most important sources of aerodynamic sound were present; however, no significant change in length of the laminar core can be seen in three mixer models. In order to quantify velocity profile and entrainment rate, the mean velocity profiles along jet centreline in Fig. (4-14 (b)) were normalized by jet mean outlet velocity. An initial increase in velocity can be seen for all three mixer models due to the velocity deficit extended from centre body within the first jet diameter from nozzle exit. The velocities remained almost constant from approximately two (2) to six (6) diameters downstream of nozzle outlet; however, the peak centreline velocity of the CONF model was ≅7% higher than the 12CL mixer and ≅10% higher than 20UH model which potentially could change the far-field sound characteristics. Looking at velocity profiles in Fig. (4-14), it is evident that 12CL and 20UH cases yielded a similar decay rate for the centreline velocity; the CONF case on the other hand exhibited greater decay rate up to $x=14D_J$ and start converging to similar decay rate as other two mixer models further downstream.

Figure (4-15 (a)) shows the contours of turbulent kinetic energy. As for VLES simulations in chapter 3, the modelled turbulent kinetic energy (TKE) obtained from the solution of turbulence equations was added to the arithmetic turbulent kinetic energy (*i.e.* direct statistical analysis) to account for the sub-grid scale energy transport. This would help to obtain more accurate values at high-velocity gradient regions (e.g. nozzle lip area). Total TKE could be written as

$$k = k_{\mathrm{mod}el} + \frac{1}{2}\left(\overline{u^{'}u^{'}} + \overline{v^{'}v^{'}} + \overline{w^{'}w^{'}}\right) , \qquad (4.20)$$

where u,v and w, are components of fluctuation velocities along Cartesian axes. By looking at the TKE contours in Fig. (4-15(a)), it is evident that TKE values for the three mixers reached the peak level at slightly different downstream locations from the nozzle exit plane. By looking at TKE profile along the centreline in Fig. (4-15(b)), The CONF mixer reached at peak turbulent energy level at around $10.1D_j$, whereas for 12CL case, the peak occurred at around $9.5D_j$, and finally the peak level reached at $9.8D_j$ for 20UH; hence the 12CL and 20UH mixers reached a peak level further upstream compared to the confluent mixer. Comparing the two lobed cases, it is observed that the 12CL reached the peak TKE level further upstream than the 20UH. The shift in TKE was also seen in experimental data by Mengle *et al.* (2002). This might be the result of high penetration depth of the 20UH mixer that tends to push the energy-containing eddies towards the nozzle walls and away from the mid zones. The TKE magnitude, for the confluent mixer was 3% higher than that of the 20UH and 5% higher than that of the 12CL further downstream, the TKE of the 12CL and 20UH mixers decayed at about the same rate, slightly faster than that of the confluent mixer. This phenomenon could also be related to the noise reduction characteristics of lobed mixers. The use of lobed mixers slightly increases the turbulence intensity along the outer shear layer, *i.e.* nozzle lip line; this could be related to the transition to turbulence by mixing effects resulted from streamwise vortices as seen in Fig (4-10 (a)). By far it was shown that lobed mixers could effectively change the external flow features; the LBM simulation could also be very helpful to study unsteady flow characteristics inside the nozzle and be utilized for shape optimization of the mixer geometry by looking at aerodynamics and mixing parameters. Figures (4-16 a, b and c) show the variation of internal velocity and turbulence intensity along the centre body as well as the mixing region, *i.e.* from root of the mixer towards nozzle exit plane. The comparison is shown for CONF and 12CL models. Figure (4-16 (a)) shows the flow acceleration rate was slightly higher in CONF model until midway towards nozzle exit, and the peak turbulence intensity appeared to be ≅14% higher along centre body as shown in Fig. (4-16 (b)). Figure (4-16 (c)) shows the velocity profile inside the core stream down to the mixing area. A large velocity gradient can be seen for the confluent mixer right at the mixer exit plane. This could be attributed weak mixing effectiveness of CONF model and abrupt interaction of fan and core streams. The 12CL mixer on the other hand shows smoother variation in velocity along the mixing line as shown in Fig. (4-16(c)), but significantly higher turbulent intensity due to the creation of streamwise vortices compared to CONF model (Fig. 4-16 (d)).

4-3-2 Effect of heat transfer and bypass ratio

Set point (4) and (5) in table (4-2) are related to simulation of lobed mixers with heated core stream. Heating the core flow would directly change density and the bypass ratio as well as the interaction and entrainment between cold and hot turbulent eddies leading to thermal mixing phenomenon. Figure (4-17(a)) shows the snapshot of temperature contours that illustrates the development of turbulent thermal boundary layer in the mixing region inside the nozzle as well as the outer shear layer. The turbulent eddy structures look slightly different compared to isothermal cases suggesting that turbulence intensity could change along the shear layer. This could also result in different pattern for the sound radiation that will be discussed in the next section. Figure (4-17(b)) shows the temperature decay rate along the jet axis for the CONF and 12CL mixers as shown earlier in Fig. (3-13) for a single-stream jet. Looking at Fig. (4-17(b)) it can be seen that the lobed mixer exhibits faster temperature drop and hence the thermal energy transport up to $x \cong 4.5D_J$. This could be attributed to the strong lateral mixing due to introduction of streamwise vortices. For $x > 4.5D_J$, the CONF model shows stronger temperature drop as the thermal boundary layer further develops towards downstream. The lobed mixers caused smoother thermal energy distribution along lateral directions at downstream locations when $x \gtrsim 5D_J$. Such behaviour was also detected in previous studies such as the plume survey performed by (Mengle *et al.*, 2002) and the cross-stream PIV measurements by (Bridges and Wernet, 2004). Fig.(4-14(c)) shows the normalized streamwise velocity profile along the jet centreline. The normalization was performed using the peak outlet velocity to compare momentum variation and velocity decay rate as a result of the heat transfer. First, by comparing Fig. (4-17(c)) with (4-14(b)), the jet potential core becomes smaller for both the confluent and the 12CL mixer types by ≅ 21% when T_J/T_0 =1.7. This phenomenon has also been reported for simple turbulent jets (Lew *et al.*, 2010b; Bogey and Marsden, 2013) as well as classical experimental studies of hot jets (Viswanathan, 2004). According to the results obtained for simple jet in the previous chapter, the reduction in potential core length was about 24%. The energy loss caused by flow separation behind the centre body led to the velocity deficit visible in the starting region of the velocity profiles. The velocity decay rate observed for the CONF model turned out to be higher compared to the 12CL both at heated and isothermal conditions; however, by heating the core flow, the momentum loss was intensified in the CONF model compared to the 12CL. Looking at the turbulent kinetic energy intensity along the jet centreline in Fig. (4-17(d)), it is evident that peak TKE occurred at shorter distance from the nozzle exit compared to isothermal cases. The peak TKE was shifted to $x \cong 9.2D_J$ for 12CL and $x \cong 7.1D_J$ for the CONF model. The appearance of the second peak in TKE values, does not seem be based on any physical phenomenon; however, time-averaging of the RMS values along centreline has been found relatively unsmooth in all LBM simulations in this study as spatial-averaging are not performed over multiple voxels. As discussed in chapter 3, it was found that spatial-averaging could improve the smoothness, but could adversely affect the accuracy and led to RMS values that underpredicts the experimental data. While reduction in the peak distance was expected and was also seen in single-stream jet case in the previous chapter, it is interesting that the CONF and 12CL mixers would act differently in reducing the distance at which the peak TKE occurs. Comparing Fig. (4-17(d)) with Fig. (4-15(b)) one could identify that peak location for the CONF model was significantly moved upstream compared to that of 12CL, whereas in isothermal case, the peak location of TKE for the CONF model was located downstream of that of the 12CL model. The latter phenomenon confirms that turbulent transitions in lobed models are less sensitive to thermal effects compared to CONF model as a result of induced streamwise vortices and enhanced mixing effects.

4-3-3 Effect of scalloping on flow field

The scalloping effects were investigated by simulating the near-field turbulent flow and far-field acoustics on medially scalloped (20MH) and deeply scalloped (20DH) mixer models. The geometry of scalloped mixer is shown in Fig. (4-1) and important parameters are listed in Table (4-1). Results were fully covered in a parallel study reported by (Gong, 2013; Gong *et al.*, 2013; Habibi *et al.*, 2013b) and compared to the previous results obtained for 20UH and CONF mixers ; in summary, it was found that the 20MH mixer model underwent turbulent transition at 0.4 D_j downstream of the nozzle exit plane while 20UH and 20DH mixer models turned fully turbulent at around twice that distance ($0.79D_j$). This was characterized by TKE variation along the shear layer as well as convection of acoustic sources. Looking at potential core length, it was found when scalloping depth increased, the laminar core length decreased. The laminar length of 20DH was about 9.0% shorter than that of the 20UH mixer. Looking at mean vortical structures, the 20DH mixer produced smaller vortices compared to 20UH. Due to scalloped sides, the mixing distance for 20DH was greater than that for the 20UH and the partial mixing process starts earlier through the side walls. It was discussed in section 4-3-2 that high penetration depth of 20UH model diverted streamwise vortices away from the jet axis and towards nozzle inner walls. Looking at the migration pattern of streamwise vortices in scalloped models *i.e.* 20MH and 20DH, an opposite direction toward jet centreline was observed. This implies vortex formation and migration were highly affected by penetration and scalloping depths which worked together in forming turbulent structure of fully mixed jet.

Looking at mean spanwise velocity distribution, the scalloped models exhibited more uniform flow compared to the CONF. The 20DH mixer seemed to have a better mixed flow profile than 20MH or 20UH. Also, for scalloped models the high velocity gradient region was closer to the nozzle edges. With regards to mean velocity profile along the jet axis, the 20UH and 20MH mixers reached a peak value upstream of the confluent mixer, at almost the same distance. The 20DH mixer was distinct from the other two mixer models by exhibiting steady velocity increase from the nozzle exit to four diameters downstream. Changes in mean flow characteristics were also consistent with more recent RANS study by DaWei *et al.* (2015) in which they also found when the degree of scalloping increased, the mixing in the downstream regions of the lobe peaks and sidewalls were accelerated; however, the primary flow in centre needed a larger mixing length. When the position of scalloped lower edge kept invariant, the radial position of the accelerated mixing region of sidewalls did not change.

Finally, by looking at TKE behaviour in the near-field, the fully turbulent state was reached at around $0.2D_j$, and $0.5D_j$ downstream to the nozzle exit plane for 20MH, and 20DH mixers respectively. The increase in scalloping depth did not lead to a monotonic decrease in the downstream peak locations. The 20MH mixer flow transition occurred at shortest distance compared to other cases. Studying the near-field vortical structures in all three 20-lobed mixers, vortices formed at the mixer tips were migrated into the nozzle lip shear layer. The strengths of the vortices in the three mixers were different. It is reasonable to conclude that the 20MH model allowed vortex growth in a way to produce the strongest turbulent eddies close to the nozzle surface causing early transition in the shear layer.

4-3-4 Thrust and mixing effectiveness

The thrust values which are represented by the thrust coefficients (C_T) were calculated based on Eqns. (3.4) and (3.5). Thrust coefficient values for different test cases are summarized in Table (4-5). The mixing effectiveness can represent how well the core and bypass flows are mixed compared to the isentropic mixing are calculated according to Eqn. (4.14) to (4.18). Based on its definition, latter criterion is only plausible and defined for heated set points "4"and "5" in Table (4-2). It can be seen that the steady state thrust coefficient value for 12CL lobed mixers were greater than their confluent counterpart for both the cold and heated set points. The thrust coefficient of the 20UH, 20MH and 20DH were smaller than that for the confluent mixer as the pressure losses were greater due to the high penetration effects. Similar conclusions were made by Mengle *et al.* (2002) at higher Mach numbers. The net thrust of the heated set points was generally greater than for cold cases. This is mainly due to slight flow acceleration inside the nozzle as the core flow is heated, which affects the density and pressure field. Although the larger jet velocity tends to reduce the thrust coefficient, the larger thrust and the lower density yields larger thrust coefficient for the heated case. The net thrust values related 20-lobed scalloped and unscalopped mixers were almost equal and of the same order of magnitude. This may confirm that scalloping does not change the pressure loss and hence, the C_T values.

On the mixing side, effectiveness criterion proposed by Kuchar and Chamberlin (1980) can provide a comparison between actual and ideal, *i.e.* isentropic, mixing. Calculated values in table

(4-5) for the 12CL and CONF model shows that about 14% higher efficiency was achieved by using 12CL compared to the CONF. The step change in mixing effectiveness was expected between the CONF and lobed mixers due to absence of streamwise vortices; however, even small changes in lobe geometry may affect the mixing efficiency. For example, a new study shows that adding small spoilers at lobe peaks of an unscalopped mixer could increase mixing efficiency by 13% calculated at $0.75D_J$ downstream to the mixer (Sheng, 2017).

4-3-5 Far-field acoustic levels

The pressure field shown in Fig. (4-18) illustrates the sound propagation in the vicinity of the nozzle. The contours shown in Fig. (4-18) were obtained by calculating the acoustic pressure field such that $|p - p_{amb}| < 30Pa$. Quantitative results indicate a significant difference between the sound directivity of the lobed-shaped and confluent mixers. Bandpass filtering of the far-field pressure spectrum was performed to evaluate the effects of mixer shape on sound directivity in different frequency bands. The overall sound pressure levels (OASPL) were evaluated over the frequency range of 100 *Hz* to grid cut-off frequency (≅ 4.8 *kHz*). The maximum resolved frequency is limited to the smallest wavelength captured at the location of the FW-H surface. In our study, the maximum resolved Strouhal number was about four (≅ 4) in regions surrounding the FW-H surface. The frequency range for the calculation of OASPL was the same as NASA's experiments (Mengle *et al.*, 2002). As shown in Fig. (4-19), the OASPL for different non-scalloped models indicates that the lobed mixers effectively reduced the overall sound pressure level by about 3 *dB* comparing to the confluent mixer. The peak noise level occurred for the microphone located at the directional angle of 140^{o}. The OASPL directivity were consistent with NASA sound measurements performed for the 12CL, 20UH and confluent test cases (Mengle *et al.*, 2002) at higher Mach numbers. The value of 145^{o} was reported in the NASA report for the peak sound pressure level; however, the sound levels reported were greater due to the larger jet Mach numbers tested.

Figure (4-20 (a), (b) and (c)) show the band-filtered directivity of sound pressure levels for the three centre frequencies of 120 Hz, 1200 Hz and 4500 Hz respectively. For the cold test cases, Fig. (4-19) shows that the sound pressure levels obtained for the 12CL and 20UH model are markedly lower than for the confluent model in all directions. This confirms that lobed mixers reduced radiated noise at low frequencies. Noise reduction capability of lobed mixers at high frequencies becomes directional and decreases as frequency increases. The bandpass filtered SPL directivity at 120 *Hz*, shown in Fig. (4-20 (a)) indicates that the confluent mixer sound level was 4 *dB* greater than that of 20UH mixer at most of observer's angles, and about 5 *dB* louder than the 12CL mixer at a shallow angle of 160 degrees. All three mixers reached a peak level at 165-degree angle. This can be explained by the fact that the jet plume usually decays far downstream of the nozzle exit, and large eddies there govern the low frequency portion of the spectra. This trend is also consistent with those reported in previous experimental studies (Mengle *et al.*, 2002). The accuracy of low-frequency noise is affected by the simulation and acquisition time described in chapter 3. Figure (4-20(b)) shows the 1200 *Hz* SPL directivity for the three mixers. The confluent mixer was not the noisiest mixer in the mid-frequency range, as found in previous experiments. Instead, the 12CL mixer yielded the highest levels at most observer angles. At locations downstream of 140 degrees, both lobed mixers yielded higher SPL levels than the confluent mixer, as expected. The peak of the lobed mixers' SPL level appeared to be shifted with the variation of lobe number and penetration depth. The 12CL and 20UH mixer had a 3*dB* difference in terms of SPL peak value. The 20UH mixer remained quieter than 12CL. However, the advantage of 20UH over 12CL in suppressing mid-frequency noise was not as significant as in the low frequency portion of the spectra. The results indicate that the dominant contribution to the overall mid-frequency noise of lobed mixers was from emissions at downstream angles between 135 and 150 degrees. The SPL directivity comparison at 4500 *Hz* is shown in Fig. (4-20(c)), except at locations between 85 and 125 degree angles, the high frequency SPL level for the confluent mixer was mostly lower than for the 12CL and 20UH mixers. At positions downstream of the 140-degree angles, the 12CL mixer was quieter than 20UH, and a reduction of 4 *dB* at a 160-degree angle was obtained. The overall high frequency SPL trends of 12CL and 20UH were similar, and the magnitude was comparable. The 20UH mixer did not seem to produce a significant increase in high frequency sound pressure but did suppress low-to-mid frequency noise. Note that the peak SPL value for 12CL and 20UH was reached at 125 and 135 degrees respectively. In comparison with the SPL trends over the mid-frequency range, the peak angles were reached further upstream because high frequency noise is usually attributable to smaller eddies which predominate near the nozzle exit plane or even inside the nozzle, according to turbulent jet theory (Abramovich *et al.*, 1984). High frequency noise is more likely to originate from upstream locations (Tam *et al.*, 2008a).

The OASPL trends for the heated cases (4) and (5) in table (4-2) are plotted in Fig. (4-21). For the 12CL and CONF mixers; comparing the far-field sound pressure levels of heated set points in Fig. (4-21) with their isothermal counterparts in Fig. (4-19), it is concluded that the mixed jets with heated core flows were noisier than the isothermal counterparts. The peak OASPL values at the observer angle of 140^{o} were 3.0 dB and 4.5 dB higher than that seen for isothermal cases for 12CL and CONF respectively. This in part, could be attributed to flow acceleration inside the nozzle and greater peak velocity or acoustic Mach number at the nozzle exit plane and also due to generation of entropic sound sources as the thermal boundary layer grows along the shear layer between the fan and core flows. The latter phenomenon is discussed in multiple studies (Viswanathan, 2004; Lew *et al.*, 2007; Casalino *et al.*, 2014a). The directivity pattern looks similar to isothermal cases for both mixer models. The 1.5 dB difference between elevated OASPL in two mixer models could be due to the fact that the CONF model exhibits a suboptimal mixing in case of flow acceleration compared to the 12CL. This leads to less uniform velocity profile and greater overshoot as seen in Fig. (4-17).

Figure (4-22 (a), (b) and (c)) show the band-filtered pressure levels as for the results presented in the previous section for isothermal flows. Contrary to the isothermal mixing where the SPL values in two mixers were highly dominated by the low-frequency noise, it can be seen that SPL values of the heated CONF model exceeds that of 12CL over almost all frequency bands. In fact the contribution of mid and high frequency bands are even more significant than the lower bands compared to isothermal set points. The elevated high frequency sound could be related to less uniform flow and large velocity overshoots as argued in (Booher *et al.*, 1993; Bridges and Wernet, 2004).

The scalloping effects on far-field sound were fully covered in the parallel study by (Gong, 2013; Gong *et al.*, 2013; Habibi *et al.*, 2013b). In this document, some of the key aerodynamic and acoustic observations are mentioned. Fig. (4-23) shows the OASPL in the far-field for the Confluent and unscalopped 20UH with medium scalloped 20MH and deeply scalloped 20DH cases. Consistent with the experiment results(Mengle *et al.*, 2002), three lobed mixers had lower OASPL level than confluent mixer at the downstream shallow angles. 20DH had the lowest OASPL level at all directional angles, and a maximum noise reduction of around 4dB with comparison of the confluent model. The OASPL level of 20UH was smaller than that for the confluent and 20MH mixer at all angels. This implies that the increase of scalloping depth does not necessarily lead to noise reduction, and there seems to be an optimal value of scalloping depth where the largest reduction of noise level can be achieved due to scalloping effect. These results are qualitatively consistent with those reported in (Mengle *et al.*, 2002) for the high-Mach operating conditions.

Spectral results are summarized in Fig. (4-24 (a), (b) and (c)). Fig. (4-24(a)), shows the directivity of the band filtered SPL at low-frequency, 120 Hz; it can be seen that all four mixers reached a maximum level at very shallow angles greater than 160^o. Such trend was consistent with previous experimental results (Mengle *et al.*, 2002) and may be explained by the ability of lobed mixers to break large scale vortices into smaller scale eddies and suppressing the low frequency noise. The 20UH mixer yielded a lowest SPL level compared to all scalloped mixers at most angular locations and ~4dB quieter than CONF at all angles. The 20MH yielded acoustic levels as high as the CONF for θ >145^o and almost followed similar trend of the CONF mixer at smaller angles. According to experimental results, such low-frequency impaired performance was expected and could be related to abrupt side mixing and flow separation along the scalloping edge. The 20DH mixer was performing better at low-frequency bands. Almost 2 dB reduction was achieved by 20DH mixer compared to CONF.

Fig. (4-24(b)) shows the 1200 Hz band-filtered directivity. Consistent with the experimental results (Mengle *et al.*, 2002), the confluent mixer demonstrated lower SPL at mid-frequency band compared to scalloped models. 20MH had the highest SPL level among the four cases at θ <115^o. 20MH on the other hand yielded the lowest SPL at θ > 135 degrees. At 45^o < θ < 90^o ,the 20DH mixer exhibits higher mid-frequency level compared to confluent and 20UH. Looking at Aerodynamics results (Gong, 2013; Gong *et al.*, 2013), the 20MH mixer showed the highest peak value in turbulent kinetic energy profile along the nozzle lip. Also 20MH demonstrated the TKE concentration region closest to the nozzle exit. In multiple jet noise studies, it was shown that TKE in the shear layer could play an important role in characterizing the noise at mid-to-high frequency bands. quadrupole sources emitting mid-to-high frequency waves are mainly generated and advected downstream to nozzle exit plane as argued by Tam *et al.* (2008b) 20MH was producing higher mid-frequency sound levels at 45^o < θ < 125^o as result of proximity of sources with high turbulent energy levels. At shallow angles, maximum noise levels occurred at different locations for scalloped lobed mixers: The noise level peaked at 140°, 120°, and 150° for the 20DH, 20MH and 20UH respectively. Directivity comparison at high-frequency band of 4500 Hz is shown in Fig. (4-24(c)). For $\theta < 125$ 125°, 20MH shows the highest SPL levels, while at $\theta > 125$, the 20UH mixer produced the highest levels compared to other models; also 20MH and 20DH mixers performed almost the same in terms of both sound levels and spectral behaviour. For $85^o < \theta < 125^o$ the scalloping depth appeared the major contributor where the lowest level was achieved by 20DH. Looking at both low-frequency and high-frequency bands, it appears that scalloping was able to decrease the noise in the high-frequency bands slightly by sacrificing the performance at low-frequency bands. The 20DH, 20MH, and 20UH mixers peaked at 120°, 115°, and 135° respectively.

4-4 Chapter highlights and main learning points

For the first time, A transient simulation in combination with the sub-grid scale turbulence modelling and hybrid thermal model were utilized to study the flow and far-field sound of dual-stream nozzles with forced mixer; however, current LBM simulations were restricted to Mach number values not greater than 0.5.

The use of lobed mixers in comparison to confluent mixers showed several advantages such as mixing enhancement, thrust improvement and noise reduction. Moreover, lobed mixers decreased low frequency noise level in almost all directions and increased high frequency sound pressure level in specific directions compared to the CONF model.

Looking at the combined effect of the lobe number and penetration depth, it was found that increasing the penetration depth and lobe number can be interpreted as extending the mixing surface and hence; enhances the mixing process between the core and the bypass flows. As it was evident in Fig. (4-7(a)) this tends to decrease the length scale of the streamwise vortices which in part, contributed to the frequency shift in the far-field sound power spectra. As the lobe number and penetration depth increase, it was found that vorticity density in the mixing area downstream of the lobes also increase leading to more azimuthal interaction of vortices in expense of loss in turbulent energy and entropy generation. It was observed that such vorticity distribution could affect the mid-frequency content of far-field spectra as shown in Fig. (4-14(b)) for 12CL and 20UH. The band filtered SPL of 20UH mixer was lower than that of 12CL.

Some far-field characteristics could be attributed to the higher penetration depth. The 20-lobe mixer, 20UH, was able to reduce the low frequency content of the spectrum that could be investigated by plume survey in the outer regions into the jet plume. Lobe penetration contributes to the radial advection of the streamwise vortices. Such radial advection governs the flow-field and vorticity dynamics close to the nozzle wall.

For heated set points, the peak OASPL values were higher than that seen for isothermal cases for 12CL and CONF. This in part, could be attributed to flow acceleration inside the nozzle and greater peak velocity or acoustic Mach number at the nozzle exit plane and also due to generation of entropic sound sources as the thermal boundary layer grows along the shear layer between the fan and core flows. Contrary to the isothermal mixing where the SPL values in two mixers were highly dominated by the low-frequency noise the contribution of mid and high frequency bands are much more significant than the lower bands compared to isothermal set points.

In order to investigate the effects of scalloping, three mixers with the same lobe counts, 20UH, 20MH and 20DH mixers along with CONF were simulated and compared. The medium scalloped mixer showed the shortest transition distance to a fully turbulent state as well as greatest TKE decay rate compared to other mixers. Results also suggested that there might exist a critical scalloping value that determines whether the mixer could yield noise reduction. Such behaviour is due to the differences in length scales and energy level of the streamwise vortices affected by the lateral leakage through scalloped sidewalls

An important result about the trust values was the fact that the 20UH model was associated with more momentum losses leading to the decrease in thrust magnitude but the scalloping did not cause additional momentum loss compared to 20UH.

As for the simple double-stream jet flow, as argued by Fisher et al. (1993), there appears to be at least two dominant regions in spectral contents of the lobed mixers. First is the low-frequency peak is governed by the fully mixed region far downstream of the nozzle and second is the mid-to-high frequency peak governed by the shear layer between the ambient flow and the partially mixed bypass and core flows close to nozzle exit plane. The lobed mixer geometry may change the mixing process and used beneficially to control either frequency ranges.

Table 4-1 Geometric parameters of nozzle-mixer configuration

Description	Mixer ID	Penetration factor H_m/H_{mp}	Mixing Length L/D_{mp}	Area Ratio A_f/A_c	Scalloping Depth L_S/H_m
Confluent	CONF	N/A	1.10	2.34	N/A
12 lobes	12CL	0.41	1.10	2.34	0.00
20 lobes with non-scalloped	20UH	0.48	1.10	2.34	0.00
20 lobe Medium scalloped	20MH	0.48	1.10	2.34	0.40
20 lobe Deeply scalloped	20DH	0.48	1.10	2.34	0.69

Table 4-2 Operating condition for cold and heated core flow setpoints for LBM simulation

Setpoint	M_a	*NPR_F	†NPR_C	‡NTR	**BPR	Attributes
1	0.45	1.22	1.18	1.01	3.0	Cold – CONF
2	0.45	1.22	1.18	1.01	3.0	Cold – 12CL
3	0.45	1.22	1.18	1.01	3.0	Cold – 20UH
4	0.50	1.22	1.18	1.68	5.0	Heated – CONF
5	0.50	1.22	1.18	1.68	5.0	Heated – 12CL
6	0.45	1.22	1.18	1.01	3.0	Cold – 20MH
7	0.45	1.22	1.18	1.01	3.0	Cold – 20DH

* Net total pressure ratio (P_{Tf}/P_a) for fan stream;
† Net total pressure ratio (P_{Tc}/P_a) for core stream;
‡ Net total temperature ratio (T_{Tc}/T_{Tf}).
** Bypass Ratio (BPR)

Table 4-3 Nozzle inlet flow condition for cold and heated cases

Inlet parameter	**Bypass (fan) Stream**	**Core Stream (cold)**	**Core Stream (heated)**
$\dot{m}$ (kg/s)	3.45	1.15	0.68
ρ(kg/m^3)	1.39	1.34	0.79
M	0.24	0.19	0.17
$\bar{u}$ (m/s)	83.67	67.32	67.32
T (K)	300.0	303.7	510.2
p^s (Pa)	119,259	117,017	117,017

Table 4-4 Computational parameters, LBM-VLES scheme for internal mixing nozzles

Model	VRs	Δr (mm)	FEV(×10^6)	FES(×10^6)	t_t (sec)	t_a (sec)	CPUh(×10^3)
12CL/CONF	9	0.370	78.0	3.56	0.22	0.34	57
20UH/20MH/20DH	9	0.370	86.0	3.82	0.26	0.34	60

Table 4-5 Mean thrust coefficients for different set points

Mixer Model	Temperature Ratio (T/T_∞)	Mach number	Thrust coefficient	Mixing effectiveness
CONF	1.00	0.45	1.95	N/A
12CL	1.00	0.45	1.97	N/A
20UH	1.00	0.45	1.94	N/A
CONF	1.70	0.48	2.16	0.78
12CL	1.70	0.48	2.19	0.89
20MH	1.00	0.45	1.94	N/A
20DH	1.00	0.45	1.93	N/A

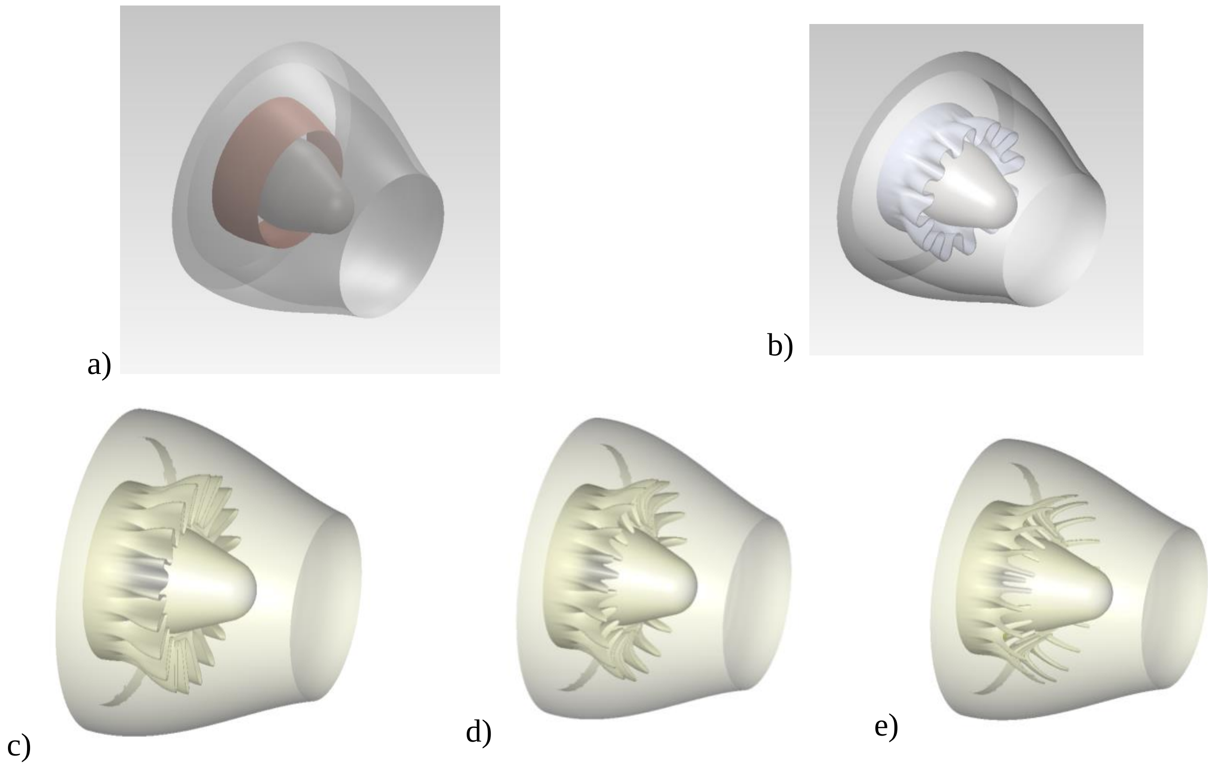

Fig. 4-1 Dual-stream mixing nozzles, a) Confluent b) 12CL, c) 20UH, d) 20MH and e) 20DH

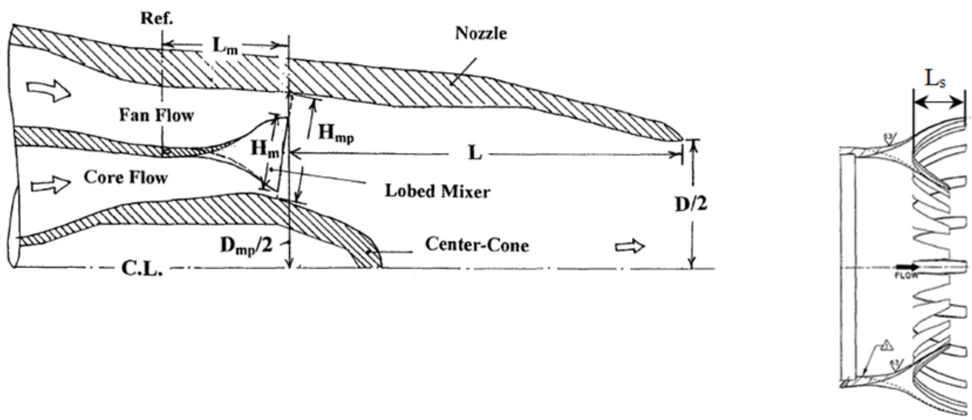

Fig. 4-2 Nozzle-Mixer characteristic Lengths (Mengle *et al.*, 2002)

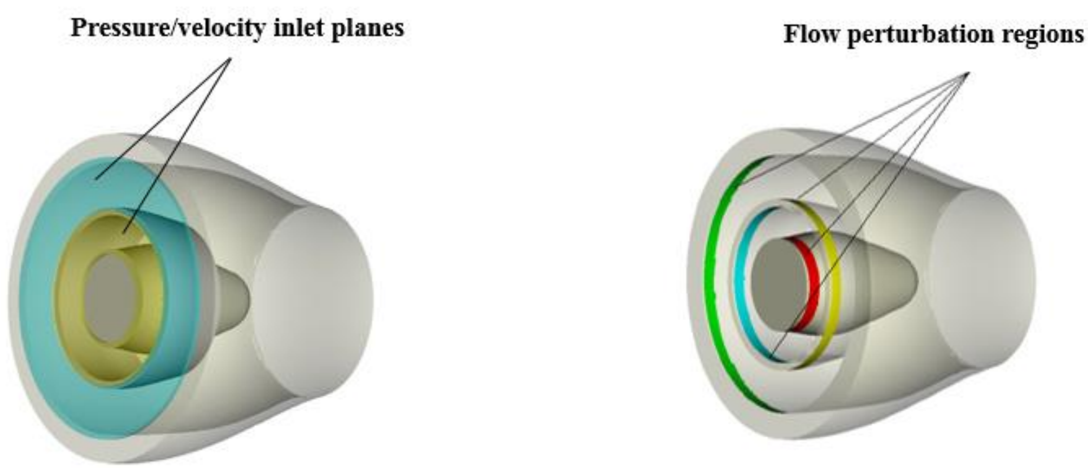

Fig. 4-3 (a) Nozzle inlet planes (b) Artificial forcing surfaces (Length≅0.1D_J)

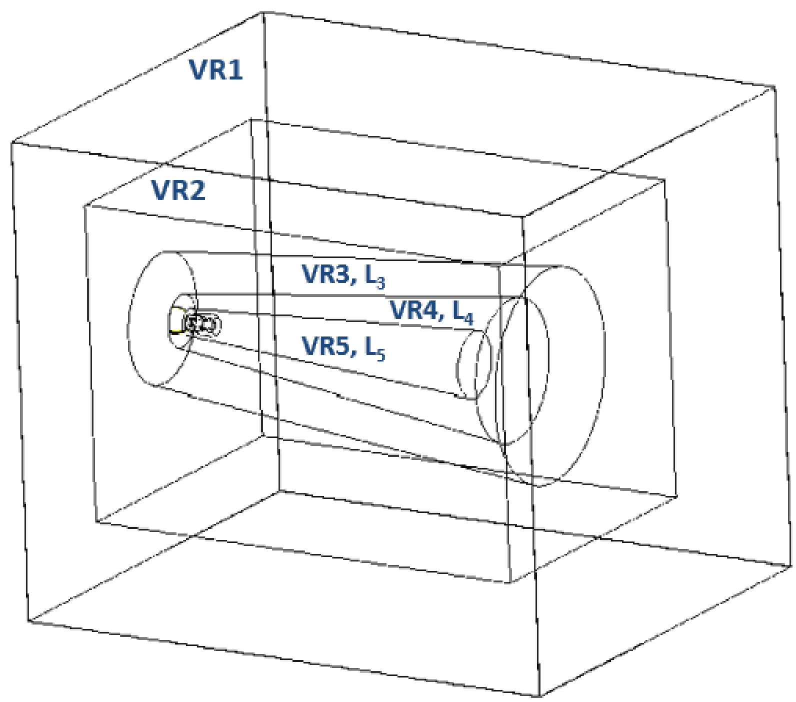

(a)

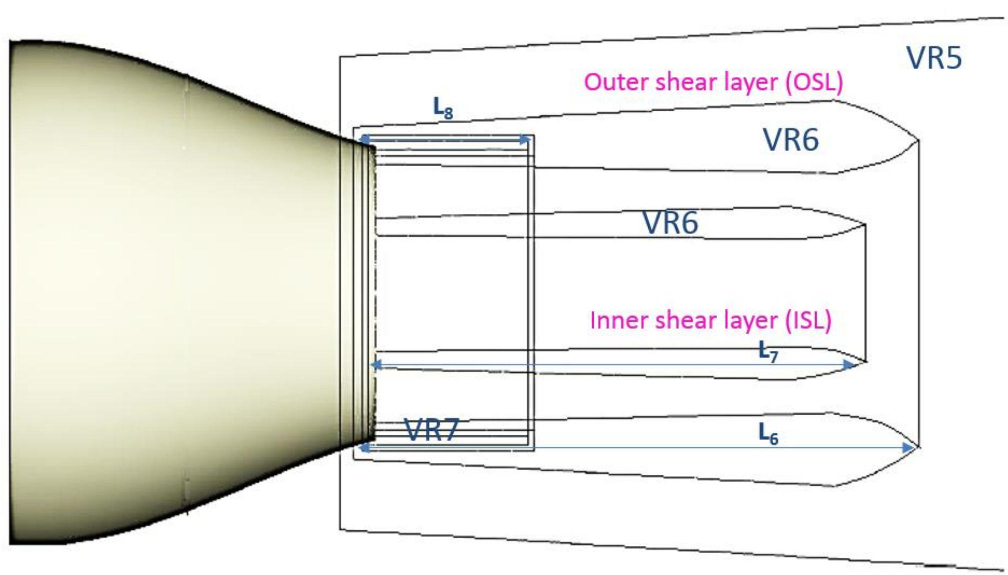

(b)

Fig. 4-4 Variable resolution region in near field (a) VR1-V5, (b) VR5-VR7 (shear Layer)

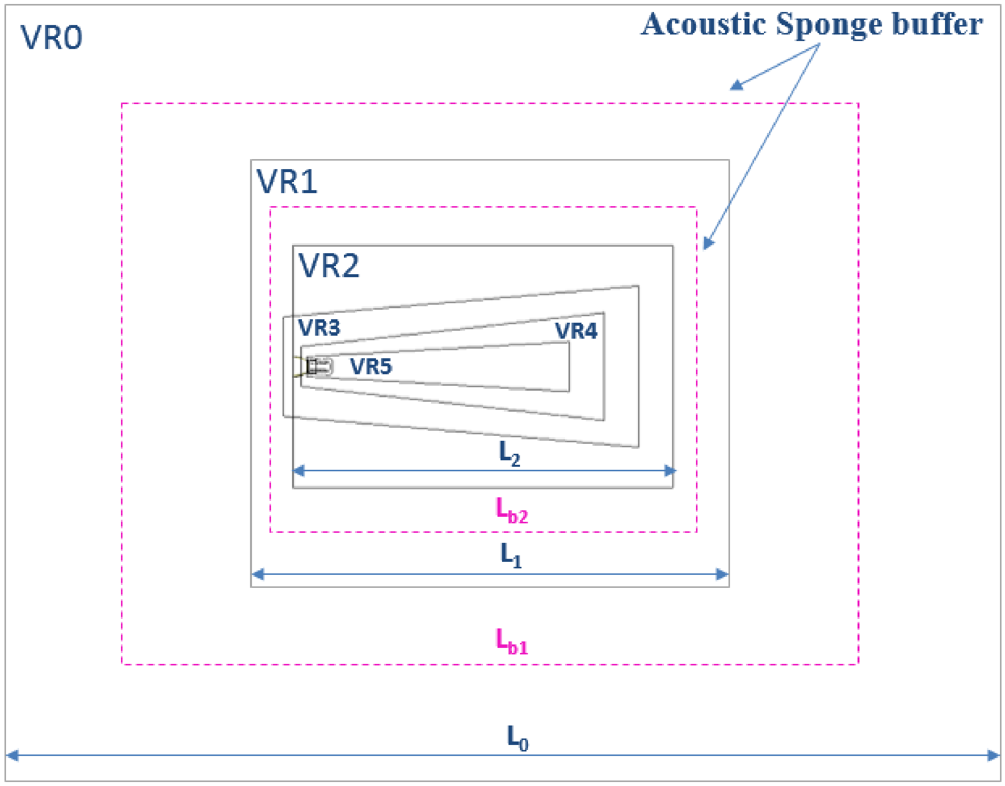

Streamwise dimensions

L_0/D	L_1/D	L_2/D	L_3/D	L_4/D	L_5/D	L_6/D	L_7/D	L_8/D	L_{b1}/D	L_{b2}/D
75.0	37.0	30.0	27.0	23.0	20.0	2.0	1.7	0.5	57.0	33.0

Rectangular regions (y/L, z/L)

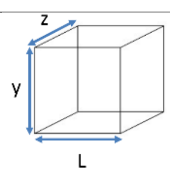	*VR0*	*VR1*	*VR2*	*Buffer_1*	*Buffer_2*
	(0.8,0.8)	(0.9,0.9)	(0.7,0.7)	(0.8,0.8)	(0.7,0.7)

Conical and circular regions (r_1/D, r_2/D)

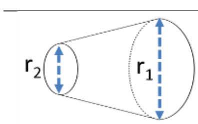	*VR3*	*VR4*	*VR5*	*VR6 (ISL)*	*VR6 (OSL)*	*VR7*
	(13.5, 5.5)	(6.5, 2.5)	(3.0,1.6)	(0.6,0.5)	(1.3,1.0)	(1.0,1.0)

Fig. 4-5 VR distribution and sponge buffers in the computational domain

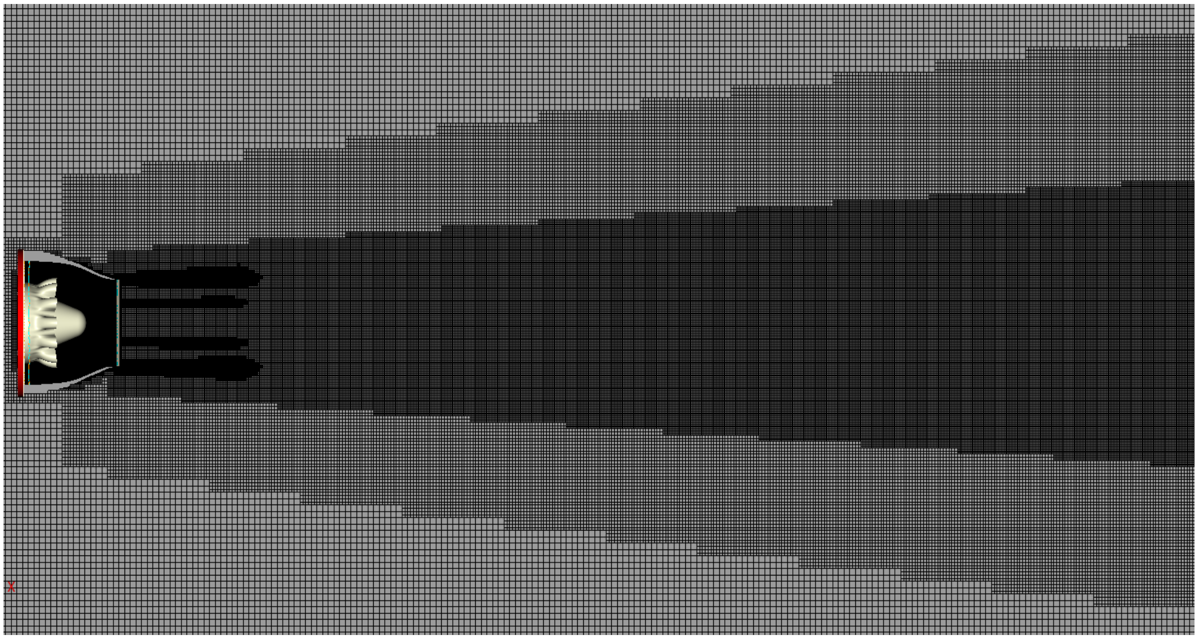

(a)

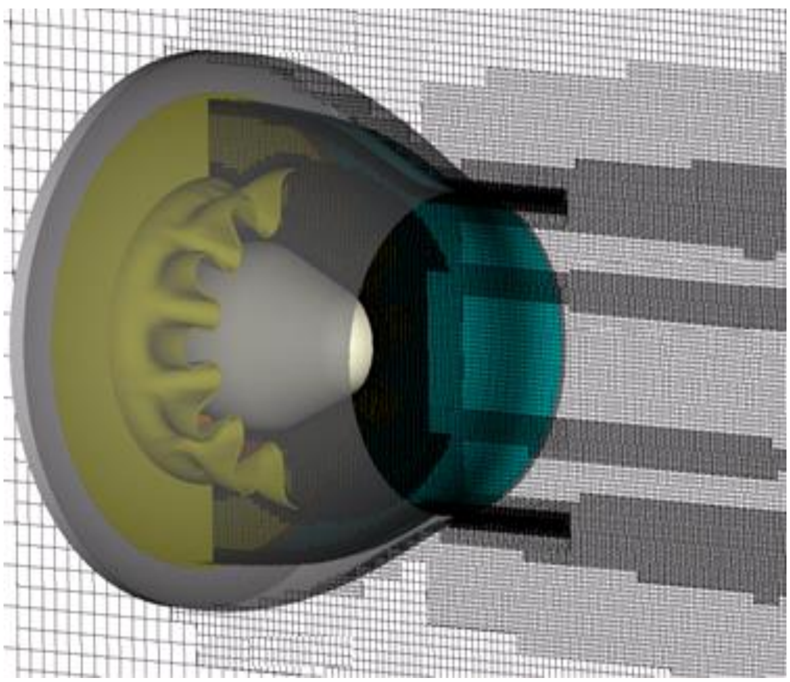

(b)

Fig. 4-6 12CL mixer, VR distribution (a) Near-field (b) inside the nozzle

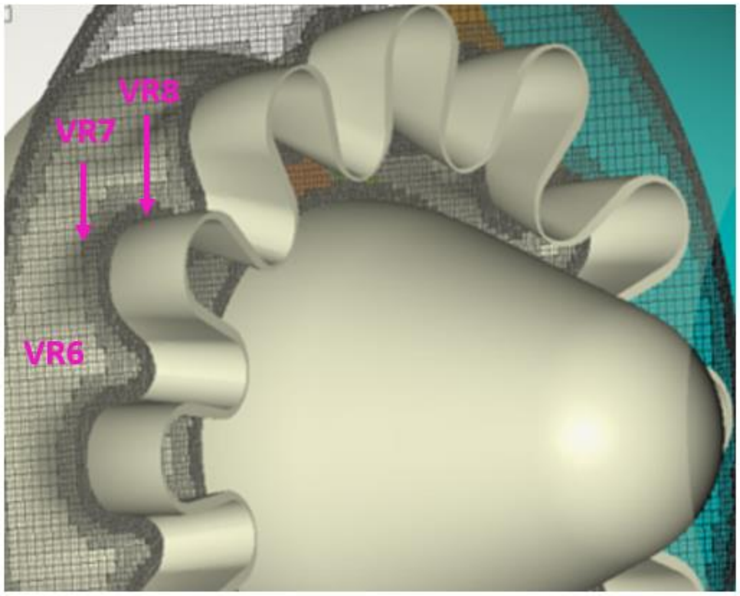

(a)

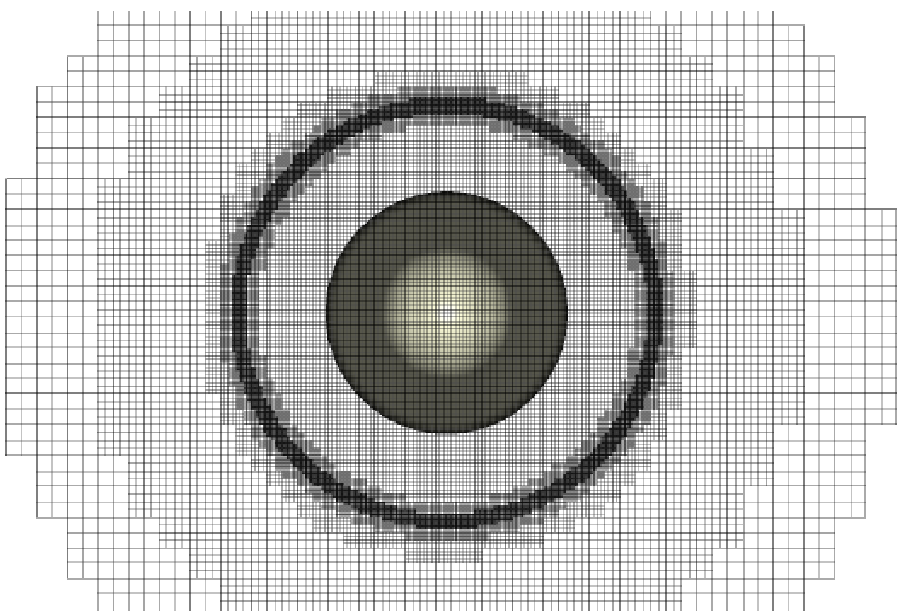

(b)

Fig. 4-7 12CL mixer, Lateral view (a) VR8 &VR9 in the mixing region and at the boundary layer around the mixer (b) VR distribution at the tip of the nozzle.

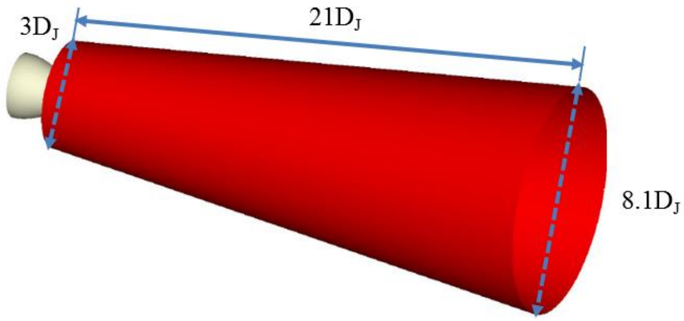

(a)

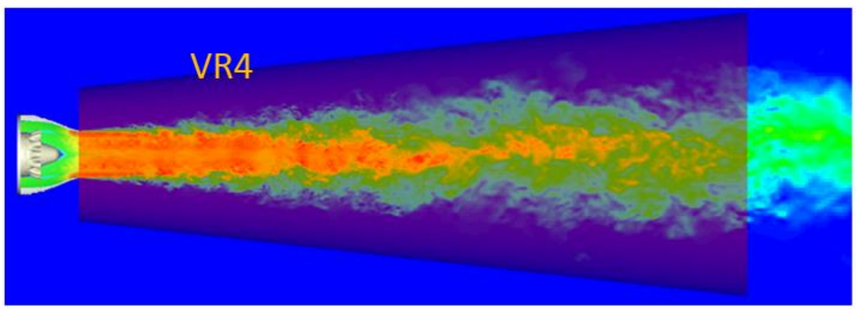

(b)

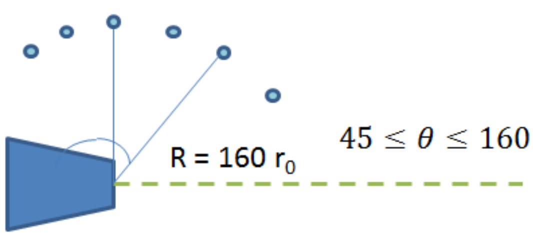

(c)

Fig. 4-8 Location of Porous FW-H surface in the computational domain. and microphone distribution over the aft polar angles.

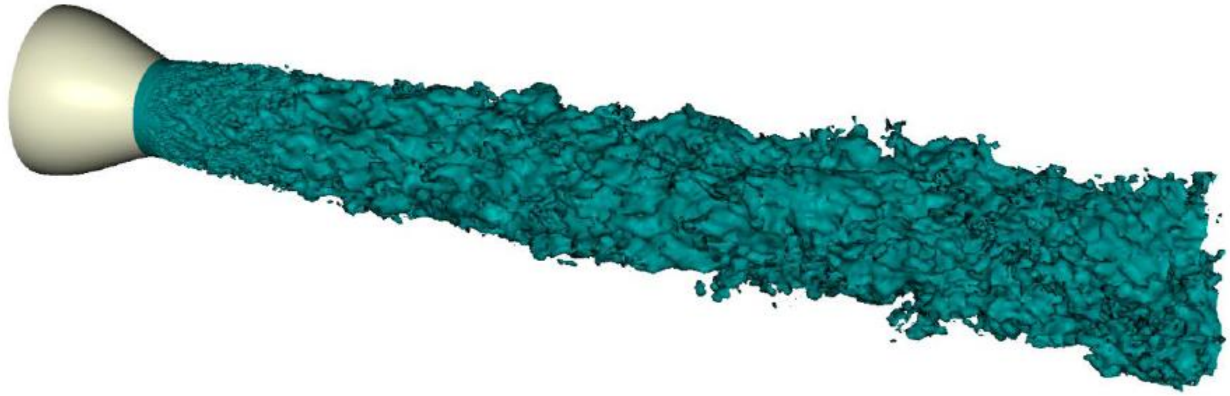

(a)

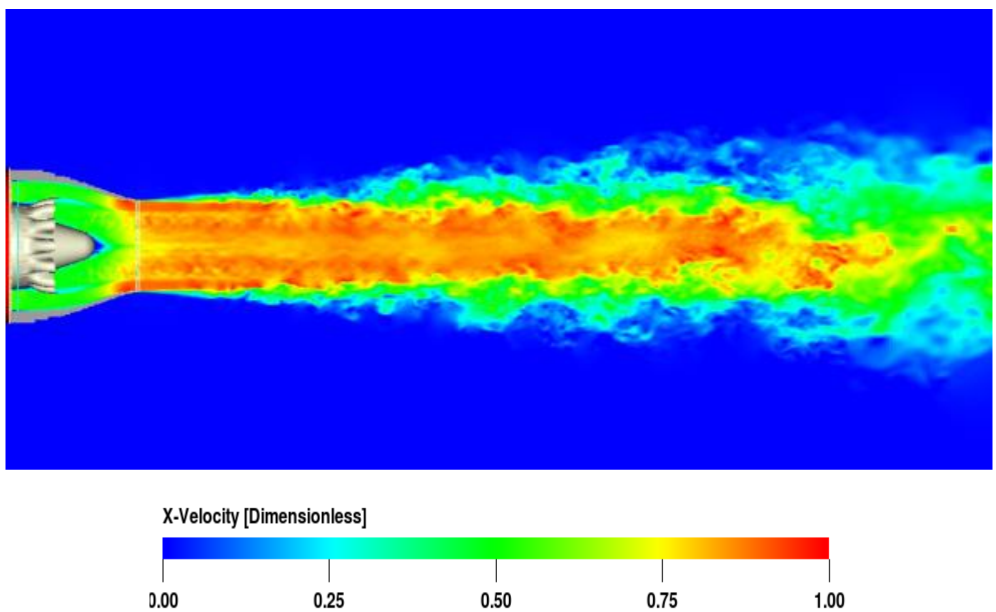

(b)

Fig. 4-9 Development of turbulent shear layer for 12CL mixer model , (a) x-Velocity iso-surface(u = 80 m/s) (b) normalized instantaneous streamwise velocity contour

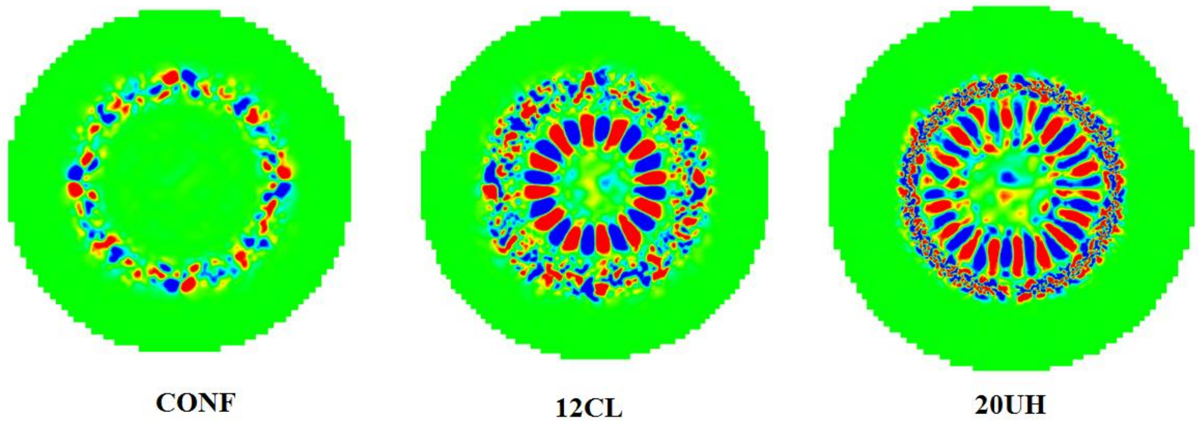

(a)

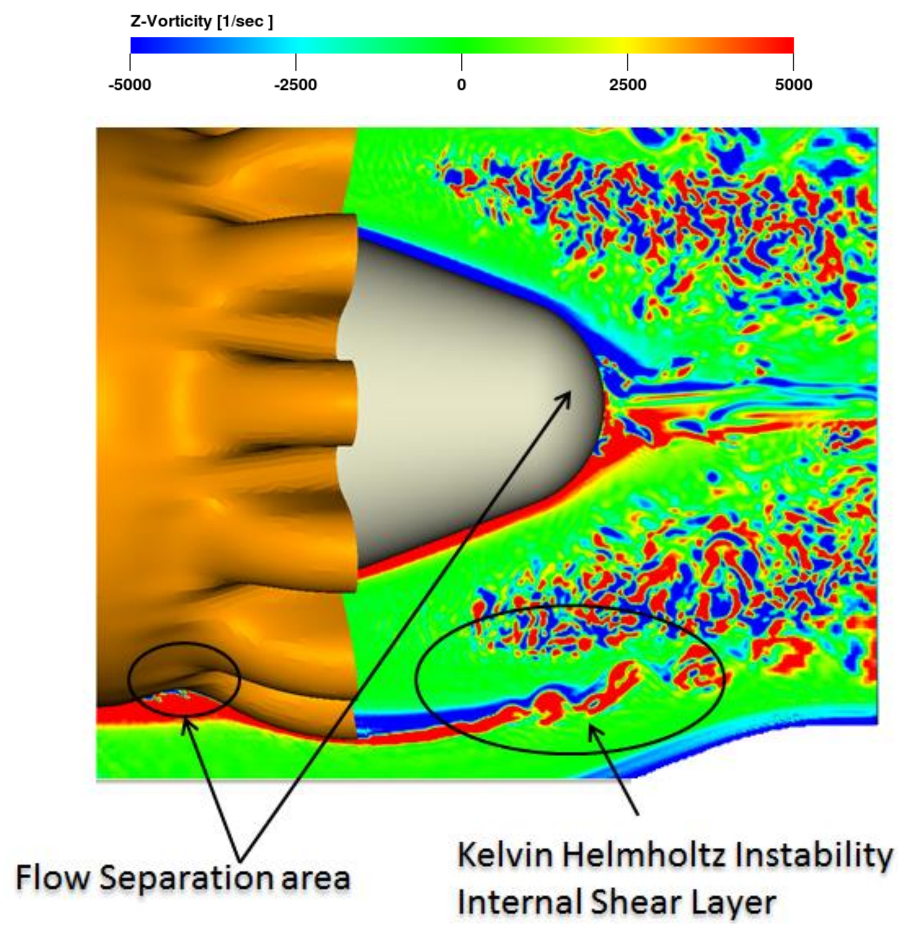

(b)

Fig. 4-10 Snapshot of vorticity contours (a) formation of streamwise vortices at 0.1D_J downstream of the mixing plane (spanwise view) (b) mixing region, and flow separation area

(a) CONF

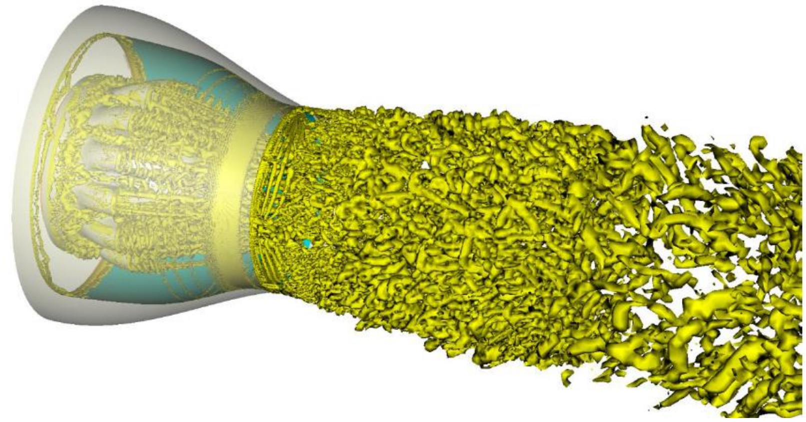

(b) 12CL

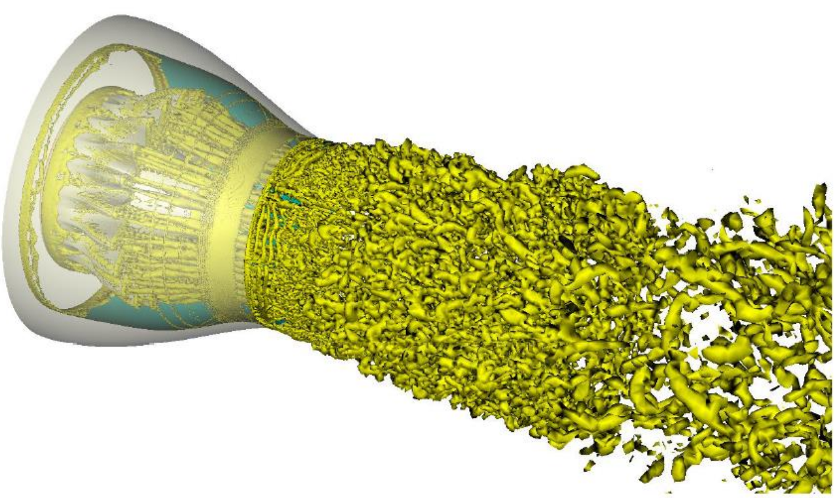

(c) 20UH

Fig. 4-11 Lambda 2 criterion iso-surface for the three mixers. (a): confluent mixer; (b): 12CL; (c): 20UH. (iso-surface value = -100)

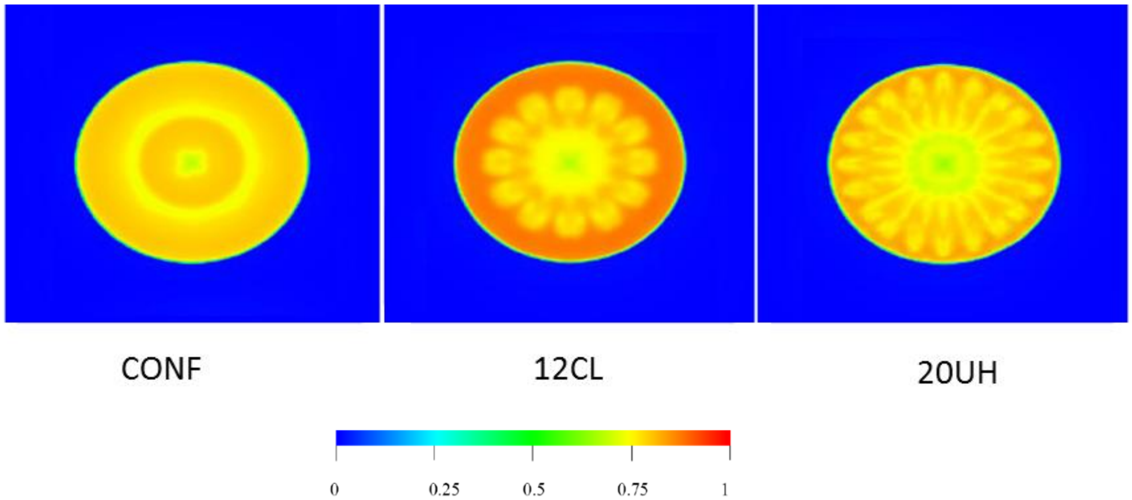

(a)

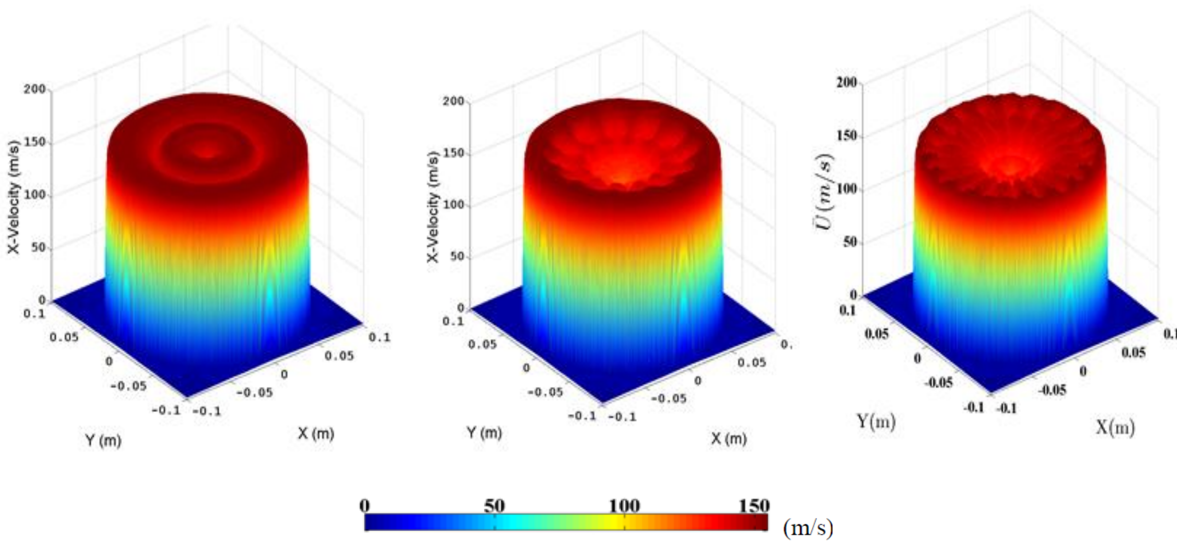

(b)

Fig. 4-12 Mean streamwise velocity (a) circular cross-section velocity contours at nozzle exit plate (*x* =0) (b) 3D velocity contours at nozzle exit plate (*x* =0)

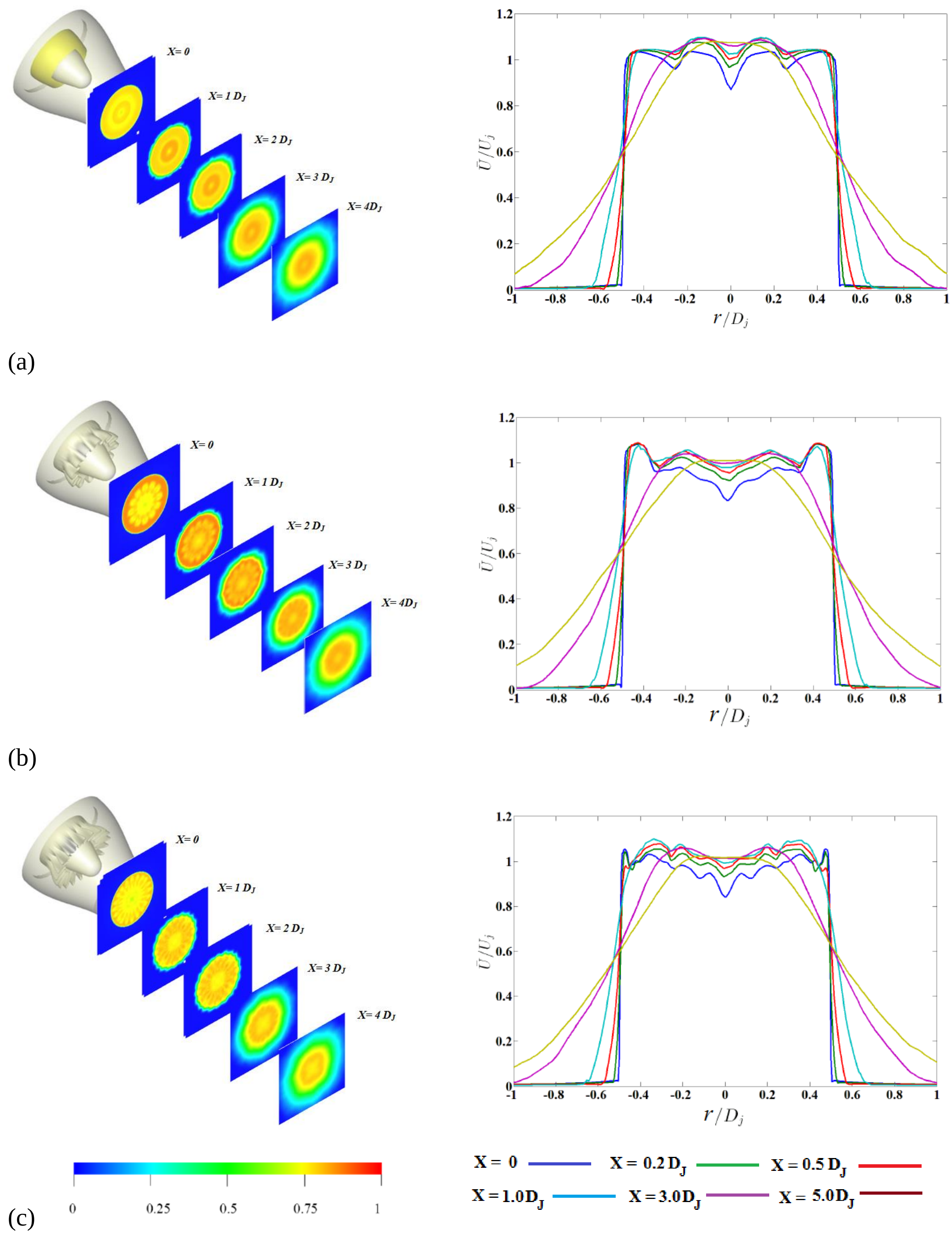

Fig. 4-13 Spanwise mean velocity contours and 2D profile at different streamwise locations , (a) CONF mixer , (b) 12CL mixer, and (c) 20UH

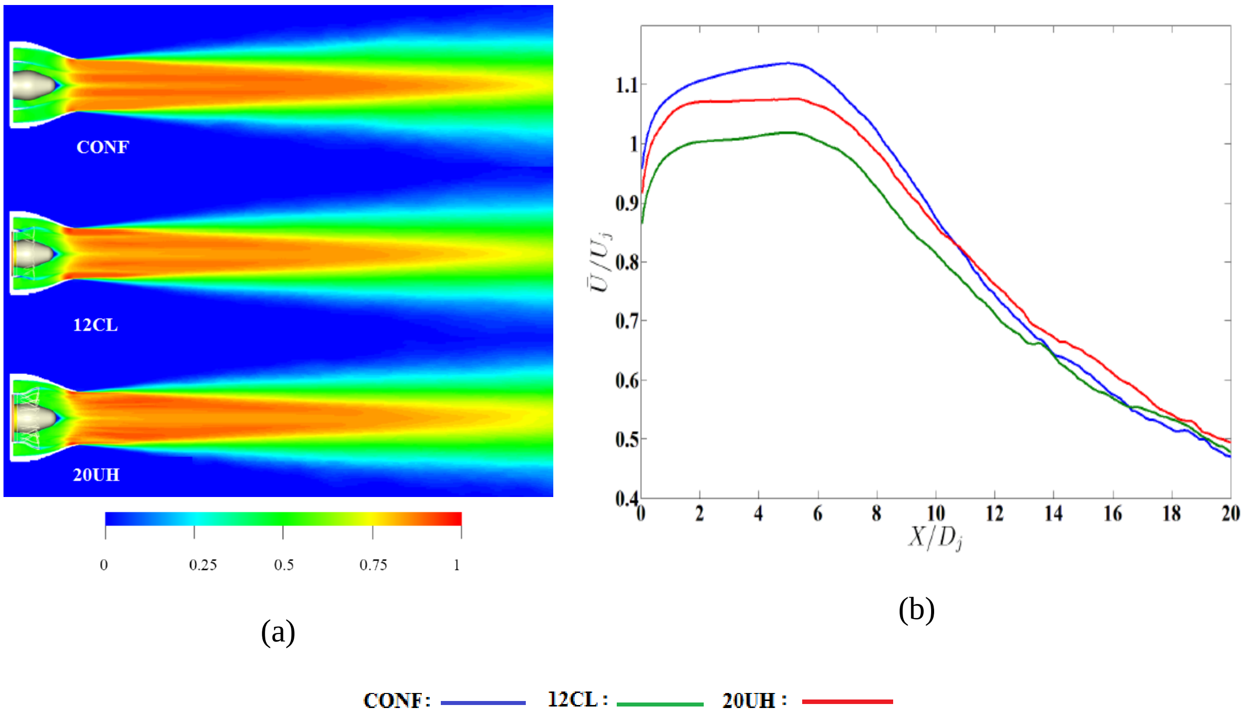

Fig. 4-14 Mean streamwise velocity (a) velocity contours in the near-field for three mixer models (b) normalized streamwise velocity profile towards downstream for the CONF, 12CL, and 20 UH mixer models.

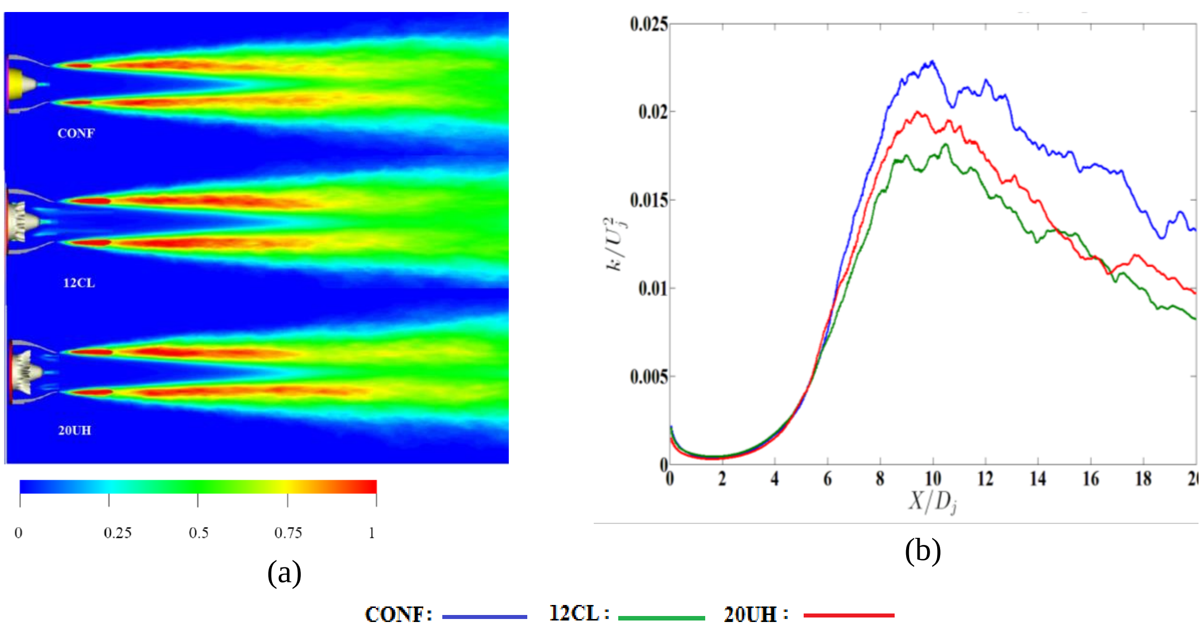

Fig. 4-15 Mean turbulent kinetic energy (TKE) (a) 2D contours in the near field (b) normalized TKE profile along jet centreline for the CONF, 12CL, and 20 UH mixer models.

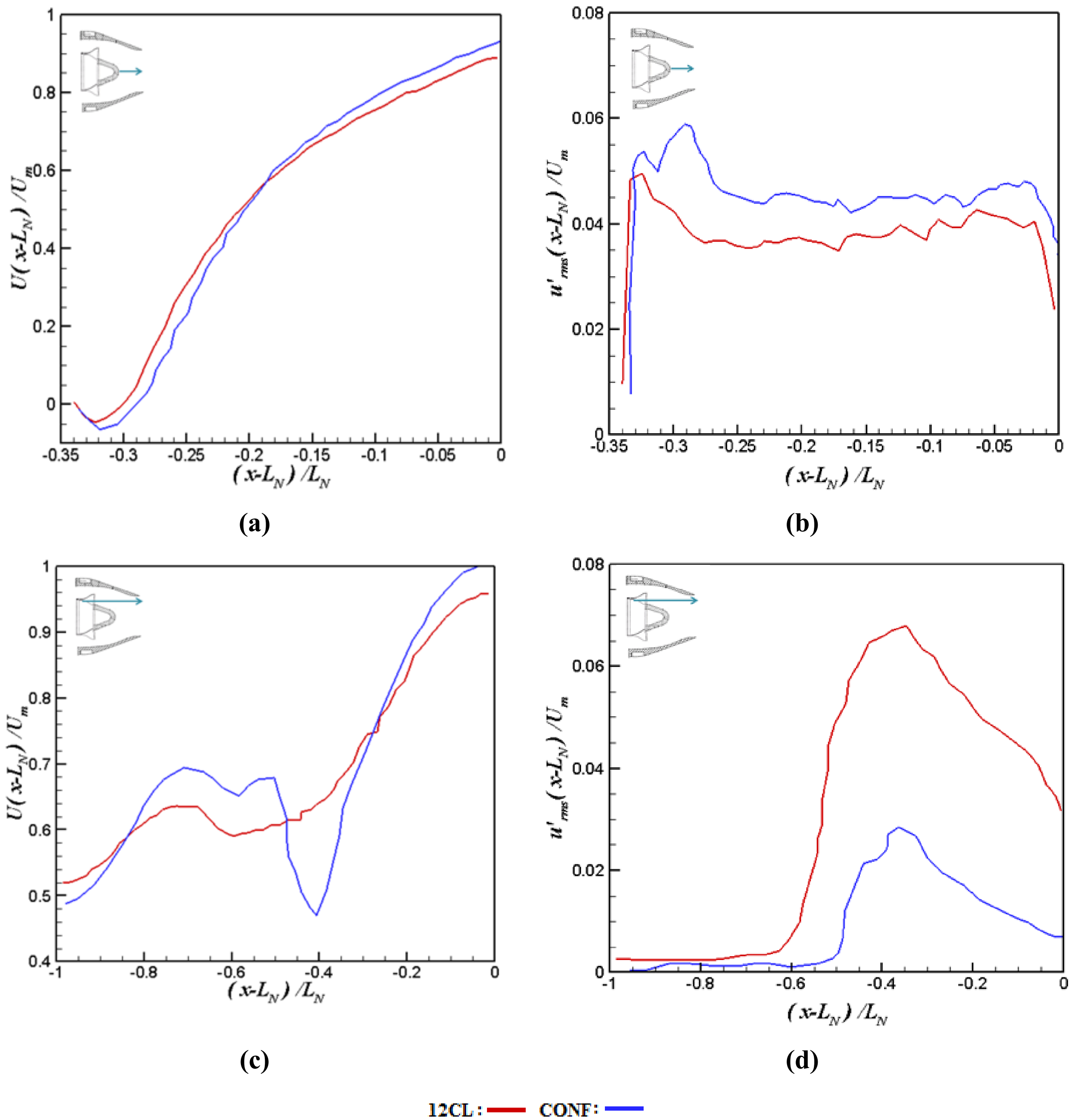

Fig. 4-16 (a) internal velocity profile from centre body towards outlet, (b) internal RMS velocity profile from centre body towards outlet (c) internal velocity profile from core inlet towards outlet, (d) internal RMS velocity profile from core inlet towards outlet

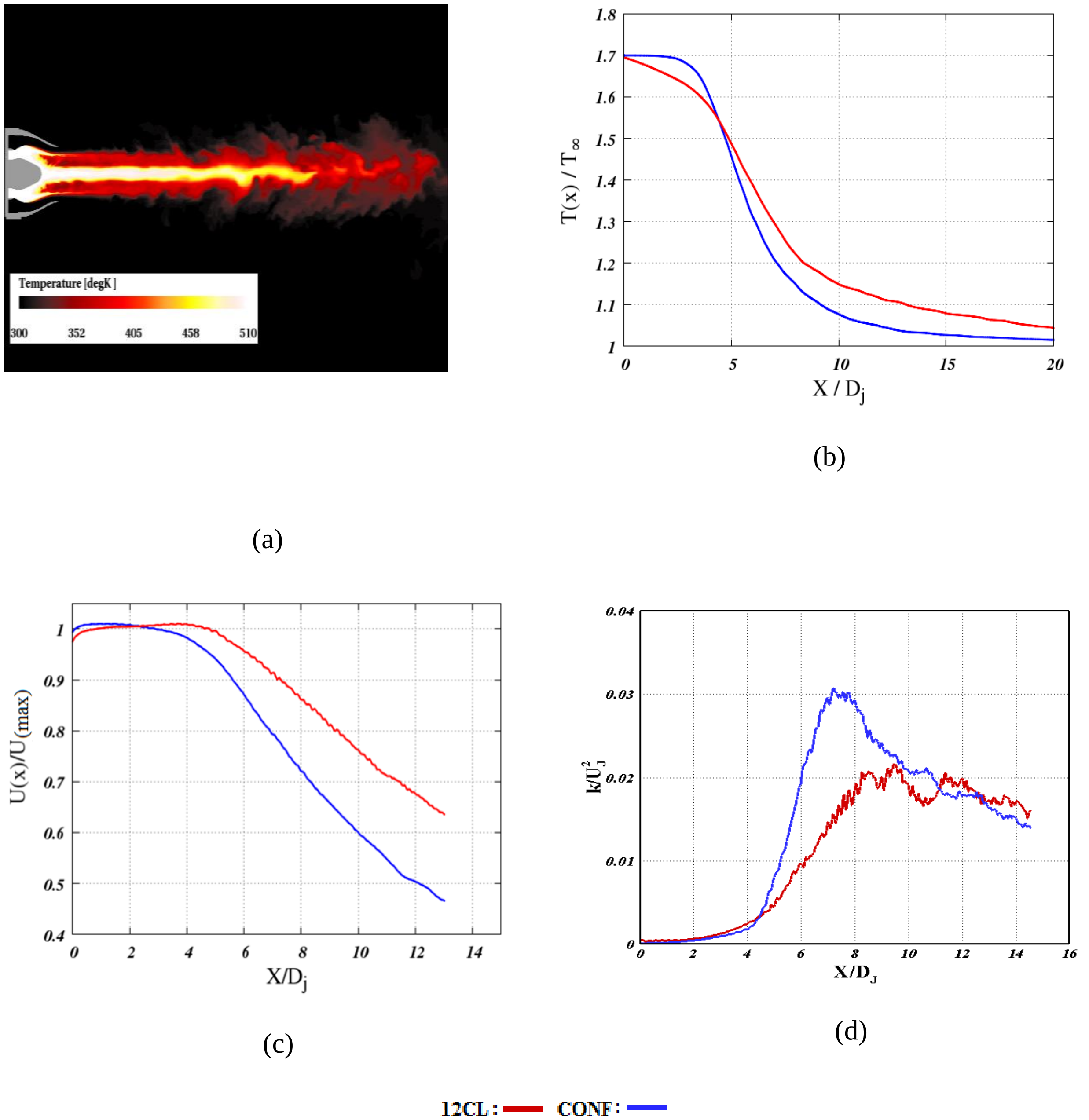

Fig. 4-17 (a) instantaneous temperature contour for 12CL mixer, (b) temperature decay rate along the centreline (c) streamwise velocity profile along the jet centreline, (d) TKE along the jet centreline.

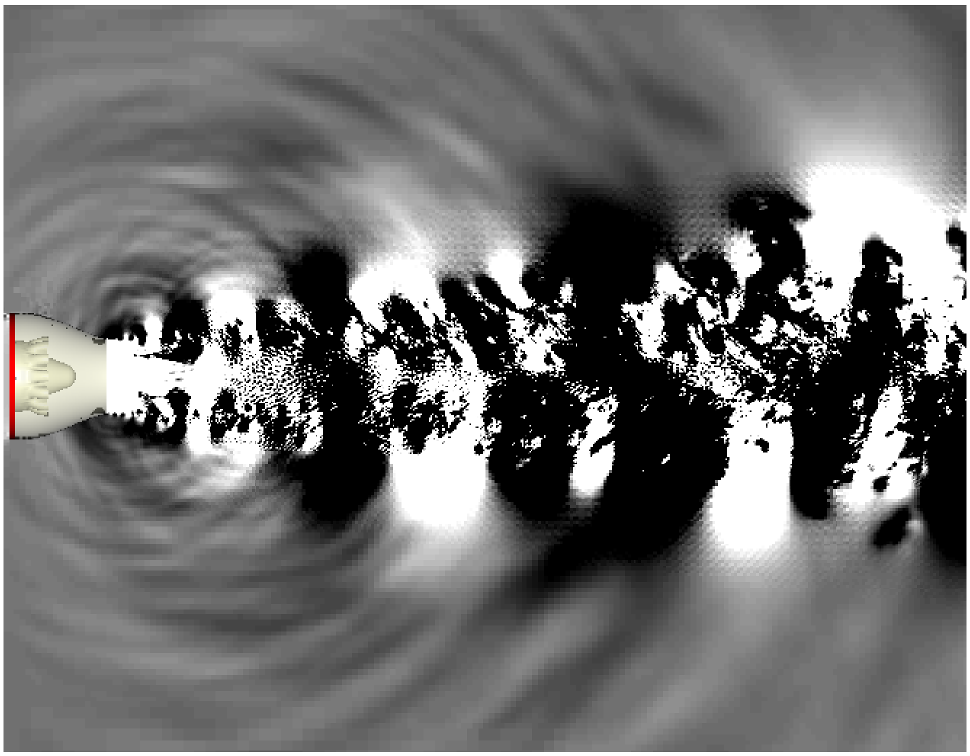

Fig. 4-18 Pressure field near the nozzle outlet grayscale colormap for the range of $|p - p_\infty| < 30Pa$.

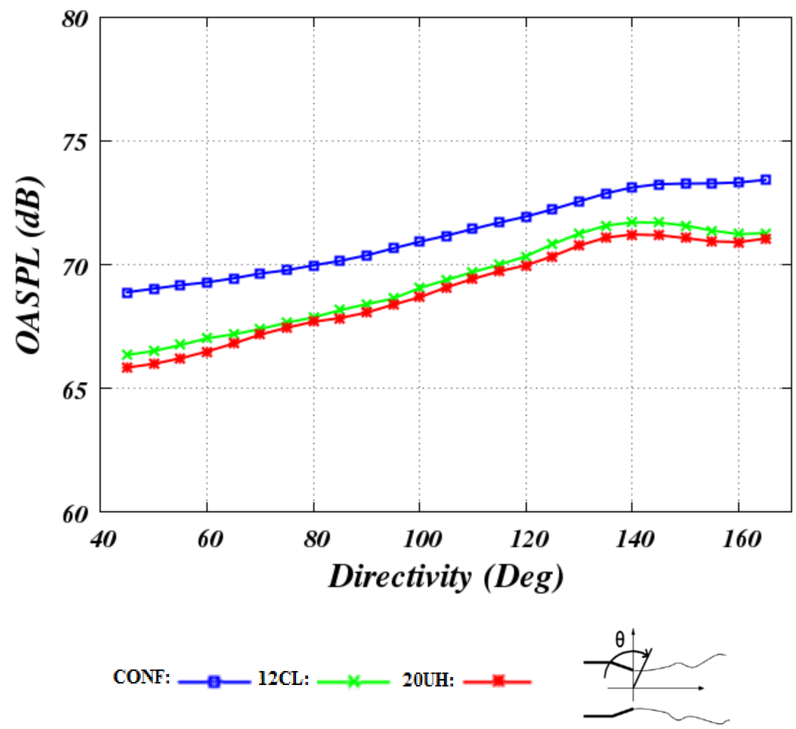

Fig. 4-19 of overall sound pressure level Directivity at $r = 160\ r_0$

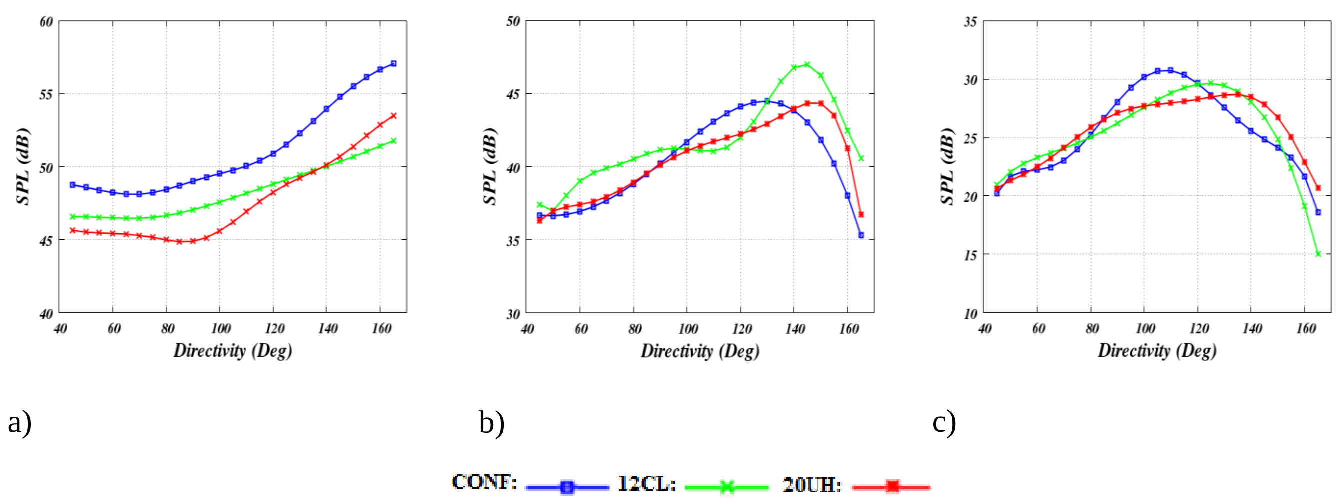

Fig. 4-20 Band Passed filtered directivity pattern of pressure levels a) 120 *Hz* b) 1200Hz c) 4500 Hz.

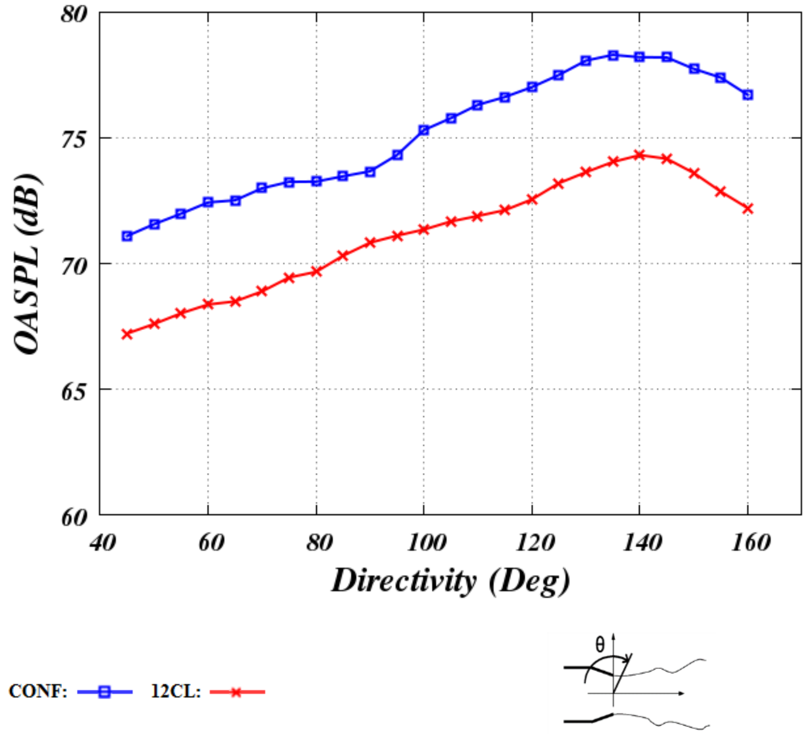

Fig. 4-21 Overall sound pressure level Directivity at r = 160 r_0, for the heated test case.

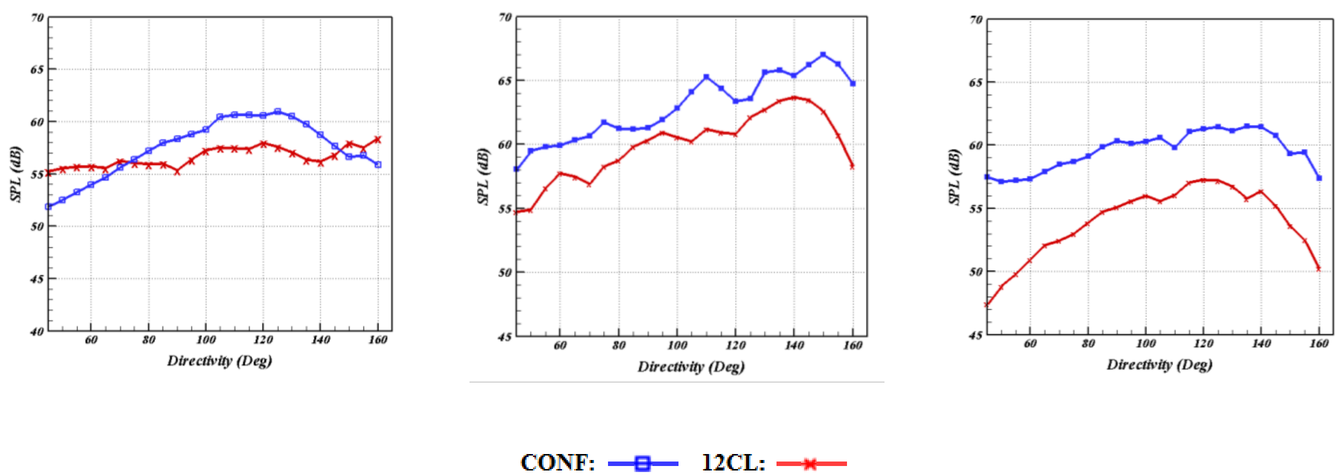

Fig. 4-22 Band Passed filtered directivity pattern of acoustic pressures at (a) 120 *Hz* b) 1200*Hz* c) 4500 Hz, for the heated case.

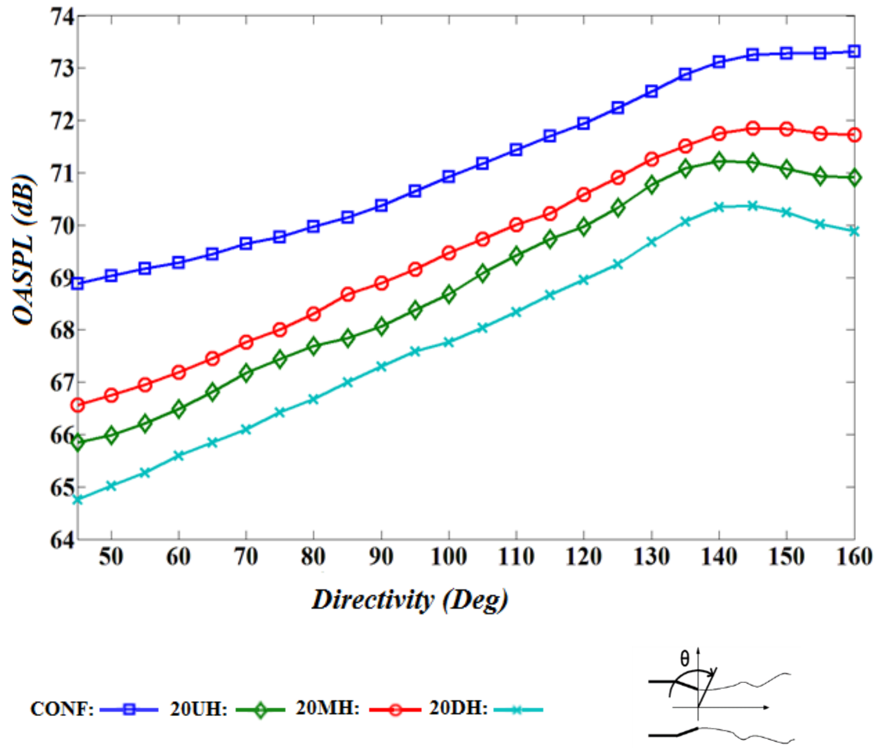

Fig. 4-23 Overall sound pressure level Directivity at $r = 160\ r_0$, for the scalloped mixers(Gong, 2013; Gong *et al.*, 2013)

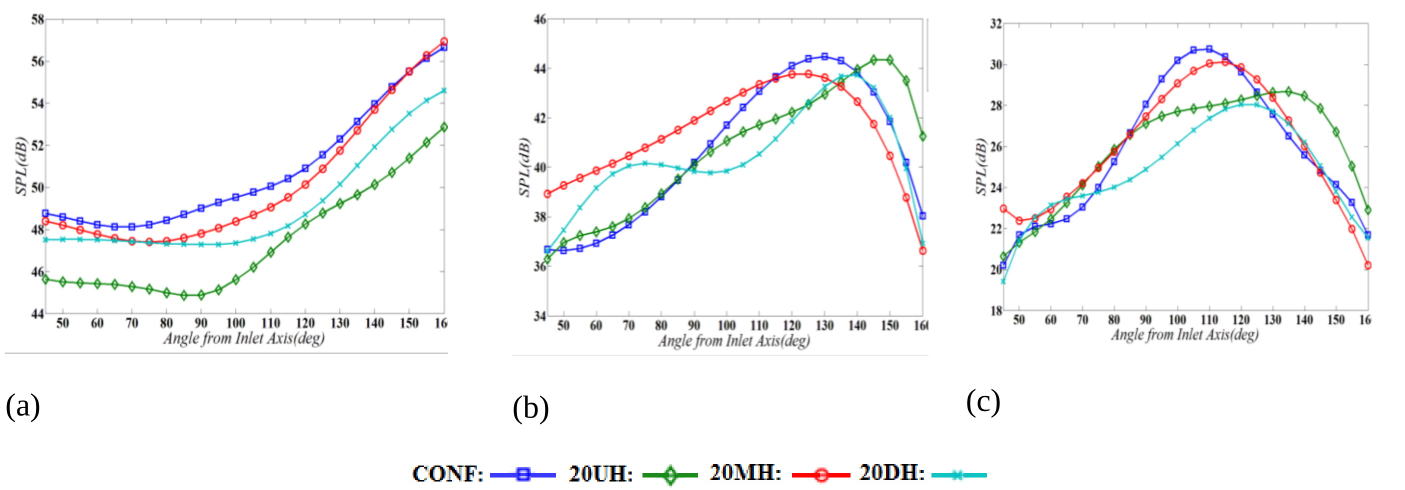

Fig. 4-24 Band Passed filtered directivity pattern of acoustic pressures at (a) 120 Hz b) 1200Hz c) 4500 Hz *(Gong, 2013; Gong et al., 2013)*

Chapter 5

Simulation of high-Mach subsonic jets using LBM-VLES

5-1 Introduction

As discussed in section 2-1-12, it is possible to use D3Q19 LBM discretization to simulate high Mach number flows; however, in order to capture compressibility effects due to high local Mach number, both numerical accuracy and the stability of the LBM scheme must be improved. Traditional BGK collision operator in Eqn. (2.10) comes with nonlinear velocity terms up to the third order dimensionless Hermite ortho-normal polynomials in the phase space. In order to increase the accuracy, collision terms can be replaced by high-order regularized collision operator; also an interaction force is introduced in the discrete Boltzmann equation (Nie *et al.*, 2009b) which controls the local speed of sound in a way that high Mach number flows can be simulated with the same degrees of freedom, *i.e.*19 stages, in the velocity space with no need to add additional velocity components in the lattice domain. Along with the momentum transport, the energy transport of high Mach flow should also be simulated correctly. Flow heating due to compression work and viscous dissipation terms must be included. A successful and numerically stable approach is using a modified hybrid method for the thermodynamics of energy field, by solving the entropy equation through a Lax-Wendroff finite difference scheme on the same Cartesian lattice.

The goal of this chapter is to compare jet noise prediction of the high-speed non-isothermal LBM formulation implemented in a PowerFLOW 5.0 with available experimental data. This investigation covers both single-stream jet ($M_a = 0.9$) and the complex internal mixing nozzle with 12CL mixer with actual operating condition. The major difference between two cases is that for the latter case, unmodified inlet boundary conditions were extracted directly from the experimental studies (Mengle *et al.*, 2002). Parts of the results in this chapter were also reported in three joint papers by McGill University and Exa Corporations (Casalino *et al.*, 2014b; Habibi *et al.*, 2014) and (Lew *et al.*, 2014).

5-2 Single-stream jet at M_a= 0.9

5-2-1 Computational setup

The cold and heated jet experiment performed in NASA Glenn research centre (Bridges and Wernet, 2010) using the SMC000 nozzle as in the low-Mach flow case in section 3-2 was modelled for two flow conditions: The well-known Tanna's setpoint 07 (SP07), characterized by a temperature ratio $TR = T_j / T_\infty = 0.842$ (cold jet) and an acoustic Mach number $M_a = U_j / c_\infty = 0.902$, and setpoint 46 (SP46), for which $TR = 2.702$ (hot jet) and $M_a = 0.901$. By adjusting the speed of sound, the corresponding nominal exit Mach numbers were 0.98 and 0.55, respectively based on the jet core temperature. Comparing to SMC000 setup described in section 3-2, the near-field VR distribution has been modified, also the grid resolution increased to maintain the accuracy in the far-filed at higher Mach numbers. Total number of VR regions were kept the same as the previous simulation in section 3-2 but changes were made in VR7 through VR12 to ensure higher resolution in the near field. Fig. (5-1) illustrates the new grid setup in the vicinity of nozzle exit plane. VR0 through VR7 were identical to setup shown in Fig (3-23-c). A total pressure inlet boundary was applied at the nozzle inlet (Fig. (5-1)) with a prescribed value of the temperature from experiment that was calculated using isentropic relations at the nozzle exit plane. This approach was in fact different compared to the low-Mach case in Chapter 3 where a constant velocity was directly imposed at the inlet and calculated using incompressible continuity relations and predictor-corrector algorithm to achieve $M_a = 0.5$ at nozzle exit plane.

Exterior boundaries of the nozzle were extended towards to the far-field outlet boundary through a funnel-shaped surface. As for the jet case in Chapter 3, the nozzle was submerged in a virtual anechoic environment consisting of three acoustic sponge layers with larger viscosity values towards the outlet boundaries. A total of 13 *VR* regions including the simulation volume (*VR0*) were used in the computational domain. A Porous FW-H surface was fully embedded in a *VR10* mesh resolution level (two coarsened levels with respect to the finest *VR12* grid resolution), which had a grid cut-off frequency estimated around 20 *k*Hz (St ~ 3.9). A numerical experiment was also performed using a lower resolution FW-H surface located at VR9 (With a cut-off ~ 10kHz). Two FW-H surfaces are shown in Fig. (5-2), with various distances from large-scale vortices in the near-field. The FW-H cup interacting with the external plume was computationally included in the sampling process but was excluded from the FW-H source integration to avoid the generation of spurious sound as a result of strong vortical fluctuations passing through the surface. One way to utilize the acoustic source information in the cup area at downstream termination of the FW-H surface is to use multiple staggered cups that, by averaging the far-field noise signals, would allow filtering the signature the strong perturbations passing through the surface, as proposed by Shur (2005a) and more recently by Mendez (2013). Such method was also utilized in a recent study by Casalino and Lele and (2014) later by Casalino and Hazir (2015) for simulation of dual stream external mixing nozzles. The *VR11* offset region has been generated from all the internal walls of the nozzle, whereas a *VR12* (finest one) offset region has been generated from a small section of the nozzle close to the exit. The overall simulation size is summarized in Table (5-1). Other details about the jet noise validation setup are reported in a joint McGill-Exa papers (Casalino *et al.*, 2014b; Lew *et al.*, 2014).

5-2-2 Results and discussions

Figures (5-3) and (5-4) illustrate the transient behaviour of the flow and fields. In fact, pressure contours in Fig. (5-3) represent the acoustic domain in the near-field for SP07 jet case. Figure (5-4) on the other hand shows development of turbulence using Lambda-2 vorticity criterion downstream of the nozzle for SP46 case. The grid setup used in both cases allows for smooth transition to turbulence and affordable computation of the far-field sound up to St~3.9. Figure (5-5) also shows instantaneous thermal field around related to Sp46 case. As discussed in Section 2-1-12, A unique temperature-momentum coupling scheme through solving the entropy equation was implemented in PowerFLOW 5.0 that allows for capturing the acoustic-thermal interactions of the flow at relatively high Mach numbers. Figures (5-6) and (5-7) show the time-averaged velocity contours and root mean squared (RMS) value of streamwise perturbation velocity respectively; for both SP07 and SP46 cases. All quantities, including the velocity RMS values exhibit a regular and symmetric pattern, and this is a qualitative indication of simulation accuracy and statistical convergence. In Figure (5-6), the high-resolution area is visible in the velocity contours. This is in fact caused by abrupt change in grid resolution by factor of two which is inevitable in the LBM and one of its fundamental drawbacks. Such distinction can be alleviated by shifting the VR interface farther downstream or outside of the shear zone with high velocity gradients. This approach could significantly increases the computational costs and should be avoided as long as VR change does not hurt simulation results. Comparing the contour plots of SP46 with SP07 Significant reduction in potential core length can be observed. This was expected and seen also in low-Mach jet cases studied in chapter 3 of this document. Such phenomenon can be attributed to modified mixing process by introducing energy transport in the system. Reductions in potential core length with temperature reduce the volume of turbulence that is contributing to the far-field noise. Also the cold jet has a lower overall level of turbulence intensity, by as much as around 10 percent (Bridges and Wernet, 2007), but temperature change does not appear to significantly alter the length scales or timescales of the turbulent jet.

A quantitative analysis of the LBM accuracy was performed by comparing the time-averaged streamwise velocity and the standard deviation along the jet centreline. is important to note that no tuning of the turbulent levels prescribed at the inlet nozzle boundary condition was performed to get the proper value of the laminar core length; flow characteristics were achieved by a genuine result of the simulations; moreover, as for the VLES simulation of low-Mach jet in chapter 3, also no random forcing was imposed at the nozzle inlet to trigger the turbulence fluctuations in the nozzle boundary layer that caused turbulence to develop naturally along the nozzle walls providing the proper boundary layer integral quantities at the nozzle exit. Therefore, the accuracy of the time-averaged centreline velocity is a good indication of the proper behaviour of the turbulence model in the shear layer, as well as in the wall region inside the nozzle.

Mean streamwise velocity centreline and RMS streamwise velocity fluctuation for jet SP07 and SP46 are plotted in Fig. (5-8) and (5-9). The streamwise velocity standard deviation was computed by making an isotropic turbulence assumption for the small unresolved turbulence scale, thus adding $\sqrt{2k/3}$ to the resolved fluctuation levels. The mean centreline decay *i.e.*, Fig. (5-8) shows a perfect agreement in terms of predicting the potential core length, *i.e.* the commencing point of decay as well as the decay rate compared to the experimental consensus of (Bridges and Wernet, 2010). The predicted potential core length for SP07 is 8.1*Dj* and compares well to the measured core length of 8.2*Dj*. The heated high-speed jet centreline decays are also in very good agreement with the measured data; however, the simulated jet decays slightly slower after ~8.0 jet diameters. The predicted potential core length for SP46 is 5.1*Dj* and compares well to the measured core length of 5.0*Dj*.

Figure (5-9-(a)) shows the standard deviation velocity comparison for both SP07 and SP46 cases. The peak location and value for the RMS fluctuation are in good agreement with experiments. However, for SP07 case, the RMS values were over-predicted in the laminar region before the peak. There could be several possibilities for such behaviour. For SP07 case, the jet centreline velocity was near sonic condition which is very close to the theoretical and stability limits of extended LBM scheme. Second reason might be related to the turbulence model and/or computational setup. Latter assumption can be investigated in future studies. Nonetheless, the qualitative agreement with experimental data is remarkable; especially the peak turbulence intensity was well predicted for SP07. Early sharp peak at x/D ~ 8, could be possibly be due to very high velocity gradient and lack of sufficient grid resolution and mismatch of the jet shear layer development. Contrary to SP07 case, the standard deviation values obtained for heated counterpart was in good agreement with the measurement consensus (Bridges and Wernet, 2010). Figure (5-9-(b)) shows that both the overall trend and the peak value of the high-speed heated jet were compared favourably with the experimental consensus. A numerical experiment was performed to unveil the effect of adding calculated standard deviation from turbulence model on top of the values obtained directly from the simulation. In Fig. (5-9-(b)), both curves were plotted and compared to the measured data. It is observed that the superimposed curve better followed the experimental trend; however, turbulence levels were still under-predicted up to one jet diameter due to late transition. In order to get better prediction at the nozzle lip area, the setup would need higher grid resolution close to the nozzle wall at the boundary layer as well as more accurate inlet conditions in terms of the velocity profile and turbulence intensity and length scales (Uzun and Hussaini, 2007; Bogey and Bailly, 2010). In order to check the grid quality as well as the convergence, it will be beneficial to look at spanwise flow parameters in the near-field. Plots at figure (5-10) and (5-11) shows the time-averaged radial distribution of streamwise velocity profiles at different axial distance for SP07 and SP46 respectively. Results show Smooth and symmetric profiles in good agreement with experimental data.

On the far-field acoustic prediction side, the overall sound pressure levels are reported in Figs. (5-12) and (5-13) for SP07 and SP46, respectively. For SP46 case, two FW-H surfaces located at VR10 and VR9 were compared. The surface at VR9 came with lower grid cut-off (St ~ 1.6) and lower resolution to estimate surface integrals using Gaussian quadrature in the FW-H scheme. For SP07 case. The noise directivity was predicted within 1 dB accuracy for observer angles greater than 40^o. For lower values at downstream, sound pressure levels were extremely under-predicted, with the maximum estimated levels about ~5.0 dB lower than in the experiments. This in part, was related to omission of the cup are on the permeable FW-H surface; thus, neglecting part of the noise contribution generated by the largest wave packets that are very effective at shallow radiation angles, in particular in almost sonic conditions. Also as discussed earlier in this section, the turbulence intensity values obtained for SP07 case were over-predicted mostly before the peak levels that could contribute to poor estimation at shallow angles which will remain an open question. Same trend can be observed for SP46 in Fig. (5-13), but the under-prediction of the maximum noise levels for observer angles less than 40^o were about 2.0 dB. Also, general over-prediction of about 1.5dB can be seen at larger angles towards upstream. This prediction was based on the sampled acoustic data on the high-resolution surface at VR10. It can be seen that the over-prediction associated with low-resolution surface (VR9) can reach up to 4.5 dB at almost all observer angles larger than 40^o; thus, not used further in our studies despite the fact that surface file was significantly smaller (*i.e.* four times) and; hence, computationally cheaper. The computed third-octave SPL spectra at 30, 60, 90 and 120 degrees were compared with measured data by (Tanna, 1977) for SP07 and SP46 and also with results by (Bridges and Brown, 2005) for SP07. Spectral results are shown in Figs. (5-14) and (5-15) for SP07 and SP46 respectively. The estimated grid cut-off frequency for the employed FW-H surface was about 20 *k*Hz or St~3.0; this appeared to be confirmed by a sharp drop-off in the noise levels around those frequencies for both cases. The low-frequency discrepancy of the predicted sound pressure spectra that appears as a sharp rise might be due to lack of statistical convergence that can be alleviated by increasing the transient simulation time. Such argument can be supported by comparing the spectra before and after the acquisition timesteps. For instance, in the LBM-VLES case in chapter 3.0, a better resolved low-frequency bands up to 0.2 dB where achieved when the simulation evolved from 7.3×10^5 to 7.5×10^5 and 7.7×10^5 timesteps. Comparing the SP07 and SP46 data from the experiments, the effect of heating the jet actually makes the jet quieter for the same jet acoustic Mach number. This was also captured by the LBM simulation. For the low speed jets discussed in chapter 3.0, the behaviour is reversed, *i.e.* one can see that the low speed heated jet was louder compared to its unheated counterpart. On the Lighthill's analogy framework, this could be explained by the fact that the effect of heating actually decreases the shear and self noise, if the Mach number is kept constant (Viswanathan, 2004; Lew *et al.*, 2007). In fact, the decrease is more significant for the low Mach jet flows compared to the high-speed ones. The entropy noise sources on the other hand could be amplified when the jet is heated. The increase in the entropy noise comes as no surprise since entropy fluctuations are directly related to temperature variations and can be well captured by the hybrid thermal LBM scheme in PowerFLOW. The compressibility effects also become important on the entropic source term for an unheated jet when the Mach number is increased (Lew *et al.*, 2007). The overall and spectral analysis would suggest that cancellations or amplification among different sources are taking place and contribute to different noise behaviour at different Mach numbers when it comes to heating.

Table 5-1 Computational parameters, LBM-VLES scheme for SP07& SP46 jets

Setpoint	VRs	Δr (mm)	FEV($\times 10^6$)	FES($\times 10^6$)	t_t (sec)	t_a (sec)	CPUh($\times 10^3$)
SP07 & SP46	13	0.198	94.3	2.8	0.15	0.19	51

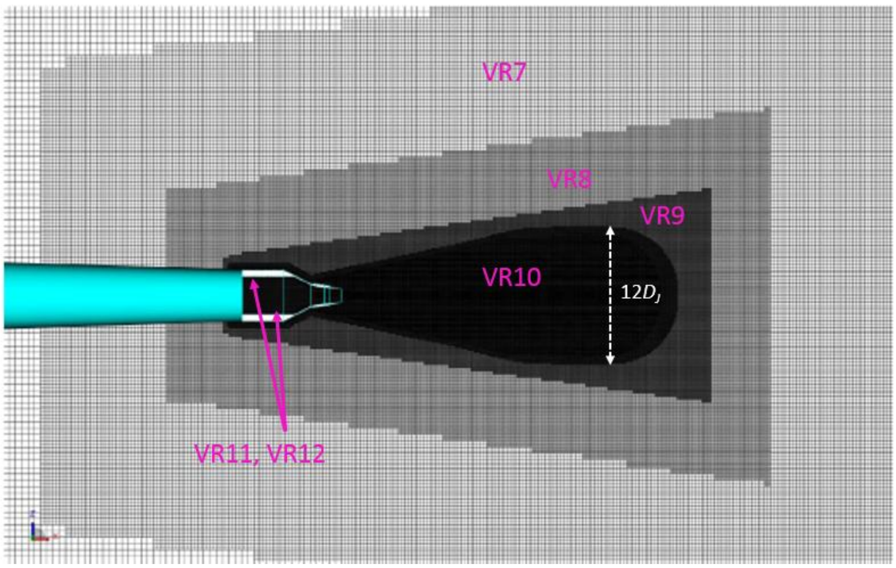

Streamwise dimensions

L_0/D	L_1/D	L_2/D	L_3/D	L_4/D	L_5/D	L_6/D	L_7/D	L_8/D	L_9/D	L_{10}/D
510.0	230.0	140.0	100.0	83.0	69.0	64.0	50.0	35.0	27.0	20.0

Conical and circular regions (r_1/D, r_2/D)

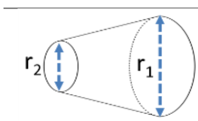

VR7	*VR8*	*VR9*	*VR10*
(90.0, 50.0)	(45.0, 25.0)	(25.0,10.0)	(12.0,5.0)

Fig. 5-1 SMC000 Single-stream High-Mach jet - computational grid

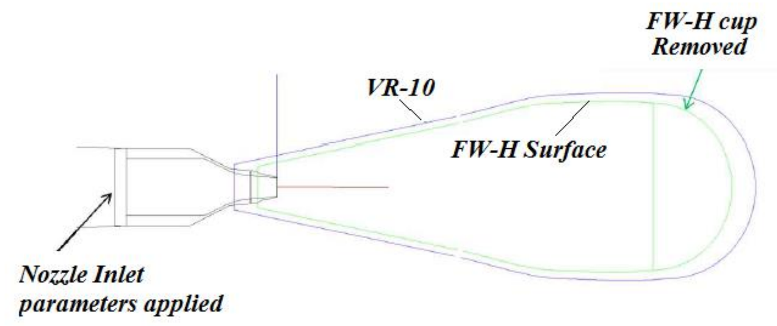

a)

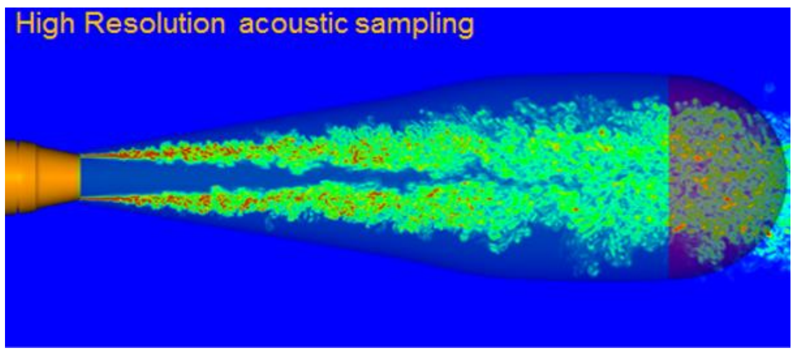

b)

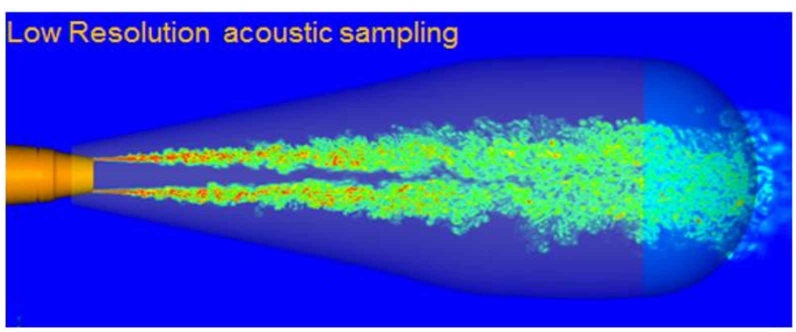

c)

Fig. 5-2 FW-H sampling surfaces a) VR position b) High resolution surface at VR10 (bottom) c) Low-resolution surface at VR09

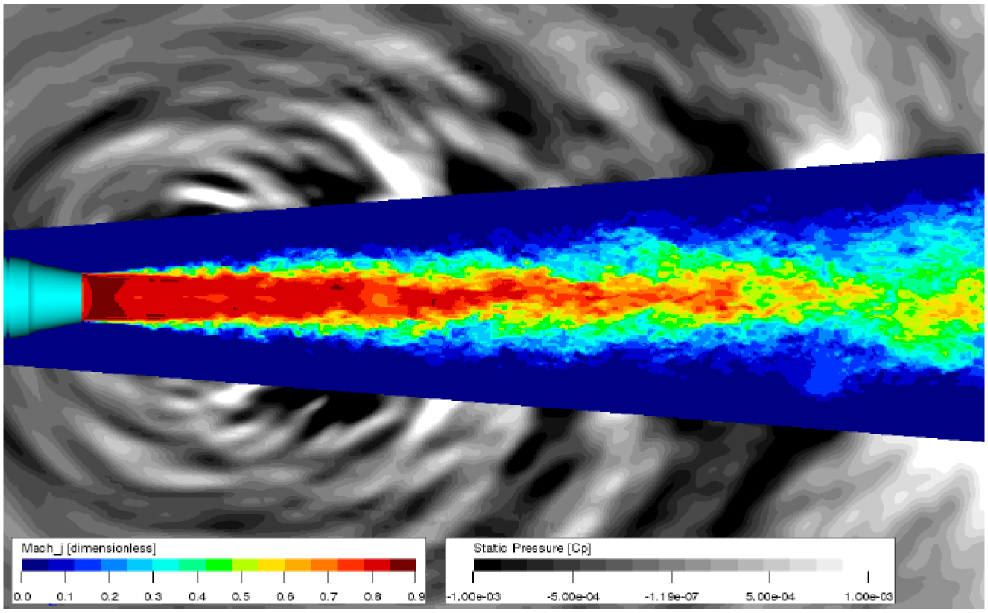

Fig. 5-3 Transient velocity and pressure contours for jet SP07, M_a=0.9 and TR= 0.86.

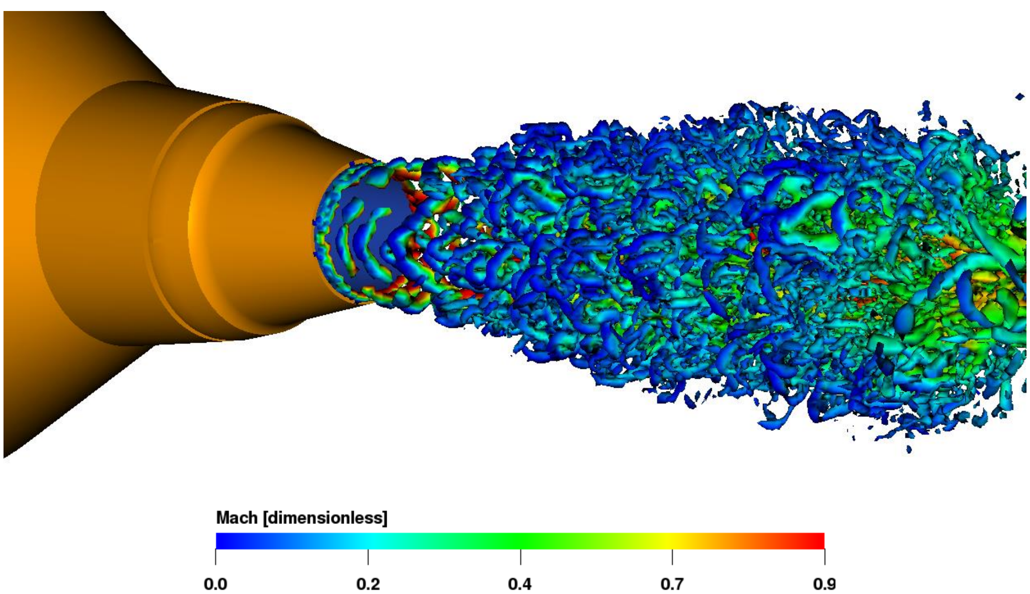

Fig. 5-4 Lambda-2 vorticity criterion (Isosurface = -10). Colors are referring to the acoustic Mach number for SP46, M_a=0.9 and TR= 2.7.

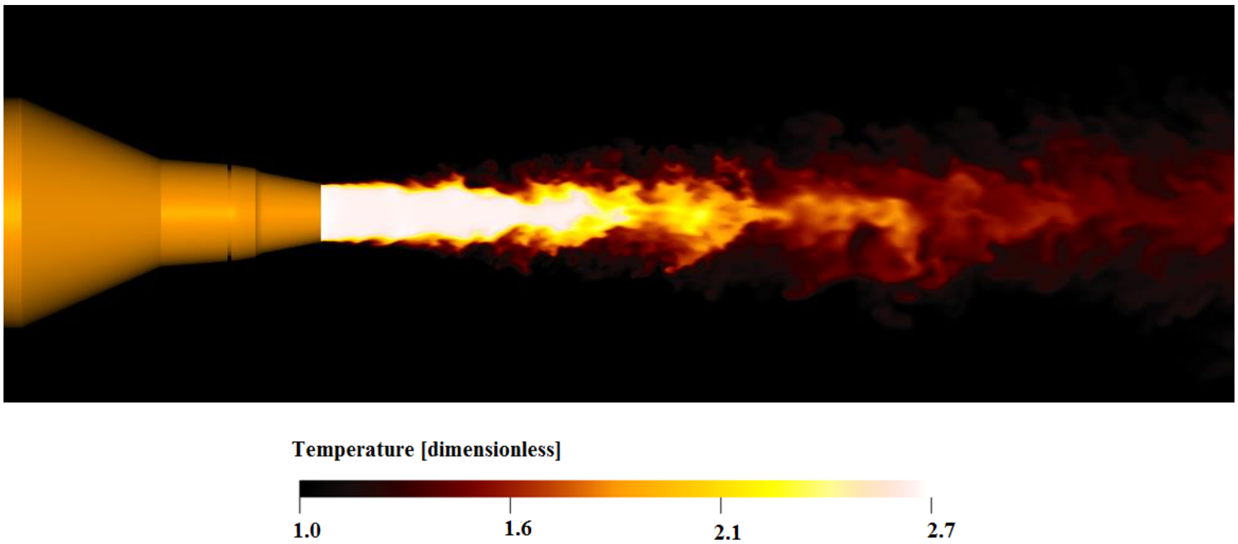

Fig. 5-5 Instantaneous temperature contours for SP46 Jet, M_a=0.9 and *TR*= 2.7.

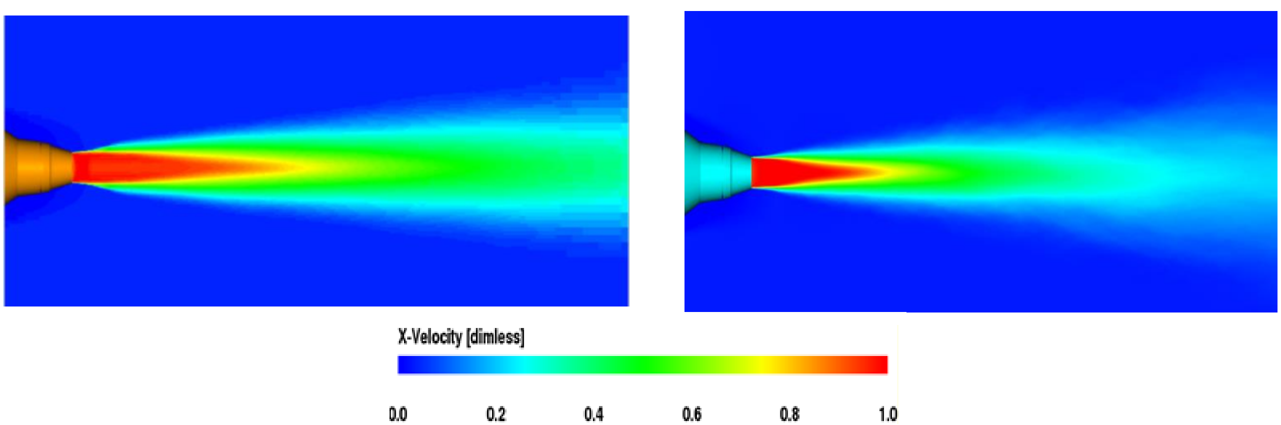

Fig. 5-6 Mean streamwise x-velocity profile (left) SP07 (right) SP46

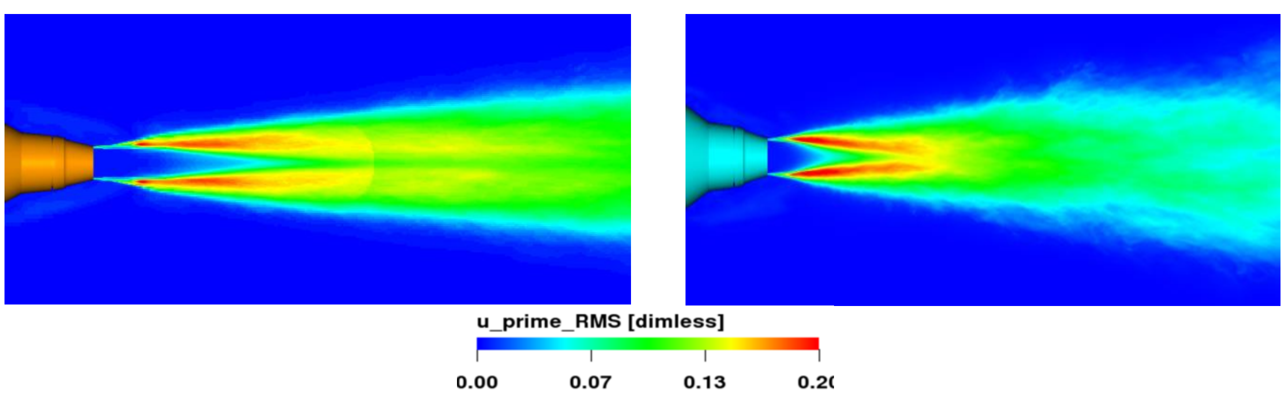

Fig. 5-7 Root mean square turbulence intensity contours (left) SP07 (right) SP46

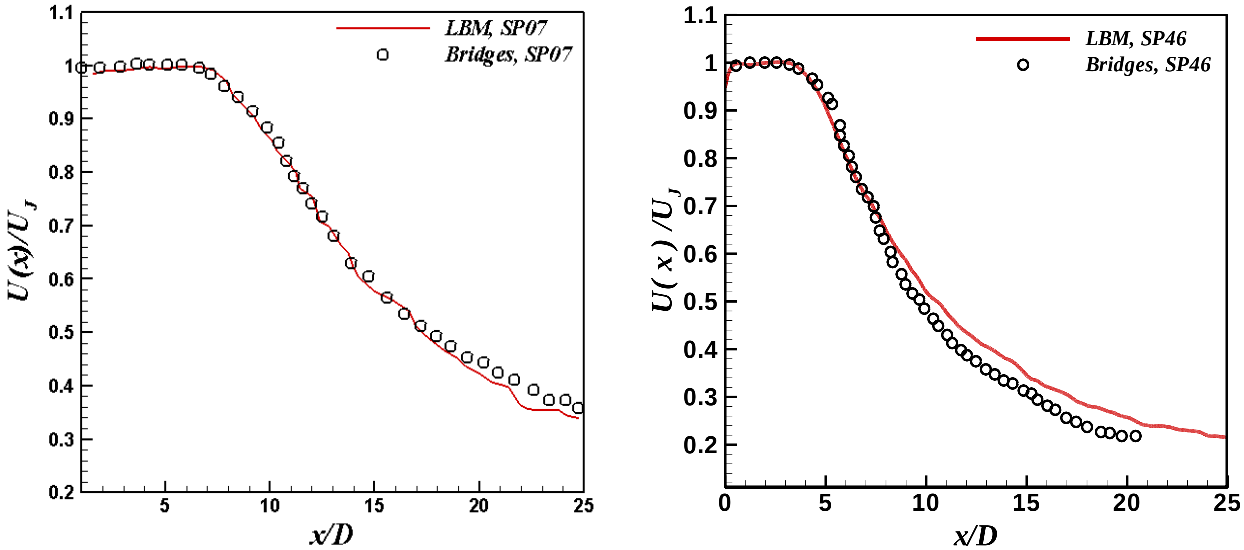

(a) (b)

Fig. 5-8 Mean centreline x-velocity profile (a) SP07 (b) SP46

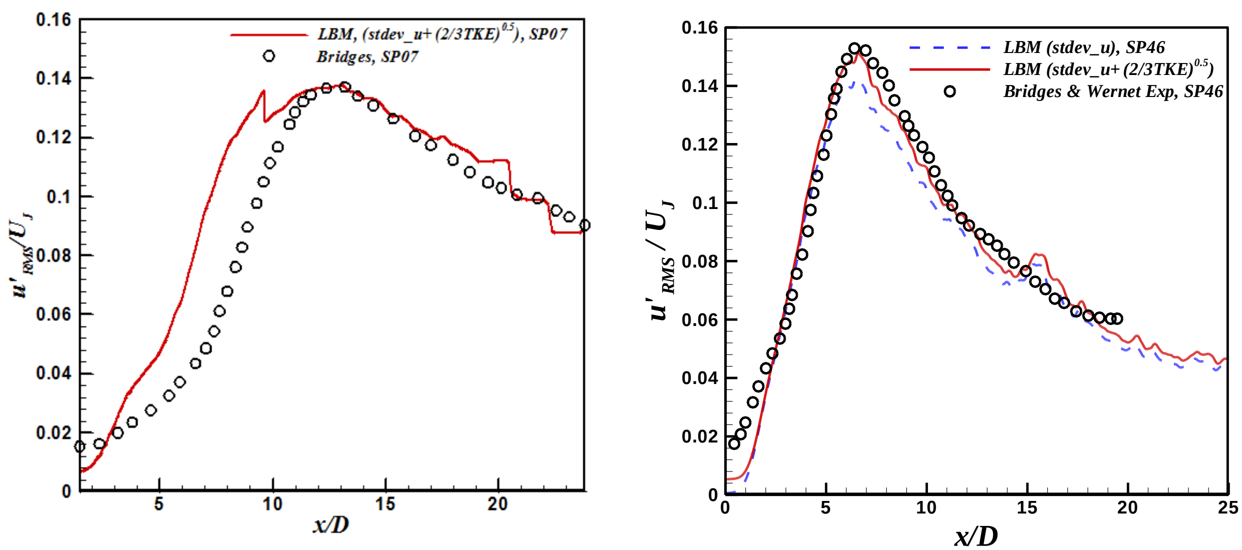

(a) (b)

Fig. 5-9 Root mean square (RMS) turbulence intensity profile (a) SP07 (b) SP46

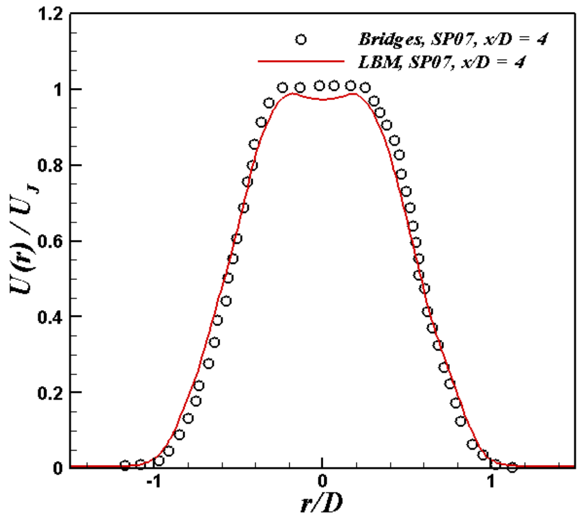

(a)

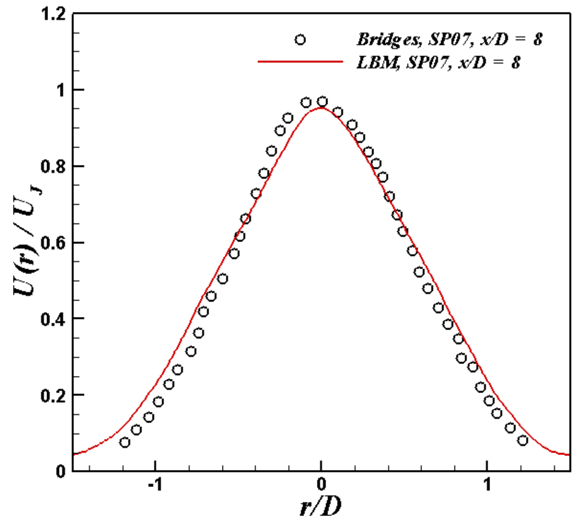

(b)

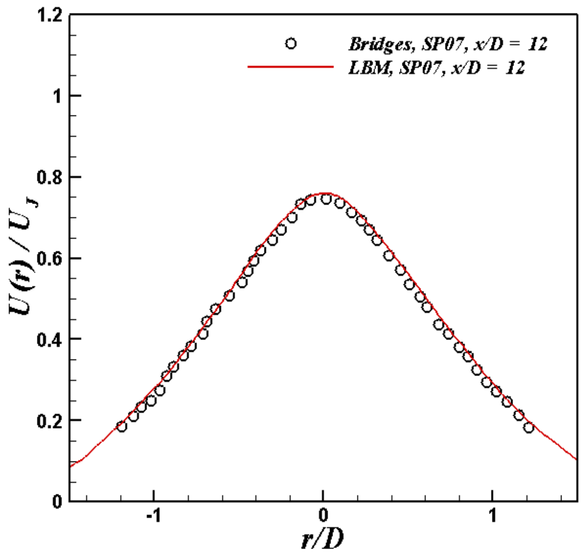

(c)

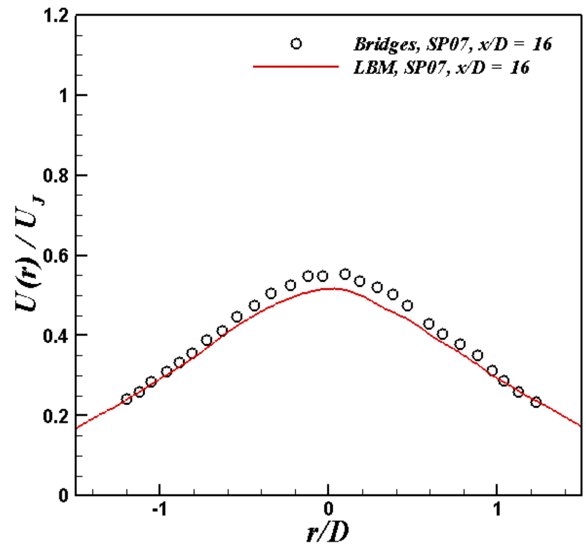

(d)

Fig. 5-10 Mean spanwise velocity profile downstream of nozzle exit plane (a) x/D=4.0 (b) x/D = 8.0 (c) x/D = 12.0 and (d) x/D =16.0 for SP07 jet

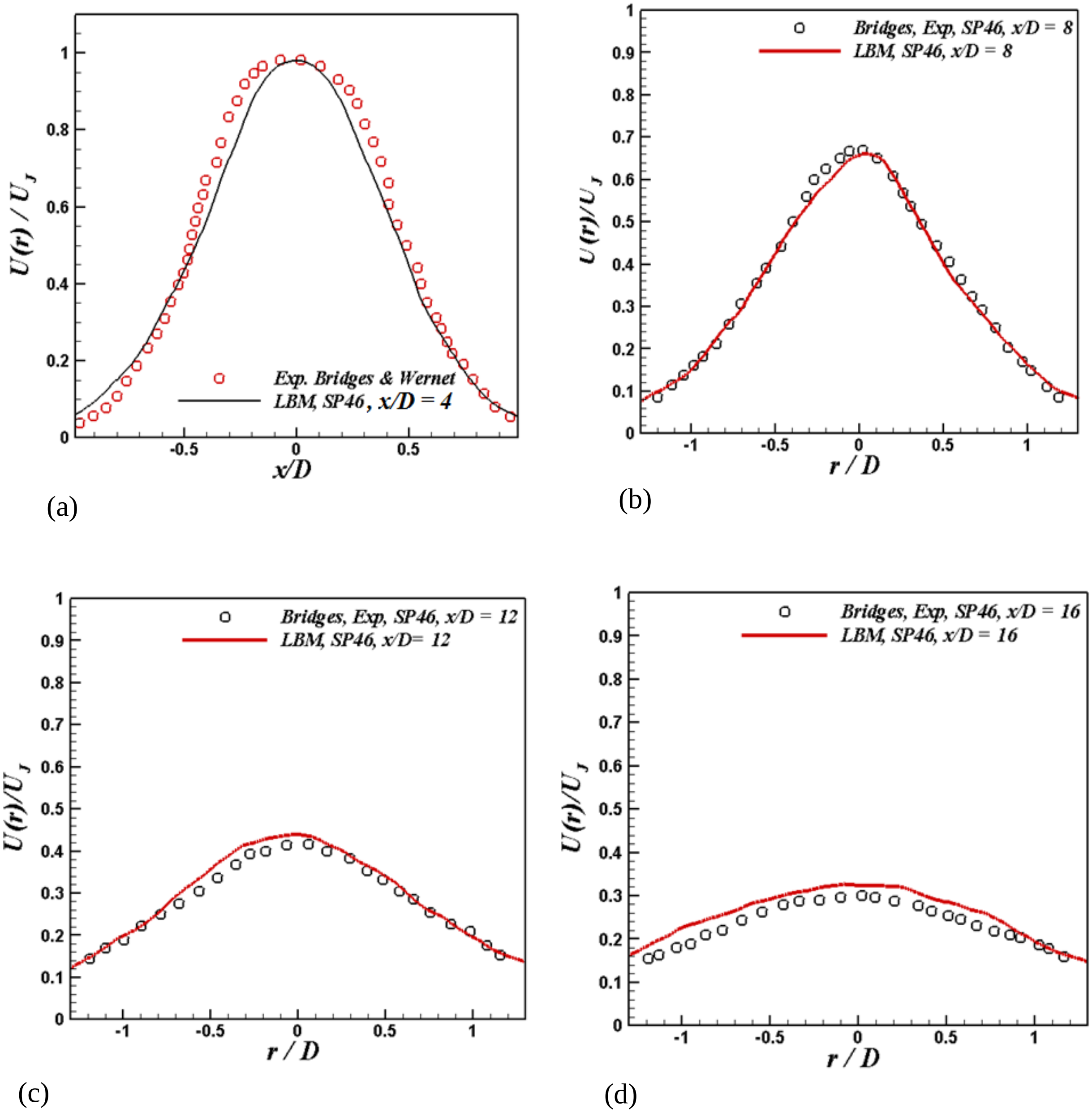

Fig. 5-11 Mean spanwise velocity profile downstream of nozzle exit plane (a) x/D=4.0 (b) x/D = 8.0 (c) x/D = 12.0 and (d) x/D =16.0 for SP46 jet

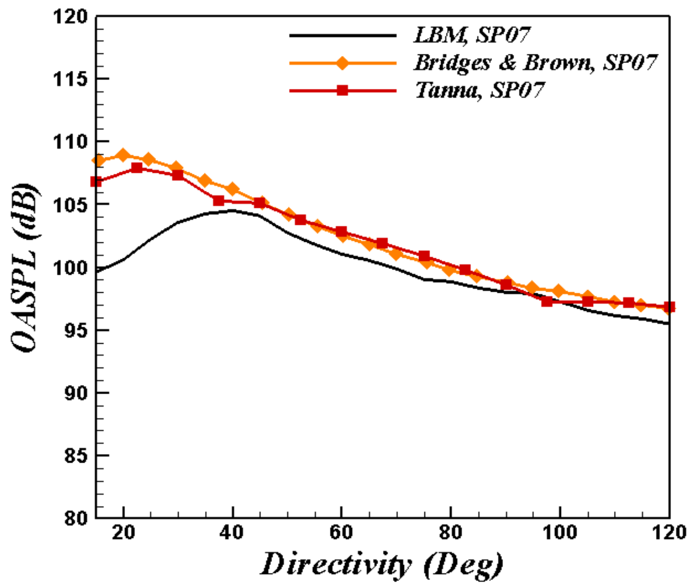

Fig. 5-12 Overall sound pressure level directivity for SP07 jet

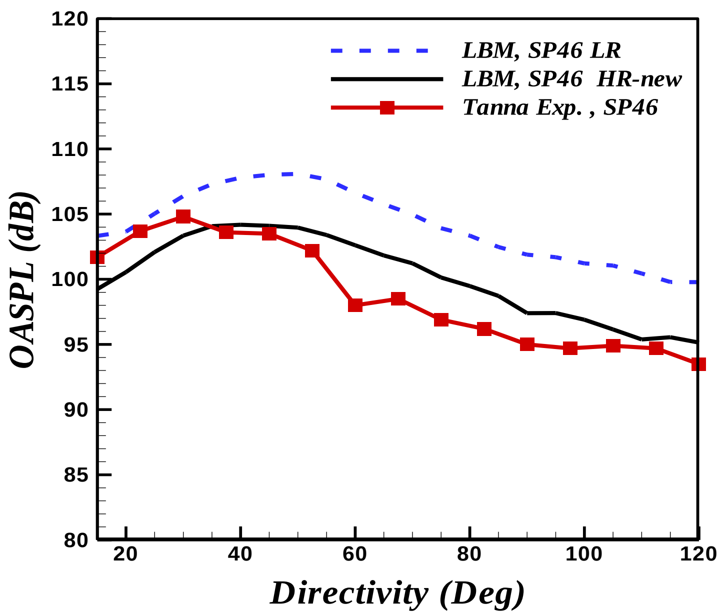

Fig. 5-13 Overall sound pressure level directivity for SP46 jet

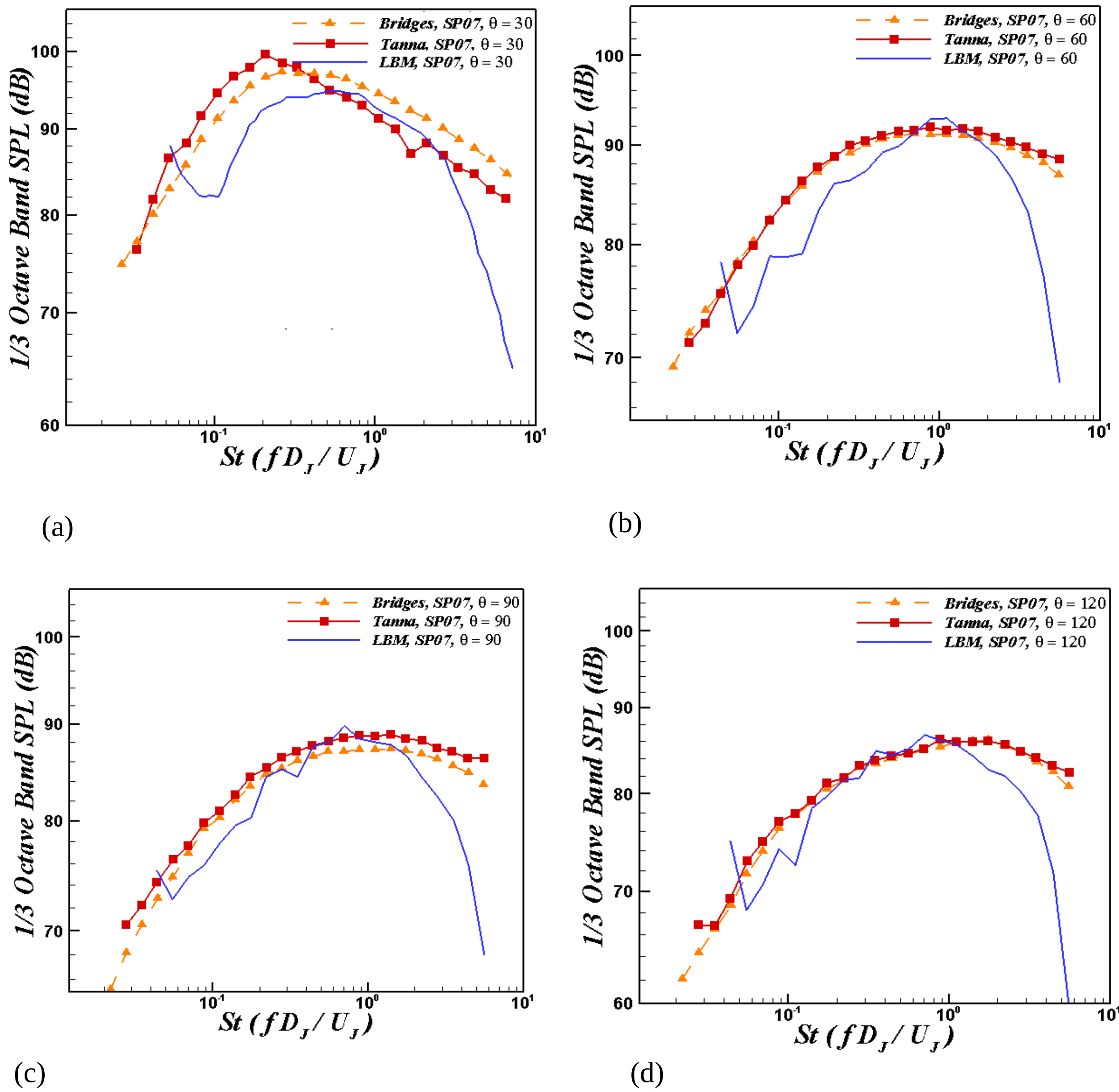

Fig. 5-14 One-third Octave spectral levels for SP07 jet at Observer angles (a) θ = 30° (b) θ = 60° (c) θ = 90° (d) θ = 120°

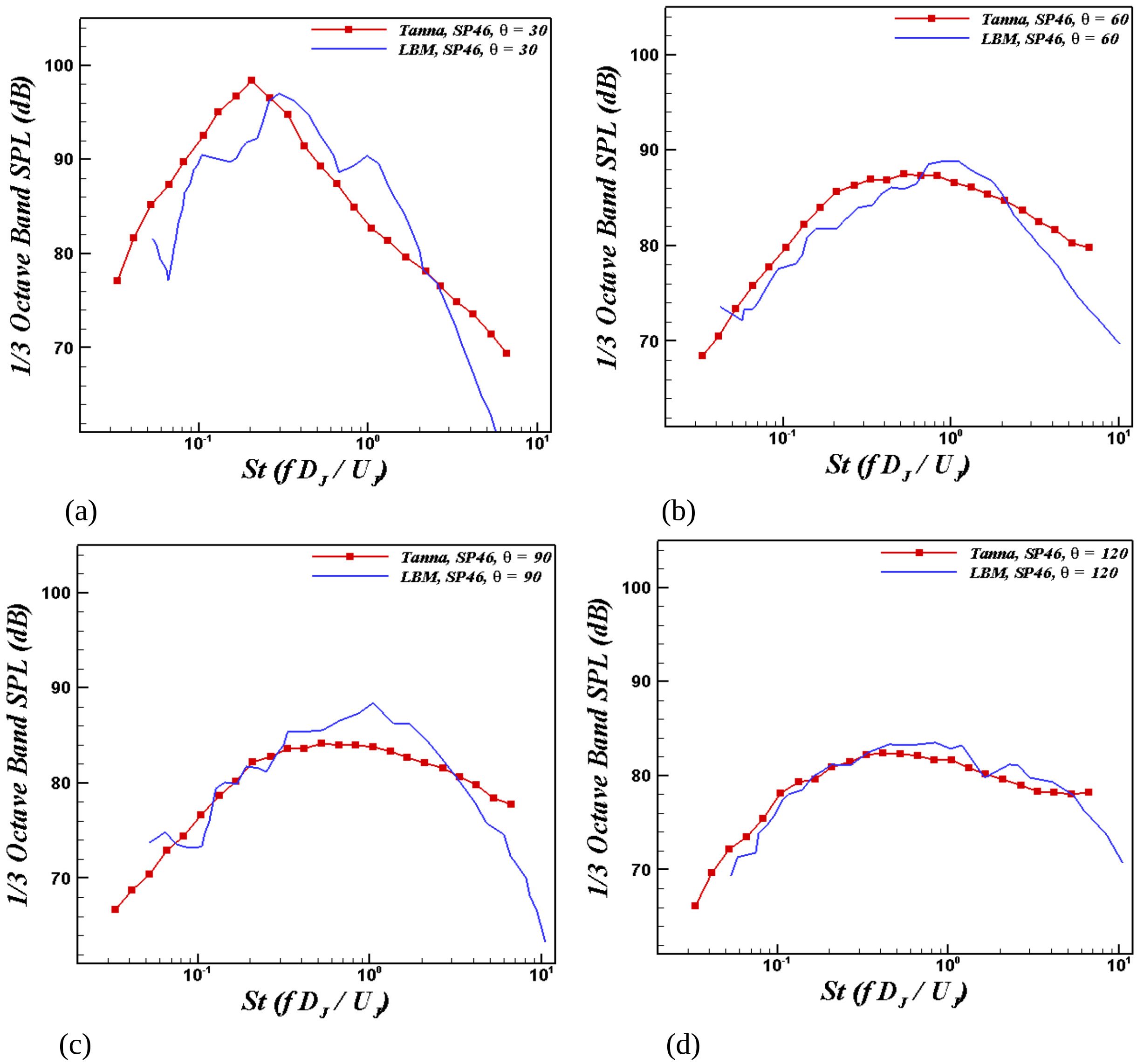

Fig. 5-15 One-third Octave spectral levels for SP46 jet at Observer angles (a) θ = 30º (b) θ = 60º (c) θ = 90º (d) θ = 120º

5-3 Dual-stream internal mixing nozzle

5-3-1 Test case and operating conditions

Results in this section is reported in (Habibi *et al.*, 2014). A baseline 12-lobed mixer with contoured nozzle and central conical body was selected from previous experimental investigations at NASA Research Centre (Mengle *et al.*, 2002). This geometry was actually the same as a test case used in Chapter 4 for the low-Mach simulations. Figure (5-16(a)), shows the 12CL mixer configuration used for high-Mach studies. Selected nozzle length, *aka* L_2 , was the shortest length used in the experiments (Mengle *et al.*, 2002). All nozzle/Mixer properties are listed in Table (5-2). The parametric sketch of a nozzle-mixer set is shown in Fig. (5-16(b)). All dimensions as well as the operating conditions were obtained from NASA reports (Mengle *et al.*, 2002). The combination of the inlet condition and nozzle length will control the acoustic Mach number at nozzle exit region that might even exceed the sonic threshold. In order to make sure the problem can be solved with extended LBM scheme, we selected a geometry set and inlet properties that would maintain a subsonic flow condition throughout the nozzle. This was verified by looking at the velocity contours in the NASA report. The operational inlet conditions used in this study is listed in Table (5-3).

It was previously mentioned in chapter 4 that the inlet boundary conditions had to be adjusted to limit the maximum Mach number to a value less than ~0.5 (Habibi *et al.*, 2013a; Habibi *et al.*, 2013b; Habibi and Mongeau, 2013). This limitation was no longer necessary in the new entropic LBM scheme that allows for moderate compressibility effects as long as the flow Mach number remains less than 1.0 (~ 0.9) . In order to simulate the exact experimental conditions, computational domain was set at flight mode in which a free stream was maintained throughout the domain (*i.e.* M_a= 0.2 or 68.0 m/s). Other aspects of the selected operating conditions used in this study are listed in Table (5-3).

5-3-2 Computational setup

A contoured convergent nozzle with a diameter of D_J =7.24” (183.9 mm) and a length of L=1.54×D_J was considered for the nozzle-mixer configuration. Fig (5-17) shows the grid setup both inside the nozzle and the shear layer. The computational domain size was extended to 300 D_J ×200 D_J ×200 D_J through extending (VR0) compared to the setup in Chapter 4, and total of 9 variable resolution zones were used in the computational domain. This was found to be necessary following a numerical experiment. VR distribution was the same as the low-Mach flow case as discussed in section 4-2-4; however, the finest grid resolution was increased to address high compressibility effects. The smallest voxel size near solid boundaries and through the shear layer was $3.36 \times 10^{-4}\ m$ and total 109 fine equivalent cells (voxels) were used. The extended high-Mach LBM capability was combined with the VLES model discussed earlier in chapter 4. Domain decomposition and the parallelization of the solver were performed using the same message passing interface (MPI) method as the regular LBM solver (*i.e.* PowerFLOW 4.x).

A hyperbolic tangent velocity profile (Eqn. 3-1) and a uniform pressure distribution were applied as inlet conditions as for the low-Mach test case described in section 4-2-3. The inlet mean velocity of fan or core streams $u_{f/c}$ as well as the pressure can be calculated using isentropic flow relations. This procedure is generally expressed as

$$(u_{f/c}, p_{f/c}) = G(BPR, NPR_f, NPR_c, NTR, \dot{m}_{f/c}) \ , \tag{5.1}$$

where the parameters and the procedure was discussed earlier in section 4-2-2 using Eqns (4.1) to (4.5). The mass flow rate value of the fan stream, $\dot{m}_f$, should be corrected based on the nozzle length as the mixer blockage cause changes in bypass ratio. The correction was performed using available plots by (Mengle *et al.*, 2002) Following an iterative procedure, the velocity, pressure, and density of each stream could be obtained. In this study, the fully mixed velocity, U_m, was used to normalize velocity and turbulence intensity (Mengle *et al.*, 2002; Bridges and Wernet, 2004) calculated by Eqn. (1.10). To achieve better turbulent inflow at the root of the mixer, a random forcing function was used according to Bogey *et al.* (2011) as also shown in Eqn. (4.11). This function was designed to minimize spurious sound radiation to the far-field. as for the low-Mach case, $\varepsilon_r(r,\theta,z,t), \varepsilon_\theta(r,\theta,z,t)$ and $\varepsilon_z(r,\theta,z,t)$ were random values between -1 and 1 updated at every time step and at every grid point. A value of α = 0.00625 was used here to achieve the desired inflow turbulence levels. A High-viscosity sponge zones were applied in the outermost (*i.e.* three coarsest) fluid regions in order to damp the outgoing acoustic waves. The coarsening of the grid towards the boundaries helps the dissipation of outgoing acoustic waves. The coupled momentum-energy setting was applied to account for heat transfer effects which is solved using the entropic energy solver as mentioned in section 5-1. The core total temperature was set to 2.37 times the fan temperature led into achieving a high bypass ratio. The temperature of the outermost boundaries inside the computational domain was set to isothermal, *i.e.* equal to the ambient temperature. The nozzle, mixer and the centre body were assumed to be adiabatic. All simulations were performed on the Mammouth parallel computer MP2 located at the Universite de Sherbrooke in Quebec. Other important simulation properties were listed in table (5-4)

5-3-3 Far-field sound calculations

Far-field sound pressure levels were calculated using a modified porous Ffowcs Williams-Hawkings (FW-H) surface integral method; designated formulation 1-C (Najafi-Yazdi *et al.*, 2011) as for all other jet noise cases in this study which is also applicable for the high-Mach flows. This method includes corrections for mean flow, moving sources and observers. It is useful for cases with mean free stream such as lobed mixer simulations at flight conditions (our case). The FW-H surface location was the same as that in chapter 4. A total of twenty-five virtual microphone coordinates were defined for the FW-H solver at fixed radial distance (*i.e.* $r=160\ r_0$) from the nozzle exit, covering 25 directional angles upstream and downstream of the nozzle exit plane (*i.e.* $45^o \leq \theta \leq 160^o$ with the increment of 5^o). Sound pressure levels were calculated over different frequency ranges. A bandwidth of 20 *Hz* was used for FFT calculations. Spectral analysis was performed via bandpass filtering for selected bands between 80 Hz and 6 *k*Hz (*i.e.* the grid cut-off frequency) to study the noise reduction potentials. Data were reported at the distance of 150 feet (245 D_J) according to the experimental setup at NASA. There was no extra correction applied for the ground absorption and reflection effects. With regard to the low distance between the microphones and the noise sources, the atmospheric attenuation was neglected in our simulation. This might be important in the fly-over high frequency acoustical measurements in which the distances are of the order of 1000 feet (~300 m) and more. Acoustic sampling was initiated after ≅ 350,000 timesteps, after which fully developed conditions become established.

5-3-4 Results and discussions

After ≅ 300,000 timesteps, the time-resolved simulation of internal-mixing nozzle yielded converged flow statistics. Extracted data include instantaneous flow structures, flow separation, and mixing layers inside the internal mixing nozzles. The mean flow characteristics and the flow statistics were also obtained inside the nozzle and within the jet plume. Figure (5-18) shows two snapshots of the simulation. Fig. (5-18 (a)) indicates the x-velocity contour that qualitatively illustrates the diffusion of the jet momentum into the moving media. The relative Mach number between the turbulent jet and free stream is ≅0.75, which is much higher than the relative Mach number between fan and core streams at the mixing plane (*i.e.* ≅0.2). This contributes to turbulent boundary layer thickness at each zone. The outer shear layer is thicker, which is due to the intensified Kelvin-Helmholtz instabilities as the relative Mach number is higher. Some coherent structures are formed in the vicinity of the nozzle outlet. Such structures are absent in the confluent configuration and seem to be originated from rotational mixing induced by lobed geometry also seen in the low-Mach flow condition (Habibi *et al.*, 2013b). It can be seen from Fig. (5-18 (b)) that significant thermal mixing occurs close to the mixer at the exit plane. For the high-order Lattice-Boltzmann scheme used in this study, the pressure work term is present in the energy equation, thus, the temperature rise due to the compression which occurs in the fan stream is accurately captured. This elevated temperature at the nozzle outlet forms the secondary thermal boundary layer (*i.e.* Fig.5-18 (b)). Contrary to the momentum field, the inner thermal boundary layer thickness is greater due to the larger temperature gradient between the core and fan streams relative to the fan and the free stream flow.

Figure (5-19) shows the Lambda-2 criterion iso-surface for the 12CL mixer (iso-surface value = -100). Lambda-2 is defined as the second eigenvalue of the symmetric tensor $S^2+\Omega^2$, where S and Ω were respectively the symmetric and anti-symmetric parts of the velocity gradient tensor. This criterion has been shown to accurately capture vortex structure and to better visualize the 3D turbulent coherent structures than other metrics (Jeong and Hussain, 1995). The iso-surface in Fig. (5-19) is coloured by the temperature magnitude in the near-field. The introduction of the downward cold fan flow to the upward hot core flow is well discernible in the root of the mixer which forms the streamwise vortices downstream of the mixer plane. The mixer is considered adiabatic in the simulation, which prevents pre-heating of the fan stream prior to the mixing plane. At first glance, this might seem a weak assumption specially due to the fact that the mixer is made of a thin and highly conductive metal plate; however, the contact length is small comparing to the $u_{f/c} \times t$ length scale. The conduction energy transfer mechanism can be neglected compared to the convection in the mixing zone via strong turbulent mixing. The time-averaged velocity and temperature fields both inside and outside of the nozzle are shown in Fig. (5-20). Using an internal mixer causes the concentration of peak velocity close to the nozzle centreline and formation of specific crown-shaped mixing layer. The second peak occurs between the centre body and the tip of the mixer. Using the similar analysis for the temperature contours in Fig. (5-20(b)), the internal energy is more concentrated close to the centreline as well as a zone very close to the mixer tip. In Fig. (5-21), the mean velocity magnitude, root mean squared (rms) value of the velocity and the time-averaged vorticity contours obtained from the simulation are compared to their counterparts from the cross-stream PIV measurements by (Bridges and Wernet, 2004). The contours are extracted at x/D = 0.2 from the nozzle exit plane. As indicated by the PIV data, the corrugated shape of the mixer affects the momentum field by accelerating the fluid particles close to the mixer tips. This trend was well captured by the LBM simulations. Other phenomena include the higher turbulence levels at the nozzle exit plane due to the introduction of streamwise vortices, as well as the twin clockwise and counterclockwise vortices formed adjacent to the lobes as shown in Fig. (5-21(c)).

Figure (5-22) illustrates the normalized centreline mean streamwise velocities with respect to the normalized distance from the mixer along the nozzle centreline. The momentum decay rate at the region located in $x/D > 2.0$ was consistent with PIV observations (Mengle *et al.*, 2002; Bridges and Wernet, 2004). The simulation trends diverge from the experimental values in the $x/D < 2.0$ located inside the nozzle, which may be due to the presence of one VR transition at the region. In Fig. (5-23), exhaust velocity profile was compared to the measured data. The profile was taken along the lobe tip at x/D =0.2 from the nozzle exit plane. The obtained profile compares favourably with experiments. This supports the choice of inlet hydrodynamic conditions. To study the mean flow characteristics of the flow-field, further investigation of the radial velocity profiles and turbulence intensity could be useful. The data from previous RANS simulations by Garrison *et al.* (2005) is also shown for the comparison. Figures (5-24 (a)&(b)) show the mean spanwise velocity profiles at x/D_J =1.0 and x/D_J =5.0 respectively. It seems that that the RANS predicted the secondary peak close to the outer shear layer with higher accuracy. This might be due to the insufficient grid resolution of LBM setup at outer layers. At x/D_J =5.0 cross section, both methods could reasonably predict the flow behaviour. In terms of the turbulent intensity prediction, as shown in Fig. (5-25 (a) & (b)), the LBM simulation yielded better results. The secondary peak was well captured by the LBM (*i.e.* in terms of both location and magnitude) at x/D_J =1.0, while the RANS simulation over predicts the intensity level by 4%. At x/D_J =5, both methods were predicting the peak correctly but LBM prediction in the inner layer region was more consistent with measured values. However, significant discrepancy between the measured and predicted turbulence intensity in the centreline is due to the fact that the flow is full transition to turbulence occurs almost at x/D_J =1.0 in the numerical simulation due to velocity deficit and lower local Reynolds number downstream of the centre body, whereas in the actual measured data, the turbulence transition occurs instantly downstream of the mixer all the way towards the nozzle exit plane. Transient pressure contours in Fig. (5-26) represents the sound field in the vicinity of the nozzle. The contours shown in Fig. (5-26) were obtained by calculating the acoustic pressure so that $|P - P_\infty| < 30\ Pa$. The effect of lobed mixers on noise reduction and parametric studies on the lobe number, penetration depth scalloping, and thermal effects were fully investigated for low-Mach configurations (Habibi *et al.*, 2013b). Quantitative results indicated a significant difference between the sound directivity of the lobed-shaped and confluent mixers. Band-passed filtering of the far-field pressure spectrum was performed to evaluate the effects of mixer shape on sound directivity in different frequency bands. To validate the high-Mach simulation against experimental data, the OASPL directivity was compared with measured data (Mengle *et al.*, 2002) in Fig. (5-27). The indirect methodology that employs the high-order LBM with FW-H formulation appeared to follow the correct trend; however, in terms of the overall levels, LBM seems to over predict the measured data by almost 2 dB at different observer's location. Spectral analyses are shown in Figs. (5-28 (a)) and 5-28 (b) related to microphone locations at 90^o and 150^o (upstream). The trend at shallower angles, *i.e.* 150^o, was in better agreement with the experimental trends; However at θ = 90^o the peak SPL was still well predicted by LBM. While the spectral levels were over predicted by the simulation, in general, the spectral trends were consistent with the measured data. The consistent over-prediction of sound pressure levels could be attributed to the TKE trends towards downstream of the jet plume. As seen in Fig. (5-25), the TKE intensity was increased further downstream of the jet plume and started overpredicting the PIV data at x=5D_J and beyond.

The increase in TKE values could be related to insufficient transient simulation time, or due to addition of instability waves as flow speed is very close to the sonic limits. Looking at the mean pressure values on the FW-H surface at different frequency bands, and also the sound pressure spectra at Fig. (5-28 (a)), one could see that the discrepancy is more relevant at grater aft angles that is controlled by high frequency structures that could be intensified by instability waves coming from the high-speed flow region that may exceed the validity range of the Mach numbers.

5-4 Chapter highlights and main learning points

A high-order hybrid Lattice-Boltzmann Model (LBM) Very Large Eddy Simulation (VLES) method for high-speed non-isothermal subsonic flows is used to simulate the unsteady jet flow as well as the associated noise spectra and directivity for a single axisymmetric nozzles and dual-stream nozzle with forced mixer, The jet exit Mach number and temperature ratio are set according to the various setpoints from the NASA experimental campaigns for both SMC000 (single-stream jet and 12CL lobed mixer configuration(Mengle *et al.*, 2002). This indeed was the first attempt in the literature to use LBM for aeroacoustics studies of high-speed jets and also the lobed mixers with realistic boundary conditions. Both isothermal and heated core flows are considered for the single-stream jet. The far-field noise is computed through a Ffowcs-Williams and Hawkings (FW-H) analogy applied to a fluid surface encompassing the jet plume. condition was performed to get the proper value of the laminar core length, which is a genuine result of the simulations; moreover, no random forcing at the nozzle inlet was employed to seed the turbulence fluctuation in the nozzle boundary layer, which develops naturally along the nozzle walls, thus providing the proper boundary layer integral quantities at the nozzle exit. Therefore, the accuracy of the time-averaged centreline velocity is a good indication of the proper behaviour of the turbulence model in the shear layer, as well as in the wall region inside the nozzle. The streamwise velocity standard deviation velocity along the jet centreline was promising for SP46, whereas a significant overestimation of the fluctuation levels in the laminar core region is predicted for SP07. It should be mentioned that SP07 is characterized by almost sonic conditions, thus constituting a challenging test case for the high-speed D3Q19-based LBM flow solver. At the present stage of the research, it is not clear whether the inaccurate prediction of the fluctuation levels for SP07 is due to the computational setup or to the fact that we approached the usage limits of the high-speed LB formulation.

For the 12CL lobed mixer case, The near-field results were in very good agreement with published experimental data for the same operating conditions which, validates the use of entropic LBM as an alternative to the computationally expensive LES schemes based on Navier-Stokes formulation. The results suggest that RANS simulations might be able to accurately predict mean flow data. But they are not very accurate for aeroacoustic studies and they require with auxiliary semi-empirical correlations for noise predictions. Such correlations cannot be generalized for different nozzle-mixer configurations and hence, cannot be used for new designs. In far-field studies, while the sound pressure directivity and 1/3 octave levels were following the expected trends, the sound levels were over-predicted by about 2dB that seems to be related to the proximity to sonic limits and stability range of the code. Future validation studies are recommended on different nozzle types such as confluent and scalloped mixer to fully identify the limitations of high Mach subsonic LBM scheme for such practical jet noise applications with complex geometries.

Table 5-2 Geometric specification of mixer

Description	Mixer ID	Penetration factor H_m/H_{mp}	Mixing Length L/D	Scalloping Depth L_S/H_m
12 lobes **low penetration**	12CL	0.41	0.79	0.00

Table 5-3 Operating Conditions.

Setpoint	M_a	M_J	*NPR_F	†NPR_C	‡NTR	**BPR	Attributes
1	0.94	0.83	1.44	1.39	2.37	4.9	Heated – 12CL

* Net total pressure ratio (P_{Tf} / P_a) for fan stream;

† Net total pressure ratio (P_{Tc} / P_a) for core stream;

‡ Net total temperature ratio (T_{Tc} / T_{Tf}).

** Bypass ratio ($\dot{m}_f / \dot{m}_c$).

Table 5-4 Computational parameters, LBM-VLES scheme for internal mixing nozzles

Model	VRs	Δr (mm)	FEV($\times 10^6$)	FES($\times 10^6$)	t_t (sec)	t_a (sec)	CPUh($\times 10^3$)
12CL/CONF	9	0.33	109.0	4.47	0.22	0.34	64

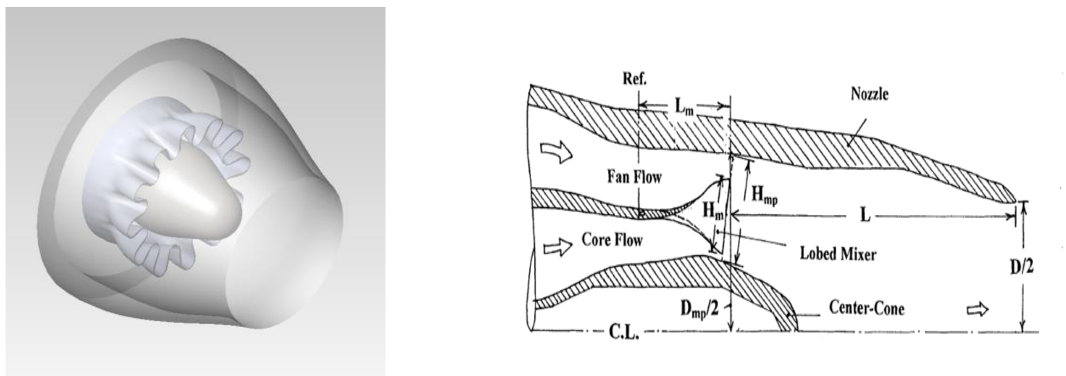

a)

b)

Fig. 5-16 **(a) 12CL geometry (Habibi *et al.*, 2013a), (b) Nozzle-Mixer characteristic Lengths (Mengle *et al.*, 2002).**

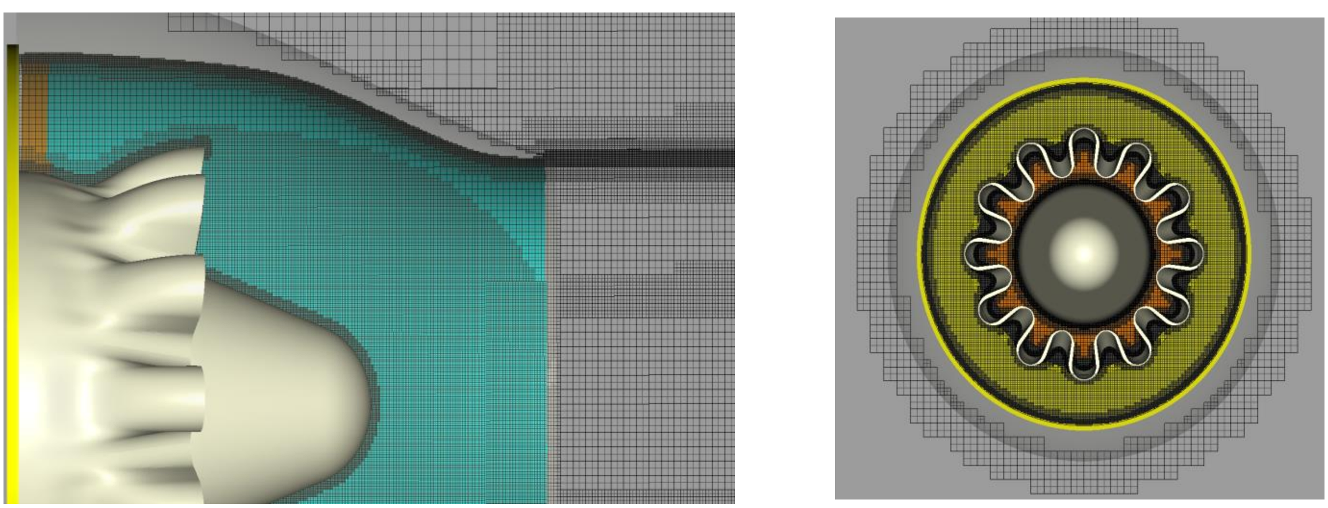

Fig. 5-17 Voxel distribution inside the computational domain for the 12CL model.

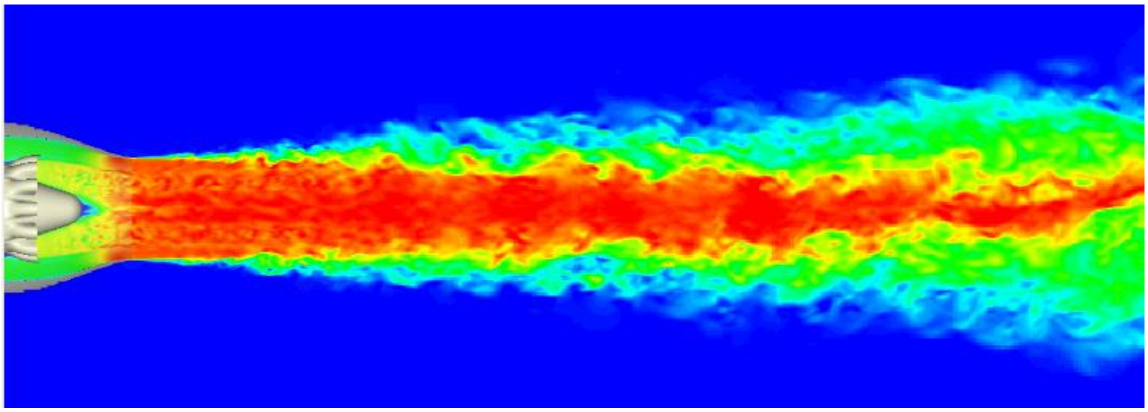

a)

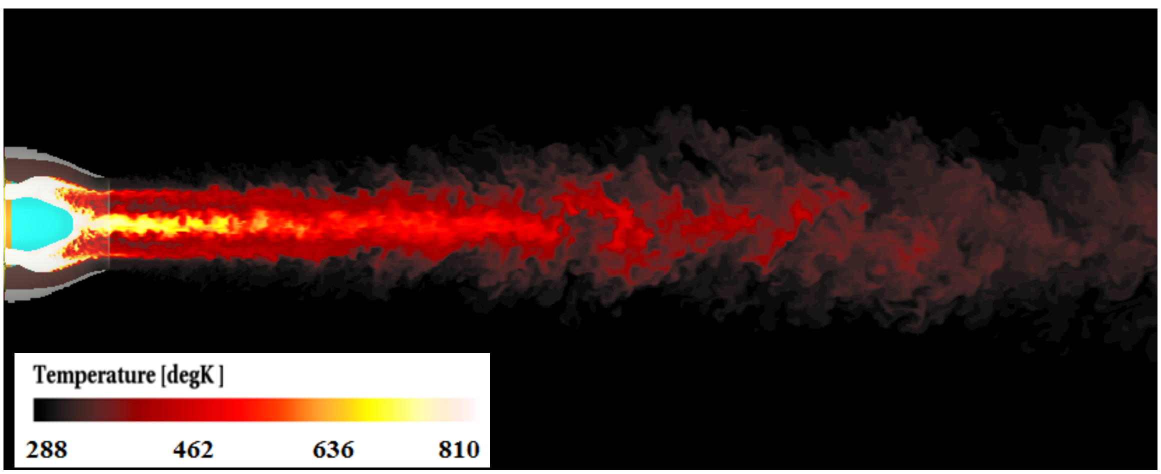

b)

Fig. 5-18 Snapshot of time-resolved thermal field (a) Streamwise velocity (b) Temperature

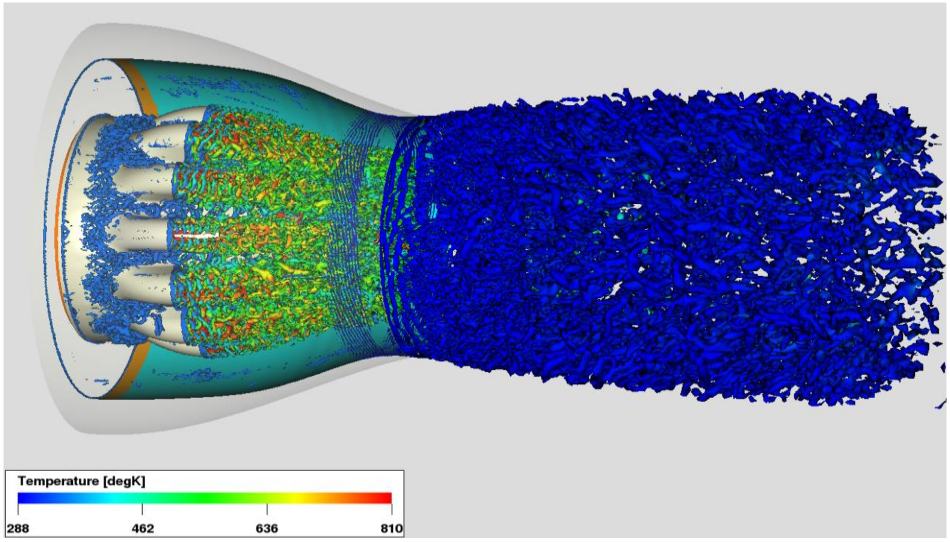

Fig. 5-19 λ_2 criterion iso-surface of 12CL mixer; (iso-surface value = -100). Colored by the temperature values.

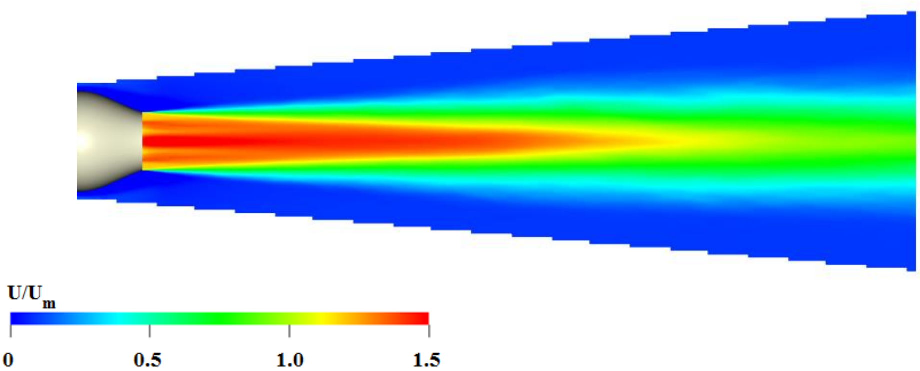

a)

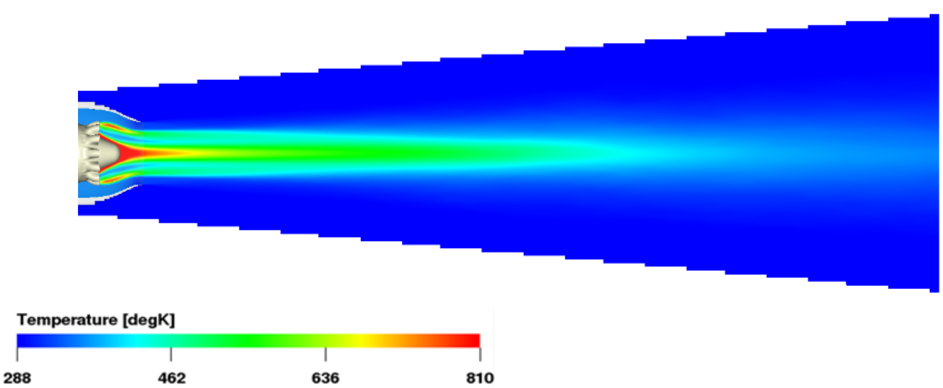

b)

Fig. 5-20 Time-averaged contoured of (a) x-velocity magnitude (b) Temperature downstream of the nozzle.

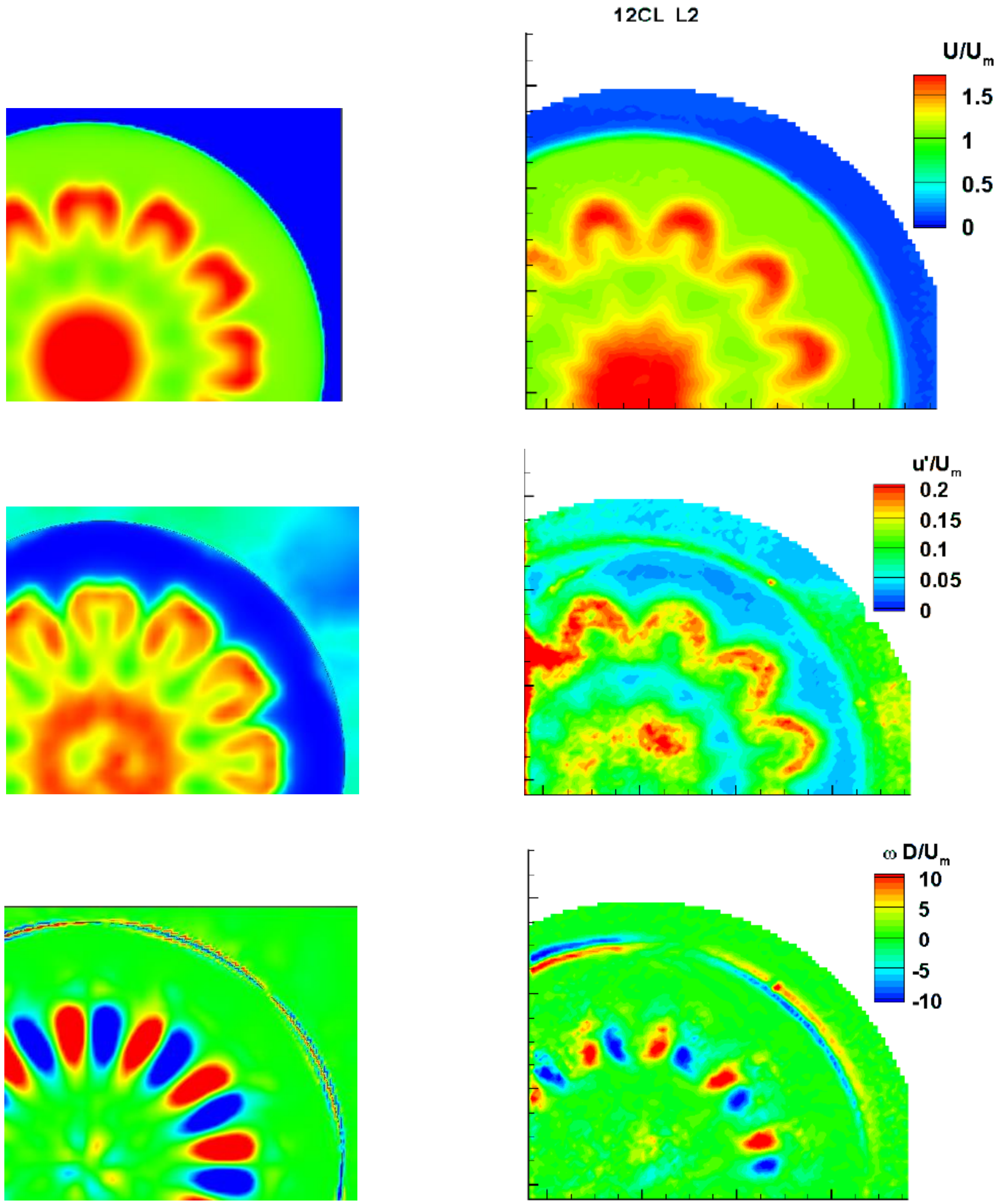

Fig. 5-21 **Comparison of LBM simulation (Left) and PIV data (Mengle *et al.*, 2002; Bridges and Brown, 2005) (right) - Contours at axial station x/D = 0.2 of (a) mean axial velocity, (b) rms axial velocity, and (c) axial vorticity for low penetration (12CL) mixer in the short (L2) nozzle**

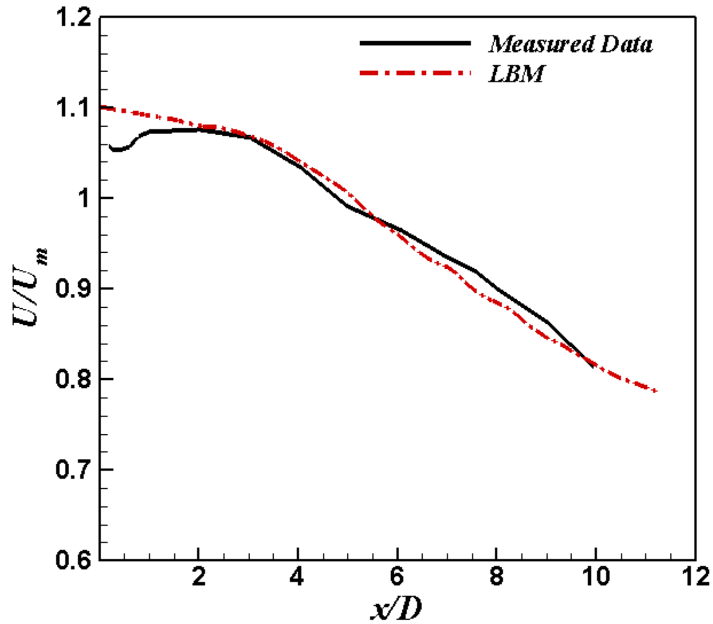

Fig. 5-22 Streamwise mean velocity profile along the nozzle centreline (Distance from the mixer plane)

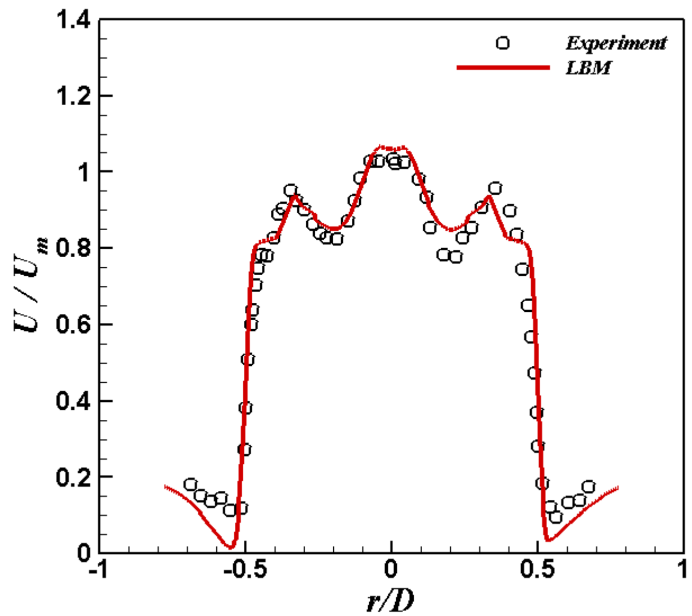

Fig. 5-23 Spanwise mean velocity profile at x=0.2 from the nozzle exit plane

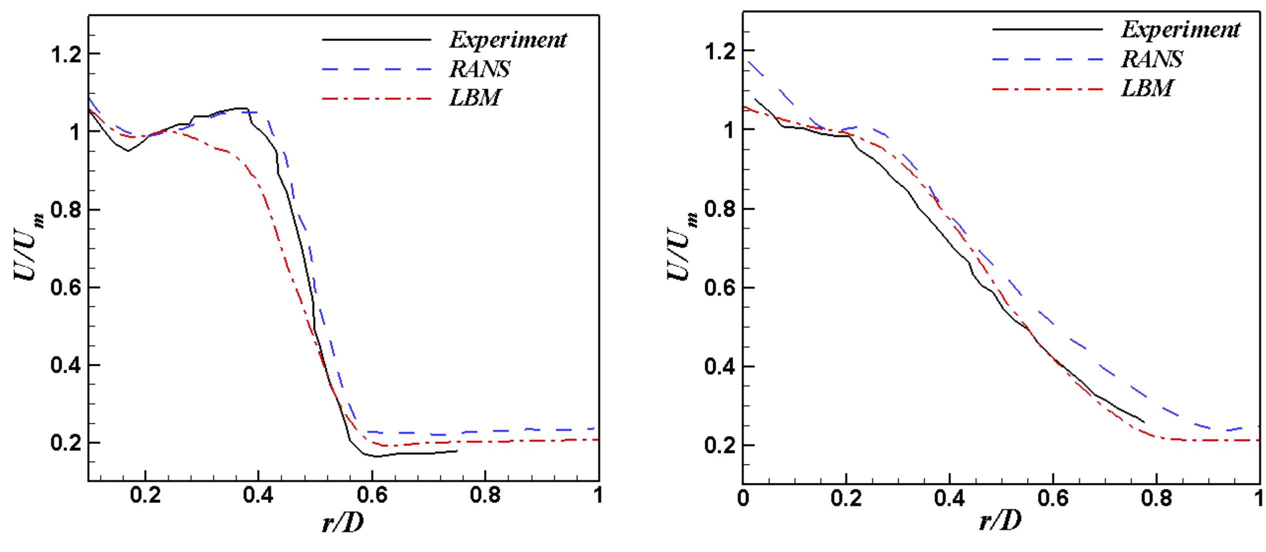

a) b)

Fig. 5-24 Radial profile of mean velocity at the lobe peak azimuthal plane (a) X/D = 1 (b) X/D = 5. Comparison between LBM simulation, RANS simulation and PIV measured data (Garrison *et al.*, 2005)

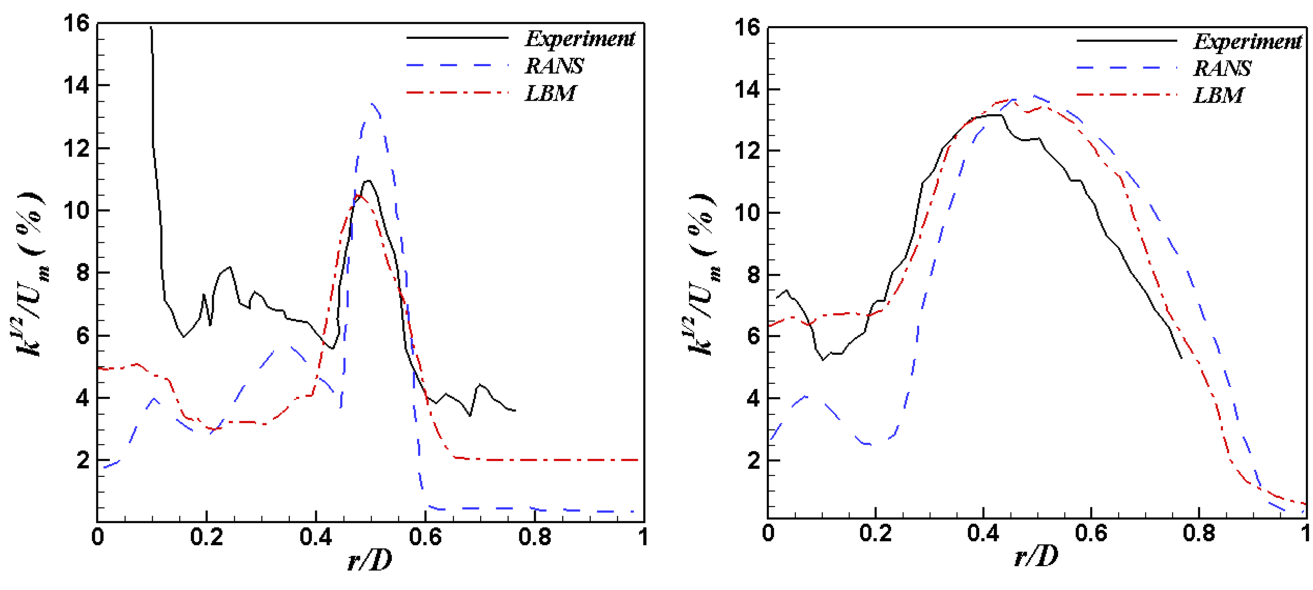

a) b)

Fig. 5-25 Radial profile of relative turbulence intensity at the lobe peak azimuthal plane (a) X/D = 1 (b) X/D = 5, Comparison between LBM, RANS (Garrison *et al.*, 2005) and PIV measured data (Bridges and Wernet, 2004)

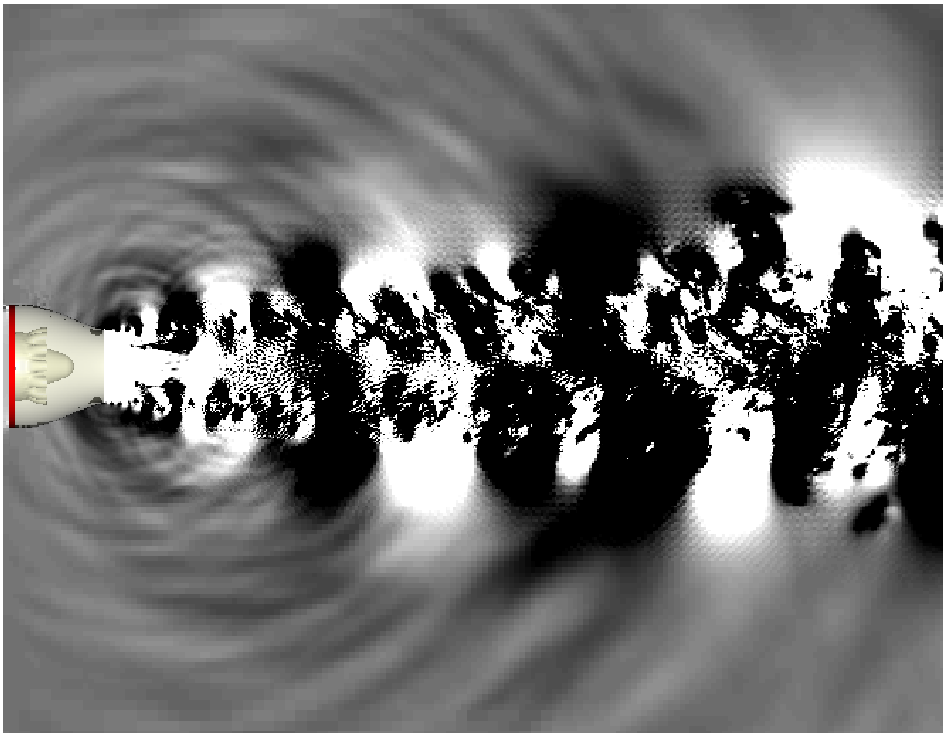

Fig. 5-26 Pressure field near the nozzle outlet

Snapshot of the acoustic pressure ($|p - p_\infty| < 30Pa$).

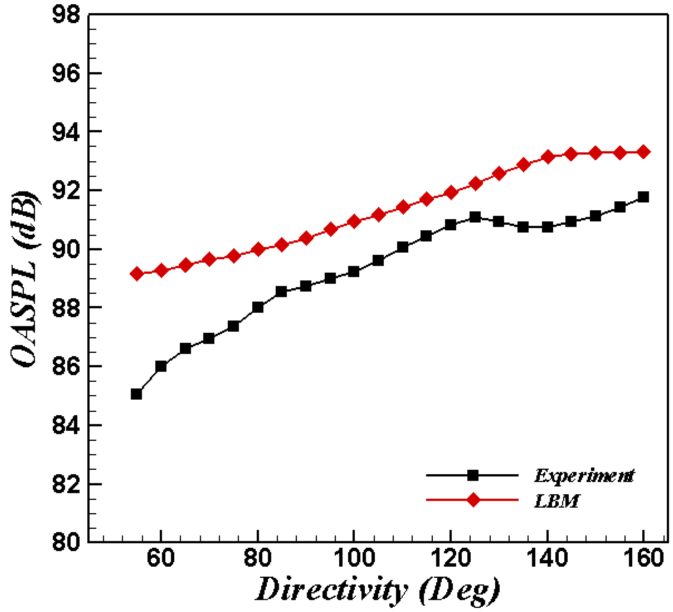

Fig. 5-27 Directivity of overall sound pressure levels. LBM-FW-H simulation compared to the measure data (Mengle *et al.*, 2002)

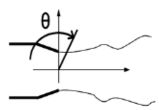

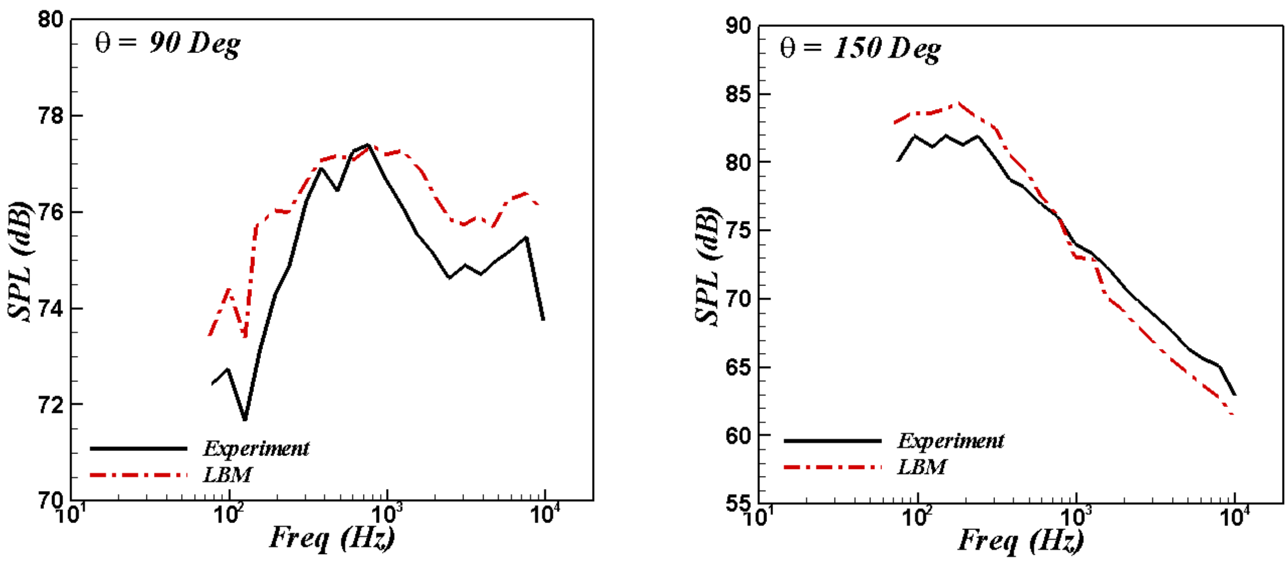

Fig. 5-28 One-third Octave band Pressure level spectra at (a) θ = 90° and (b) θ = 150°. LBM-FW-H simulation compared to the measure data. (Mengle *et al.*, 2002)

Part B- Acoustic absorption of jet flows

Chapter 6

Sound absorption by turbulent jets

6-1 Motivation

Interaction between the fluid flow and sound waves is an interesting phenomenon in physics and has been the focus of many studies in field of aeroacoustics. The propagation of sound inside a confined space, *e.g.* inside the pipes, mufflers, aeroengines and etc. could be highly affected by the geometry, acoustic treatments of walls and the mean flow characteristics. Effective noise cancellation using passive techniques is only achievable via thorough study of the mean flow, turbulence, acoustic paths and sound attenuation.

Jet flows are mostly known as a source of aerodynamic sound; however, jet flows can also absorb acoustic energy propagating from sources upstream from the jet. Such incident waves at nozzle exit area can change the turbulence characteristics such as turbulence intensity and transition distance of the jet flow (Ginevsky *et al.*, 2004).

A simulation tool that is capable of capturing such phenomena should be able to model multi-scale problem including the transient turbulent flow structures at the jet region, acoustic flow in the upstream region, *i.e.* broadband spectrum and tonality as well as the interaction of sound waves with solid boundaries and attenuation due to turbulence and viscosity.

In Part (B) of the present study, the LBM that was used in previous chapters to simulate jet noise is now challenged by simulation of acoustic-flow interaction with significant application in industrial noise control.

In order to show the capabilities of the LBM in such acoustic flow setup, the propagation of sound in a circular pipe with mean flow and an orifice plate was selected as a benchmark problem. The mean flow causes the jet to discharge to the downstream region by passing through the orifice plate. The jet is also affected by the sinusoidal sound source as the pipe inlet boundary. Lessons learned, and experiences achieved in the jet noise setup from chapter 3, *i.e.* grid resolution and VR distribution, were applied to capture sufficient turbulent scales at the orifice location and sound absorption parameters such as the absorption ratio and acoustic impedance of the orifice plate with were compared against the experimental data. The Simulation results presented in this chapter are also based on the published materials by the author (Habibi and Mongeau, 2015).

The simulation of pure acoustic pulses without mean flow over solid boundaries was studied separately by the author, (Habibi *et al.*, 2012) and presented in Appendix C of this document, in which the LBM results were compared with an in-house experimental setup.

6-2 Introduction

The absorption of sound waves by single or multiple orifice plates has broad applications for the design of liners and other devices for the suppression of tonal and broadband aerodynamic noise. It is well known that sound waves in ducts with flow are absorbed during transmission and reflection by orifices or nozzles. The primary sound absorption mechanism involves the conversion of sound energy into turbulence kinetic energy and also the formation and shedding of vortices at the orifice discharge (Bechert *et al.*, 1978; Bechert, 1980). This phenomenon is of great importance in the design of quiet exhaust systems, absorbing sound barriers, acoustic liners in aeroengines, and many other applications. Shear flow instabilities, the shape and profile of the orifice, and possible interactions with the tube wall are factors that may affect the acoustic characteristics of the orifice plate Manning (1991)in presence of a superimposed mean flow. Most of the energy transferred, *i.e.* absorbed, through the orifice is supplied by the kinetic energy of the mean flow inside the channel. It is argued that flow disturbances at the orifice inlet and the Kutta condition[1] (Anderson Jr, 2010) at the edge cause toroidal vortical structures to be formed and shed from the orifice plate (Bechert *et al.*, 1978; Bechert, 1980). Bechert's predictions and semi-empirical model were corroborated by measurements, and comparisons with previous experimental data (Bechert, 1980). A theoretical framework for the problem was proposed by Howe (1979; 1984). He proposed a linearized model, assuming that the Mach number of the orifice

1- The Kutta condition is a principle in aerodynamics, that regulates the flow downstream of solid bodies with sharp corners, such as orifices or the trailing edges of airfoils. It is named after German mathematician and aerodynamicist Martin Kutta .

jet flow is relatively low. He also assumed that the incident acoustic energy is dissipated by two distinct mechanisms (Howe, 1979), first the acoustic characteristics of medium at orifice downstream, in which the directivity of transmitted sound waves is more universal and equivalent to magnitude, produced by monopole and dipole sources. Second is the formation of vortex waves excited by the shedding of vortices from the nozzle edge, which are triggered by the large-scale instabilities of the jet. Most of Howe's derivations are based on the extended vortex sound theory (Howe, 1975), which originated from Powell's vortex sound hypothesis (Powell, 1964). Wendoloski (1998) extended Howe's theory to deal with orifice plates in ducts with mean flow using a Green's function expansion, using a novel renormalization technique.

Three dimensionless parameters define the orifice flow regime: (1) the Mach number at the orifice plate, M_o, based on the orifice mean flow velocity; (2) the nominal Strouhal number, St_o, based on the excitation frequency and velocity amplitude as well as the orifice diameter, D_o , and (3) the open area ratio, σ_o, defined as the ratio of the orifice area and the tube area (D_o^2 / D_T^2). For the case of multiple orifices in parallel, the opening area ratio is replaced by the porosity of the plate (Wendoloski, 1998).

The driving pressure amplitude has a great impact on the orifice absorption phenomenon. Ingard and Ising (1967) performed parametric studies of the effects of excitation amplitude on the absorption coefficient. The relation between the absorption coefficient and the acoustic pressure and velocity amplitudes was found to be strongly nonlinear for relatively high excitation amplitudes (Ingard and Ising, 1967).

The acoustic characteristics of orifice plates have been investigated in more recent experimental studies. Ahuja *et al.* (2000) have conducted comprehensive experiments to measure the impedance of a single orifice plate in presence of a bias flow. Parametric studies were performed on the effects of various driver set points as well as mean flow strengths in terms of orifice Mach number. The absorption coefficient and orifice impedance values were reported (Ahuja *et al.*, 2000). Hughes and Dowling (1990), and also Jing and Sun (1999) measured the impedance of perforated orifice plates. The results were found to be in good agreement with Howe's Rayleigh conductivity model (Howe, 1998). Attempts were made to find the acoustic properties of orifice plates using computational fluid dynamics techniques. Tam *et al.* (2005) performed direct numerical simulations (DNS) of flow through a slit resonator. They investigated the orifice impedance over the frequency range of 0.5 to 3 kHz for two slit geometries (*i.e.*, 90^o straight and 45^o beveled slits). The Navier-Stokes equations were discretized using the Dispersion Relation Preserving (DRP) scheme. A wave decomposition method based on the virtual two-microphone model was used to determine the reflection factor. The absorption coefficients were found to agree with experimental data obtained at the NASA Glen Research Centre (Tam *et al.*, 2005). In a previous study, Tam *et al.* (2001) used the same DNS method for numerical simulations of acoustic flows through straight slit orifices. The energy dissipation rate was calculated and used to determine the absorption coefficient. Results were compared to experimental data obtained by (Ahuja *et al.*, 2000; Tam *et al.*, 2001) and found to be in good agreement. Despite its accuracy, the DNS method is not always practical for realistic engineering applications because of its prohibitive costs. For the low frequency excitation as well as the low Mach number at orifice discharge, two-dimensional simulations have yielded relatively accurate results at reasonable cost, as argued by Ji and Zhao (2013).The 2D planar flow assumption was also found to be useful in predictions of tonal whistling phenomena (Kierkegaard *et al.*, 2012). In their study, the Reynolds Averaged Navier-Stokes (RANS) method was first used to determine the mean flow. The linearized Navier-Stokes method was then used for the calculation of transient flow characteristics.

Development of a generic and reliable computational method for the accurate prediction of orifice at normal flow incidence can also help to tackle the important problem of sound absorption in presence of grazing flows (Kooijman *et al.*, 2008). This configuration is used in the design of acoustic liners for ventilation ducts, turbofan engine nacelles and the exhaust systems of internal combustion engines (Motsinger and Kraft, 1991).

For the case of high speed flows through the orifice, the accurate prediction of sound absorption will highly depend on the quality of turbulent jet simulation downstream of the orifice. For higher Mach numbers, a three-dimensional numerical scheme as well as sufficient grid resolution is required to simulate the turbulent shear layer right at the edge of the orifice. The selected numerical scheme should have reasonable computational cost and should be capable of capturing details of orifice geometry.

In the present study, the Lattice-Boltzmann Method (LBM) coupled with the large eddy simulation methodology (LBM-VLES) was used for numerical simulations to predict sound absorption by an orifice plate in the presence of mean flow in a full-scale, 3D virtual impedance tube apparatus. LBM simulation of acoustic flows over solid boundaries was studied (Habibi *et al.*, 2012) which is presented in Appendix C of this document. As mentioned in section 6-1, Simulation setup and results of this part are based on the published materials by the author (Habibi and Mongeau, 2015) where broad frequency range of 380 Hz to 6 *k*Hz and Mach numbers, 0.05 to 0.2, were considered. The three-dimensional 19-stage LBM could resolve the turbulent jet formed through the orifice. Three-dimensional assumption will help to accurately model the vortex stretching phenomena which contributes to the formation of turbulent jet downstream of the orifice as well as the energy absorption. As for the jet noise studies discussed in chapters 3, 4 and 5, this method was combined to the Very Large Eddy simulation (VLES) method in which the large-scale turbulent structures are simulated directly, and sub-grid scales are modelled. This methodology features less computational cost comparing to the DNS schemes (Tam *et al.*, 2001). The setup can be used for even higher Mach numbers and higher frequency ranges. Also unlike RANS simulation proposed by Kierkegaard *et al.* (2012), the LBM-VLES is highly suitable in unsteady simulation of flow separation at the edge of the orifice plates and since the method is intrinsically transient, there is no need to combine it with an transient model to get acoustic characteristics and could save several computational steps comparing to the RANS simulations. All dimensions, scales and flow characteristics used in this study were based on the experimental setup described by Ahuja *et al.* (2000). The complex reflection factor was determined using a wave decomposition technique which involved simultaneously recording the pressure and velocity history at multiple locations upstream of the orifice plate.

6-3 Problem Description and main parameters

One common method to determine the absorption coefficient and the acoustic impedance of a material is to use the impedance tube (IT). For permeable samples including the orifice, the apparatus consists of an acoustic driver at one end of a rigid tube and an anechoic termination is provided at the other end. An orifice plate is located somewhere in the tube. A typical IT device was described by Ahuja *et al.* (2000). In the experimental setup, in order to maintain a mean flow inside the channel, a vacuum pump was connected to the downstream section of tube with acoustically insulated terminals placed upstream to balance the pressure inside the channel. The

IT measurements are usually performed in accordance with international standards such as *ASTM -E1050* (ASTM, 2010). The bandwidth of the experiments is limited to tube size. The upper limit is to ensure plane wave propagation through the pipe while the lower limit depends on the microphones spacing and the accuracy of the phase measurements for the finite difference approximations of the acoustic pressure and velocity.

A schematic configuration of a simple IT is shown in Fig. (6-1). Different parameters affect the measurements and the acoustic properties of the orifice. The list of important variables is shown in Table (6-1). The orifice Mach number and the nominal Strouhal number govern the acoustic behaviours of the orifice plates (Wendoloski, 1998); however, the excitation amplitude and thickness are also reported to affect the physics of sound absorption (Ingard and Ising, 1967). In this study, the IT was modeled based on full-scale dimensions provided by (Ahuja *et al.*, 2000). The orifice under consideration was circular with diameter of 0.1954 inches (4.96 mm) and the following geometrical variables in figure (6-1) were normalized by the orifice diameter and remained fixed throughout the simulation; $D_T/D_o = 5.73$, $t_o/D_o = 0.16$, $L_1/D_o = 110.67$, $L_2/D_o = 88.92$, $L_a/D_o = 10.00$.

6-4 Computational Setup

The computational domain was divided into structured lattice arrays with variable resolutions (VR). In the numerical setup, four levels of VR regions were used upstream of the orifice. As discussed in chapter 1 and 2, this procedure is analogous to grid stretching used in finite-difference and finite-volume numerical schemes. The lattice length from one VR to another always varies by a factor of two to ensure appropriate particle convection along pre-assigned discretized velocity directions. Figure (6-2) shows the grid setup and VR regions used in this study. The huge computational domain in the streamwise direction downstream of the orifice and use of coarser grid at outermost layers ensured reflected sound wave attenuation and provided a uniform region for probing the flow history at the upstream boundary for acoustic calculations.

A total of 15.8 million grid cells (voxels) were used. As shown in Fig. (6-2), four variable resolution area with conical shape were introduced in the computational domain. VR0 is related to the coarsest grid resolution while VR3 is the finest grid at upstream and downstream of the orifice. The aspect ratios of the cones were 3.0, 2.0 and 1.6 for VR1, VR and VR3 respectively. The positions of VR regions with respect to the orifice are shown in Fig. (6-2). The smallest voxel size of $0.050 \times D_o$ was placed near the orifice entrance and in the jet plume shear layer. The specified resolution is set in such a way to resolve the shortest wave length (*i.e.* highest frequency limit) by over sixty voxels ($x_{max} \cong 60\ \lambda_{min}$) at the coarsest level upstream of the orifice which deemed sufficiently fine to achieve very low numerical dissipation rate. A previous study performed by Brés *et al.* (Bres *et al.*, 2009) showed that a minimum of fifty points per wavelength is required to achieve numerical absorption level of 0.01 dB/λ and less for a simulation that incudes turbulence modelling.

The Reynolds number was matched to that of experimental setup based on the orifice diameter and mean orifice jet velocity for all set points for each orifice Mach number. Turbulent sub-grid scale structures were modelled using the Very Large Eddy Simulation (VLES) method (Chen *et al.*, 2003),

The volumetric boundary scheme (Chen, 1998) was used to handle particle bounce-back at the solid boundaries. As discussed earlier, this algorithm is well customized for complex geometries as shown in chapter 4 and 5 in simulation of double-stream jets involving complex nozzle-mixer geometries. Turbulent wall boundary conditions are applied by a generalized LBM slip algorithm and a modified wall-shear stress model significantly reducing the near wall grid resolution required for capturing turbulent structures close to the solid boundaries. The outermost region near the outlet, $L_a = 10\ D_o$ combines relatively coarse grid with high viscosity that provides proper viscous damping effects for further dissipation of outgoing waves, thus acting systematically as a 'sponge' zone.

The inclusion of the orifice solid body in the computational domain ensures sufficient initial perturbations at the orifice exit for the jet to breakup close to the orifice trailing edge, even at low Reynolds numbers. The inlet boundary condition was set to the fluctuating positive pressure as defined as

$$P/P_a = 1 + \left(A^*/2\right)\left(1 + cos(\omega t)\right), \tag{6.1}$$

where $A^* = A/P_a$, A is the acoustic pressure amplitude and P_a is the ambient pressure. In the experimental setup, The flow is entering the impedance tube through eight 1/8 inch diameter holes equi-spaced around tube 19.875 inch from the orifice (Ahuja *et al.*, 2000). A fixed mass flow rate was imposed at the tube outlet. The magnitudes were selected to match available experimental data (Ahuja *et al.*, 2000). The mass flow rate value could maintain desired Mach number at the orifice outlet.

6-5 Acoustic Calculations

Six virtual probes were considered in random intervals upstream from the orifice plate to be used for acoustic sampling. The locations of the probes in this study are indicated in Fig. (6-3). The average value of the pressure and velocity over four lattice length in the vicinity was calculated. The averaging process is necessary to reduce spatial noise and to account for the effects of finite microphone size. A random spacing was selected for probe distribution. Jones and Parrott (1989) argue that a uniform spacing might be inaccurate at certain frequencies. They might be located near acoustic nodes and hence sensing very small amplitudes of the same order of magnitude as the experimental or numerical errors. Acoustic calculations included a wave decomposition procedure of the standing sound wave field upstream of the orifice plate. This process was initiated by extracting the pressure and velocity history at the probe locations. These data were used to calculate the reflection factor from which the absorption coefficient and the acoustic impedance of the orifice plate were obtained. The calculations were done in the frequency domain. Each probe sampled both pressure and velocity signals at the same location. Using linearized wave solution that considers the presence of a mean flow, the relationship between the acoustic velocity and pressure was obtained. The complex pressure and velocity at each probe location were obtained using the Fourier transform. To get an accurate signal, the sampling frequency and start time are of great importance. Around 2×10^5 timesteps were required to achieve a steady state periodic wave field inside the tube as shown in Fig. (6-4). Sampling started after the steady periodic state was achieved and extended over a sufficient time of about 0.08 seconds to achieve the maximum spectral resolution of $\Delta f \cong 12$ Hz. The complex acoustic pressure and velocity magnitudes should be corresponded to the excitation frequency. To minimize the bias due to the spectral leakage errors, the amplitude of the tonal signals was obtained by summing up consecutive frequency components on energy basis. The five-point stencil was used. This energy summation method was also compared to the case in which Hann windowing was applied and resulted in almost the same magnitude with a maximum 3% variation.

The acoustic field in the orifice upstream region was decomposed into incident and reflected waves. The acoustic pressure phasor of the j^{th} probe may be generally decomposed as

$$\hat{P}_j = \hat{P}_j^I e^{i\Gamma_I x_j} + \hat{P}_j^R e^{i\Gamma_R x_j}, \tag{6.2}$$

where superscripts I and R denote the incident and reflection values respectively, subscript j refers to the location of the j^{th} probe. The reference point (*i.e.* $x=0$) is the orifice location. The complex wave number, Γ, in Eqn. (6.2) is defined as

$$\Gamma_{I,R} = \pm\left(k_{I,R} + i\alpha_{I,R}\right), \tag{6.3}$$

The wave number, k, is modified to account for the mean flow (Jones and Parrott, 1989) which is presented as

$$k_{I,R} = (\omega / c)/(1 \pm M_T), \tag{6.4}$$

where M_T is the mean Mach number of the tube flow upstream from the orifice. Turbulence and thermo-viscous losses were modeled using the correlations by Ingard and Singhal (1974), who have estimated the effect of the tube wall absorption coefficient in the presence of mean flow using the following relation which is

$$\alpha_{I,R} = (\beta_T + \beta_\nu)/(1 \pm M_T), \tag{6.5}$$

where, β_T is corresponding to the dissipation of acoustic energy due to the turbulence inside the channel, β_υ quantifies thermo-viscous losses in channel walls, and M_T is the Mach number in the upstream direction. The amount of losses owing to turbulence in the channel have been suggested by Ingard and Singhal (1974) as

$$\beta_T = (2\psi M_T / D_T)\left[1\big/\left(1 + 0.869\sqrt{\psi}\right)\right], \tag{6.6}$$

where D_T is the tube diameter, ν is the kinematic viscosity, and c is the speed of sound. Ψ is the friction coefficient which can be calculated using Prandtl universal resistance law (Jones and Parrott, 1989) stated by,

$$1/\psi = 2Log_{10}\left(\text{Re}\sqrt{\psi} - 0.8\right). \tag{6.7}$$

Neglecting heat transfer through walls, and assuming a fully turbulent flow, viscous losses can be estimated by Kirchoff's relation (Jones and Parrott, 1989) as

$$\beta_v = \left(1/D_T c\right)\left(2\omega\nu\right)^{1/2}. \tag{6.8}$$

An alternate method to include the visco-thermal attenuation in which the turbulent losses are neglected has been suggested by Dokumaci (1997). As the Mach number in the tube far from the orifice is small ($M_T \sim 0.017$), based on Eqn. (6.6), β_T, would have a small magnitude and the effect on the absorption coefficient would be less than one percent and can indeed be neglected. The thermal losses, on the other hand, cannot be distinguished from viscous losses in LBM simulation due to the isothermal assumption and the presence of the numerical dissipation. The turbulence dissipation, however, is resolved by the LBM. To capture the viscous losses, an auxiliary energy equation that contains viscous dissipation terms must be coupled with the momentum equations. This approach was not used in the current study.

In the present study the viscous attenuation factor β_υ was replaced with the numerical dissipation factor β_n. To evaluate the dissipation rate, a numerical experiment was performed inside a three-dimensional tube of the same dimension scales as the main orifice setup using the finest grid resolution and viscosity. The fundamental frequencies and amplitudes were also selected as for the main orifice case. The length of the channel was set to $18D_T$. The amplitude was assumed to be P_0, the pressure distribution along tube was assumed to obey the relation:

$$P = \Re\left\{P_0 e^{-\alpha x}.e^{ikx}\right\}. \tag{6.9}$$

By tracking the maxima of pressure magnitude, the pressure decay rate from the LBM simulation corresponding to the numerical dissipation can be calculated. This procedure is illustrated in Fig. (6-5) for frequency of 6 kHz. This study was repeated for other frequencies (*i.e.* 1-6 *k*Hz) and the results are listed in Table (6-2). Calculated values in Table (6-2) suggest that numerical dissipation was a weak function of frequency and mostly related to the grid resolution and bulk viscosity (Crouse *et al.*, 2006a). In our main numerical study, we replaced the thermo-viscous factor, β_υ, with the numerical dissipation factor, β_n, which was extracted from Table (6-2) based on the frequency and the grid resolution. The acoustic velocity could be calculated based on the linearized Euler equation taking into account non-zero mean flow in the field is written as

$$\hat{V}_j = \left(1/Y\right)\left(\hat{P}_j^I e^{i\Gamma_I x_j} + \hat{P}_j^R e^{i\Gamma_R x_j}\right), \tag{6.10}$$

where Y is the modified characteristic impedance taking into accounting the losses (Munjal and

Munjal, 1987) defined as

$$Y = \rho c\left[1 - \left(\beta_T + \beta_n\right)/k + i\left(\beta_T - \beta_n\right)/k\right]. \tag{6.11}$$

Equations (6.2) and (6.10) constitute two sets of complex equations with two complex unknowns: $\hat{P}_j^I$ and $\hat{P}_j^R$. By solving for these complex values, the absorption coefficient of the orifice plate, α_o defined by the ratio of acoustic energy absorbed by the orifice plate to the incident energy. The absorption coefficient and the impedance values at orifice location, *i.e.* $x = 0$, were obtained using

$$\alpha_o = 1 - \left| P_j^R / P_j^I \right|^2, \tag{6.12}$$

and

$$\hat{Z}_o = R + Xi = Y\left(1 + P_j^R / P_j^I\right) / \left(1 - P_j^R / P_j^I\right). \tag{6.13}$$

The absorption coefficient values were calculated for six probes, *i.e.* $j_{max} = 6$, located randomly upstream of the orifice. The final absorption coefficient, $\alpha_{o,t}$ for each set point was obtained by averaging over six values given as as

$$\alpha_{o,t} = \frac{1}{j_{\max}} \sum_{j=1}^{j=j_{\max}} \alpha_{o,j}, \tag{6.14}$$

6-6 Results and discussion

The simulation was completed for the acoustic excitation amplitude fixed at 145 dB and a low frequency set point of 380Hz, *i.e.* $kD_T = 0.2$, and five high frequency cases of 1, 2, 3, 4 and 6 *k*Hz. The high frequency cases were used to compare LBM results with experimental data (Ahuja *et al.*, 2000). The analytical solutions proposed by (Wendoloski, 1998) covers both high and low frequency ranges. The mean flow strength was characterized by the orifice Mach number. Both the experiments and the numerical simulations were done for Mach number values of 0.05, 0.1, 0.15, and 0.2 using the mass flow rate 0.55, 1.20, 2.00 and 3.1 ft^3/s[1] at the outer boundary. The maximum Reynolds number based on the orifice diameter was ≃21,500 whereas the maximum Reynolds number based on the mean velocity upstream of the tube and the tube dimeter reached ≃3700. Selected Mach number range was less than 0.5, that falls well inside the validity range of the D3Q19 LBM. In the absence of acoustic waves, velocity profiles along the tube cross section

[1] - 1 ft^3/m (CFM) = 0.0283168 m^3/s

in the vicinity of the orifice plate at x = 10D_o were compared with hot wire measurement data (Ahuja *et al.*, 2000). Non-dimensional velocity profiles for different orifice Mach numbers are shown in Fig. (6-6) with respect to the distance from the lower wall (*i.e.* $0 \le y \le D_T$). This comparison allowed the verification of the predicted tube outlet boundary condition used in the simulations, by comparing to the mass flow rate values given by the experimental data (Ahuja *et al.*, 2000). The velocity profile for M_o = 0.05 is parabolic and laminar as shown in Fig. (6-6). For higher Mach numbers, *i.e.* Re_T >1200 the velocity profile was more logarithmic, as expected for a fully turbulent flows inside a confined tube.

The periodic acoustic flow through the orifice causes the formation of ring vortices at the orifice trailing edge. This phenomenon was studied by observing the pressure contours inside the IT. Figure (6-7 (a)) shows the shedding of vortices from the orifice edge. Figure (6-7 (b)) depicts a velocity iso-surface of a turbulent jet formed downstream of the orifice, the strength of which characterizes sound absorption of the orifice plate. The absorption coefficient obtained from the LBM simulation for the case of kD_T = 0.2 was compared with the analytical solution and plotted in Fig. (6-8) as a function of orifice Mach number. The optimum Mach number corresponding to the maximum absorption is predicted to be 0.09 for this condition. As explained in Wendoloski (1998), the area ratio or the porosity in cases where there are several orifices is the key factor affecting the absorption efficiency should be taken into account for more detailed parametric studies. The frequency dependence of the orifice absorption for a fixed Mach number of 0.005 from LBM results, experimental data (Ahuja *et al.*, 2000) and the analytical solution (Wendoloski, 1998) are shown in Fig. (6-9). It shows that an increase in excitation frequency reduces the sound absorption of the orifice over the frequency range above 1 kHz. According to Fig. (6-9), the absorption coefficient for the low frequency range (*i.e.* kD_T < 1.5) was better predicted by LBM comparing to the analytical solution. This is due to the fact that large scale turbulent structures in the vicinity of the orifice edge together with energy transmission from upstream channel are simulated via LBM. Effects of sub-grid scale structures are also included in the turbulence model implemented in the LBM code. Numerical method has several advantages over the analytical formulation proposed in Wendoloski (1998) as well as similar analytical solution using Howe's Rayleigh conductivity concept (Howe, 1998). First, the large eddy simulation method used in this study can better capture the physics of the turbulent jet which becomes more important as Mach numbers increases. Second, the details of the orifice and duct geometries can be included into computational domain without any simplifying assumptions. Figure (6-10) shows the predicted sound absorption comparing to measured values for high frequencies. The trends and magnitudes of the absorption coefficient are in reasonable agreement with the measured data (Ahuja *et al.*, 2000). An interesting observation in Fig. (6-10), is the fact the Mach number dependence of the sound absorption coefficient varies with the frequency or the wave number. From a physical point of view, this implies that the contribution of high frequency acoustic waves to supply energy for vortex shedding increases when the Mach number is increased; hence, more energy is absorbed by increasing the Mach number, *i.e.* larger α magnitude. For the low frequency waves, the mean flow seems to have more contribution on supplying required kinetic energy for vortex formation process and hence, less acoustic energy required from the upstream channel, *i.e.* smaller α values. This observation is consistent with the acoustic model developed by Howe (1998) and Wendoloski (1998). Figure (6-11) and (6-12) show the real part ,*i.e.* Resistance *(R)*, and the imaginary part, *i.e.* Reactance (X), of the impedance (Z) value respectively. As for the absorption coefficient, both values were averaged over all probe locations. The calculated impedance value at each frequency and orifice Mach number was normalized by the characteristics impedance (ρc). The results show consistent variations of impedance values comparing to experimental data.

6-7 Chapter highlights and main learning points

In this chapter, a one-microphone was developed to predict acoustic absorption coefficient of jet flows through an orifice. This study was the base of a new studies by Mann *et al.* (2013) to characterize the acoustic liners. In our approach, We proposed a method to correct losses due to numerical dissipation. Also, a multi-probe system was proposed to alleviate numerical noise and reduce acquisition time. The relation between the orifice Mach number and acoustic absorption was predicted with good accuracy compared to experimental data Acoustic flow over a flat spoiler were simulated as ide study to validate acoustic flows using in-house PIV data .Variations of the sound absorption coefficient with respect to orifice mean velocity and the excitation frequency were studied and compared with the available analytical solution and experimental data. Both flow and acoustic results were in good agreement with the experimental measurements. The LBM was shown to be a powerful tool for modelling low-Mach complex fluid flows interacting with the acoustic waves. The VLES turbulence scheme was found to be an effective and accurate method to capture realistic behaviour of the acoustic-flow field, correct prediction of velocity profiles as well as the turbulence dissipation rate.

Table 6-1 Main parameters

Variable	Description	Non-dimensional
D_o	Orifice diameter	-
D_T	Tube Diameter	D_T/D_o
t_o	Orifice plate thickness	t_o/D_o
L_1	Upstream length	L_1/D_o
L_2	Downstream Length	L_2/D_o
L_a	Absorption Thickness	L_a/D_o
U_m	Mean Flow velocity	Orifice Mach number ($M_o = U_m/c$*)
f_{ex}	Excitation frequency	Orifice Strouhal number $(f_{ex} . D_o) / U_{ex}$
A_{ex}	Excitation Amplitude (Pressure)	$SPL = 20\text{Log}(P/P_0$**$)$

* *c* denotes speed of sound at the laboratory temperature $c = (\gamma RT)^{0.5}$

** P_0 denotes the reference pressure: $P_0 = 2\times10^{-5}\ Pa$

Table 6-2 Attenuation factor (β) comparison

Frequency (Hz)	1000	2000	3000	4000	6000
β_n from LBM	0.0235	0.0242	0.0245	0.0257	0.0273
β_ν from Eqn. (6.8)	0.0711	0.100	0.123	0.142	0.1743

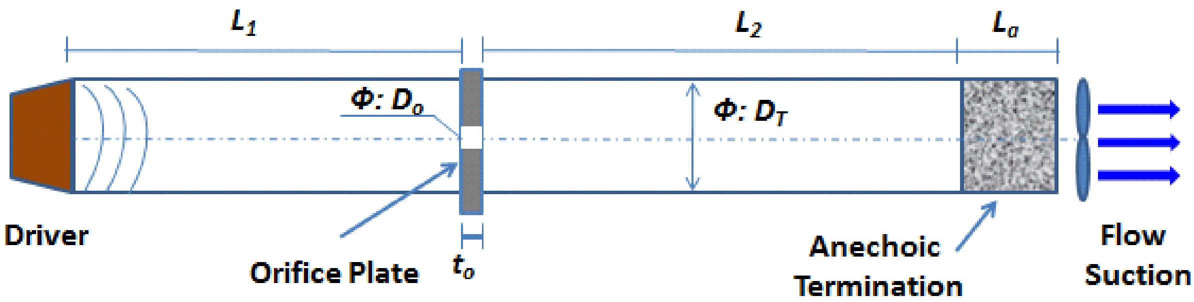

Fig. 6-1 Orifice plate configuration in an impedance tube for acoustic measurements

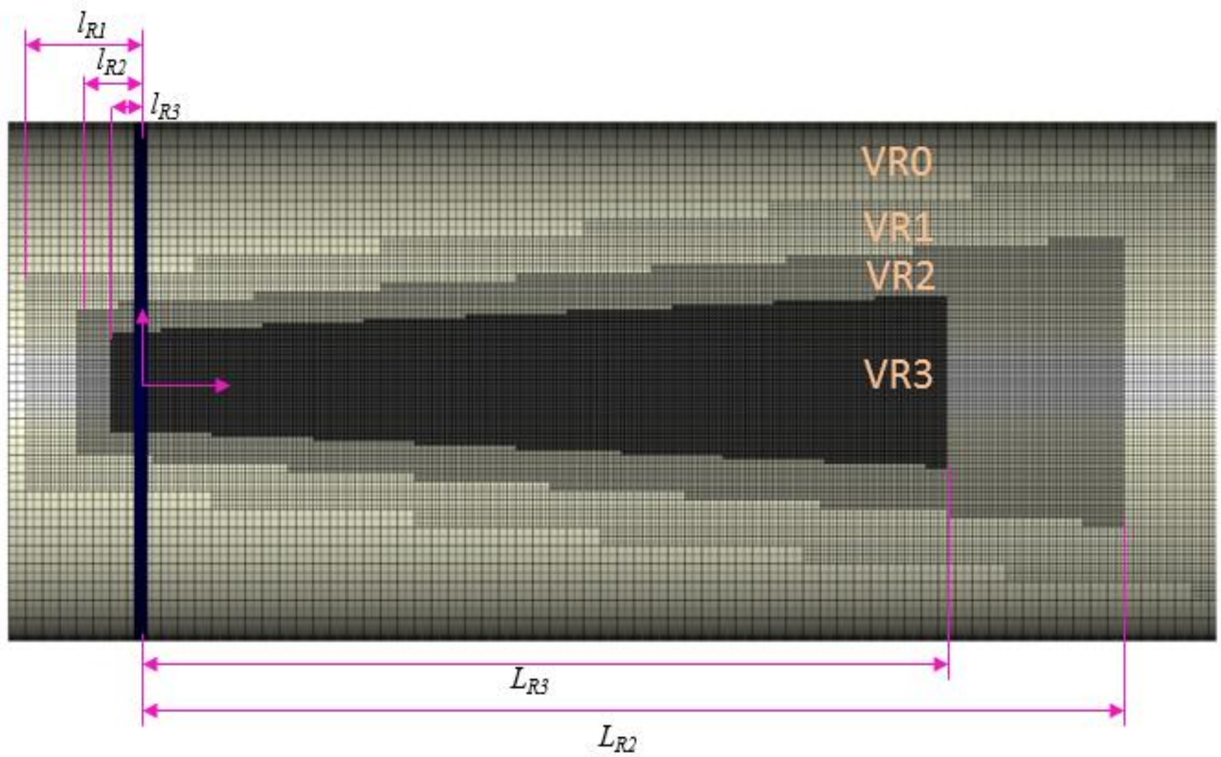

L_{R1}/D_0	L_{R2}/D_0	L_{R3}/D_0	l_{R1}/D_0	l_{R2}/D_0	l_{R3}/D_0
16.0	13.0	11.0	1.8	1.0	0.4

Fig. 6-2 Structured grid (lattice) distribution near the orifice plate.

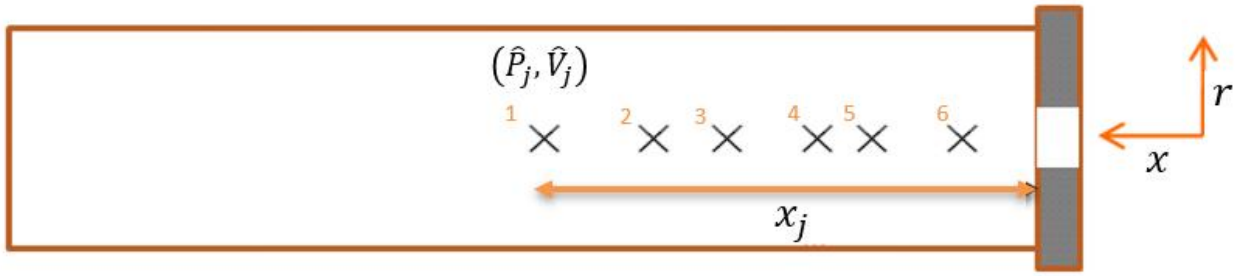

Probe location	x_1 / D_0	x_2 / D_0	x_3 / D_0	x_4 / D_0	x_5 / D_0	x_6 / D_0
	6.8	**5.3**	**4.2**	**3.1**	**2.2**	**0.8**

Fig. 6-3 Probe locations upstream of the orifice.

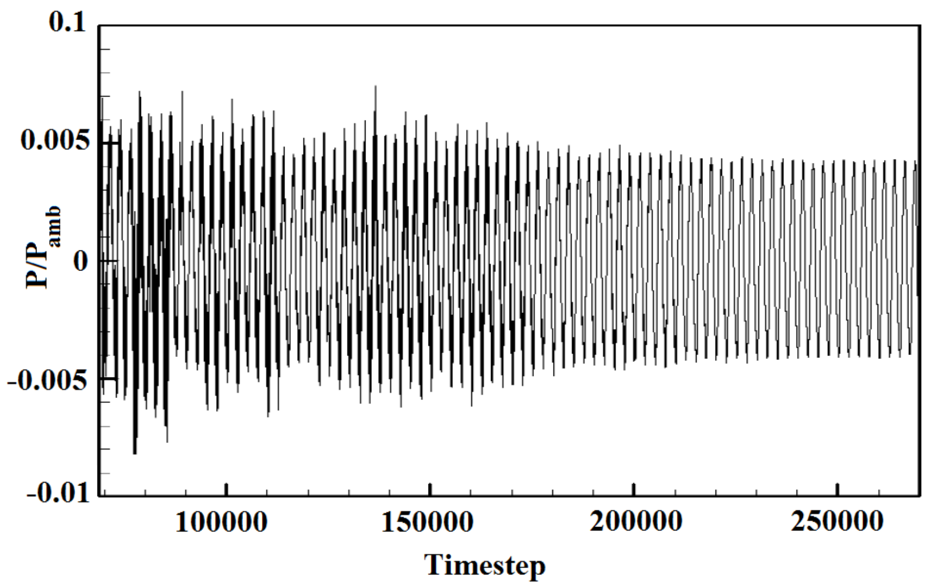

Fig. 6-4 Acoustic pressure signal recorded by probe at $x = 6D_o$ upstream of the orifice plate.

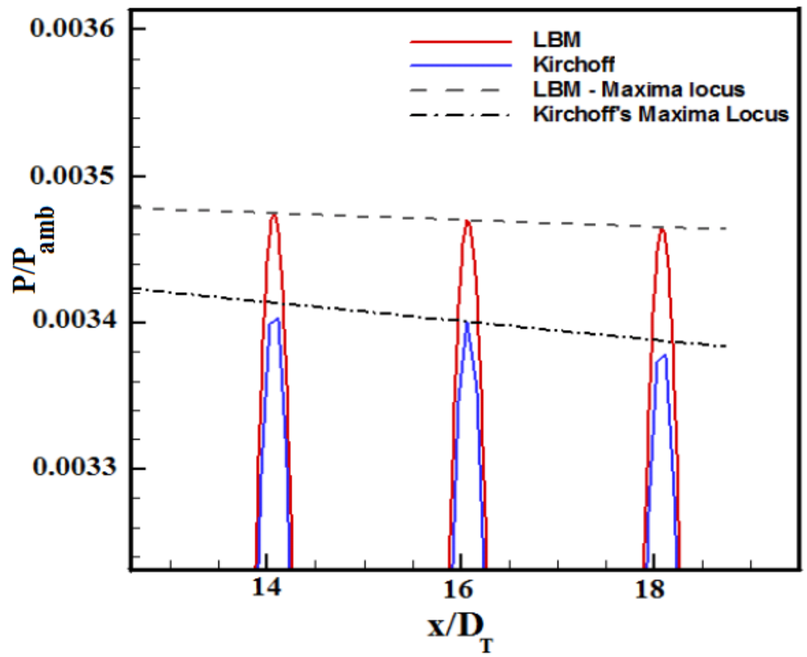

Fig. 6-5 Sound attenuation due to the numerical dissipation vs. analytical thermo-viscous dissipation.

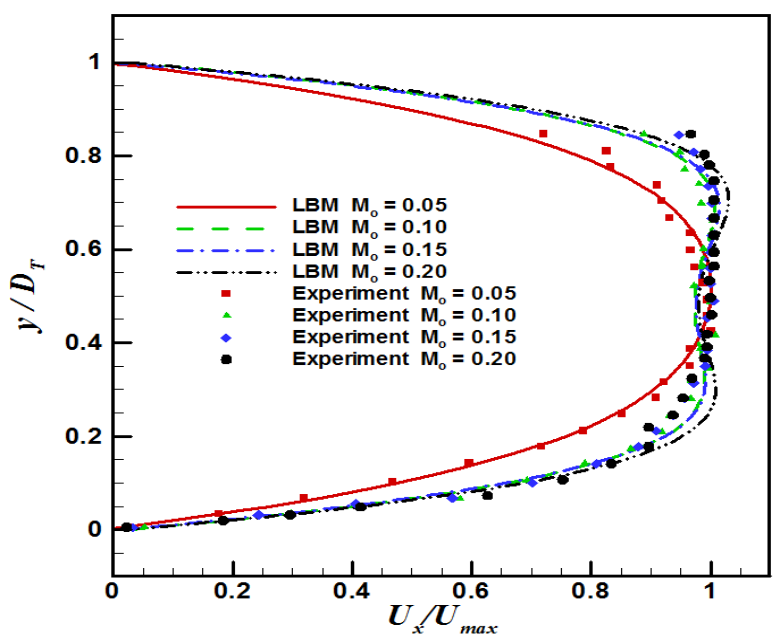

Fig. 6-6 Streamwise velocity profile at orifice upstream (x~10D_o).

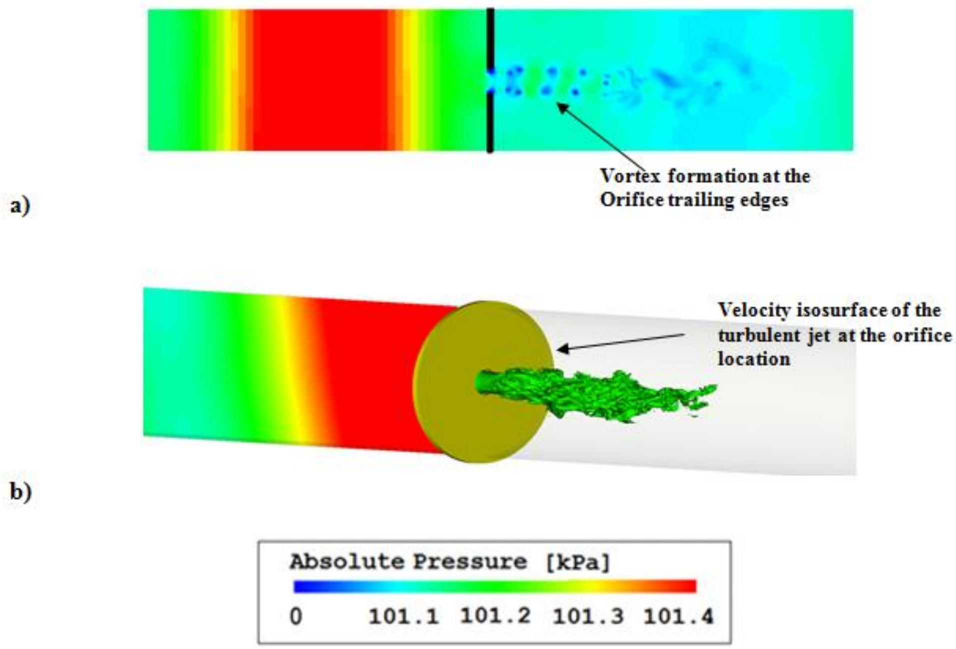

Fig. 6-7 a) Vortex formation and shedding at the edge of orifice b) Velocity iso-surface (*i.e.* 0.5 m/s) of turbulent jet originated from the noisy mean flow across the orifice.

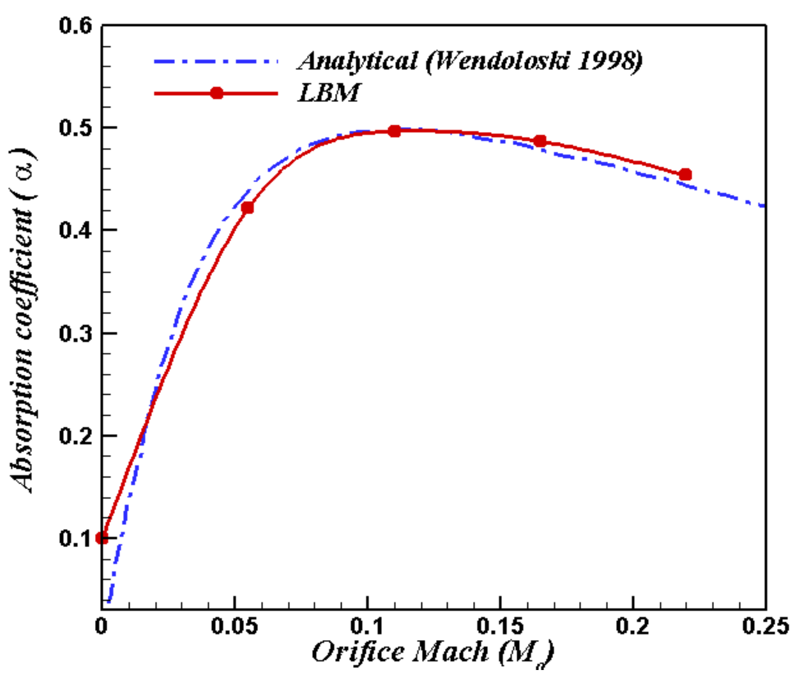

Fig. 6-8 Sound absorption coefficient with respect to orifice Mach number for low frequency case (kD_T = 0.2).

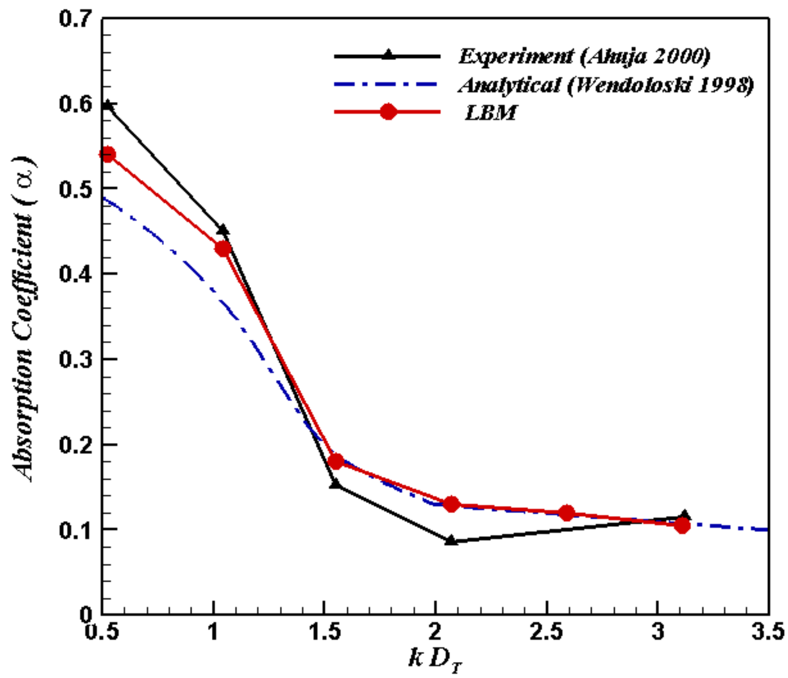

Fig. 6-9 - Frequency dependence of sound absorption coefficient at fixed orifice Mach number (*i.e.* M_o = 0.05).

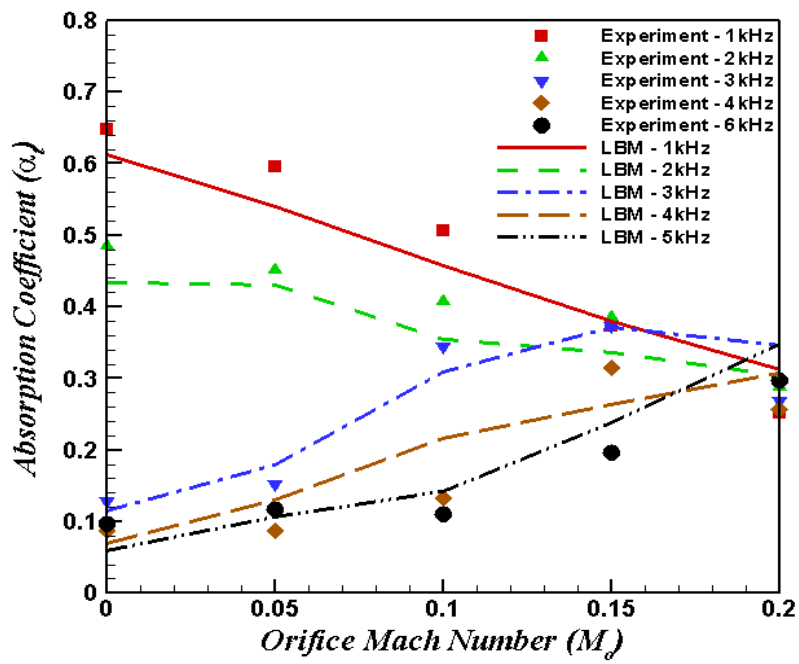

Fig. 6-10 Sound absorption coefficient variation with mean flow strength and the excitation frequency.

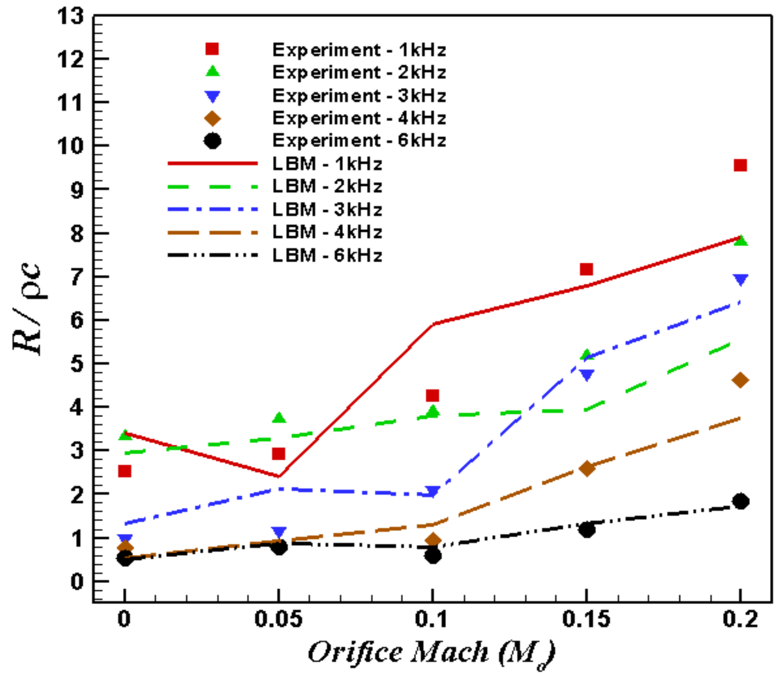

Fig. 6-11 Variation of the normalized orifice resistance with the Mach number and the excitation frequency.

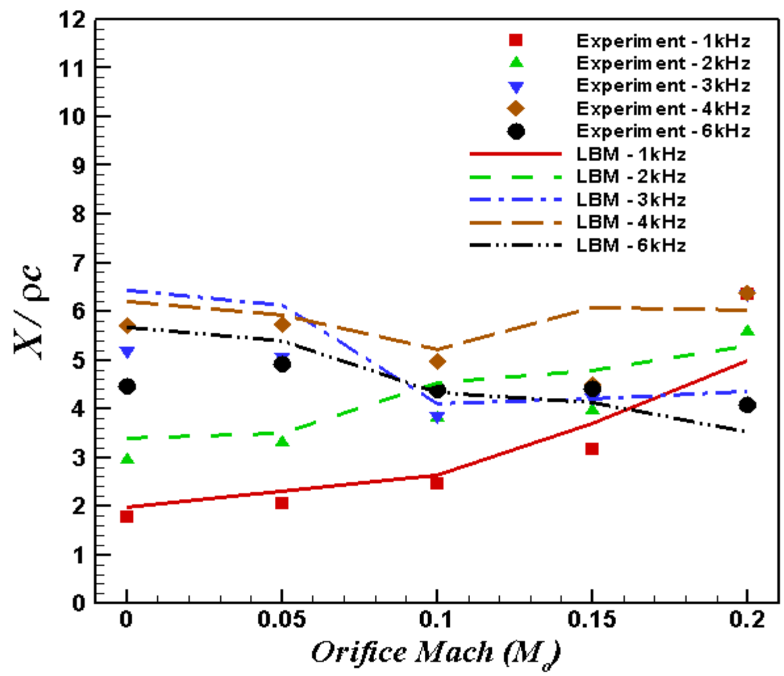

Fig. 6-12 Variation of the normalized orifice reactance with the Mach number and the excitation frequency.

Chapter 7

Conclusions and future work

7-1 Conclusions

7-1-1 Single-stream jet noise simulation

From the results obtained in Chapter 3 for the simulation of single-stream jets, the sound produced by isothermal and heated turbulent jet flows at low and moderate Mach numbers were simulated using 19-stage D3Q19 LBM using both under-resolved DNS (uDNS) scheme as well as VLES method with turbulence modelling. A robust hybrid heat transfer model compatible with LBM was used to obtain the temperature field and study the effects of heat transfer on the far-field radiated sound. The near-field flow variables as well as flow statistical parameters such as axial turbulence velocity distribution were found to be in good agreement with experimental data. The OASPL trends as well as the spectral levels were also found to compare favourably with Tanna's measured values at relatively low Mach flow conditions. Increasing temperature ratio while keeping the Mach number constant tends to increase the radiated sound levels and act as extra sound source for low Mach number flow. Current setup was restricted to jet Mach number values smaller than 0.2 for heated set points and Mach number up to $\cong 0.5$ for Isothermal set points and also low Reynolds numbers.

Based on the results obtained for the VLES methodology, it is concluded that the method was capable of predicting sound levels with better accuracy despite some discrepancy in larger observer angles and mostly on high frequency bands. Using turbulence model, it looks that flow characteristics close to nozzle exit can be a better representative for actual flow condition.

Internal mixing nozzles

The sound produced by flow through internal mixing nozzles was simulated using LBM. Time resolved simulation in combination with the sub-grid scale turbulence modelling and hybrid thermal model were found to be a promising tool for simulation of double-stream shear flows includes complex geometries; however, current LBM simulations were restricted to Mach number values not greater than 0.5..

The use of lobed mixers in comparison to confluent mixers showed several advantages such as mixing enhancement, thrust improvement and noise reduction. Moreover, lobed mixers decreased low frequency noise level in almost all directions and increased high frequency sound pressure level in specific directions compared to the CONF model.

Looking at the combined effect of the lobe number and penetration depth, it was found that increasing the penetration depth and lobe number can be interpreted as extending the mixing surface and hence; enhances the mixing process between the core and the bypass flows. As it was evident in Fig. (4-7(a)) this tends to decrease the length scale of the streamwise vortices which in part, contributed to the frequency shift in the far-field sound power spectra. As the lobe number and penetration depth increase, it was found that vorticity density in the mixing area downstream of the lobes also increase leading to more azimuthal interaction of vortices in expense of loss in turbulent energy and entropy generation. It was observed that such vorticity distribution could affect the mid-frequency content of far-field spectra as shown in Fig. (4-14(b)) for 12CL and 20UH. The band filtered SPL of 20UH mixer was lower than that of 12CL.

Some far-field characteristics could be attributed to the higher penetration depth. The 20-lobe mixer, 20UH, was able to reduce the low frequency content of the spectrum that could be investigated by plume survey in the outer regions into the jet plume. Lobe penetration contributes to the radial advection of the streamwise vortices. Such radial advection governs the flow-field and vorticity dynamics close to the nozzle wall. This in part would change the characteristics of the shear layer at nozzle exit area, and also modify the TKE transport in the outer shear layer. The 12CL low-penetration mixer kept the streamwise vortices in the vicinity of the jet axis. This should, to some extent, prevent the core flow from effective interaction with the outer shear layer, and hence reduce the energy of turbulent eddies related to the mid-to-high frequency content emitted from that area. However, such vortices also change the length scale of turbulent eddies further downstream and affect both high and low-frequency noise characteristics.

For heated set points, the peak OASPL values were higher than that seen for isothermal cases for 12CL and CONF. This in part, could be attributed to flow acceleration inside the nozzle and greater peak velocity or acoustic Mach number at the nozzle exit plane and also due to generation of entropic sound sources as the thermal boundary layer grows along the shear layer between the fan and core flows. Contrary to the isothermal mixing where the SPL values in two mixers were highly dominated by the low-frequency noise the contribution of mid and high frequency bands are much more significant than the lower bands compared to isothermal set points.

In order to investigate the effects of scalloping, three mixers with the same lobe counts, 20UH, 20MH and 20DH mixers along with CONF were simulated and compared. Scalloped mixers exhibit fairly uniform velocity profile at the nozzle exit, and the velocity overshoot seen in CONF and 12CL were absent which the most credit on this respect should be given to the lobe counts rather than scalloping; scalloping on the other hand could shift the large velocity gradient area far closer to the nozzle walls. The medium scalloped mixer showed the shortest transition distance to a fully turbulent state as well as greatest TKE decay rate compared to other mixers. Results also suggested that there might exist a critical scalloping value that determines whether the mixer could yield noise reduction. Such behaviour is due to the differences in length scales and energy level of the streamwise vortices affected by the lateral leakage through scalloped sidewalls (Gong, 2013). Among the three mixers, 20MH had the highest and 20DH had the lowest OASPL level. Scalloping did not yield the same low-frequency noise reduction as did for the 20UH unscalloped case, but the most reduction benefits were achieved in the low-frequency domain as expected from experimental observations in (Mengle *et al.*, 2002) . The 20DH results showed that deep scalloping was successful in decreasing the noise in the high-frequency domain but performed rather poor on the low frequency part. Looking at the band filtered SPL directivity there was a shift in peak frequency associated with the scalloping depth variation (Gong, 2013).

An important result about the trust values was the fact that the 20UH model was associated with more momentum losses leading to the decrease in thrust magnitude but the scalloping did not cause additional momentum loss compared to 20UH.

As for the simple double-stream jet flow, as argued by Fisher *et al.* (1993), there appears to be at least two dominant regions in spectral contents of the lobed mixers. First is the low-frequency peak is governed by the fully mixed region far downstream of the nozzle and second is the mid-to-high frequency peak governed by the shear layer between the ambient flow and the partially mixed bypass and core flows close to nozzle exit plane. The lobed mixer geometry may change the mixing process and used beneficially to control either frequency ranges.

7-1-2 High-Mach subsonic LBM scheme to simulate high speed jet flows

Numerical simulations using a high-Mach subsonic lattice-Boltzmann methodology (LBM) (Nie *et al.*, 2009b; a; Gopalakrishnan *et al.*, 2013) was performed on Two high subsonic jets. One unheated jets and one heated jet. The mean flow characteristics including centreline velocity and fluctuations qualitative were in good agreement with measurements. Differences and discrepancies that were observed mostly on SP07 case were probably due to the Mach number limit of the extended LBM solver, omitting the cup region from FW-H sampling as well as the computational setup or the constants of current two-equation turbulence model. The development of this extended LBM methodology for high Mach number applications are still undergoing more validation studies but nonetheless have shown promising results. Other than jet noise and internal mixing noise case that were covered in this work, other studies on external mixing nozzles (Casalino and Lele, 2014; Casalino and Hazir, 2015) and full aircraft simulation (Fares *et al.*, 2016) have been performed using the extended version of the LBM implemented on PowerFLOW 5.0 solver. for the jet noise case, further near-field studies could be interesting, looking at parameters such as Reynolds stresses, mass flux rates, jet growth rates, lip-line turbulent intensities, and possibly mean flow results with second and third order moments such as cross-sectional skewness and kurtosis. Moreover, noise source identification methods can be utilized such as those proposed by Lighthill (1952) and Powell (1964).

7-1-3 Internal mixing nozzles with realistic boundary conditions

The results presented in this study complement those from the previous study by the author (Habibi *et al.*, 2013a; Habibi *et al.*, 2013b; Habibi and Mongeau, 2013). The sound produced by flow through internal mixing nozzles for high Mach set points were simulated using a novel entropic LBM capable of resolving Mach numbers up to the M_a =0.95. Time-resolved simulations in combination with the sub-grid scale turbulence modeling and hybrid thermal model were utilized for simulation of double-stream shear flows through a lobed mixer with a complex geometry. The results were in agreement with published experimental data for the same operating conditions which, validates the use of entropic LBM as an alternative to the computationally expensive LES schemes based on Navier-Stokes formulation. The results suggest that RANS simulations might be able to accurately predict mean flow data. But they are not very accurate for aeroacoustic studies and they require with auxiliary semi-empirical correlations for noise predictions. Such correlations cannot be generalized for different nozzle-mixer configurations and hence, cannot be used for new designs.

Future validation studies are recommended on different nozzle types such as confluent and scalloped mixer to fully identify the limitations of high Mach subsonic LBM scheme for such practical jet noise applications with complex geometries.

7-1-4 Acoustic absorption by turbulent jets

A numerical simulation of a noise-induced flow through an orifice plate was performed using the LBM. The solution of the linear wave equation, modified for the presence of mean flow, was used to decompose the wave upstream of the orifice plate and to calculate the absorption coefficient and acoustic impedance. Visco-thermal losses denoted by β_v in semi-empirical correlations were replaced by the numerical dissipation coefficient β_n. The same empirical value β_T was used to account for the turbulent losses. A case study was done for the fixed acoustic amplitude 145 dB. Variations of the sound absorption coefficient with respect to orifice mean velocity and the excitation frequency were studied and compared with the available analytical solution and experimental data. Both flow and acoustic results were in good agreement with the experimental measurements. The LBM was shown to be a powerful tool for modeling low-Mach complex fluid flows interacting with the acoustic waves. The VLES turbulence scheme was found to be an effective and accurate method to capture realistic behaviour of the acoustic-flow field, correct prediction of velocity profiles as well as the turbulence dissipation rate.

7-2 Suggestions for the future work

In general, present work has covered several jet noise simulation cases ranging from low-Reynolds and low-Mach jets (Re=6,000 and M_a=0.2) up to much higher Reynolds number (Re ~1.5×10^6) and Mach number greater than 0.9 and High-Mach. During our studies, it was found that VR distribution in the shear layer could affect resolving the quadrupole sources and the prediction of far-field sound. It is suggested that thorough grid resolution study and VR distribution is performed for both inside and outside of the nozzle for future studies. Also for High-Mach cases, it was found that the turbulent data as well as acoustics levels were diverging from measured values at certain locations or observer's angles when the Mach number was close to the sonic limit (SP07 case); thus, further investigation is required to identify the source of such discrepancies and see if that is related to the stability LBM at sonic zones or could be improved by modifying the computation setup, *e.g.* by using higher grid resolution in the shear layer or VR distribution in the near-field; moreover, due to the fact that the cup region of the FW-H was removed for all jet noise cases, it is recommended to investigate the error related to missing sources downstream of sampling surface using available methods. One way to utilize the acoustic source information in the cup area at downstream termination of the FW-H surface is to use multiple staggered cups as proposed by Shur (2005a) and more recently by Mendez (2013) . Such method was also utilized in a recent study by Casalino and Lele and (2014) later by Casalino and Hazir (2015) for simulation of dual stream external mixing nozzles.

In this work several key parameters of a lobed mixer include lobe numbers, penetration depth, bypass ratio, thermal effects and scalloping depth, were investigated at low-Mach number (M_J = 0.5). We also investigated the realistic boundary conditions using High-Mach subsonic LBM scheme on 12CL mixer model, It is recommend that full validation study is performed on different mixer types and operating conditions as specified in the NASA report (Mengle *et al.*, 2002). Simulation results may also feed a shape optimization code to further optimize the mixer geometry in order to achieve the least noise emission with minimal impact on thrust and specific fuel consumption. The combination of LBM-VLES and shape optimization algorithm can be integrated into design process of turbofan engines.

It is also recommended that existing jet setup with high-Mach capabilities is extended and used to simulate external-mixing nozzles with various noise reduction configurations such as chevrons on both core and bypass nozzles; some basic configurations of external mixing nozzles has been performed by Casalino and Lele (2015) and Khorrami *et al.* (2014) using LBM.

In regard to the sound absorption problem, this work has covered the absorption effects of jet flows in standard 3D impedance tube setup; this problem can be extended to cover more practical applications such as sound attenuation by liners in grazing flow configuration. With new impedance boundary condition capability in Exa PowerFLOW (Sun *et al.*, 2013), it is possible to avoid detailed flow simulations inside the liners and redefine the problem by setting proper impedance distribution inside the turbofan engine flow passages.

APPENDIX A – Derivation of LBE

A-1 Derivation of the Lattice Boltzmann Equation (LBE)

In this section, the Lattice Boltzmann equation (LBE) stated by Eqn. (2.6) will be derived from the continuous Boltzmann kinetic equation and then further expanded in a way to recover macroscopic momentum equation.

The first step can be done through a Hermite-expansion based phase space discretization (Shan *et al.*, 2006). The continuum Boltzmann equation can describe the evolution of the single-particle distribution function $f(\hat{x},c,t)$ in D-dimensional space (*i.e.* phase velocities) based on the BGK collision model; the general format can be expressed by

$$\frac{\partial f(\hat{x},c,t)}{\partial t}+c.\nabla f(\hat{x},c,t)=-\frac{1}{\tau_0}\left[f(\hat{x},c,t)-f^{eq}(\hat{x},c,t)\right]. \tag{A.1}$$

As described in chapter 2, here, τ is the characteristic relaxation time of collisions towards equilibrium state that is related to fluid kinematic viscosity ν as $\tau_0=\nu/T$. f^{eq} will represent a local equilibrium distribution function based on the Maxwell-Boltzmann model in an inertial frame that moves with the bulk flow defined as

$$f^{eq}(x,c,t)=\frac{\rho(x,t)}{(2\pi\theta)^{D/2}}\exp\left[-\frac{\left(c-\hat{u}(x,t)\right)^2}{2T_0}\right], \tag{A.2}$$

where, T_0 is the characteristic temperature. The distribution function $f(\hat{x},c,t)$ can be mapped onto a Hermite basis series using dimensionless orthonormal polynomials $H^{(n)}(c)$ that are defined in phase space *c as*

$$f(x,c,t)=\omega(c)\sum_{n=0}^{\infty}\frac{1}{n!}\alpha^{(n)}(x,t)H^{(n)}(c), \tag{A.3}$$

where the dimensionless expansion coefficients, $a^{(n)}(\hat{x},t)$, can be obtained by integration over the entire dimensionless phase space of *c* given by

$$a^{(n)}\left(x,t\right)=\int f\left(x,c,t\right)H^{n}(c)\,dc\,. \qquad \text{(A.4)}$$

The advantage of Hermite based expansion is the fact that all the coefficients can be related to the linear combination of the velocity moments of the particle distribution function, *f*, and the first few terms can be directly represented by five fundamental thermophysical properties, density (ρ), lattice velocity, (u), the energy, $\theta = 2\varepsilon/D$, and the tensor of momentum flux, P

$$\alpha^{(0)}=\int f dc=\rho\,, \qquad \text{(A.5)}$$

$$\alpha^{(1)}=\int fcdc=\rho\hat{u}\,, \qquad \text{(A.6)}$$

and $$\alpha^{(2)}=\int f\left(c^{2}-\delta\right)dc=P+\rho\left(\hat{u}^{2}-\delta\right)=Q+\hat{u}\alpha^{(2)}\left(D-1\right)\rho\hat{u}^{3}\,, \qquad \text{(A.7)}$$

where ε, is the kinetic energy density .Since the leading moments of a distribution function are preserved by truncations of the higher order terms up to N^{th} order in its Hermite expansion, $f\left(\hat{x},c,t\right)$ can be approximated by truncated terms $f^{N}\left(\hat{x},c,t\right)$, the first N Hermite polynomials can be projected onto a Hilbert type subspace without changing the first N moments as

$$f\left(x,c,t\right)\cong f^{N}\left(x,c,t\right)=\omega\left(c\right)\sum_{n=0}^{N}\frac{1}{n!}\alpha^{(n)}\left(x,t\right)H^{(n)}(c)\ , \qquad \text{(A.8)}$$

Such representation allows fluid dynamic system to be reconstructed by a finite set of macroscopic variables (Shan *et al.*, 2006). The discretization of Hermite-based distribution function $f^{N}\left(\hat{x},c,t\right)$ includes the use of the Gauss-Hermite quadrature to obtain the coefficients, $a^{(n)}(\hat{x},t)$, which can be represented by a weighted sum of distribution functions evaluated at discrete phase velocities c_i as (Shan *et al.*, 2006)

$$a^{(n)}=\sum_{i=1}^{d}\frac{\omega_i}{\omega\left(c_i\right)}f^{\mathrm{N}}\left(x,c_i,t\right)H^{(n)}\left(c_i\right), \qquad \text{(A.9)}$$

Where ω_i terms are the weight coefficients and $\omega\left(c_i\right), i=1,2,..,d$, are the abscissa of a Gauss-Hermite quadrature (degree $\geq 2N$) . By substituting equation A.9 and A.8 into the continuous Boltzmann equation A.1 and by recasting the convection and diffusion terms, the governing equations for discretized phase velocity distributions can be written in terms of c_i by

$$\frac{\partial f_a}{\partial t}+c_i.\nabla f_i=-\frac{1}{\tau}\left[\,f_i-f_i^{eq}\,\right]\quad a=1,...,d\ . \qquad \text{(A.10)}$$

The equilibrium distribution function f_i^{eq} on the RHS is equal to

$$f_i^{eq} = \omega_i \rho \left[1 + c_i.u + \frac{1}{2}\left[(c_i.\hat{u})^2 - u^2 + (T_0 - 1)(c_i^2 - D) \right] \right.$$
$$\left. + \frac{1}{6}(c_i.\hat{u})\left[(c_i.\hat{u})^2 - 3\hat{u}^2 + 3(T_0 - 1)(c_i^2 - D - 2) \right] + \ldots \right]. \qquad \text{(A.11)}$$

Equation (A.10) is in fact a differential form for the discrete phase velocity distributions which in turn, can be discretized in time and space integrating along the velocity characteristics in time

$$f_i(x + c_i,\, t+1) - f_i(x,t) = -\frac{1}{\tau}\int_t^{t+1} \left[f_i(x + c_i(t'-t), t') - f_i^{eq}(x + c_i(t'-t), t') \right] dt'. \qquad \text{(A.12)}$$

Using the trapezoidal intergration rule, the RHS of Eqn. (A.12) can be estimated by

$$f_i(x + c_i,\, t+1) - f_i(x,t) \approx -\frac{1}{2\tau}\left[f_i(x,t) - f_i^{eq}(x,t) \right]$$
$$- \frac{1}{2\tau}\left[f_i(x + c_i, t+1) - f_i^{eq}(x + c_i,\, t+1) \right]. \qquad \text{(A.13)}$$

Adjusted distribution can be defined as (He *et al.*, 1998)

$$\overline{f}_i(x,\, t) = f_i(x,\, t) + \frac{1}{2\tau}\left[f_i(x,\, t) - f_i^{eq}(x,\, t) \right], \qquad \text{(A.14)}$$

where substitution into Eqn (A.13) leads to the approximated form of the BGK Lattice Boltzmann equation as

$$\overline{f}_i(x + c_i,\, t+1) - \overline{f}_i(x,\, t) \approx -\frac{1}{\tau_0 + 1/2}\left(\overline{f}_i(x,\, t) - f_i^{eq}(x,t) \right), \qquad \text{(A.15)}$$

where $\tau = \tau_0 + 1/2 = \nu/T_0 + 1/2$, and using the "adjusted" distribution in the discrete equation, the standard form of the Lattice Boltzmann Eqn. (2.6) can be obtained. Notice, in this derivation, since both x and $x + c_i$ are lattice centroid positions that directly imply a unity CFL number: $|c_i \Delta t| / \Delta x = 1$ as discussed in chapter 2.

A-2 Recovering macroscopic continuity and momentum equations

In order to derive the conservation laws at macroscopic scale and small Knudsen number, Kn ,where the compressible Navier-Stokes equations are valid, a multi-scaled Chapman-Enskog expansion (Chapman and Cowling, 1970) can be used. The Knudsen number is a dimensionless number defined as the ratio of the molecular mean free path length to a representative physical length scale. The expansion of discrete particle distribution f_i and time derivative, $\P_t$, in powers of Kn can be written

$$\begin{cases} f_i = f_i^{(0)} + Kn\, f_i^{(1)} + Kn^2\, f_i^{(2)} + \ldots\ ; \\ \partial_t = Kn\,\partial_t^{(0)} + Kn^2\, \partial_t^{(1)} + \ldots \end{cases}, \tag{A.16}$$

where $f_i^{(0)} = f_i^{(eq)}$ identity is related to equilibrium distribution in Eqn. (2.10). Substituting the Eqn. (A.16) into the discrete momentum Boltzmann Eqn. (A.10), and equating the terms with the same order of Kn, the Boltzmann-BGK equation can be represented by an infinite series of equations according to the order of Kn,

$$\sum_{k=0}^{n-1} \partial_{t_k} f_i^{(n-k-1)} + c_i.\nabla f_i^{(n-1)} = -\frac{1}{\tau} f_i^{(n)} \text{ for } n = 1, 2, \ldots, \tag{A.17}$$

The first and the second order of distributions, we can write

$$\left(\partial_t^{(0)} + c_i.\, \nabla\right) f_i^{(0)} = -\frac{1}{\tau} f_i^{(1)}, \tag{A.18}$$

and

$$\left(\partial_t^{(0)} + c_i.\, \nabla\right) f_i^{(1)} + \partial_t^{(1)} f_i^{(0)} = -\frac{1}{\tau} f_i^{(2)}. \tag{A.19}$$

Taking the first two moments of Eqns (A.18) and (A.19) and recasting the terms, conservation equations for mass and momentum are

$$\partial_t \rho + \nabla.\,(\rho u) = 0, \tag{A.20}$$

and

$$\partial_t (\rho u) + \nabla.\,(P) = 0, \tag{A.21}$$

in which $P = P^{(0)} + P^{(1)}$ is the tensor of the momentum flux, In general $P_{ij}^{(k)}$ can be defined as

$$P_{ij}^{(k)} = \sum_i c_i c_j f_i^{(k)},\ k = 0, 1, \tag{A.22}$$

And for the for the D3Q19 model which is used in this study, and the equilibrium distribution function given by Eqn. (2.10), Eqn. (A.22) can recover the stress tensor in the Navier-Stokes equation as

$$P_{ij}^{(0)} = p\delta_{ij} + \rho u_i u_j, \tag{A.23}$$

$$P_{ij}^{(1)} = -\nu\left(\nabla_i (\rho u_j) + \nabla_j (\rho u_i)\right), \tag{A.24}$$

were p is the pressure that obeys the equation of state for ideal gas $p = \rho / 3$, and $\nu = (\tau - 0.5)/3$ is the kinematic viscosity (He *et al.*, 1998). It can be shown that the resulting momentum equation is the same as the Navier-Stokes equations with an error of $O(Ma^3)$ (Shan *et al.*, 2006)

APPENDIX B – Simulation of porous nozzles (Technical note)

B-1 Introduction

As a side study, we evaluated the PowerFLOW capability in simulation of flow through porous medium for jet noise applications. Although the use of acoustic liners at intake, exhaust and through the air passages of aeroengines are now deemed a usual practice in aerospace industry (Huff, 2007), several other studies have shown that increasing the exhaust containment length of nozzles using acoustic absorbing porous materials or perforated modules, could potentially reduce the signature of the aerodynamic sound at the exhaust of the nozzles. Among those studies, (Golosnoy *et al.*, 2008), showed that adding a cylinder made of a highly porous metallic material at the exhaust of a turbofan nozzle could reduce both the broadband sound at high frequency range as well the tonal audibility level at blade passing frequency. In another study, using a perforated tube as a nozzle extension was found to be effective in reducing the broadband sound and the screech tone of the supersonic jets (Seto *et al.*, 1987). There have been few studies on the effect of the structure of porous materials on the frequency dependence of their sound absorption. For example, one study reported that, isentropic porous copper with typical porosity in the range of 40–60 % (Xie *et al.*, 2004), also it was found that sound absorption increased with increasing frequency, between 2.0 and 5.0 *k*Hz. that sound absorption was more effective with higher porosity levels and finer pore diameters (Xie *et al.*, 2004). Metals are much more likely to be able to meet requirements in the aerospace applications. The hot environment in turbofan engine exhausts that may involve the peak combusted gas temperatures of ∼500 to 800°C almost rules out typical macromolecular and polymeric materials, while various metallic or ceramic materials are stable at these temperatures. The thermo-mechanical stability requirements generated by exposure to thermal shock, temperature gradient or thermal cyclic effects as well as the impact of high velocity combustion products are quite demanding (Golosnoy *et al.*, 2008).

The propagation of sound in a porous material is a phenomenon that governed by physical characteristics of a porous medium, such as porosity, flow resistivity, and viscous and thermal characteristic lengths. Also the attenuation of sound in porous media are highly dependent on the thickness of the porous layer which makes it quite challenging to absorb low-frequency components where the wavelength is greater than the thickness of the layer (Johnson *et al.*, 1987).

The acoustical behaviour of a absorptive porous layer can also be investigated from its basic acoustic quantities such as characteristic impedance or the absorption coefficient. Once these values are known, the sound propagation, absorption or reflection can be modelled. Recent studies have been able to combine the impedance characteristic of a porous layer with the solution of the flow-field using the Lattice Boltzmann Method. (Mann *et al.*, 2013; Sun *et al.*, 2013).

The aim of this section is to show the how the porous model in the PowerFLOW solver can tackle the jet noise study including a nozzle with porous extension. As mentioned in section 2-1-11. The PowerFLOW solver implements a porous medium model by applying flow resistivity as an external force; thus, Porous medium regions can be processed with very little additional computational expense compared to ordinary fluid region; however, the regular model in PowerFLOW does not take visco-thermal attenuation into account; in other word, while current porous model in the PowerFLOW can effectively simulate the impact of the porous layer on the flow-field it does cannot well simulate the sound propagation or attenuation inside the porous layer.

A recently patented method by Exa Corporation, *aka* the Acoustic Porous Model (APM)) in PowerFLOW 5.x (Sun *et al.*, 2015) is able to estimate surface impedance using three main parameters: the viscous resistance R, the porosity (ε) and the porous thickness (d).Using this model one may estimate the sound absorption without solving the flow inside the layer. The characteristic surface impedance of the APM, say Z_{APM} (f, R, ε, d), can be fully determined with these variables via an analytical model, where f is the frequency in Hertz; Z_{APM} is also parameterized through quantities that are directly related to the LB formulation (Casalino *et al.*, 2014a), but such details are beyond the scope pf the present study; also for jet noise applications, this model cannot directly be used as we cannot neglect the flow field inside the porous layer due to significant impact on the turbulent behaviour and hence, acoustic sources.

As mentioned in section 2-1-12 for PowerFLOW solver, porous medium is treated as bulk to avoid the cost of resolving all of the fine scale geometrical structures, such as fins or pores. The model specifies a pressure drop in porous regions, as a function of local density, velocity and resistance parameters. Using this approach, porous components can be integrated within larger simulations.

The method used to simulate flow inside the porous extension is based on the Darcy formulation as described in section 2-1-12 that is bundled with LBE using a method proposed by Freed (1998). In order to seed data from the experiment into the simulation, resistant factors in Eqn. (2.45) can be presented with respect to physical parameters of the porous material that includes permeability (K), passability (η) which is written as

$$-\nabla P = \frac{\mu}{K}\vec{u} + \frac{\rho}{\mu}\vec{u}\left|\vec{u}\right| \ , \tag{B.1}$$

where $\vec{u}$ is the bulk, *i.e.* macroscopic, velocity and μ is the dynamic viscosity.

B-2 Computational Setup and Operating Conditions

The nozzle was a circular pipe with a diameter of D_J = 0.0508 m and a length of L=10D_J similar to the geometry used in Chapter 3 with modifications in grid distribution and resolutions. A circular porous nozzle sections with different lengths (1D_J, 3D_J and 5D_J) were considered. The resistance coefficients were selected based on metal foam properties. Selected material was known as INCO NP1 1.3 metal foam, (K= 3.14×10^{-9} $m^{2,}$ μ= 5.34 $\times10^{-4}$ m) (Gerbaux *et al.*, 2009). Turbulence model was enabled, and the Reynolds number was 1.0×10^5. The centreline acoustic Mach number at porous exit plane was M_a = 0.3. The characteristic temperature and pressure were set to standard values as for the isothermal jet setup in section 3-2. The smallest voxel size was set ~0.2 mm. Grid setup is shown in Fig. (B-1). Total of eight VR regions were used around the main nozzle. The finest grid resolution, VR8, was used inside the nozzle boundary layer and extended through the porous layer. The thickness of the porous layer and the nozzle lip were equivalent to eight voxels. Statistical convergence was achieved after 400,000 timesteps. Only the plug with length of 3D_J was used for acoustic study in the near-field, the other two plugs were only used to compare thrust coefficient. PowerFLOW version 4.3d was used for the simulations.

Far-field analysis was performed as for the simple jet which was discussed in chapter 3 of this document. A funnel-shaped FW-H sampling surface was located at VR7 and 11 virtual microphones were positioned evenly at radiation angles in range of $50 \leq \theta \leq 130$. Also, in order to complete spectral analysis in the near-field. Two additional microphones were located at x =1.5 D_J and x = 3D_J and radial distance of r = 4D_J.

B-3 Results and discussions

Figure (B-2) shows the velocity iso-surface, V= 10m/s, around the porous nozzle. The turbulent flow pattern is drastically affected by introducing the porous layer. Transient flow is leaking through the porous nozzle from different zones at different timesteps. Compared to the free jet, shape of the coherent structures and large eddies at nozzle exit plane will change. This could potentially change the shear layer and TKE spectra in the near-field. Figure (B-3) shows the pressure contours in the near-field. One can observe that the strong pressure cells are formed through the porous layer starting at one-third of the porous length from the exit plane. This also implies that the transition to turbulence has been shifted farther from the nozzle compared to the simple nozzle without porous plug at which the transition occurs almost at one jet diameter, D_J. Looking at the time-averaged contours in Fig. (B-4), it is observed that the jet potential core was shortened by introducing the porous layer. The presence of a porous zone also led to faster decay in the potential core length that primarily caused by flow resistance along the jet axis and also periodic flow suction and blow out in parts of the porous region followed by impingement on the main stream at the discharge region of porous nozzle. The comparison between velocity decay rates can be seen in Fig. (B-5). The turbulent kinetic energy was also increased inside the porous nozzle. The decay rate toward the downstream was greater in comparison with the simple nozzle.

Aerodynamic thrust coefficient was also calculated using Eqn. (3.3) and (3.4) for different porous lengths. Results have been summarized in Table (B-1). The addition of a porous nozzle was found to have adverse effects on the thrust efficiency. Increasing the length up to $5D_J$ resulted in almost 18.2% reduction in thrust magnitude. Such adverse effects on thrust , *i.e.* up to 10%, was previously reported for supersonic nozzle equipped with perforated tube with porosity of 0.3 (Khan *et al.*, 2004); however, the LBM results were in contrast with the low-speed jet case reported by (Golosnoy *et al.*, 2008) in which the thrust effects was found to be negligible.

Far-field OASPL results for the porous nozzle, $Lp = 3D_J$, was compared to the circular nozzle in Fig. (B-6). The overall noise reduction with porous nozzle was seen for all observer's angles when $\theta > 40^o$. The broadband noise reduction levels were between 2-4 dB. The noise reduction benefit reported in the experiments for M_J = 0.3-0.88 was 5-10 dB (Golosnoy *et al.*, 2008) at almost all directions. It is important to note that the LBM simulation did not account for viscous dissipation rate which affects the dissipation rate of the sound waves generated in the shear layer. Aslo one-to-one comparison between the LBM and experimental results by (Golosnoy *et al.*, 2008) was not possible due to presence of fan in their setup. Figure Fig. (B-6) shows the power spectral density (PSD) of the pressure at two probe location in the near field with same radial distance from the jet axis but at different angles. The spectral levels show that the pressure fluctuations are lower near the porous layer; this is the results of higher effective viscosity in the porous layer and the nonlinear effects of the passability terms in the Darcy model. It is interesting to see that the viscous damping of the porous layer was able to lower the fluctuation levels at all moderate and high frequencies; however, it was more effective in the frequency angle between 3.0 to 10 kHz. Also based on the results in Fig. (B-6), damping effect was almost ineffective for low-frequency levels below 2 kHz. This phenomenon was also expected due to limited thickness of the porous layer that can be improved by adding more material and using thicker layer.

Table B-1 Operating conditions

Test Case	Trust Coefficient	Thrust loss (%)
Free Jet	1.154	N/A
Porous-1D_J	1.112	3.6 %
Porous-3D_J	1.033	10.5 %
Porous-5D_J	0.943	18.2 %

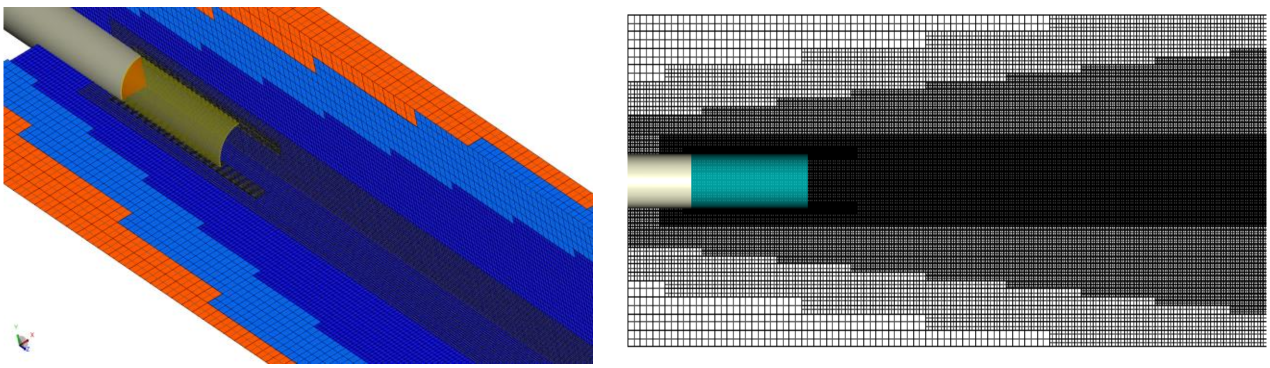

Fig. B-1 Grid setup near the porous extension

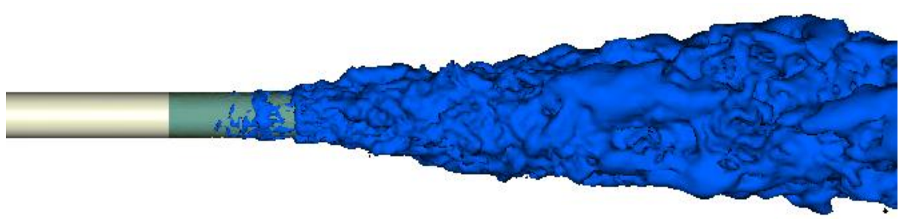

Fig. B-2 Velocity Iso surface (V= 10 m/s), flow leakage is shown around the porous area

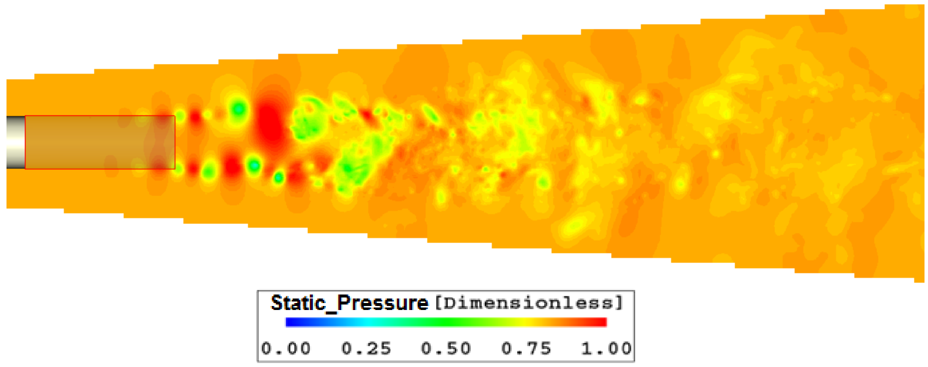

Fig. B-3 Pressure field in shear layer around the porous nozzle

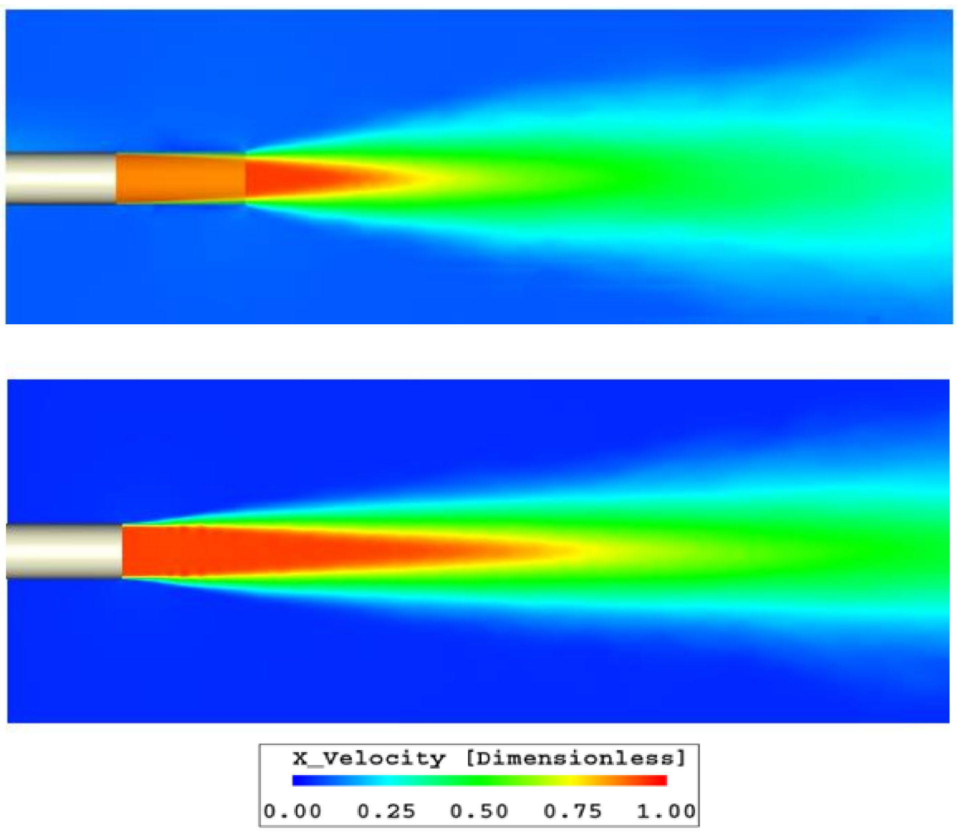

Fig. B-4 comparison of the time averaged velocity contours in the vicinity of the circular nozzle and the nozzle with porous extension

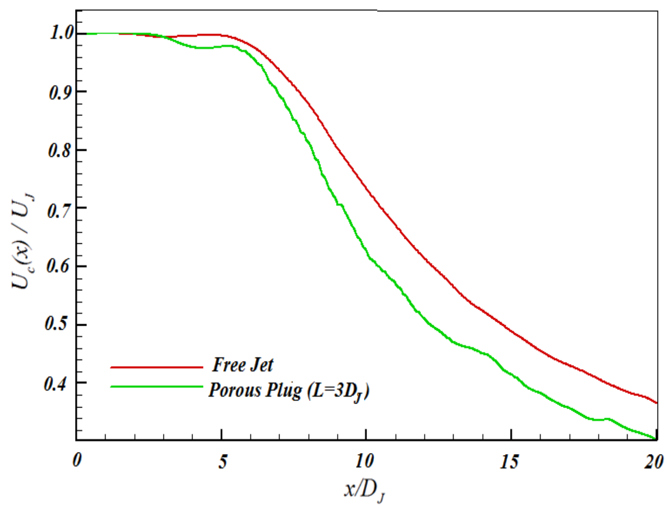

Fig. B-5 Time-averaged x-velocity profile along the centreline for the circular nozzle and nozzle with porous extension

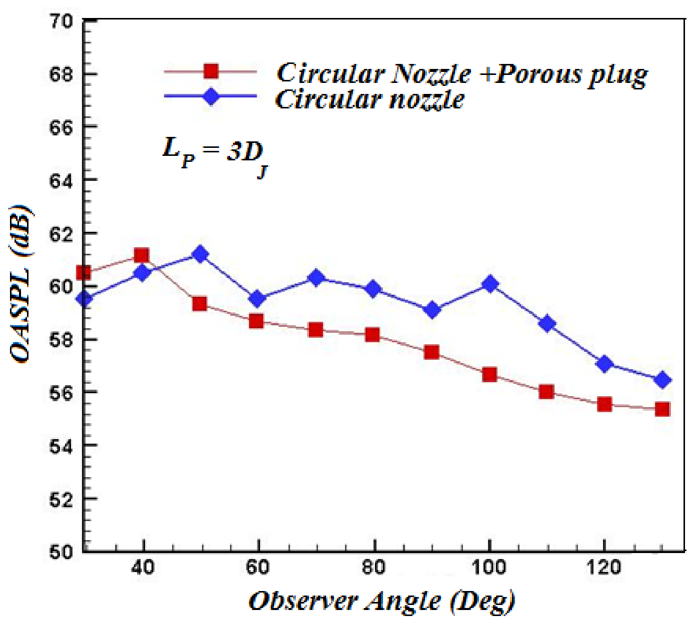

Fig. B-6 OASPL variation in the far-field (r =50 D_J) for the simple circular nozzle and nozzle with porous extension

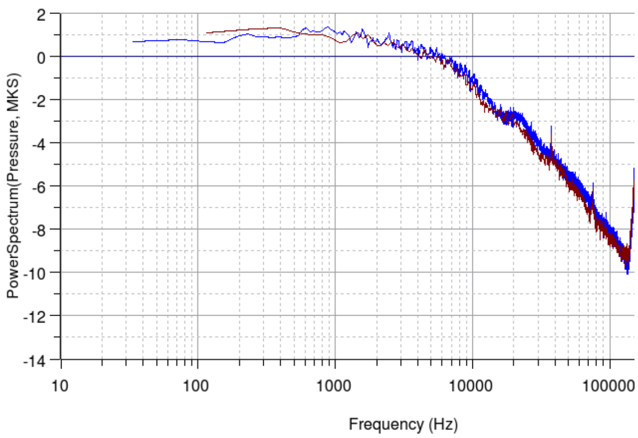

(a)

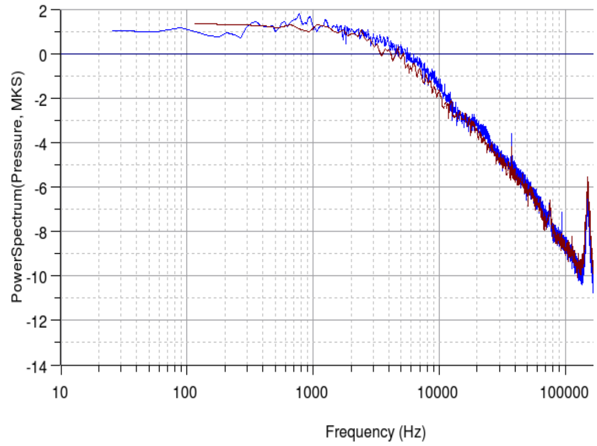

(b)

Fig. B-6 Power spectral Density (PSD) of the pressure field at (a) $x = 1.5D_J$ r= 4D_J and (b) $x = 3D_J$ and $r = 4D_J$, Red (--) Porous nozzle. and Blue (--) simple nozzle

APPENDIX C - LBM-LES to model acoustic flows interacting with solid boundaries

C-1 Motivation

In this section the capability of the LBM is evaluated in simulation of oscillatory flows over solid bodies. In-house experimental data are used to verify the numerical results. The acoustically driven flow past a flat plate (spoiler) in a standing wave resonator was studied using Particle Image Velocimetry (PIV). The LBM model was able to reproduce the results obtained in the experiments with remarkable accuracy. PowerFLOW 4.3d was used in this section as for the orifice absorption case in chapter 6. The results confirm the importance of vortex formation and turbulence around the solid boundaries (spoiler). Validation process in this section supports the benefits of using LBM to simulate acoustic flows such as the orifice absorption case discussed in Chapter 6. Results in this section were extracted from the published work by the author (Habibi *et al.*, 2012). The experimental setup was primarily used to study the streaming process in thermoacoustic refrigeration system (Rafat, 2014). The test section was simplified to be used for the validation purposes in this study.

C-2 Introduction

Thermoacoustic cooling systems use environmentally benign working gasses to convert acoustic energy into heat pumping. Within the stack, the interactions between high amplitude acoustic waves and the solid substrate, here a stack of thin parallel plates, leads to heat pumping through net time-averaged enthalpy flux within boundary layers, where there is in-phase phasing between temperature and velocity. The interactions between high amplitude acoustic waves and the stack-heat exchanger couple create complex flow structures which regulate convective heat transfer. The formation of vortices at the stack end, their interaction with the heat exchangers and acoustic streaming need to be characterized to better quantify their effects on the performance of thermoacoustic devices. Models based on linear acoustic theory commonly neglect the production of vorticity at the stack boundaries. A better understanding of the interactions between the acoustic waves and the stack ends is needed in order to optimize and increase the efficiency of thermoacoustic engines.

Flow measurement techniques such as hot wire anemometry or using pressure transducers can be intrusive. Non-intrusive techniques such as Laser Doppler Anemometry (LDA) and Particle Image Velocimetry (PIV) do not disturb the flow but due to close proximity of stack and heat exchangers and also highly pressurized gases being used in realistic thermoacoustic refrigerators, optical access is limited, and it is difficult to use these non-intrusive techniques. Recently, PIV has been used in idealized configurations to study the flow structures behind the stack. A detailed study of the flow structures around the stack of a simplified thermoacoustic refrigerator operated in ambient air was performed by Berson *et al.* (2008). They measured the acoustic particle velocity inside the boundary layer between the stacks. Symmetric pairs of counter-rotating vortices were identified near the end of the stack at low pressure levels. Vortex shedding and loss of symmetry was observed for high acoustic pressures. Mao *et al.* (2008) suggested the characterization of fluid motion around the stack using ensemble-averaged, phase-locked PIV. They stressed the need for a better understanding of the turbulence characteristics of oscillatory flows past a stack of parallel plates. Due to limitations of experimental methods of the direct measurement of flow variables in real thermoacoustic refrigerators, numerical techniques can be employed to better capture the complex flow interactions present in stack-heat exchanger couples. Analytical and numerical studies of the effects of reciprocating flows on heat transfer in channels can be found in the literature. Siegel (1987) studied the heat transfer in channels with periodically oscillating flow. A review of similar studies is given in (Cooper *et al.*, 1994). Zhao and Cheng (1995) showed that the oscillatory flows may enhance heat transfer in ducts and enclosures. In more recent study, Sert and Beskok (2003) studied the effects of frequency on flow and heat transfer in two-dimensional channels with reciprocating flow. Other mechanisms such as the addition of a porous layer have been shown to have a significant effect on the heat transfer in oscillatory flows in channels (Habibi *et al.*, 2011a).

Few numerical studies of the flow over stacks inside thermoacoustic devices have been performed. A low-Mach-number compressible flow model of unsteady, thermally stratified flow in two-dimensional thermoacoustic stacks was developed by Worlikar *et al.* (1998). Both fluid flow and heat transfer between two ideal stack plates were modeled using the finite difference method. Marx and Blanc-Benon (2004) investigated the two-dimensional flow in coupled heat exchanger-stack configurations by solving the Navier-Stokes equations coupled with energy equations including viscous dissipation terms. They performed simulations for high-amplitude acoustic waves. The formulation of Worlikar *et al.* was used in addition to the thin-plate stack assumption (Knio, 2001) to find the thermal efficiency of thermacoustic heat exchangers and characteristics of cooling loads, using the finite-volume method.

In the present study, the lattice Boltzmann Method (LBM) was used to simulate the acoustic flow field around a single-plate stack with finite thickness and to capture the vortex formation phenomenon. The numerical setup was tailored to closely match an experimental setup used to visualize and quantify the flow field using PIV.

C-3 Experimental Setup

C-3-1 Instrumentation

A schematic of the experimental setup is shown in Fig. (C-1). The acoustic resonator (C-1-*j*) used in this experimental study had a square cross section, 4.0 cm × 4.0 cm and a length of 98.0 cm. The walls of the resonator were 9 mm thick. A 200 W acoustic driver (e) with a DC coil resistance of 8 Ω excited the acoustic standing wave in the resonator. A function generator (C-1-a) produced a sinusoidal excitation signal which was fed to a 200 W, *RMS* power amplifier (C-1-d). A power analyzer (C-1-b) was connected in parallel with the acoustic driver to monitor the instantaneous true RMS voltage, current and power fed to the acoustic driver. Two high-resolution ICP pressure transducers were mounted flush near the two extremities of the resonator for measuring the dynamic pressure. The particle image velocimetry (PIV) system was a dual-cavity, time-resolved (TR) *Nd:YLF* laser (C-1-g) with a maximum repetition rate of 10 kHz per cavity. A CCD-CMOS camera (C-1-f) with a frame rate of 2000 fps and a resolution of 1280×1024 pixels was used. The pixel pitch of the camera was 12 μm. The camera was mounted on a traversing mechanism (C-1-i) which allowed mapping of the velocity field over the entire length of the resonator. A controller unit (C-1-c) supplied by the PIV system manufacturer was employed in order to synchronize the camera and the laser. A Laskin nozzle seeding generator, using olive oil, produced 1μm particles which were used for flow seeding process.

C-3-2 Data acquisition and analysis

To obtain vortex patterns and acoustic velocity at different phases the phase-locked ensemble averaging method described by Nabavi *et al.* (2007) was employed. To synchronize PIV acquisition and acoustic waves, the signal from a pressure transducer mounted at the rigid end of the channel was used. The time duration between two laser pulses, Δt, was enough to allow the seeding particles to move quarter of the interrogation region. The size of interrogation region was 16×16 pixels. At each phase (Φ), 150 images were captured. The phase averaged data were acquired for 20 distinct phases per acoustic cycle.

C-4 Numerical setup and case study

A schematic representation of the two-dimensional computational domain and the test section is shown in Fig. (C-2). Experiments were performed for one acoustic amplitude of 2.5 m/s and excitation frequency, 245.5 Hz, that corresponds to one of resonance frequencies of the channel. The temperature of the experiment was 295.6 K. The key dimensionless geometrical quantities were $a/\lambda = 0.03$, $t / \lambda = 7.13\times10^{-4}$, $L/\lambda = 0.7$, $L_s/\lambda = 1.4\times10^{-2}$ and where in this case, λ is the wavelength, a denotes the size of the resonator, t is the thickness of the spoiler, and L, is the length of the resonator and L_s is the finite length of the spoiler. One of the key operating parameters in the oscillatory flows is the acoustic penetration depth, *aka* acoustic boundary layer thickness, given as

$$\delta_\upsilon = \sqrt{2\nu/\omega}\,, \tag{C.1}$$

where, ν, is the kinematic viscosity of working fluid, *i.e.* air, and ω is the angular velocity ($\omega = 2\pi f$). In this case study, δ_υ was 1.43×10^{-4} m. Other flow characteristics of the simulation are summarized in table (C-1). The finest grid resolution was 0.005 mm or $3.57\times10^{-6}\lambda$. The Reynolds number based on spoiler thickness and particle acoustic velocity amplitude was 160, which was low relatively small; hence, turbulence equations were decoupled from LBM to fully resolve the near-wall flow properties. Total of 28 grid points were placed inside the acoustic penetration depth, which was found sufficient to capture vortical structures close to the spoiler. In the numerical setup, seven variable resolution zones were introduced inside the resonator. The process of partitioning the computational domain into variable resolution regions in LBM was performed as for that in the previous chapters for jet noise studies. Fluid viscosity was matched with that of the experiment.

The fluid domain consisted of 1.6 million grid cells (voxels). A schematic of the grid distribution near the stack plate is shown in Fig. (C-2). The excitation was provided by imposing a sinusoidal, constant amplitude and single frequency velocity at the inlet and outlet in form of

$$V_{Inlet} = \Re(V(x=0)\,e^{i\omega t}) = V_0 \cos(\omega t)\,. \qquad \text{(C.2)}$$

A no-slip wall boundary condition (V*(L) = 0*) was imposed on the spoiler walls.

C-5 Results and discussion

The running time of the simulation was 18 hours using 32 cores on Colossus compute cluster located in Laval, Quebec. The time history was enough to capture *21* complete acoustic cycles. Each time step was equal to 8.3×10^{-8} sec. Data sampling started after the fourth cycle. The flow phase-locked data (pressure, velocity and vorticity) were ensemble averaged over ten cycles.

The vorticity contours at time corresponding to different phases within an acoustic cycle are shown in Fig. (C-3) that compares vorticity values obtained from the LBM with PIV measurements. Vortical structures in the measurement seems to be well predicted by the LBM for each phase. Vortex shedding may occur based on the local Reynolds number and the nominal Keulegan-Carpenter number which is similar to the Strouhal number but more common in the literature for pulsating flows (Rafat, 2014). The spectral density of the velocity at a location *0.5t* along the lip line of the stack edge is shown in Fig. (C-4) while the spectrum is dominated by the periodic excitation frequency and its harmonic, one can detect a frequency component close to the 400 Hz, which is compatible with the value obtained by tracking the snapshots of the vorticity field and from the time intervals between consecutive shedding.

The axial velocity profiles are plotted perpendicular to the spoiler surface at a distance of one spoiler thickness from the leading edge are shown in Fig. (C-5) at selected phases during one acoustic cycle. The middle two profiles (*i.e.* the red circle and khaki squares) illustrate the flow reversal that is seen acoustic flows (Habibi *et al.*, 2011a). Those profiles correspond to Φ_3 and Φ_4 phases shown in Fig. (C-3). The velocity profile trends and magnitudes are in general agreement with experimental results. Some discrepancies in the region near the spoiler wall are seen that can be related to the parallax effect which causes fictitious particle movement on the solid surface.

Also, farther from the wall. Up to 0.4 m/s deviation can be seen between the velocity magnitudes from the LBM and measured data.

The drag coefficient quantifies the overall losses within the stack. The pressure losses across the stack affect the operating condition and performance of thermoacoustic devices. The total drag force, *D*, exerted by the spoiler is defined as the sum of the pressure drag obtained from a surface integral of the normal stress tensor, $\tilde{P}$ projected in the x-direction and the friction drag (surface integral of the shear stress tensor, $\tilde{\tau}_w$ projected in x-direction, Eqn. (C.3). The total drag coefficient, Eqn. (C.4), is calculated by normalizing the drag force with dynamic force based on the acoustic excitation velocity amplitude and the projected area ($A_P=t\times 1m$).

$$D=\int_A \tilde{P}.\vec{n}_x\, dA+\int_A \tilde{\tau}_w.\vec{n}_x\, dA\,, \tag{C.3}$$

$$C_D=\frac{D}{\frac{1}{2}\rho V_0^2 A_p}\,. \tag{C.4}$$

The drag coefficient based on Eqns. (C.4) and (C.5), is shown in Fig. (C-6). The drag coefficient exhibits a transient oscillating behaviour as the shear stress and the normal surface pressure change during flow reversal. The impact of previously convected vortices in consecutive cycles also adds to the chaotic nature of the flow. A comparison between the excitation velocity response, shown in Fig. (C-6), and the time history of drag shows a phase difference between the excitation velocity amplitude and the maximum drag. Such phase difference varies cycle to cycle with an average value around 0.43 *rad*.

C-6 Closing remarks

Numerical simulation of an unsteady 2D reciprocating flow over a rectangular plate in a channel was performed using the Lattice Boltzmann method. The velocity field was obtained experimentally using particle image velocimetry (PIV). A comparison between the results indicates that the LBM accurately captures the physics of acoustic flows over solid bodies. The vortex shedding phenomena was visualized and quantified by processing the velocity signals near the edge of the stack. The transient behaviour of the resultant drag force was studied by calculating the instantaneous total drag force imposed by the stack. The drag force variation was periodic but not sinusoidal. A phase lag was also detected between the maxima of drag force and the maximum excitation velocity, which is different from laminar steady flow over solid bodies where the change in drag force is in phase with change in flow velocity.

Table C-1 Operating conditions

Parameter	Value
Acoustic viscous Penetration depth ($\delta_\upsilon = \sqrt{2\nu/\omega\rho}$)	1.43×10^{-4} m
Nominal Reynolds Number ($\mathrm{Re} = V_{x=0}t/\nu$)	160
Womersley number ($\alpha = t\sqrt{\omega/\nu}$)	9.92
Keulegan-Carpenter number ($KC = V_{x=0}/(f_{exc}t)$)	10.2

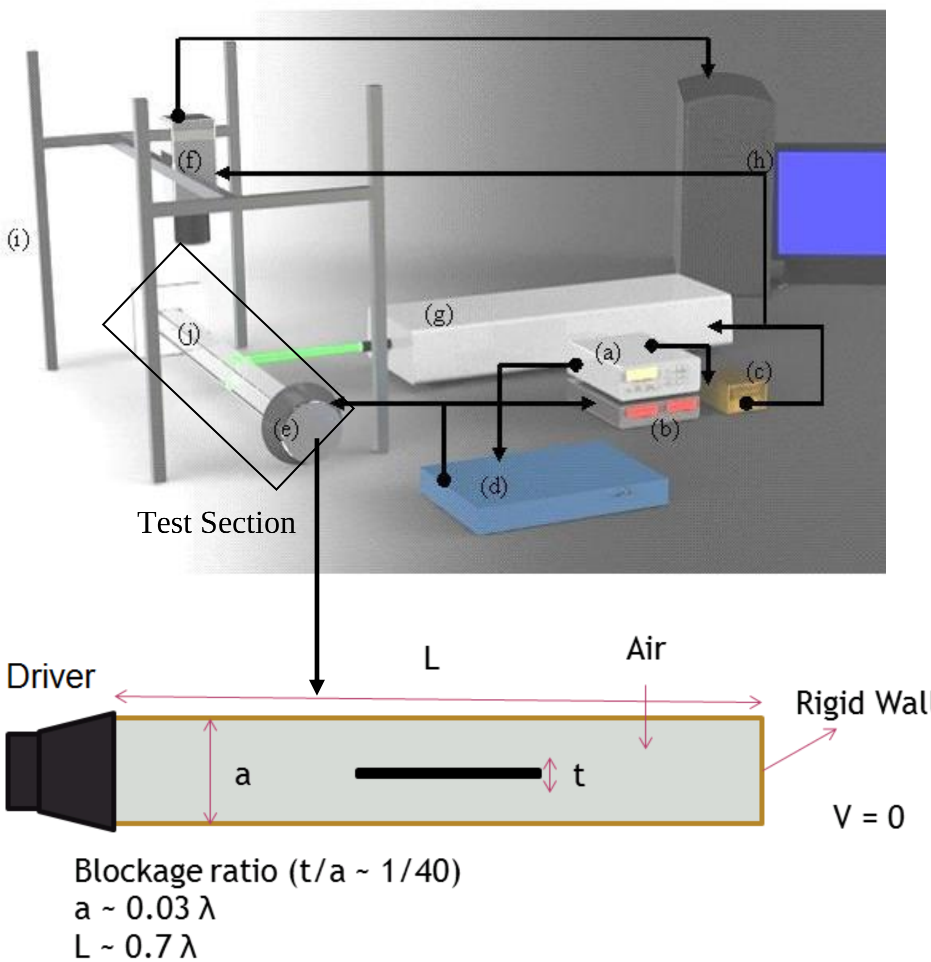

Fig. C-1 Schematic of the experimental setup. (a) Function generator; (b) Power analyzer; (c) Synchronization unit; (d) Power amplifier; (e) Acoustic driver; (f) CCD camera; (g) Laser; (h) Computer with frame grabber; (i) Traversing mechanism; (j) Resonator tube.

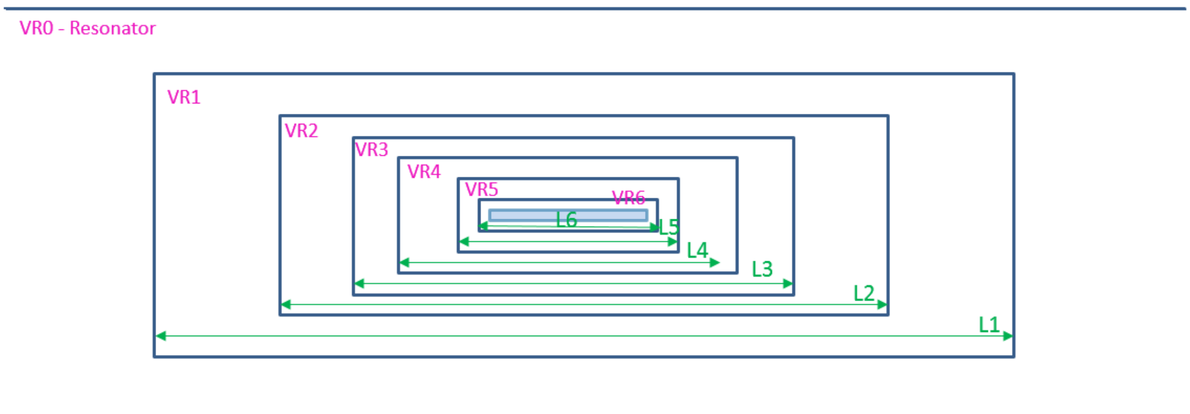

L_1/t	L_2/t	L_3/t	L_4/t	L_5/t	L_6/t
95	70	50	40	25	20

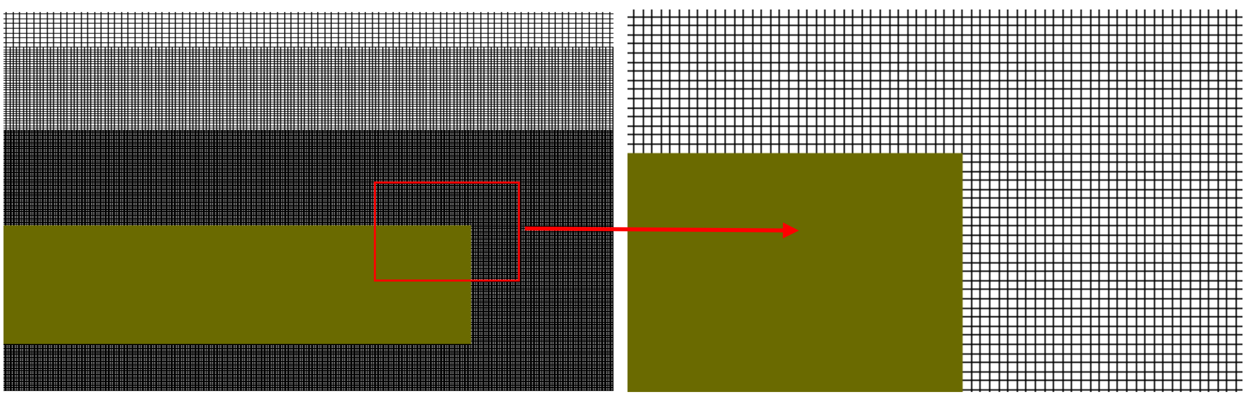

Fig. C-2 Voxel distribution near the Spoiler.

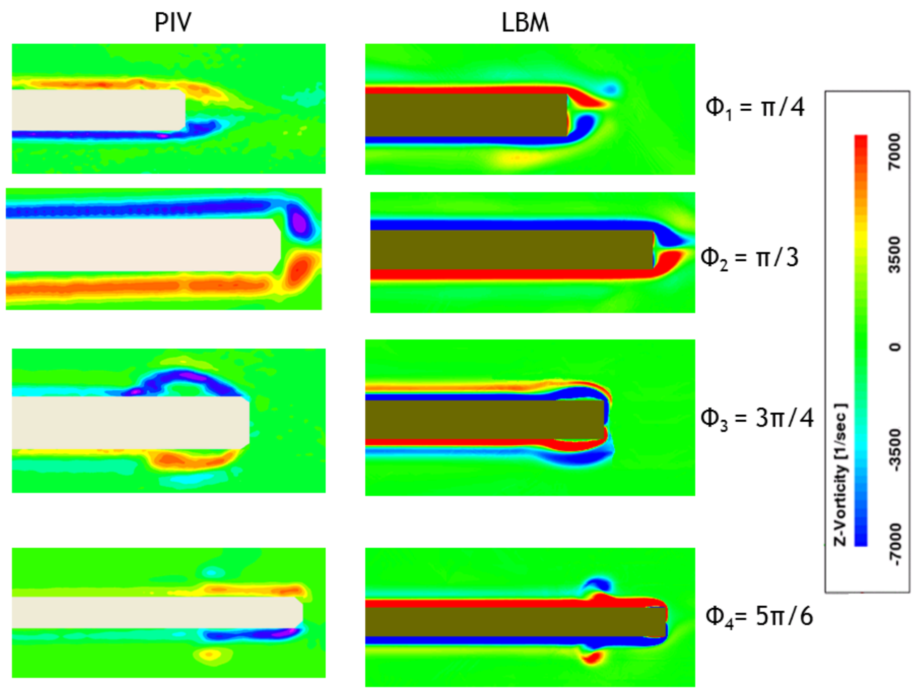

Fig. C-3 Vorticity contours near the edge of the spoiler in one period

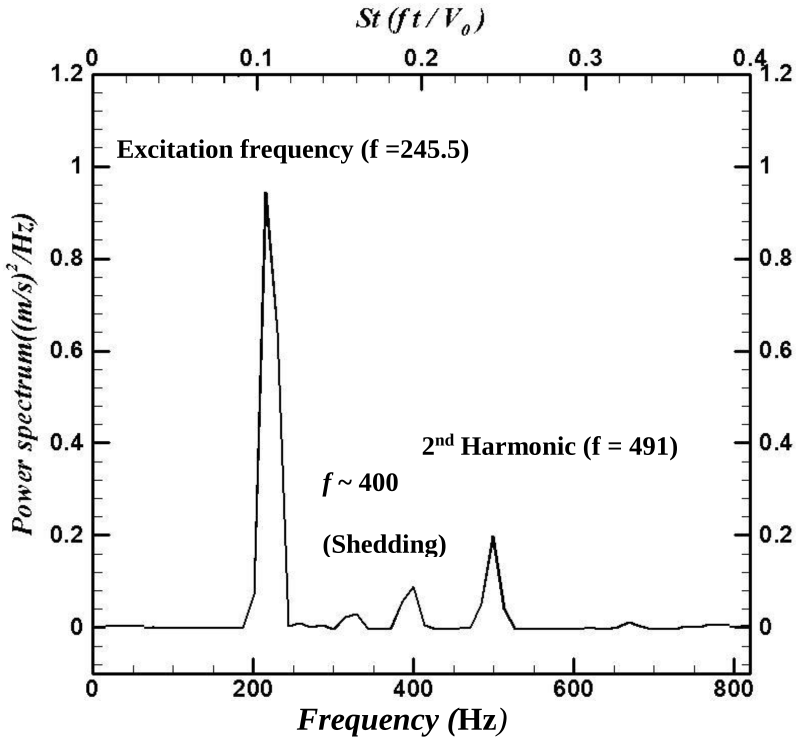

Fig. C-4 Velocity spectrum at a probe located along the lip line of the spoiler (at *x/t*= 0.5).

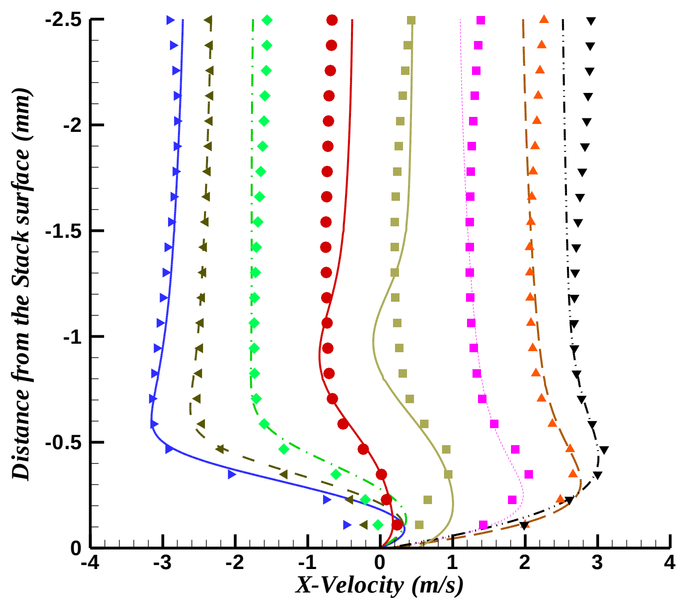

Fig. C-5 Acoustic velocity profiles for different phases from right (Φ_0=0) to left (Φ_8=π) at *x/t*=1 from the edge of the spoiler. LBM results are presented by lines and symbols corresponds to the experimental data.

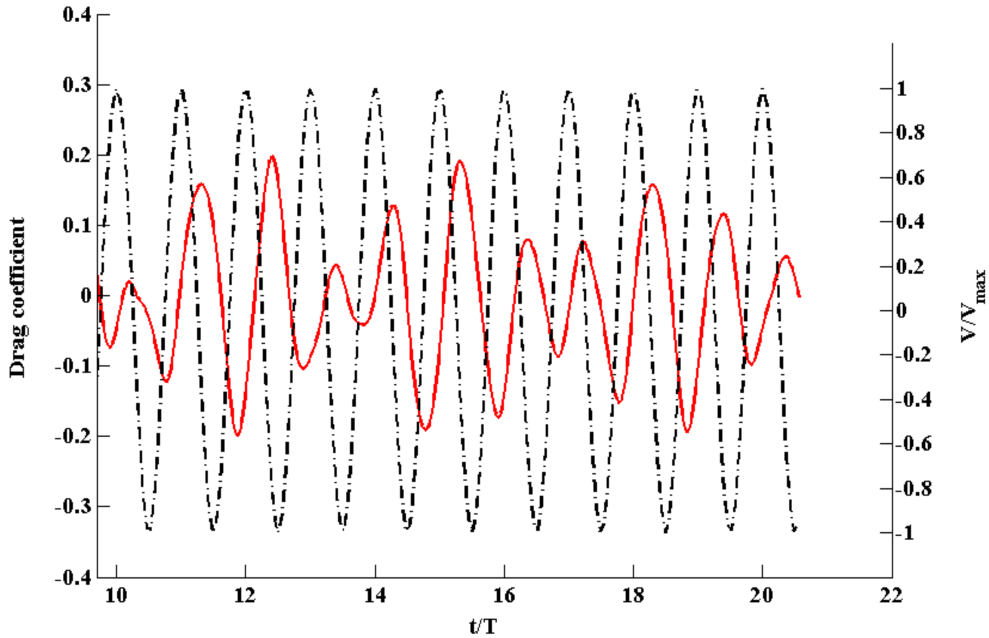

Fig. C-6 Time history of total drag coefficient over the spoiler
(– · –) Velocity response, (——), Drag coefficient.

REFERENCES

Abolfadl, M., and Sehra, A. (**1991**). "Application of three-dimensional viscous analysis to turbofan forced mixers," in *AIAA, Aerospace Sciences Meeting, 29 th, Reno, NV* (AIAA paper), p. 1991.

Abramovich, G. N., Girshovich, T., Krasheninnikov, S. I., Sekundov, A., and Smirnova, I. (**1984**). "The theory of turbulent jets," Moscow Izdatel Nauka **1**.

Aftosmis, M. J. (**1997**). "Solution adaptive cartesian grid methods for aerodynamic flows with complex geometries," VKI Lecture Series **2**, 1997.

Ahuja, K., Gaeta, R., and D'Agostino, M. (**2000**). *Acoustic absorption characteristics of an orifice with a mean bias flow* (National Aeronautics and Space Administration, Langley Research Centre).

Alexander, C. G., Chen, H., Kandasamy, S., Shock, R. A., and Govindappa, S. R. (**2001**). "Simulations of engineering thermal turbulent flows using a lattice Boltzmann based algorithm," ASME-PUBLICATIONS-PVP **424**, 115-126.

Amielh, M., Djeridane, T., Anselmet, F., and Fulachier, L. (**1996**). "Velocity near-field of variable density turbulent jets," International Journal of Heat and mass transfer **39**, 2149-2164.

Anderson, J. D. (**1990**). *Modern compressible flow: with historical perspective* (McGraw-Hill New York).

Anderson Jr, J. D. (**2010**). *Fundamentals of aerodynamics* (Tata McGraw-Hill Education).

Andersson, N., Eriksson, L.-E., and Davidson, L. (**2005a**). "Large-eddy simulation of subsonic turbulent jets and their radiated sound," AIAA journal **43**, 1899-1912.

Andersson, N., Eriksson, L.-E., and Davidson, L. (**2005b**). "LES prediction of flow and acoustic field of a coaxial jet," in *11th AIAA/CEAS Aeroacoustics Conference*, p. 2884.

ASTM (**2010**). "Standard test method for impedance and absorption of acoustical materials using a tube, two microphones and a digital frequency analysis system."

Baehr, H. D., and Stephan, K. (**2004**). *Heat and Mass Transfer, 2nd edition* (Springer DE, Chapter 3).

Barber, T. (**1988**). "Turbofan Forced Mixer Lobed Flow Modeling, II-three dimensional Inviscid Mixer analysis,," NASA Report **CR 4147-II**.

Barber, T., Moore, G. C., and Blatt, J. R. (**1988a**). "Turbofan Forced Mixer Lobe Flow Modeling, III - Application to Augment engines. ," NASA Report **CR 4147-III**.

Barber, T., Muller, G., Ramsay, S., and Murman, E. (**1986a**). "Three-dimensional inviscid flow in mixers. I-Mixer analysis using a Cartesian grid," Journal of Propulsion and Power **2**, 275-281.

Barber, T., Muller, G., Ramsay, S., and Murman, E. (**1986b**). "Three-dimensional inviscid flow in mixers. II-Analysis of turbofan forced mixers," Journal of Propulsion and Power **2**, 339-344.

Barber, T., Paterson, R. W., and Skebe, S. A. (**1988b**). "Turbofan Forced Mixer Lobed Flow Modeling, I-Experimental and Analytical assessment " NASA Report **CR 4147-III**.

Bechert, D. (**1980**). "Sound absorption caused by vorticity shedding, demonstrated with a jet flow," Journal of Sound and Vibration **70**, 389-405.

Bechert, D. W., Michel, U., and Pfizenmaier, E. (**1978**). "Experiments on the transmission of sound through jets," AIAA Journal **16**, 873-874.

Belovich, V., Samimy, M., and Reeder, M. (**1996**). "Dual stream axisymmetric mixing in the presence of axial vorticity," Journal of propulsion and power **12**, 178-185.

Benzi, R., and Succi, S. (**1990**). "Two-dimensional turbulence with the lattice Boltzmann equation," Journal of Physics A: Mathematical and General **23**, L1.

Bergman, T. L., Incropera, F. P., and Lavine, A. S. (**2011**). *Fundamentals of heat and mass transfer* (John Wiley & Sons).

Bernsdorf, J., Durst, F., and Schäfer, M. (**1999**). "Comparison of cellular automata and finite volume techniques for simulation of incompressible flows in complex geometries," International Journal for Numerical Methods in Fluids **29**, 251-264.

Berson, A., Michard, M., and Blanc-Benon, P. (**2008**). "Measurement of acoustic velocity in the stack of a thermoacoustic refrigerator using particle image velocimetry," Heat and Mass Transfer **44**, 1015-1023.

Bhandari, V. (**2002**). "Detailed investigations of transport properties in complex reactor components," Master's thesis, Lehrstuhl fiir Stromungsmechanik, Universitat Erlangen-Niirnberg.

Bhatnagar, P. L., Gross, E. P., and Krook, M. (**1954**). "A model for collision processes in gases. I. Small amplitude processes in charged and neutral one-component systems," Physical review **94**, 511.

Birch, S. F., Paynter, G. C., Spalding, D., and Tatchell, D. (**1978**). "Numerical modeling of three-dimensional flows in turbofan engine exhaust nozzles," Journal of Aircraft **15**, 489-496.

Bodony, D. J., and Lele, S. K. (**2005**). "On using large-eddy simulation for the prediction of noise from cold and heated turbulent jets," Physics of Fluids **17**, 085103.

Bodony, D. J., and Lele, S. K. (**2008**). "Current status of jet noise predictions using large-eddy simulation," AIAA journal **46**, 364-380.

Boersma, B. J. (**2004**). "Numerical simulation of the noise generated by a low Mach number, low Reynolds number jet," Fluid Dynamics Research **35**, 425-447.

Bogey, C., and Bailly, C. (**2003**). "LES of a high Reynolds, high subsonic jet: effects of the sub-grid modellings on flow and noise," in *16th AIAA Computational Fluid Dynamics Conference* (Orlando, FL), pp. AIAA 2003-3557.

Bogey, C., and Bailly, C. (**2005**). "Investigation of sound sources in subsonic jets using causality methods on LES data," AIAA paper **2885**, 2005.

Bogey, C., and Bailly, C. (**2006**). "Large eddy simulations of round free jets using explicit filtering with/without dynamic Smagorinsky model," International journal of heat and fluid flow **27**, 603-610.

Bogey, C., and Bailly, C. (**2010**). "Influence of nozzle-exit boundary-layer conditions on the flow and acoustic fields of initially laminar jets," Journal of Fluid Mechanics **663**, 507-538.

Bogey, C., Bailly, C., and Juvé, D. (**2003**). "Noise investigation of a high subsonic, moderate Reynolds number jet using a compressible large eddy simulation," Theoretical and Computational Fluid Dynamics **16**, 273-297.

Bogey, C., Barré, S., Juvé, D., and Bailly, C. (**2009**). "Simulation of a hot coaxial jet: Direct noise prediction and flow-acoustics correlations," Physics of fluids **21**, 035105.

Bogey, C., and Marsden, O. (**2013**). "Numerical investigation of temperature effects on properties of subsonic turbulent jets," in *19th AIAA/CEAS Aeroacoustics Conference*, pp. 1-19.

Bogey, C., Marsden, O., and Bailly, C. (**2011**). "Large-eddy simulation of the flow and acoustic fields of a Reynolds number 105 subsonic jet with tripped exit boundary layers," Physics of Fluids (1994-present) **23**, 035104.

Booher, M. E., Kwon, O., BARTA, A. B., Vittal, B. R., and Krishnan, M. R. (**1993**). "Development of an advanced exhaust mixer for a high bypass ratio turbofan engine," in *AIAA/SAE/ASME/ASEE Joint Propulsion Conference* (AIAA, Monterey, CA).

Brentner, K. S., and Farassat, F. (**1997**). "An analytical comparison of the acoustic analogy and Kirchhoff formulation for moving surfaces."

Brentner, K. S., and Farassat, F. (**2003**). "Modeling aerodynamically generated sound of helicopter rotors," Progress in Aerospace Sciences **39**, 83-120.

Bres, G. A., Pérot, F., and Freed, D. (**2009**). "Properties of the lattice-Boltzmann method for acoustics," in *15th AIAA/CEAS Aeroacoustics Conference*.

Bridges, J., and Brown, C. (**2004**). "Parametric testing of chevrons on single flow hot jets," in *10th AIAA/CEAS Aeroacoustics Conference*, p. 2824.

Bridges, J., and Brown, C. A. (**2005**). "Validation of the small hot jet acoustic rig for aeroacoustic research," AIAA Paper **2846**, 2005.

Bridges, J., and Wernet, M. P. (**2003**). "Measurements of the aeroacoustic sound source in hot jets," in *9th AIAA/CEAS Aeroacoustics Conference* (Hilton Head, SC), pp. AIAA-2003-3130.

Bridges, J., and Wernet, M. P. (**2004**). "Cross-stream PIV measurements of jets with internal lobed mixers," AIAA paper **2896**.

Bridges, J., and Wernet, M. P. (**2007**). "Effect of temperature on jet velocity spectra," AIAA paper **3628**, 2007.

Bridges, J., and Wernet, M. P. (**2010**). "Establishing consensus turbulence statistics for hot subsonic jets," in *16th AIAA/CEAS Aeroacoustics Conference*, pp. 1-41.

Brinkerhoff, J. R., Oria, H., and Yaras, M. I. (**2013**). "Experimental and computational study of mixing mechanisms in an axisymmetric lobed mixer," Journal of Propulsion and Power **29**, 1017-1030.

Brogi, F., Malaspinas, O., Bonadonna, C., Chopard, B., and Ripepe, M. (**2015**). "Towards a Numerical Description of Volcano Aeroacoustic Source Processes using Lattice Boltzmann Strategies," in *AGU Fall Meeting Abstracts*.

Callender, B., Gutmark, E., and Martens, S. (**2008**). "Near-field investigation of chevron nozzle mechanisms," AIAA journal **46**, 36-45.

Callender, B., Gutmark, E. J., and Martens, S. (**2005**). "Far-field acoustic investigation into chevron nozzle mechanisms and trends," AIAA journal **43**, 87-95.

Cappello, F., and Etiemble, D. (**2000**). "MPI versus MPI+ OpenMP on the IBM SP for the NAS Benchmarks," in *Supercomputing, ACM/IEEE 2000 Conference* (IEEE), pp. 12-12.

Casalino, D., and Hazir, A. (**2015**). "Computation of Dual-Stream Unsteady Jet Flows and Noise," in *Proceeding of The 22nd International Congress of Sound and Vibration*.

Casalino, D., and Lele, S. (**2014**). "Lattice-boltzmann simulation of coaxial jet noise generation," in *CTR, Proceedings of the Summer Program*, p. 231.

Casalino, D., Ribeiro, A., Fares, E., Nölting, S., Mann, A., Perot, F., Li, Y., Lew, P.-T., Sun, C., and Gopalakrishnan, P. (**2014a**). "Towards lattice-Boltzmann prediction of turbofan engine noise," in *20th AIAA/CEAS Aeroacoustics Conference*, pp. 192-215.

Casalino, D., Ribeiro, A., Fares, E., Nölting, S., Mann, A., Perot, F., Li, Y., Lew, P., Sun, C., and Gopalakrishnan, P. (**2014b**). "Towards Lattice-Boltzmann Prediction of Turbofan Engine Noise," AIAA Paper **3101**.

Casalino, D., Ribeiro, A. F., and Fares, E. (**2014c**). "Facing rim cavities fluctuation modes," Journal of Sound and Vibration **333**, 2812-2830.

Casalino, D., Ribeiro, A. F., Fares, E., and Nölting, S. (**2014d**). "Lattice–Boltzmann Aeroacoustic Analysis of the LAGOON Landing-Gear Configuration," AIAA journal **52**, 1232-1248.

Chapman, S., and Cowling, T. G. (**1970**). *The mathematical theory of non-uniform gases: an account of the kinetic theory of viscosity, thermal conduction and diffusion in gases* (Cambridge university press, Chapter 4).

Chen, H. (**1998**). "Volumetric formulation of the lattice Boltzmann method for fluid dynamics: Basic concept," Physical Review E **58**, 3955-3963.

Chen, H., Chen, S., and Matthaeus, W. H. (**1992a**). "Recovery of the Navier-Stokes equations using a lattice-gas Boltzmann method," Physical Review A **45**, R5339-R5342.

Chen, H., Kandasamy, S., Orszag, S., Shock, R., Succi, S., and Yakhot, V. (**2003**). "Extended Boltzmann kinetic equation for turbulent flows," Science **301**, 633-636.

Chen, H., Teixeira, C., and Molvig, K. (**1997**). "Digital physics approach to computational fluid dynamics: some basic theoretical features," International Journal of Modern Physics C **8**, 675-684.

Chen, H., Zhang, R., and Gopalakrishnan, P. (**2013**). "Lattice Boltzmann Collision Operator Enforcing Isotropy and Galilean Invariance," in *US patent*, edited by U. p. pending (US).

Chen, S., Chen, H., Martnez, D., and Matthaeus, W. (**1991**). "Lattice Boltzmann model for simulation of magnetohydrodynamics," Physical Review Letters **67**, 3776.

Chen, S., and Doolen, G. D. (**1998**). "Lattice Boltzmann method for fluid flows," Annual review of fluid mechanics **30**, 329-364.

Chen, S., Gojon, R., and Mihaescu, M. (**2018**). "High-temperature effects on aerodynamic and acoustic characteristics of a rectangular supersonic jet," in *2018 AIAA/CEAS aeroacoustics conference*, p. 3303.

Chen, S., Wang, Z., Shan, X., and Doolen, G. D. (**1992b**). "Lattice Boltzmann computational fluid dynamics in three dimensions," Journal of Statistical Physics **68**, 379-400.

Chikatamarla, S., Frouzakis, C., Karlin, I., Tomboulides, A., and Boulouchos, K. (**2010**). "Lattice Boltzmann method for direct numerical simulation of turbulent flows," Journal of Fluid Mechanics **656**, 298-308.

Choi, D., Barber, T., Chiappetta, L., and Nishimura, M. (**1999**). "Large eddy simulation of high-Reynolds number jet flows," in *37th AIAA Aerospace Sciences Meeting* (Reno, NV), pp. AIAA 1999-1230.

Clausen, J. R., Reasor, D. A., and Aidun, C. K. (**2010**). "Parallel performance of a lattice-Boltzmann/finite element cellular blood flow solver on the IBM Blue Gene/P architecture," Computer Physics Communications **181**, 1013-1020.

Constantinescu, G., and Lele, S. (**2001**). "Large eddy simulation of a near sonic turbulent jet and its radiated noise," in *30th AIAA Aerospace Sciences Meeting* (Reno, V), pp. AIAA 2001-0376.

Cooper, W., Nee, V., and Yang, K. (**1994**). "An experimental investigation of convective heat transfer from the heated floor of a rectangular duct to a low frequency, large tidal displacement oscillatory flow," International journal of heat and mass transfer **37**, 581-592.

Crighton, D. (**1981**). "Acoustics as a branch of fluid mechanics," Journal of Fluid Mechanics **106**, 261-298.

Crouch, R., Coughlin, C., and Paynter, G. (**1977**). "Nozzle exit flow profile shaping for jet noise reduction," Journal of Aircraft **14**, 860-867.

Crouse, B., Senthooran, S., Freed, D., Balasubramanian, G., Gleason, M., Puskarz, M., Lew, P., and Mongeau, L. (**2006a**). "Experimental and numerical investigation of a flow-induced cavity resonance with application to automobile buffeting," AIAA Paper.

Crouse, B., Senthooran, S., Freed, D., Balasubramanian, G., Gleason, M., Puskarz, M., Lew, P., and Mongeau, L. (**2006b**). "Experimental and Numerical Investigation of a Flow Induced Cavity Resonance with Application to Automobile Buffeting," in *12th AIAA/CEAS Aeroacoustics Conference* (Cambridge, MA), pp. AIAA 2006-2494.

DaWei, L., Jun, H., Zhiqiang, S., and Jinzu, J. (**2015**). "The effects of scalloping width and position on jet mixing of lobed nozzles," Journal of Aerospace Technology and Management **7**, 425-431.

Di Francescantonio, P. (**1997**). "A new boundary integral formulation for the prediction of sound radiation," Journal of Sound and Vibration **202**, 491-509.

Dokumaci, E. (**1997**). "A note on transmission of sound in a wide pipe with mean flow and viscothermal attenuation," Journal of sound and vibration **208**, 653-655.

Eckerle, W., Sheibani, H., and Awad, J. (**1992**). "Experimental measurement of the vortex development downstream of a lobed forced mixer," Journal of engineering for gas turbines and power **114**, 63-71.

Elliot, J., Manning, T., Qiu, Y., Greitzer, E., Tan, C., and Tillman, T. (**1992**). "Computational and experimental studies of flow in multi-lobed forced mixers," in *AIAA/SAE/ASME/ASEE Joint Propulsion conference* (Nashville, TN), pp. AIAA paper 92-3568.

Eschricht, D., Yan, J., Michel, U., and Thiele, F. (**2008**). "Prediction of jet noise from a coplanar nozzle," in *14th AIAA/CEAS Aeroacoustics Conference (29th AIAA Aeroacoustics Conference)*, p. 2969.

Farassat, F. (**1981**). "Linear acoustic formulas for calculation of rotating blade noise," AIAA journal **19**, 1122-1130.

Farassat, F. (**2007**). "Derivation of Formulations 1 and 1A of Farassat."

Farassat, F., and Succi, G. P. (**1982**). "The prediction of helicopter rotor discrete frequency noise," in *In: American Helicopter Society, Annual Forum, 38th, Anaheim, CA, May 4-7, 1982, Proceedings.(A82-40505 20-01) Washington, DC, American Helicopter Society, 1982, p. 497-507.*, pp. 497-507.

Fares, E. (**2006**). "Unsteady flow simulation of the Ahmed reference body using a lattice Boltzmann approach," Computers & Fluids **35**, 940-950.

Fares, E., Duda, B., and Khorrami, M. R. (**2016**). "Airframe Noise Prediction of a Full Aircraft in Model and Full Scale Using a Lattice Boltzmann Approach."

Fayard, B., Rahier, G., Vuillot, F., and Kerhervé, F. (**2008**). "Flow field analysis for double stream nozzle: application to jet noise," in *14th AIAA/CEAS Aeroacoustics Conference (29th AIAA Aeroacoustics Conference)*, p. 2983.

Ffowcs Williams, J. (**1963**). "The noise from turbulence convected at high speed," Phil. Trans. R. Soc. Lond. A **255**, 469-503.

Ffowcs Williams, J., and Hawkings, D. L. (**1969**). "Sound generation by turbulence and surfaces in arbitrary motion," Philosophical Transactions of the Royal Society of London A: Mathematical, Physical and Engineering Sciences **264**, 321-342.

Filippova, O., and Hänel, D. (**1998**). "Grid refinement for lattice-BGK models," Journal of Computational Physics **147**, 219-228.

Fisher, M., Lush, P., and Bourne, M. H. (**1973**). "Jet noise," Journal of Sound and Vibration **28**, 563-585.

Fisher, M., Preston, G., and Bryce, W. (**1993**). "A modeling of the noise from simple co-axial jets," in *15th Aeroacoustics Conference*, p. 4413.

Fisher, M., Preston, G., and Mead, C. (**1998**). "A modelling of the noise from simple coaxial jets, part II: with heated primary flow," Journal of Sound and Vibration **209**, 405-417.

Fleury, V., Bailly, C., Jondeau, E., Michard, M., and Juvé, D. (**2008**). "Space-time correlations in two subsonic jets using dual particle image velocimetry measurements," AIAA journal **46**, 2498-2509.

Freed, D. M. (**1998**). "Lattice-Boltzmann method for macroscopic porous media modeling," International Journal of Modern Physics C **9**, 1491-1503.

Freund, J. B. (**1999**). "Direct numerical simulation of the noise from a Mach 0.9 jet," FEDSM Paper.

Freund, J. B. (**2001**). "Noise sources in a low-Reynolds-number turbulent jet at Mach 0.9," Journal of Fluid Mechanics **438**, 277-305.

Frisch, U., d'Humieres, D., Hasslacher, B., Lallemand, P., Pomeau, Y., and Rivet, J.-P. (**1987**). "Lattice gas hydrodynamics in two and three dimensions," Complex systems **1**, 649-707.

Frost, T. (**1966**). "Practical bypass mixing systems for fan jet aero engines(Exhaust mixing process in Rolls-Royce by-pass jet engines, noting stream mixing in common duct with corrugated metal interface on inlet side)," Aeronautical quarterly **17**, 141-160.

Garrison, L., Dalton, W., Lyrintzis, A., and Blaisdell, G. (**2004**). "On the development of semi-empirical noise models for the prediction of the noise from jets with forced mixers," AIAA paper **2898**, 1011.

Garrison, L., Lyrintzis, A., and Blaisdell, G. (**2006**). "RANS-based noise predictions of jets with internal forced mixers," in *12th AIAA/CEAS Aeroacoustics Conference (27th AIAA Aeroacoustics Conference)*, p. 2599.

Garrison, L., Lyrintzis, A., Blaisdell, G., and Dalton, W. (**2005**). "Computational fluid dynamics analysis of jets with internal forced mixers," AIAA paper **2887**.

Geller, S., Krafczyk, M., Tölke, J., Turek, S., and Hron, J. (**2006**). "Benchmark computations based on lattice-Boltzmann, finite element and finite volume methods for laminar flows," Computers & Fluids **35**, 888-897.

Gerbaux, O., Vercueil, T., Memponteil, A., and Bador, B. (**2009**). "Experimental characterization of single and two-phase flow through nickel foams," Chemical Engineering Science **64**, 4186-4195.

Ginevsky, A. S., Vlasov, Y. V., and Karavosov, R. K. (**2004**). *Acoustic control of turbulent jets* (Springer).

Gojon, R., Baier, F., Gutmark, E. J., and Mihaescu, M. (**2017**). "Temperature effects on the aerodynamic and acoustic fields of a rectangular supersonic jet," in *55th AIAA aerospace sciences meeting*, p. 0002.

Goldstein, M. (**1984**). "Aeroacoustics of turbulent shear flows," Annual Review of Fluid Mechanics **16**, 263-285.

Goldstein, M. E. (**2003**). "A generalized acoustic analogy," Journal of Fluid Mechanics **488**, 315-333.

Goldstein, M. E., and Howes, W. L. (**1973**). "New aspects of subsonic aerodynamic noise theory."

Golosnoy, I., Tan, J., and Clyne, T. (**2008**). "Ferrous fibre network materials for jet noise reduction in aeroengines part I: Acoustic effects," Advanced Engineering Materials **10**, 192-200.

Gong, H. (**2013**). "Numerical study of jet noise generated by turbofan engine nozzles equipped with internal forced lobed mixers using the lattice boltzmann method," in *Mechanical Engineering* (McGill Univeristy, Montreal).

Gong, H., Habibi, K., and Mongeau, L. (**2013**). "Effects of scalloping depth on the sound generated by turbofan engine lobed mixers," in *Proceedings of Meetings on Acoustics* (Acoustical Society of America), p. 030122.

Gopalakrishnan, P., Zhang, R., and Chen, H. (**2013**). "Improved Temperature Coupling Algorithm for Hybrid Thermal Lattice Boltzmann Method," edited by U. patent (USA).

Gopalakrishnan, P., Zhang, R., and Chen, H. (**2016**). "Temperature coupling algorithm for hybrid thermal lattice boltzmann method," (Google Patents).

Habibi, K., Gong, H., and Mongeau, L. (**2013a**). "A robust numerical approach for the prediction of turbofan engine noise," in *Proceedings of Meetings on Acoustics* (Acoustical Society of America), p. 040068.

Habibi, K., Gong, H., Najafi-Yazdi, A., and Mongeau, L. (**2013b**). "Numerical Simulations of Sound radiated from Internal Mixing Nozzles with Forced Mixers using the Lattice Boltzmann Method."

Habibi, K., and Mongeau, L. (**2013**). "Numerical Predictions of Exhaust Noise Emissions from Internal-Mixing Nozzles " in *60th CASI Aeronautics Confeence and AGM* (Toronto, Canada).

Habibi, K., and Mongeau, L. (**2015**). "Prediction of sound absorption by a circular orifice termination in a turbulent pipe flow using the Lattice-Boltzmann method," Applied Acoustics **87**, 153-161.

Habibi, K., Mongeau, L., Casalino, D., and Lew, P.-T. (**2014**). "Aeroacoustic study of Internal Mixing Nozzles with Forced Lobed Mixers using a High-Mach Subsonic Lattice Boltzmann Scheme," AIAA Paper **3313**.

Habibi, K., Mosahebi, A., and Shokouhmand, H. (**2011a**). "Heat transfer characteristics of reciprocating flows in channels partially filled with porous medium," Transport in porous media **89**, 139-153.

Habibi, K., Najafi-Yazdi, A., Lew, P.-T., and Mongeau, L. (**2011b**). "Simulation of sound radiated from turbulent heated jets using the lattice-Boltzmann method," in *Proc. 17th AIAA/CEAS Aeroacoustics Conf.(Portland, OR, 5–8 June 2011)*.

Habibi, K., Rafat, Y., Mongeau, L., and Taher, R. (**2012**). "Numerical and experimental characterization of oscillatory flows over a flat spoiler in a duct," in *INTER-NOISE and NOISE-CON Congress and Conference Proceedings* (Institute of Noise Control Engineering), pp. 2702-2712.

Hartmann (**1969**). "Studies of Mixing in Ducted Fan Jet Engines," NASA Report **TTF-12**.

He, X., Chen, S., and Doolen, G. D. (**1998**). "A novel thermal model for the lattice Boltzmann method in incompressible limit," Journal of Computational Physics **146**, 282-300.

He, X., and Luo, L.-S. (**1997**). "Theory of the lattice Boltzmann method: From the Boltzmann equation to the lattice Boltzmann equation," Physical Review E **56**, 6811.

Higuera, F., and Jimenez, J. (**1989**). "Boltzmann approach to lattice gas simulations," EPL (Europhysics Letters) **9**, 663.

Hileman, J., and Samimy, M. (**2001**). "Turbulence structures and the acoustic far field of a Mach 1.3 jet," AIAA journal **39**, 1716-1727.

Hirsch, C. (**2007**). *Numerical Computation of Internal and External Flows: The Fundamentals of Computational Fluid Dynamics: The Fundamentals of Computational Fluid Dynamics* (Butterworth-Heinemann).

Hoch, R., Duponchel, J., Cocking, B., and Bryce, W. (**1973**). "Studies of the influence of density on jet noise," Journal of Sound and Vibration **28**, 649-668.

Howe, M. (**1975**). "Contributions to the theory of aerodynamic sound, with application to excess jet noise and the theory of the flute," Journal of Fluid Mechanics **71**, 625-673.

Howe, M. (**1979**). "Attenuation of sound in a low Mach number nozzle flow," Journal of Fluid Mechanics **91**, 209-229.

Howe, M. (**1984**). "On the absorption of sound by turbulence and other hydrodynamic flows," IMA Journal of Applied Mathematics **32**, 187-209.

Howe, M. S. (**1998**). *Acoustics of fluid-structure interactions* (Cambridge University Press).

Howe, M. S. (**2003**). *Theory of vortex sound* (Cambridge University Press).

Hubbard, H. H. (**1991**). "Aeroacoustics of flight vehicles: Theory and practice. volume 1. noise sources," (DTIC Document).

Huff, D. L. (**2007**). "Noise reduction technologies for turbofan engines."

Hughes, I., and Dowling, A. (**1990**). "The absorption of sound by perforated linings," Journal of Fluid Mechanics **218**, 299-335.

Ingard, U., and Ising, H. (**1967**). "Acoustic nonlinearity of an orifice," The journal of the Acoustical Society of America **42**, 6-17.

Ingard, U., and Singhal, V. K. (**1974**). "Sound attenuation in turbulent pipe flow," The Journal of the Acoustical Society of America **55**, 535-538.

Jeong, J., and Hussain, F. (**1995**). "On the identification of a vortex," Journal of fluid mechanics **285**, 69-94.

Ji, C., and Zhao, D. (**2013**). "Numerical investigation of acoustically excited flow through an orifice using lattice Boltzmann method," The Journal of the Acoustical Society of America **133**, 3265-3265.

Jing, X., and Sun, X. (**1999**). "Experimental investigations of perforated liners with bias flow," The Journal of the Acoustical Society of America **106**, 2436-2441.

Johnson, D. L., Koplik, J., and Dashen, R. (**1987**). "Theory of dynamic permeability and tortuosity in fluid-saturated porous media," Journal of fluid mechanics **176**, 379-402.

Jones, M. G., and Parrott, T. L. (**1989**). "Evaluation of a multi-point method for determining acoustic impedance," Mechanical Systems and Signal Processing **3**, 15-35.

Kandula, M. (**2008**). "On the scaling laws and similarity spectra for jet noise in subsonic and supersonic flow," International Journal of Acoustics and Vibrations **13**, 3-16.

Karon, A. Z., and Ahuja, K. (**2013**). "Effect of nozzle-exit boundary layer on jet noise," AIAA Paper **615**, 13.

Kays, W. M., Crawford, M. E., and Weigand, B. (**2012**). *Convective heat and mass transfer* (Tata McGraw-Hill Education).

Kearney-Fischer, M., Kim, J.-H., and Samimy, M. (**2009**). "Control of a high Reynolds number Mach 0.9 heated jet using plasma actuators," Physics of Fluids (1994-present) **21**, 095101.

Khan, M. T. I., Seto, K., Xu, Z., and Ohta, H. (**2004**). "An approach to noise reduction of a supersonic jet with a spherical reflector," Acoustical Science and Technology **25**, 136-143.

Khavaran, A., and Bridges, J. (**2010**). "Jet noise scaling in dual stream nozzles," in *16th AIAA/CEAS Aeroacoustics Conference*, p. 3968.

Khavaran, A., and Dahl, M. (**2012**). "Acoustic Investigation of jet mixing noise in Dual stream nozzles," in *17th AIAA/CEAS Aeroacoustics Conference (32nd AIAA Aeroacoustics Conference)*, p. 2701.

Khavaran, A., Krejsa, E. A., and Kim, C. M. (**1994**). "Computation of supersonic jet mixing noise for an axisymmetric convergent-divergent nozzle," Journal of Aircraft **31**, 603-609.

Khorrami, M. R., Fares, E., and Casalino, D. (**2014**). "Towards Full-Aircraft Airframe Noise Prediction: Lattice-Boltzmann Simulations," AIAA Paper **2481**, 2014.

Kierkegaard, A., Allam, S., Efraimsson, G., and Åbom, M. (**2012**). "Simulations of whistling and the whistling potentiality of an in-duct orifice with linear aeroacoustics," Journal of sound and vibration **331**, 1084-1096.

Kim, Y.-H. (**2010**). *Sound propagation: an impedance based approach* (John Wiley & Sons).

Knio, E. B., Omar M (**2001**). "Numerical study of thermoacoustic heat exchangers in the thin plate limit," Numerical Heat Transfer: Part A: Applications **40**, 445-471.

Ko, N., and Kwan, A. (**1976**). "The initial region of subsonic coaxial jets," Journal of Fluid Mechanics **73**, 305-332.

Koelman, J. (**1991**). "A simple lattice Boltzmann scheme for Navier-Stokes fluid flow," EPL (Europhysics Letters) **15**, 603.

Koh, S. R., Schröder, W., and Meinke, M. (**2013**). "Noise sources in heated coaxial jets," Computers & Fluids **78**, 24-28.

Kollmannsberger, S., Geller, S., Düster, A., Tölke, J., Sorger, C., Krafczyk, M., and Rank, E. (**2009**). "Fixed-grid fluid–structure interaction in two dimensions based on a partitioned Lattice Boltzmann and p-FEM approach," International journal for numerical methods in engineering **79**, 817-845.

Kooijman, G., Hirschberg, A., and Golliard, J. (**2008**). "Acoustical response of orifices under grazing flow: Effect of boundary layer profile and edge geometry," Journal of Sound and Vibration **315**, 849-874.

Körner, C., Pohl, T., Rüde, U., Thürey, N., and Zeiser, T. (**2006**). "Parallel lattice Boltzmann methods for CFD applications," in *Numerical Solution of Partial Differential Equations on Parallel Computers* (Springer), pp. 439-466.

Koutmos, P., and McGuirk, J. (**1989**). "Turbofan forced mixer/nozzle temperature and flow field modelling," International journal of heat and mass transfer **32**, 1141-1153.

Kozlowski, H., and Kraft, G. (**1980**). "Experimental evaluation of exhaust mixers for an Energy Efficient Engine," in *AIAA/SAE/ASME joint propulsion conference* (AIAA, Hartfort, CT).

Kreskovsky, J., Briley, W., and McDonald, H. (**1984**). "Investigation of mixing in a turbofan exhaust duct, part i: analysis and computational procedure," AIAA journal **22**, 374-382.

Kuchar, A., and Chamberlin, R. (**1980**). "Scale Model Performance Test Investigation of Exhaust System Mixers for an Energy Efficient Engine (E3) Propulsion System," AIAA paper **80**, 0229.

Larkin, M. J., and Blatt, J. R. (**1984**). "Energy efficient energy exhaust mixer model technology report addendum, Phase III test program," NASA report **CR-174792**.

Lau, J. (**1981**). "Effects of exit Mach number and temperature on mean-flow and turbulence characteristics in round jets," Journal of Fluid Mechanics **105**, 193-218.

Lele, S. K. (**1992**). "Compact finite difference schemes with spectral-like resolution," Journal of Computational Physics **103**, 16-42.

Lepicovsky, J. (**1999**). "Experimental research on mixing enhancement in heated free jet flows," ASME FEDSM paper **997247**.

Lew, P.-T., Blaisdell, G. A., and Lyrintzis, A. S. (**2007**). "Investigation of noise sources in turbulent hot jets using large eddy simulation data," in *45th AIAA Aerospace Sciences Meeting* (Reno, NV), pp. AIAA 2007-0016.

Lew, P.-T., Mongeau, L., and Lyrintzis, A. (**2010a**). "Noise prediction of a subsonic turbulent round jet using the lattice-Boltzmann method," Journal of the Acoustical Society of America **128**, 1118-1127.

Lew, P.-T., Mongeau, L., and Lyrintzis, A. (**2010b**). "Noise prediction of a subsonic turbulent round jet using the lattice-Boltzmann method," The Journal of the Acoustical Society of America **128**, 1118-1127.

Lew, P.-T., Najafiyazdi, A., and Mongeau, L. (**2013**). "Unsteady numerical simulation of a round jet with impinging microjets for noise suppression," Journal of the Acoustical Society of America **134**.

Lew, P., Blaisdell, G., and Lyrintzis, A. (**2005**). "Recent progress of hot jet aeroacoustics using 3-D large eddy simulation," AIAA paper **3084**, 2005.

Lew, P., Gopalakrishnan, P., Casalino, D., Shock, R., Li, Y., Zhangk, R., Chen, H., Habibi, K., and Mongeau, L. (**2014**). "An Extended Lattice Boltzmann Methodology for High Subsonic Jet Noise Prediction," in *20th AIAA/CEAS Aeroacoustics Conference (AVIATION 2014)*.

Li, Y., Shock, R., Zhang, R., and Chen, H. (**2004**). "Numerical study of flow past an impulsively started cylinder by the lattice-Boltzmann method," Journal of Fluid Mechanics **519**, 273-300.

Lighthill, M. J. (**1952**). "On sound generated aerodynamically. I. General theory," in *Proceedings of the Royal Society of London A: Mathematical, Physical and Engineering Sciences* (The Royal Society), pp. 564-587.

Lilley, G. M. (**1974**). "On the noise from jet," AGARD Conf. Proc., 1974 **131**, 13.11-13.12.

Lockard, D. P. (**2000**). "An efficient, two-dimensional implementation of the Ffowcs Williams and Hawkings equation," Journal of Sound and Vibration **229**, 897-911.

Luo, L.-S., Qi, D., and Wang, L.-P. (**2002**). *Applications of the lattice Boltzmann method to complex and turbulent flows* (Springer).

Lush, P. (**1971**). "Measurements of subsonic jet noise and comparison with theory," Journal of Fluid Mechanics **46**, 477-500.

Lyrintzis, A., and Mankbadi, R. (**1996**). "Prediction of the far-field jet noise using Kirchhoff's formulation," AIAA journal **34**, 413-416.

Lyrintzis, A. S. (**2003**). "Surface integral methods in computational aeroacoustics—From the (CFD) near-field to the (Acoustic) far-field," International journal of aeroacoustics **2**, 95-128.

Malecki, R., and Lord, W. (**1990**). "Navier-Stokes analysis of a lobed mixer and nozzle," AIAA paper, 90-0453.

Mankbadi, R. R., Hayder, M. E., and Povinelli, L. A. (**1994**). "Structure of supersonic jet flow and its radiated sound," AIAA journal **32**, 897-906.

Mann, A., Pérot, F., Kim, M.-S., and Casalino, D. (**2013**). "Characterization of acoustic liners absorption using a Lattice-Boltzmann method," in *19th AIAA/CEAS Aeroacoustics conference, Berlin, Germany*.

Manning, T. A. (**1991**). "Experimental studies of mixing flows with streamwise vorticity," (Massachusetts Institute of Technology).

Mao, X., Yu, Z., Jaworski, A. J., and Marx, D. (**2008**). "PIV studies of coherent structures generated at the end of a stack of parallel plates in a standing wave acoustic field," Experiments in fluids **45**, 833-846.

Martys, N. S., and Chen, H. (**1996**). "Simulation of multicomponent fluids in complex three-dimensional geometries by the lattice Boltzmann method," Physical Review E **53**, 743.

Marx, D., and Blanc-Benon, P. (**2004**). "Numerical simulation of stack-heat exchangers coupling in a thermoacoustic refrigerator," AIAA journal **42**, 1338-1347.

Mathew, J., Lechner, R., Foysi, H., Sesterhenn, J., and Friedrich, R. (**2003**). "An explicit filtering method for large eddy simulation of compressible flows," Physics of fluids **15**, 2279.

McCormick, D. C., and Ennett, J. (**1994**). "Vortical and turbulent structure of a lobed mixer free shear layer," AIAA journal **32**, 1852-1859.

McNamara, G. R., Garcia, A. L., and Alder, B. J. (**1997**). "A hydrodynamically correct thermal lattice Boltzmann model," Journal of statistical physics **87**, 1111-1121.

McNamara, G. R., and Zanetti, G. (**1988**). "Use of the Boltzmann equation to simulate lattice-gas automata," Physical Review Letters **61**, 2332.

Meade, J. P. (**1994**). "Acoustic evaluation of a forced mixer on a high bypass ratio engine," AIAA Paper.

Mendez, S., Shoeybi, M., Lele, S., and Moin, P. (**2013**). "On the use of the Ffowcs Williams-Hawkings equation to predict far-field jet noise from large-eddy simulations," International Journal of Aeroacoustics **12**, 1-20.

Mengle, V. G., Baker, V. D., and Dalton, W. N. (**2002**). "Lobed Mixer Design for Noise Suppression Plume, Aerodynamic and Acoustic Data (Vol.1 & 2)," NASA Report **CR-210823-1 & CR-210823-2**.

Menter, F. R. (**1994**). "Two-equation eddy-viscosity turbulence models for engineering applications," AIAA journal **32**, 1598-1605.

Meslioui, S.-A. (**2007**). "Jet noise prediction model for turbofan engines with internal forced mixers," Canadian Acoustics **35**, 24-25.

Meslioui, S.-A., Cunningham, M., and Germain, P. (**2007**). "Determination of CFD Turbulence Scales for Lobed Mixer Jet Noise Prediction," in *ASME Turbo Expo 2007: Power for Land, Sea, and Air* (American Society of Mechanical Engineers), pp. 1541-1549.

Mihaescu, M., Gutmark, E., Szasz, R., and Fuchs, L. (**2006**). "Flow and acoustics of a coaxial nozzle: A sensitivity study to the inlet boundary conditions," in *44th AIAA Aerospace Sciences Meeting and Exhibit*, p. 619.

Morfey, C. (**1973**). "Amplification of aerodynamic noise by convected flow inhomogeneities," Journal of Sound and Vibration **31**, 391-397.

Morfey, C., Szewczyk, V., and Tester, B. (**1978**). "New scaling laws for hot and cold jet mixing noise based on a geometric acoustics model," Journal of Sound and Vibration **61**, 255-292.

Morgans, A. S., Karabasov, S. A., Dowling, A. P., and Hynes, T. P. (**2005**). "Transonic helicopter noise," AIAA journal **43**, 1512-1524.

Morris, P., and Harper-Bourne, M. (**2010**). "Jet noise measurements: past and present," International Journal of Aeroacoustics **9**, 559-588.

Morris, P. J. (**2009**). "A note on noise generation by large scale turbulent structures in subsonic and supersonic jets," International Journal of Aeroacoustics **8**, 301-315.

Motsinger, R., and Kraft, R. (**1991**). "Design and performance of duct acoustic treatment."

Munjal, M. L., and Munjal, M. (**1987**). *Acoustics of ducts and mufflers with application to exhaust and ventilation system design* (Wiley New York (NY) et al.).

Nabavi, M., Siddiqui, M. K., and Dargahi, J. (**2007**). "Simultaneous measurement of acoustic and streaming velocities using synchronized PIV technique," Measurement Science and Technology **18**, 1811.

Najafi-Yazdi, A. (**2011**). "Large eddy simulation of sound generation by turbulent reacting and nonreacting shear flows," (McGill University).

Najafi-Yazdi, A., Brès, G. A., and Mongeau, L. (**2011**). "An acoustic analogy formulation for moving sources in uniformly moving media," Proceedings of the Royal Society A: Mathematical, Physical and Engineering Science **467**, 144-165.

Najafi-Yazdi, A., and Mongeau, L. (**2012a**). "An absorbing boundary condition for the lattice Boltzmann method based on the perfectly matched layer," Computers & fluids **68**, 203-218.

Najafi-Yazdi, A., and Mongeau, L. (**2012b**). "A low-dispersion and low-dissipation implicit Runge-Kutta scheme," Journal of computational physics **233**, 315-323.

Nie, X., Shan, X., and Chen, H. (**2009a**). "A Lattice-Boltzmann/finite-difference hybrid simulation of transonic flow," in *47th AIAA Aerospace Sciences Meeting Including the New Horizons Forum and Aerospace Exposition*, p. 139.

Nie, X., Shan, X., and Chen, H. (**2009b**). "Lattice Boltzmann/finite-difference hybrid simulation of transonic flow," AIAA Paper **139**.

Noise, F. I. C. o. (**1992**). *Federal agency review of selected airport noise analysis issues* (Federal Interagency Committee on Noise).

Packman, A., Kozlowski, H., and Gutierrez (**1977**). "Jet noise characteristics of unsuppressed duct burning turbofan exhaust system," Journal of Aircraft **14**, 227-232.

Paliath, U., and Morris, P. J. (**2004**). "Prediction of noise from jets with different nozzle geometries," in *10th AIAA/CEAS Aeroacoustics Conference* (Manchester, UK), pp. AIAA 2004-3026.

Paterson, R. W. (**1981**). "Turbofan Forced Mixer-Nozzle internal flow field Vol. A - Benchmarl experimental Study," NASA Report **CR-3492**.

Peng, Y., Liao, W., Luo, L.-S., and Wang, L.-P. (**2010**). "Comparison of the lattice Boltzmann and pseudo-spectral methods for decaying turbulence: Low-order statistics," Computers & Fluids **39**, 568-591.

Perot, F., Kim, M., Meskine, M., and Freed, D. (**2012**). "NREL wind turbine aerodynamics validation and noise predictions using a Lattice Boltzmann Method," in *18th AIAA/CEAS Aeroacoustics Conference (33rd AIAA Aeroacoustics Conference), AIAA*.

Pervaiz, M. M., and Teixeira, C. M. (**1999**). "Two equation turbulence modeling with the lattice-Boltzmann method," ASME-PUBLICATIONS-PVP **397**, 15-24.

Phillips, O. M. (**1960**). "On the generation of sound by supersonic turbulent shear layers," Journal of Fluid Mechanics **9**, 1-28.

Pierce, A. D. (**1981**). *Acoustics: an introduction to its physical principles and applications* (McGraw-Hill New York).

Pilon, A. R., and Lyrintzis, A. S. (**1996**). "An improved Kirchhoff method for jet aeroacoustics," AIAA Paper.

Pilon, A. R., and Lyrintzis, A. S. (**1998**). "Development of an improved Kirchhoff method for jet aeroacoustics," AIAA journal **36**, 783-790.

Pitts, W. M. (**1991**). "Effects of global density ratio on the centreline mixing behaviour of axisymmetric turbulent jets," Experiments in Fluids **11**, 125-134.

Pohl, T., Kowarschik, M., Wilke, J., Iglberger, K., and Rüde, U. (**2003**). "Optimization and profiling of the cache performance of parallel lattice Boltzmann codes," Parallel Processing Letters **13**, 549-560.

Poinsot, T. J., amp, and Lelef, S. (**1992**). "Boundary conditions for direct simulations of compressible viscous flows," Journal of computational physics **101**, 104-129.

Pope, S. B. (**2000**). *Turbulent flows* (Cambridge university press).

Povinelli, L. A., and Anderson, B. (**1984**). "Investigation of mixing in a turbofan exhaust duct. II Computer codeapplication and verification," AIAA journal **22**, 518-525.

Powell, A. (**1964**). "Theory of vortex sound," The journal of the acoustical society of America **36**, 177-195.

Presz, W. M., Gousy, R., and Morin, B. (**1988**). "Forced mixer lobes in ejector designs," Journal of Propulsion and Power **4**, 350-360.

Presz, W. M., Morin, B. L., and Blinn, R. F. (**1987**). "Short efficient ejector systems," in *AIAA/SAE/ASME/ASEE Joint Propulsion conference* (AIAA, Hartfort, CT).

Presz, W. M., Reynolds, G., and McCormick, D. (**1994**). "Thrust augmentation using mixer-ejector-diffuser systems," in *32nd Aerospace sciences Meeting* (AIAA paper, Reno, NV).

Qian, Y., d'Humières, D., and Lallemand, P. (**1992**). "Lattice BGK models for Navier-Stokes equation," EPL (Europhysics Letters) **17**, 479.

Qian, Y. H. (**1990**). "Lattice gas and lattice kinetic theory applied to the Navier-Stokes equations," Doktorarbeit, Universite Pierre et Marie Curie, Paris.

Rafat, Y. (**2014**). "Experimental and Numerical Study of Acoustic Streaming with Applications in Thermoacoustic Refrigerator," (McGill University Libraries).

Russ, S., and Strykowski, P. (**1993**). "Turbulent structure and entrainment in heated jets: The effect of initial conditions," Physics of Fluids A: Fluid Dynamics **5**, 3216-3225.

Salman, H. (**2001**). "Numerical simulation of streamwise vorticity enhanced mixing," (© Hayder Salman).

Salman, H., McGuirk, J. J., and Page, G. J. (**1999**). "A numerical study of vortex interactions in lobed mixer flow fields," in *30th Fluid Dynamics Conference*.

Saravanamuttoo, H., Rogers, G. F., Cohen, H., and Straznicky, P. (**2001**). *Gas turbine theory 6th edition* (Pearson Education Canada, Chapter 9).

Schlichting, H., Gersten, K., and Gersten, K. (**2000**). *Boundary-layer theory* (Springer Science & Business Media).

Seiner, J. M., Ponton, M. K., Jansen, B. J., and Lagen, N. T. (**1992**). "The effects of temperature on supersonic jet noise emission," in *14th DGLR/AIAA aeroacoustics conference*, pp. 295-307.

Semlitsch, B. (**2014**). "Large eddy simulation of turbulent compressible jets," (KTH Royal Institute of Technology).

Semlitsch, B., Mihaescu, M., Fuchs, L., and Gutmark, E. (**2013**). "Analyzing the impact of the inlet temperature on the acoustic noise production form a supersonic jet using large eddy simulations," in *Proceedings of Meetings on Acoustics ICA2013* (ASA), p. 030011.

Sert, C., and Beskok, A. (**2003**). "Numerical simulation of reciprocating flow forced convection in two-dimensional channels," Journal of Heat Transfer **125**, 403-412.

Seto, K., Matsouka, M., and Maeda, T. (**1987**). "Study of Porous Tubes as a Noise Suppressor: 1st Report, Experiments on Fundamental Characteristics and Optimal Length," JSME international journal: bulletin of the JSME **30**, 1505.

Shan, X. (**1997**). "Simulation of Rayleigh-Bénard convection using a lattice Boltzmann method," Physical Review E **55**, 2780.

Shan, X., Yuan, X.-F., and Chen, H. (**2006**). "Kinetic theory representation of hydrodynamics: a way beyond the Navier–Stokes equation," Journal of Fluid Mechanics **550**, 413-441.

Sheng, Z.-q. (**2017**). "Jet mixing of lobed nozzles with spoilers located at lobe peaks," Applied Thermal Engineering.

Shock, R. A., Mallick, S., Chen, H., Yakhot, V., and Zhang, R. (**2002**). "Recent results on two-dimensional airfoils using a lattice Boltzmann-based algorithm," Journal of aircraft **39**, 434-439.

shumpert, P. K. (**1980**). "An experimental model investigation of Turbofan Engine Internal Exhaust Gas /Mixer Configurations " in *18th Aerospace Sciences Meeting* (AIAA, Pasadena, CA), pp. AIAA-

Shur, M. L., Spalart, P. R., and Strelets, M. K. (**2005a**). "Noise prediction for increasingly complex jets. Part I: Methods and tests," International Journal of Aeroacoustics **4**, 213-246.

Shur, M. L., Spalart, P. R., and Strelets, M. K. (**2005b**). "Noise prediction for increasingly complex jets. Part II: Applications," International Journal of Aeroacoustics **4**, 246-266.

Siegel, R. (**1987**). "Influence of oscillation-induced diffusion on heat transfer in a uniformly heated channel," Journal of heat transfer **109**, 244-247.

Stone, J., Krejsa, E., and Clark, B. (**2003**). "Semi-Empirical Model for Coannular Nozzle Component Noise Extraction and Correlation Including the Effects of Noise Reduction Devices," in *41st Aerospace Sciences Meeting and Exhibit*, p. 1060.

Succi, S. (**2001**). *The lattice Boltzmann equation: for fluid dynamics and beyond* (Oxford university press).

Succi, S., Karlin, I. V., and Chen, H. (**2002**). "Colloquium: Role of the H theorem in lattice Boltzmann hydrodynamic simulations," Reviews of Modern Physics **74**, 1203.

Sun, C., Pérot, F., Zhang, R., Freed, D. M., and Chen, H. (**2013**). "Impedance Boundary Condition for Lattice Boltzmann Model," COMMUNICATIONS IN COMPUTATIONAL PHYSICS **13**, 757-768.

Sun, C., PéRot, F. L., Zhang, R., Chen, H., Freed, D. M., and Staroselsky, I. (**2015**). "Computer simulation of fluid flow and acoustic behaviour," (Google Patents).

Tam, C. K., Golebiowski, M., and Seiner, J. M. (**1996**). *On the two components of turbulent mixing noise from supersonic jets* (American Institute of Aeronautics and Astronautics).

Tam, C. K., Ju, H., Jones, M. G., Watson, W. R., and Parrott, T. L. (**2005**). "A computational and experimental study of slit resonators," Journal of Sound and Vibration **284**, 947-984.

Tam, C. K., Kurbatskii, K. A., Ahuja, K., and Gaeta Jr, R. (**2001**). "A numerical and experimental investigation of the dissipation mechanisms of resonant acoustic liners," Journal of Sound and Vibration **245**, 545-557.

Tam, C. K., Viswanathan, K., Ahuja, K., and Panda, J. (**2008a**). "The sources of jet noise: experimental evidence," Journal of Fluid Mechanics **615**, 253-292.

Tam, C. K., Viswanathan, K., Ahuja, K., and Panda, J. (**2008b**). "The sources of jet noise: experimental evidence," Journal of Fluid Mechanics **615**, 253-292.

Tanna, H. (**1977**). "An experimental study of jet noise Part I: Turbulent mixing noise," Journal of Sound and Vibration **50**, 405-428.

Tanna, H., Dean, P., and Burrin, R. (**1976**). "The generation and radiation of supersonic jet noise; volume III turbulent mixing noise data," Afapl–tr–76–65, Air Force Aeropropulsion Laboratory, Lockheed Georgia Company, Marietta, Georgia **30063**.

Teixeira, C. M. (**1998**). "Incorporating turbulence models into the lattice-Boltzmann method," International Journal of Modern Physics C **9**, 1159-1175.

Tennekes, H., Lumley, J. L., and Lumley, J. (**1972**). *A first course in turbulence* (MIT press).

Tester, B., and Morfey, C. (**1976**). "Developments in jet noise modelling—theoretical predictions and comparisons with measured data," Journal of Sound and Vibration **46**, 79-103.

Tester, B., and Morfey, C. (**2009**). "Jet mixing noise: a review of single stream temperature effects," AIAA Paper **3376**, 2009.

Tester, B. J., and Fisher, M. J. (**2004**). "A contribution to the understanding and prediction of jet noise generation in forced mixers, Part II: Flight effects," in *11th AIAA/CEAS Aeroacoustics Conference*, p. 3094.

Tester, B. J., and Fisher, M. J. (**2006**). "A contribution to the understanding and prediction of jet noise generation by forced mixers: Part III applications," AIAA Paper **2542**.

Tester, B. J., Fisher, M. J., and Dalton, N. (**2004**). "A contribution to the understanding and prediction of jet noise generation by forced mixers," AIAA Paper **2897**.

Thompson, K. W. (**1990**). "Time-dependent boundary conditions for hyperbolic systems, II," Journal of Computational Physics **89**, 439-461.

Tinney, C., and Jordan, P. (**2008**). "The near pressure field of co-axial subsonic jets," Journal of Fluid Mechanics **611**, 175-204.

Toman, K. (**1984**). "Christian Doppler and the Doppler effect," Eos, Transactions American Geophysical Union **65**, 1193-1194.

Travin, A., Shur, M., Spalart, P., and Strelets, M. (**2004**). "On URANS solutions with LES-like behaviour," in *Proceedings of ECCOMAS congress on Computational Methods in Applied Science and Engineering, Jyväskylä, Finland*, pp. 24-28.

Tristanto, I., Page, G., and McGuirk, J. (**2006**). "Large-Eddy Simulation of Hot Coaxial Jets," in *12th AIAA/CEAS Aeroacoustics Conference (27th AIAA Aeroacoustics Conference)*, p. 2497.

Uzun, A., and Hussaini, M. Y. (**2006**). "High frequency noise generation in the near nozzle region of a jet," in *12th AIAA/CEAS Aeroacoustics Conference* (Cambridge, MA), pp. AIAA 2006-2499.

Uzun, A., and Hussaini, M. Y. (**2007**). "Noise generation in the near-nozzle region of a chevron nozzle jet flow," in *13th AIAA/CEAS Aeroacoustics Conference* (Tallahassee, FL), pp. AIAA 2007-3596.

Uzun, A., Lyrintzis, A. S., and Blaisdell, G. A. (**2004**). "Coupling of integral acoustics methods with LES for jet noise prediction," International Journal of Aeroacoustics **3**, 297-346.

Viswanathan, K. (**2002**). "Analysis of the two similarity components of turbulent mixing noise," AIAA journal **40**, 1735-1744.

Viswanathan, K. (**2004**). "Aeroacoustics of hot jets," Journal of Fluid Mechanics **516**, 39-82.

Viswanathan, K., Shur, M., Spalart, P., and Strelets, M. (**2006**). "Computation of the flow and noise of round and beveled nozzles," in *12th AIAA/CEAS Aeroacoustics Conference (27th AIAA Aeroacoustics Conference)*, p. 2445.

Vlasenko, V., Bosniakov, S., Mikhailov, S., Morozov, A., and Troshin, A. (**2010**). "Computational approach for investigation of thrust and acoustic performances of present-day nozzles," Progress in Aerospace Sciences **46**, 141-197.

Vuillemin, A., Loheac, P., Rahier, G., Vuillot, F., and Lupoglazoff, N. (**2005**). "Aeroacoustic numerical method assessment for a double stream nozzle," in *11th AIAA/CEAS Aeroacoustics Conference*, p. 3043.

Waitz, I., Qiu, Y., Manning, T., Fung, A., Elliot, J., Kerwin, J., Krasnodebski, J., O'Sullivan, M., Tew, D., and Greitzer, E. (**1997**). "Enhanced mixing with streamwise vorticity," Progress in Aerospace Sciences **33**, 323-351.

Wells, V., and Han, A. (**1995**). "Acoustics of a moving source in a moving medium with application to propeller noise," Journal of sound and vibration **184**, 651-663.

Wendoloski, J. (**1998**). "Sound absorption by an orifice plate in a flow duct," The Journal of the Acoustical Society of America **104**, 122-132.

Wenisch, P., Treeck, C. v., Borrmann, A., Rank, E., and Wenisch, O. (**2007**). "Computational steering on distributed systems: Indoor comfort simulations as a case study of interactive CFD on supercomputers," International Journal of Parallel, Emergent and Distributed Systems **22**, 275-291.

Werle, M., Presz Jr, W., and Paterson, R. (**1987**). "Flow structure in a periodic axial vortex array," in *25th AIAA Aerospace Sciences Meeting*.

Wheatley, P. O., and Gerald, C. F. (**1984**). *Applied Numerical Analysis* (Addison-Wesley Publishing Company).

White, F. M., and Corfield, I. (**2006**). *Viscous fluid flow* (McGraw-Hill New York).

Wilcox, D. C. (**1998**). *Turbulence modeling for CFD* (DCW industries La Canada, CA).

Wittmann, M., Zeiser, T., Hager, G., and Wellein, G. (**2013**). "Comparison of different propagation steps for lattice Boltzmann methods," Computers & Mathematics with Applications **65**, 924-935.

Witze, P. (**1974**). "Centreline velocity decay of compressible free jets," AIAA Journal **12**, 417-418.

Wolf-Gladrow, D. A. (**2000**). *Lattice-gas cellular automata and lattice Boltzmann models: An Introduction* (Springer).

Worlikar, A. S., Knio, O. M., and Klein, R. (**1998**). "Numerical Simulation of a Thermoacoustic Refrigerator: II. Stratified Flow Around the Stack," Journal of Computational Physics **144**, 299-324.

Xie, Z., Ikeda, T., Okuda, Y., and Nakajima, H. (**2004**). "Sound absorption characteristics of lotus-type porous copper fabricated by unidirectional solidification," Materials Science and Engineering: A **386**, 390-395.

Yakhot, V., and Orszag, S. A. (**1986**). "Renormalization group analysis of turbulence. I. Basic theory," Journal of scientific computing **1**, 3-51.

Yakhot, V., Orszag, S. A., and Yakhot, A. (**1987**). "Heat transfer in turbulent fluids—I. Pipe flow," International journal of heat and mass transfer **30**, 15-22.

Yu, H., and Girimaji, S. S. (**2005**). "Near-field turbulent simulations of rectangular jets using lattice Boltzmann method," Physics of Fluids (1994-present) **17**, 125106.

Zaman, K. (**1986**). "Flow field and near and far sound field of a subsonic jet," Journal of sound and vibration **106**, 1-16.

Zaman, K. (**1998**). "Asymptotic spreading rate of initially compressible jets—experiment and analysis," Physics of Fluids **10**, 2652.

Zaman, K. (**2012**). "Effect of initial boundary-layer state on subsonic jet noise," AIAA journal **50**, 1784-1795.

Zhang, R., and Chen, H. (**2002**). "A Lattice Boltzmann method for simulations of liquid-vapor thermal flows," Physical Review E **67**, 066711.

Zhao, T., and Cheng, P. (**1995**). "A numerical solution of laminar forced convection in a heated pipe subjected to a reciprocating flow," International journal of heat and mass transfer **38**, 3011-3022.

Zhao, W. (**2000**). "A numerical investigation of sound radiated from subsonic jets with application to human phonation," in *Mechanical Engineering* (Purdue).

Zhou, Y., Zhang, R., Staroselsky, I., and Chen, H. (**2004**). "Numerical simulation of laminar and turbulent buoyancy-driven flows using a lattice Boltzmann based algorithm," International journal of heat and mass transfer **47**, 4869-4879.

Zou, Q., and He, X. (**1997**). "On pressure and velocity boundary conditions for the lattice Boltzmann BGK model," Physics of Fluids (1994-present) **9**, 1591-1598.